

PRE-FAILURE STRESS-STRAIN BEHAVIOR  
AND STRENGTH OF BANGKOK CLAY

Miss. Wanwarang Ratananikom

A Dissertation Submitted in Partial Fulfillment of the Requirements  
for the Degree of Doctor of Philosophy Program in Civil Engineering

Department of Civil Engineering

Faculty of Engineering

Chulalongkorn University

Academic Year 2011

Copyright of Chulalongkorn University

บทคัดย่อและแฟ้มข้อมูลฉบับเต็มของวิทยานิพนธ์ตั้งแต่ปีการศึกษา 2554 ที่ให้บริการในคลังปัญญาจุฬาฯ (CUIR)  
เป็นแฟ้มข้อมูลของนิสิตเจ้าของวิทยานิพนธ์ที่ส่งผ่านทางบัณฑิตวิทยาลัย

The abstract and full text of theses from the academic year 2011 in Chulalongkorn University Intellectual Repository(CUIR)  
are the thesis authors' files submitted through the Graduate School.

พฤติกรรมความเค้น-ความเครียดก่อนการวิบัติและกำลังของดินเหนียวกรุงเทพฯ

นางสาววรรณวรางค์ รัตนานิคม

วิทยานิพนธ์นี้เป็นส่วนหนึ่งของการศึกษาตามหลักสูตรปริญญาวิศวกรรมศาสตรดุษฎีบัณฑิต

สาขาวิชาวิศวกรรมโยธา ภาควิชาวิศวกรรมโยธา

คณะวิศวกรรมศาสตร์ จุฬาลงกรณ์มหาวิทยาลัย

ปีการศึกษา 2554

ลิขสิทธิ์ของจุฬาลงกรณ์มหาวิทยาลัย

Thesis Title            PRE-FAILURE STRESS-STRAIN BEHAVIOR AND  
STRENGTH OF BANGKOK CLAY  
By                         Miss Wanwarang Ratananikom  
Field of Study           Civil Engineering  
Thesis Advisor         Associate Professor Suched Likitlersuang, D.Phil  
Thesis Co-advisor     Assistant Professor Fumihiko Fukuda, Ph.D.

---

Accepted by the Faculty of Engineering, Chulalongkorn University in  
Partial Fulfillment of the Requirements for the Doctoral Degree

.....Dean of the Faculty of Engineering  
(Associate Professor Boonsom Lerthirunwong, Dr.Ing.)

#### THESIS COMMITTEE

..... Chairman  
(Associate Professor Supot Teachavorasinskun, D.Eng.)

..... Thesis Advisor  
(Associate Professor Suched Likitlersuang, D.Phil)

..... Thesis Co-advisor  
(Assistant Professor Fumihiko Fukuda, Ph.D.)

..... Examiner  
(Associate Professor Boonchai Ukritchon, Sc.D.)

..... Examiner  
(Associate Professor Tirawat Boonyatee, D.Eng.)

..... External Examiner  
(Assistant Professor Siam Yimsiri, Ph.D.)

วรรณวรางค์ รัตนานิคม: พฤติกรรมความเค้น-ความเครียดก่อนการวิบัติและกำลังของดินเหนียวกรุงเทพฯ. (Pre-failure stress-strain behavior and strength of Bangkok Clay)  
 อ. ที่ปรึกษาวิทยานิพนธ์หลัก: รศ.ดร. สุเชษฐ์ ลิขิตเลอสรวง, อ. ที่ปรึกษาวิทยานิพนธ์ร่วม:  
 ผศ.ดร. พุมิอิโกะ ฟูกุดะ, 182 หน้า.

งานวิจัยจำนวนมากแสดงว่าความสัมพันธ์ระหว่างความเค้นและความเครียดของดินมีลักษณะแบบไม่เป็นเส้นตรง นอกจากนั้นค่าโมดูลัสของดินที่ระดับความเครียดต่ำมีความสำคัญมากในการวิเคราะห์ปัญหาทั่วไปทางด้านวิศวกรรมธรณีเทคนิค แม้ว่าในปัจจุบันพฤติกรรมของดินเหนียวกรุงเทพฯจะถูกศึกษาวิจัยอย่างกว้างขวาง แต่อย่างไรก็ตามการศึกษาเกี่ยวกับความสัมพันธ์ระหว่างความเค้นและความเครียดของดินกรุงเทพฯในช่วงความเครียดระดับต่ำถึงปานกลางโดยใช้เครื่องมือวัดความเครียดภายในยังคงขาดแคลนอยู่ ดังนั้นวัตถุประสงค์ของงานวิจัยนี้คือศึกษาความสัมพันธ์ระหว่างความเค้นและความเครียดที่ไม่เป็นเส้นตรงของดินเหนียวกรุงเทพฯในช่วงระดับความเครียดต่ำถึงปานกลาง รวมถึงศึกษาพฤติกรรมที่ไม่เท่ากันทุกทิศทางของดินเหนียวกรุงเทพฯด้วย แต่เนื่องจากระดับความเครียดที่สนใจนี้เล็กกว่าความสามารถของเครื่องทดสอบแรงอัดสามแกนแบบดั้งเดิมที่จะวัดได้ ดังนั้นจึงมีการพัฒนาการทดสอบแรงอัดสามแกนให้สามารถศึกษาพฤติกรรมที่ไม่เป็นเส้นตรงของดินนี้ได้โดยเฉพาะในช่วงความเครียดต่ำ โดยติดตั้งระบบวัดความเครียดภายในและระบบเบนเดอริอิลิเมนต์ การทดสอบการอัดตัวคายน้ำแบบเท่ากันทุกทิศทางและเงื่อนไขด้วยแรงอัดแบบไม่ระบายน้ำและระบายน้ำถูกทดสอบขึ้นในตัวอย่างดินเหนียวกรุงเทพฯที่ถูกตัดทิ้งในทิศทางแนวตั้งและแนวนอน เพื่อให้สามารถศึกษาพฤติกรรมที่ไม่เท่ากันทุกทิศทางของดินเหนียวกรุงเทพฯได้ นอกจากนั้นงานวิจัยนี้ยังศึกษาเกี่ยวกับผลกระทบของทิศทางความเค้นหลักและขนาดความเค้นกลางที่เปลี่ยนไปต่อพฤติกรรมของดินเหนียวกรุงเทพฯในเงื่อนไขแบบไม่ระบายน้ำด้วย ผลการทดสอบที่ได้จากงานวิจัยนี้สามารถทำให้เข้าใจในพฤติกรรมของดินเหนียวกรุงเทพฯในเชิงลึกและสามารถนำไปใช้เป็นข้อมูลพื้นฐานในการพัฒนาแบบจำลองทางคณิตศาสตร์ของดินเหนียวกรุงเทพฯต่อไปในอนาคตได้

ภาควิชา.....วิศวกรรมโยธา..... ลายมือชื่อนิสิต.....  
 สาขาวิชา.....วิศวกรรมโยธา..... ลายมือชื่อ อ.ที่ปรึกษาวิทยานิพนธ์หลัก.....  
 ปีการศึกษา.....2554..... ลายมือชื่อ อ.ที่ปรึกษาวิทยานิพนธ์ร่วม.....

# # 487 18506 21: MAJOR CIVIL ENGINEERING

KEYWORDS: STRESS-STRAIN BEHAVIOR / ANISOTROPY / LOCAL MEASUREMENT / BENDER ELEMENT / TRIAXIAL TEST / MAJOR PRINCIPAL STRESS / INTERMEDIATE PRINCIPAL STRESS / TORSIONAL SHEAR HOLLOW CYLINDER TEST / BANGKOK CLAY

WANWARANG RATANANIKOM: PRE-FAILURE STRESS-STRAIN BEHAVIOR AND STRENGTH OF BANGKOK CLAY. ADVISOR: ASSOC.PROF.SUCHED LIKITLERSUANG, D.Phil., CO-ADVISOR: ASST.PROF.FUMIHIKO FUKUDA, Ph.D., 182 pp.

Many recent research works have suggested that the stress-strain behavior of soil is highly non-linear and the small strain stiffness of soil is very important for the analysis of the boundary value problems. Although, there are a lot of studies on the behaviors of Bangkok Clay, there is not data on the stress-strain behavior at small- and intermediate-strain level from local strain measurement available at present. This research aims to investigate the stress-strain non-linearity behavior of undisturbed sample of Bangkok Clay with particular attention to its small- and intermediate-strain behavior and also anisotropic characteristic by using the conventional triaxial apparatus incorporating with the local strain measurement systems and bender element system. Both of isotropically consolidated undrained and drained compression tests (CIUC/CIDC) were performed on the vertically and horizontally cut specimens in order to study anisotropic characteristic. Moreover, this research also studies the effects of principal stress rotation and intermediate principal stress on undrained behavior of Bangkok Clay. The results of torsional shear hollow cylinder with various principal stress directions and various magnitude of intermediate principal stress on undisturbed Bangkok Clay are presented. These experimental results should provide further understanding about Bangkok Clay behavior and be also useful for the development of new constitutive models for Bangkok Clay.

Department : ..... Civil Engineering ..... Student's Signature .....

Field of Study : ..... Civil Engineering ..... Advisor's Signature .....

Academic Year : ..... 2011 ..... Co-advisor's Signature .....

## **ACKNOWLEDGEMENTS**

The research would have not been possible without the support of many people whom it is appropriate to acknowledge and thank.

I would like to express my sincere gratitude to my advisor, Associate Professor Dr. Suched Likitlersuang and co-advisor, Assistant Professor Dr. Siam Yimsiri for their valuable suggestions and guidance throughout my research.

I would like to extend my sincere gratitude to thank Assistant Professor Dr. Fumihiko Fukuda from Hokkaido University, Japan for giving me a chance to conduct some parts of my research in his lab and for his valuable advices, helps and suggestions thought out the whole time in Japan. All his members in the Lab are also appreciated for their helps and supports.

I specially thank The Commission on Higher Education, Thailand for providing the Ph.D. scholarship.

Finally, I owe the greatest debt of gratitude to my beloved family; my parents, my aunts and my sister for their continuous encouragements, supports and belief.

# CONTENTS

|  | Page |
|--|------|
| <b>ABSTRACT (THAI)</b> .....   | iv   |
| <b>ABSTRACT (ENGLISH)</b> .....  | v    |
| <b>ACKNOWLEDGEMENTS</b> .....  | vi   |
| <b>CONTENTS</b> .....  | vii  |
| <b>LIST OF TABLES</b> .....  | xi   |
| <b>LIST OF FIGURES</b> .....   | xiii |
| <b>LIST OF SYMBOLS</b> .....   | xx   |
| <b>CHAPTERS</b>  |      |
| <b>1 Introduction</b>  |      |
| 1.1 Background.....  | 1    |
| 1.2 Objectives .....   | 2    |
| 1.3 Scope.....   | 3    |
| 1.4 Layout .....   | 3    |
| <b>2 Literature review</b>   |      |
| 2.1 Introduction.....  | 5    |
| 2.2 Factors affecting small-strain behavior.....                         | 6    |
| 2.2.1 Effective stress state.....  | 9    |
| 2.2.2 Stress history .....   | 11   |
| 2.2.3 Void ratio .....   | 11   |
| 2.2.4 Stress ratio.....  | 13   |
| 2.2.5 Aging and time effect.....   | 14   |
| 2.2.6 Recent stress history (immediate stress path) .....                | 14   |
| 2.3 Measurement of stress-strain characteristic at wide strain range.... | 17   |
| 2.3.1 Advanced triaxial test .....                                       | 18   |
| 2.3.2 Bender element test.....   | 19   |
| 2.3.3 Shear-plate transducer.....  | 19   |
| 2.3.4 Resonant column test .....   | 20   |
| 2.3.5 Torsional shear hollow cylinder test.....                          | 20   |
| 2.4 Anisotropy.....  | 21   |

|  | Page |
|--|------|
| 2.4.1 Inherent anisotropy .....  | 21   |
| 2.4.2 Stress induced anisotropy .....  | 24   |
| 2.4.3 Practical implications of soil anisotropy .....  | 26   |
| 2.5 Study of anisotropy using torsional shear hollow cylinder test .....                                   | 29   |
| 2.5.1 Definitions of $\alpha$ and $b$ .....  | 29   |
| 2.5.2 Suitability of torsional shear hollow cylinder apparatus to<br>study soil anisotropic behavior ..... | 31   |
| 2.5.3 Non-uniformity on hollow cylinder specimen .....   | 33   |
| 2.5.4 Previous studies of stress and strain non-uniformity .....   | 35   |
| 2.5.5 Previous studies of effects of $\alpha$ and $b$ on soil response .....                               | 44   |
| <b>3 Triaxial Testing Apparatus, Testing Procedures and Testing Program</b>                                |      |
| 3.1 Introduction .....   | 60   |
| 3.2 Triaxial test .....  | 60   |
| 3.2.1 Conventional triaxial testing system .....   | 60   |
| 3.2.2 Triaxial system set-up .....   | 61   |
| 3.3 Development of conventional triaxial apparatus .....   | 63   |
| 3.3.1 Local strain measurement system .....  | 63   |
| 3.3.2 Pulse transmission by bender element system .....  | 65   |
| 3.4 Triaxial testing program .....   | 69   |
| 3.4.1 Sampling .....   | 69   |
| 3.4.2 Sample preparation .....   | 70   |
| 3.4.3 Specimen set-up .....  | 71   |
| 3.4.4 Saturation .....   | 71   |
| 3.4.5 Isotropic consolidation .....  | 71   |
| 3.4.6 Rest period .....  | 72   |
| 3.4.7 Compression shearing .....   | 72   |
| 3.4.8 Data processing .....  | 72   |
| <b>4 Results of triaxial test</b>  |      |
| 4.1 Introduction .....   | 75   |
| 4.2 Isotropic consolidation .....  | 75   |



|  | Page |
|--|------|
| 4.2.1 Consolidation parameters .....   | 75   |
| 4.2.2 Anisotropic deformation during isotropic consolidation .....                                     | 77   |
| 4.2.3 Bulk modulus during isotropic consolidation .....  | 81   |
| 4.3 Small-strain stiffness characteristics.....  | 83   |
| 4.3.1 Small-strain shear modulus obtained from bender element<br>test .....                            | 83   |
| 4.3.2 Small-strain Young's modulus obtained from triaxial test ...                                     | 84   |
| 4.3.3 Anisotropy of small-strain shear modulus .....   | 86   |
| 4.3.4 Determination of cross-anisotropic elastic parameters .....                                      | 86   |
| 4.3.5 Application of cross-anisotropic elastic parameters .....  | 89   |
| 4.4 Small-strain stiffness characteristics.....  | 95   |
| 4.4.1 Non-linearity in undrained and drained condition .....   | 95   |
| 4.4.2 Anisotropy of stress-strain relationship .....   | 96   |
| 4.5 Optimization of cross-anisotropic elastic parameters .....   | 101  |
| 4.5.1 Three-parameter cross-anisotropic elastic model proposed<br>by Graham & Houlsby (1983) .....     | 101  |
| 4.5.2 Optimization .....   | 103  |
| <b>5 Torsional Shear Hollow Cylinder Testing Apparatus, Testing Procedures and<br/>Testing Program</b> |      |
| 5.1 Introduction.....  | 110  |
| 5.2 Torsional shear hollow cylinder testing system.....  | 110  |
| 5.3 Principal of torsional shear hollow cylinder test.....   | 114  |
| 5.4 Stress and strain calculation.....   | 115  |
| 5.5 Computer control and data acquisition .....  | 118  |
| 5.6 Torsional shear hollow cylinder program .....  | 121  |
| 5.6.1 Sampling .....   | 121  |
| 5.6.2 Sample preparation .....   | 121  |
| 5.6.3 Specimen set-up .....  | 124  |
| 5.6.4 Saturation .....   | 126  |
| 5.6.5 Isotropic consolidation.....   | 126  |
| 5.6.6 Checking of excess pore water pressure .....   | 127  |

|   | Page |
|---|------|
| 5.6.7 Compression shearing.....   | 127  |
| <b>6 Results of Torsional Shear Hollow Cylinder Test</b>                    |      |
| 6.1 Introduction.....   | 128  |
| 6.2 Isotropic consolidation.....  | 129  |
| 6.2.1 Compressibility of isotropic consolidated Bangkok Clay ....           | 129  |
| 6.2.2 Anisotropic deformation during isotropic consolidation .....          | 130  |
| 6.3 Stress-strain and pore pressure behavior.....                           | 132  |
| 6.3.1 Effects of $\alpha$ on stress-strain and pore pressure behavior ..... | 132  |
| 6.3.2 Effects of $b$ on stress-strain and pore pressure behavior.....       | 135  |
| 6.4 Strength behavior .....   | 137  |
| 6.4.1 Undrained shear strength .....  | 137  |
| 6.4.2 Friction angle .....  | 140  |
| 6.4.3 Excess pore water pressure .....                                      | 146  |
| 6.5 Stiffness characteristics.....  | 148  |
| 6.5.1 Effects of $\alpha$ on stiffness characteristics .....                | 148  |
| 6.5.2 Effects of $b$ on stiffness characteristics .....                     | 152  |
| 6.5.3 Effects of $\alpha$ on Young's modulus .....                          | 155  |
| 6.6 Relationships between individual stress and strain components ....      | 156  |
| 6.6.1 Cross-coupling terms .....  | 156  |
| 6.6.2 Plain strain condition .....  | 158  |
| 6.6.3 Directions of principal stress and strain inclination.....            | 158  |
| 6.7 Failure surface.....  | 162  |
| <b>7 Conclusions</b>  |      |
| 7.1 Deformation under isotropic consolidation .....                         | 167  |
| 7.2 Cross-Anisotropic elastic parameter of Bangkok Clay.....                | 167  |
| 7.3 Anisotropy of Bangkok Clay .....  | 168  |
| 7.4 Effects of $\alpha$ and $b$ on Bangkok Clay characteristic .....        | 168  |
| 7.5 Failure surface and plastic potential .....                             | 169  |
| <b>REFERENCE</b> .....  | 171  |
| <b>BIOGRAPHY</b> .....  | 182  |

## LIST OF TABLES

|   | Page |
|---|------|
| Table 2.1 Constants of proposed equations of small-strain modulus in the form of $\frac{G_{\max}}{p_a} = Sf(e)\left(\frac{p'}{p_a}\right)^n$ (Yimsiri and Soga, 2000) ..... | 7    |
| Table 2.2 The ratio of anisotropy of shear wave velocity from in-situ tests (Jamiołkowski <i>et al.</i> , 1995).....  | 24   |
| Table 2.3 HCA tests on reconstituted $K_0$ recompression clayey soils and non-plastic silt at Imperial College London.....  | 52   |
| Table 3.1 Characteristics of the transducers used .....   | 74   |
| Table 4.1 Specimen characteristics for detailed study .....   | 77   |
| Table 4.2 Ratios of $\Delta\varepsilon_a/\Delta\varepsilon_r$ during isotropic consolidation .....  | 79   |
| Table 4.3 Small-strain bulk modulus during isotropic consolidation .....  | 82   |
| Table 4.4 Small-strain Young's modulus .....  | 85   |
| Table 4.5 Small-strain Poisson's ratios.....  | 87   |
| Table 4.6 Predictions of undrained small-strain Young's modulus.....  | 94   |
| Table 4.7 Measured values of elastic parameters .....   | 105  |
| Table 4.8 Calculated values of elastic parameters .....   | 107  |
| Table 5.1 Characteristics of the transducers used .....   | 113  |
| Table 5.2 Specimen characteristics for detailed study .....   | 120  |
| Table 5.3 Details of stress during saturation.....  | 127  |
| Table 6.1 Values of $\alpha$ and $b$ in the torsional shear testing program .....   | 129  |
| Table 6.2 Ratios of $\Delta\varepsilon_1/\Delta\varepsilon_3$ during isotropic consolidation .....  | 131  |
| Table 6.3 Values of $s_u/p_o'$ at varies $b$ and $\alpha$ .....   | 139  |
| Table 6.4 Values of $\phi'_{\max}$ at varies $\alpha$ and $b$ .....   | 142  |
| Table 6.5 Values of $u_f/p_o'$ at varies $\alpha$ and $b$ .....   | 146  |
| Table 6.6 Values of $G_{oct(eq=0.01\%)/p_o'}$ at varies $\alpha$ and $b$ .....  | 149  |
| Table 6.7 Values of non-linearity index of stiffness degradation curve .....  | 149  |
| Table 6.8 Failure criteria.....   | 163  |
| Table 6.9 Summarized $\phi'_{\max}$ and $M_{\max}$ in failure surface .....   | 164  |

|   | Page |
|---|------|
| Table 6.10 Lode angles of stress and strain increment ..... | 164  |
| Table 7.1 Summary of effects of $\alpha$ and $b$ .....      | 168  |

## LIST OF FIGURES

|   | Page |
|---|------|
| Figure 2.1 Stiffness degradation curve (a) the strain levels observed during the typical geotechnical structures construction (after Mair, 1993) and (b) the strain levels that can be observed by various techniques (after Atkinson, 2000)..... | 5    |
| Figure 2.2 Effect of stress level on small-strain shear modulus of many geomaterials (Coop and Jovicic, 1999 ).....   | 9    |
| Figure 2.3 Figure 2.3 Shear wave velocities variation in different directions as a function of anisotropic stress (Stokoe et al., 1995).....  | 10   |
| Figure 2.4 P-wave velocities variation in different directions as a function of anisotropic stress (Stokoe et al., 1995).....   | 10   |
| Figure 2.5 Effect of void ratio on shear stiffness of HRS for (a) isotropic effective stress state and (b) anisotropic effective stress state (Kuwano, 1999) .....  | 12   |
| Figure 2.6 Time (creep) effect on the shear stiffness of calcareous sand samples (Jovicic and Coop, 1997) .....   | 15   |
| Figure 2.7 Effect of recent stress history on stiffness degradation; (a) stress paths and (b) stiffness degradation on <i>OX</i> stress path (Atkinson et al., 1990) .....  | 16   |
| Figure 2.8 Strain ranges achieved from various tests (Ishihara, 1996) .....   | 18   |
| Figure 2.9 Shear-plate transducer (Brignoli et al., 1006).....  | 20   |
| Figure 2.10 Effect of Syncrude sand sample formation on undrained simple shear response (Vaid et al., 1995).....  | 22   |
| Figure 2.11 Anisotropic stiffness of London clay under isotropic stress conditions (Jovicic and Coop, 1998) .....   | 22   |
| Figure 2.12 Sample orientation, stress paths and definition of measurement of anisotropy in the DSC (Wong and Arthur, 1985).....  | 25   |
| Figure 2.13 Stress-strain relationship of inherently anisotropic dense sand (Wong and Arthur, 1985).....  | 26   |

|   | Page |
|---|------|
| Figure 2.14 Contours of $\sigma_1$ under embankment on soft clay from non-linear numerical analysis (Yeats, 1983).....                          | 27   |
| Figure 2.15 Contours of $\sigma_1$ directions close to an excavation in Thames gravel overlaying on London clay (Jardine, 1994).....            | 27   |
| Figure 2.16 (a) Plane view and (b) Cross-section of the Saint-alban test embankment (Zdravkovic et al., 2001a).....                             | 28   |
| Figure 2.17 Comparison of failure heights from different analyzes (Zdravkovic et al., 2001a).....   | 29   |
| Figure 2.18 Stress components acting on a soil element (a) Independent stress component (b) Principal stresses component.....                   | 30   |
| Figure 2.19 Directional shear cell (a) Stress components (b) Principal stresses and their directions .....                                      | 32   |
| Figure 2.20 Applicable stress states at failure in some the advanced laboratory strength devices .....  | 32   |
| Figure 2.21 Stress component in hollow cylinder samples including end-effects (after Saada and Townsend, 1981).....                             | 34   |
| Figure 2.22 Definitions used for stress non-uniformity (Hight et al., 1983)...  | 36   |
| Figure 2.23 Stress distributions across the hollow cylinder specimen wall (Hight et al., 1983).....   | 36   |
| Figure 2.24 Linear elastic analysis of stress distribution in fixed-end hollow cylinder elements of different heights (Hight et al., 1983)..... | 37   |
| Figure 2.25 Elastoplastic and elastic analyses of fixed-end 200 mm height hollow cylinder samples (Hight et al., 1983).....                     | 38   |
| Figure 2.26 Schematic diagram of “no-go” areas proposed by Hight et al. (1983).....   | 39   |
| Figure 2.27 Elastic stresses across the wall of hollow cylinder specimens (Sayão and Vaid, 1991) .....  | 40   |
| Figure 2.28 Effect of stress ratio on non-uniformity coefficients (Sayão and Vaid, 1991) .....  | 41   |
| Figure 2.29 Distribution of stress ratio across the wall of a hollow cylinder   |      |

|   | Page |
|---|------|
| sample at $p' = 300$ kPa, $R = 2.0$ and $Dr = 30\%$ (Wijewickreme and Vaid, 1991).....  | 42   |
| Figure 2.30 Contours of ${}_R\beta$ at $p' = 300$ kPa, $R = 2.0$ and $Dr = 30\%$ (Wijewickreme and Vaid, 1991).....   | 43   |
| Figure 2.31 Contours of ${}_R\beta$ at $p' = 300$ kPa, $R = 3.0$ and $Dr = 30\%$ (Wijewickreme and Vaid, 1991).....   | 43   |
| Figure 2.32 Stress ratio versus octahedral shear strain from HCA tests on isotropically consolidated, medium-loose HRS sheared drained with $b=0.5$ (Symes, 1983).....  | 45   |
| Figure 2.33 Mobilised $\phi'_{\text{peak}}$ at peak stress ratio from HCA tests on isotropically consolidated HRS sheared drained with $b=0.5$ (Symes, 1983) .....  | 45   |
| Figure 2.34 Stress-strain relationship from plane strain tests on isotropically consolidated dense Toyoura sand (Oda et al., 1978) .....  | 47   |
| Figure 2.35 Anisotropy of mobilised $\phi'$ at peak from plane strain tests on isotropically consolidated dense Toyoura sand (data from Oda et al., 1978); Note that $\alpha = 90 - \delta$ .....   | 48   |
| Figure 2.36 Development of octahedral shear strain in HCA tests on isotropically consolidated, medium-loose HRS with $b=0$ and various values of $\alpha$ (Shibuya, 1985).....  | 49   |
| Figure 2.37 Effective stress paths from HCA tests on isotropically consolidated HRS with $b=0$ and various values of $\alpha$ (Shibuya, 1985). Insert corresponds to the normalised undrained shear strength.....   | 49   |
| Figure 2.38 Anisotropy of undrained shear strength from isotropically and $K_0$ - consolidated HRS sand HCA samples (data from Shibuya, 1985 and Shibuya and Hight, 1996) .....   | 50   |
| Figure 2.39 Anisotropy of undrained shear strength at $b = 0.5$ of normally $K_0$ -consolidated soils ( $OCR = 1$ ) from the Imperial College database (Jardine et al., 1997). Values of $s_u$ taken at peak shear stress, and at phase transformation point (PT) for HPF4 specimens..... | 51   |

|  | Page |
|--|------|
| Figure 2.40 Effect of the principal stress direction on the ESP of isotropically consolidated Toyoura sand (Nakata et al., 1998).....  | 53   |
| Figure 2.41 Anisotropy of normalised undrained shear strength of isotropically consolidated Toyoura sand (data from Nakata et al., 1998) .....                                 | 53   |
| Figure 2.42 Effect of $b$ on the stress-strain response of isotropically consolidated medium-loose HRS ( $OCR=1$ ); (Symes, 1983) ...  | 54   |
| Figure 2.43 Effect of $b$ on the ultimate $\phi'$ of isotropically consolidated medium-loose HRS ( $OCR=1$ ); (Symes, 1983) .....  | 55   |
| Figure 2.44 Effect of $b$ on strain response of Syncrude sand (Sayão and Vaid, 1996) .....   | 56   |
| Figure 2.45 Effect of $b$ on the anisotropy of peak $\phi'$ (adapted from Zdravkovic, 1996).....   | 56   |
| Figure 2.46 Effect of $b$ on the response of isotropically consolidated HRS ( $OCR=1$ ); data from Shibuya (1985) .....  | 58   |
| Figure 2.47 Effect of $b$ on the undrained behaviour of isotropically consolidated Toyoura sand (Yoshimine et al, 1998) .....  | 59   |
| Figure 2.48 Effect of $b$ on the undrained strength of two isotropically consolidated sands sheared with $=45^\circ$ (data from Yoshimine et al., 1998 and Shibuya, 1985)..... | 59   |
| Figure 3.1 Triaxial system.....  | 61   |
| Figure 3.2 Digital pressure controller (Menzies, 1988) .....   | 62   |
| Figure 3.3 Floating-type LVDT .....  | 65   |
| Figure 3.4 Proximity transducer .....  | 65   |
| Figure 3.5 Piezoceramic bender element connected in series and parallel ...  | 66   |
| Figure 3.6 Bender element (Dyvik and Madshus, 1985) .....  | 67   |
| Figure 3.7 Set-up of bender element test (Viggiani and Atkinson, 1995b)...   | 67   |
| Figure 3.8 Typical oscilloscope signals form a bender element test.....  | 68   |
| Figure 3.9 Layout of vertical and horizontal specimen.....   | 70   |
| Figure 4.1 Isotropic consolidation curves .....  | 76   |
| Figure 4.2 Set-up of local strain measurements and bender element system   | 79   |



|   | Page |
|---|------|
| Figure 4.3 Anisotropic deformations during isotropic consolidation.....   | 80   |
| Figure 4.4 Ratios of $\Delta\varepsilon_a/\Delta\varepsilon_r$ with depth during isotropic consolidation .....  | 80   |
| Figure 4.5 Secant bulk modulus degradation curve .....  | 82   |
| Figure 4.6 Relationship between small-strain shear modulus and isotropic<br>confining stress .....  | 84   |
| Figure 4.7 Relationship between small-strain Young's modulus and<br>isotropic confining stress .....  | 85   |
| Figure 4.8 Predictions of undrained small-strain Young's modulus.....   | 93   |
| Figure 4.9 Predictions of undrained stress path direction .....   | 93   |
| Figure 4.10 Normalized stiffness degradation curves from undrained triaxial<br>compression tests .....  | 97   |
| Figure 4.11 Figure 4.11 Normalized stiffness degradation curves by small-<br>strain Young's modulus .....   | 98   |
| Figure 4.12 Anisotropy in undrained behavior .....  | 99   |
| Figure 4.13 Anisotropy in drained behavior .....  | 100  |
| Figure 4.14 Comparison between measured and calculated values of<br>Young's moduli .....  | 108  |
| Figure 4.15 Comparison between measured and calculated values of shear<br>moduli .....  | 108  |
| Figure 4.16 Comparison between measured and calculated values of<br>Poisson's ratios .....  | 109  |
| Figure 5.1 Torsional shear apparatus .....  | 111  |
| Figure 5.2 Hollow cylinder testing (a) Boundary loads (b) Individual stress<br>components and (c) Principal stresses and their directions<br>(Reinaldo, 2003) ..... | 112  |
| Figure 5.3 Definition of the major principal stress rotation angle $\alpha$<br>(Reinaldo, 2003) .....   | 114  |
| Figure 5.4 Generalized stress state: (a) Principal stresses; (b) Deviatoric<br>plane (Reinaldo, 2003).....  | 118  |
| Figure 5.5 Tools used for the preparation of hollow cylinder specimen.....  | 122  |

|             |  |      |
|-------------|--|------|
| Figure 5.6  | Stage of preparation of hollow cylinder specimen .....   | 123  |
|             |  | Page |
| Figure 5.7  | Stage of hollow cylinder specimen set-up .....   | 124  |
| Figure 5.8  | Top and bottom porous stones with radial brass blades .....  | 125  |
| Figure 6.1  | Compression curve in $e$ - $\ln p'$ plane .....  | 129  |
| Figure 6.2  | Anisotropic deformations during isotropic consolidation.....   | 131  |
| Figure 6.3  | Ratios of $\Delta\varepsilon_v/\Delta\varepsilon_h$ with depth during isotropic consolidation .....  | 132  |
| Figure 6.4  | Curves of (a) stress-strain relationship (b) effective stress path<br>(c) normalized excess pore water pressure for $\alpha=0^\circ$ , $45^\circ$ and $90^\circ$ | 134  |
| Figure 6.5  | Curves of (a) stress-strain relationship (b) effective stress path<br>(c) normalized pore water pressure for $b=0$ , $0.5$ and $1$ .....                         | 136  |
| Figure 6.6  | Effects of $\alpha$ on normalized undrained shear strength of<br>Bangkok Clay.....   | 138  |
| Figure 6.7  | Effects of $\alpha$ on normalized peak undrained shear strength.....   | 138  |
| Figure 6.8  | Effects of $b$ on normalized peak undrained shear strength of<br>Bangkok Clay.....   | 140  |
| Figure 6.9  | Effects of $b$ on normalized peak undrained shear strength.....  | 140  |
| Figure 6.10 | Effects of $\alpha$ on friction angle of Bangkok Clay.....   | 142  |
| Figure 6.11 | Effects of $\alpha$ on friction angle .....  | 143  |
| Figure 6.12 | Effects of $b$ on friction angle of Bangkok Clay .....   | 144  |
| Figure 6.13 | Effects of $b$ on friction angle .....   | 145  |
| Figure 6.14 | Effects of $\alpha$ on excess pore water pressure.....   | 147  |
| Figure 6.15 | Effects of $b$ on excess pore water pressure .....   | 147  |
| Figure 6.16 | Normalized octahedral shear stiffness degradation curves.....  | 150  |
| Figure 6.17 | Effects of $\alpha$ on normalized octahedral shear modulus at 0.01%<br>of strain .....   | 151  |
| Figure 6.18 | Normalized octahedral shear stiffness degradation curves.....  | 151  |
| Figure 6.19 | Effects of $\alpha$ on non-linearity index at 0.01% to 0.1% and 0.1%<br>to 1% of strain.....   | 152  |
| Figure 6.20 | Normalized octahedral shear stiffness degradation curve .....  | 153  |

|   | Page |
|---|------|
| Figure 6.21 Effects of $b$ on normalized octahedral shear modulus at 0.01% of strain .....  | 154  |
| Figure 6.22 Effects of $\alpha$ on non-linearity index at 0.01% to 0.1% and 0.1% to 1% of strain.....   | 154  |
| Figure 6.23 Normalized Young's modulus degradation curves.....  | 155  |
| Figure 6.24 Relationships between strains in A45B00, A45B05 and A45B10 tests.....   | 157  |
| Figure 6.25 Relationships between individual strains.....   | 160  |
| Figure 6.26 Evolutions of principal stress and strain increment directions ....   | 161  |
| Figure 6.27 Variation of $\phi'_{max}$ and $M_{max}$ at failure versus $b$ parameter for (a) $\alpha=0^\circ&90^\circ$ and (b) $\alpha=45^\circ$ .....              | 165  |
| Figure 6.28 Three-dimensional failure surface for Bangkok Clay in an octahedral plane ( $p'=100$ kPa) (a) $\alpha=0^\circ&90^\circ$ and (b) $\alpha=45^\circ$ ..... | 166  |

## LIST OF SYMBOLS

|                        |   |
|------------------------|---|
| $b$                    | intermediate principal stress parameter                       |
| $E_u$                  | undrained Young's modulus                                     |
| $E_{u,sec}$            | secant undrained Young's modulus                              |
| $E'_{sec}$             | secant drained Young's modulus                                |
| $E_v, E^*$             | Young's moduli in the vertical direction                      |
| $E_v^u$                | undrained Young's moduli in vertical direction                |
| $E_h$                  | Young's moduli in horizontal direction                        |
| $E_h^u$                | undrained Young's moduli in horizontal direction              |
| $G_{vh}, G_{hh}$       | shear modulus for shearing in a vertical and horizontal plane |
| $G_{max}$              | small-strain shear stiffness                                  |
| $G_{oct}$              | octahedral shear stiffness                                    |
| $G^*$                  | modified shear modulus  |
| $J$                    | coupling modulus  |
| $K_{sec}$              | secant bulk modulus   |
| $K^*$                  | modified bulk modulus   |
| $LL, PL, PI$           | liquid limit, plastic limit, and plasticity index             |
| $M_T$                  | torque  |
| $M, M_f$               | stress ratio  |
| $OCR$                  | overconsolidation ratio                                       |
| $p_i$                  | inner cell pressure   |
| $p_o$                  | outer cell pressure   |
| $p'$                   | mean normal effective stress                                  |
| $p_0'$                 | in-situ mean normal effective stress                          |
| $q$                    | deviatoric stress   |
| $s_u$                  | undrained shear strength                                      |
| $W$                    | axial force   |
| $w_n$                  | natural water content   |
| $\Delta u, \Delta u_f$ | excess pore pressure  |
| $\alpha$               | anisotropy factor   |

|  |   |
|--|---|
| $\alpha$   | major principal stress direction  |
| $\alpha, \alpha_\sigma$  | major principal stress and major principal stress increment directions  |
| $\alpha_\varepsilon, \alpha_{\dot{\varepsilon}}$                     | major principal strain and major principal strain increment directions  |
| $\gamma$   | total unit weight   |
| $\varepsilon_p$  | volumetric strain   |
| $\varepsilon_q$  | deviatoric strain   |
| $\varepsilon_1, \varepsilon_2, \varepsilon_3$                        | major, intermediate and minor principal strains   |
| $\varepsilon_z, \varepsilon_r, \varepsilon_\theta, \gamma_{z\theta}$ | axial, radial, circumferential and shear strains  |
| $\varepsilon_v, \varepsilon_h$                                       | vertical and horizontal strains   |
| $\sigma_1, \sigma_2, \sigma_3$                                       | major, intermediate and minor principal stresses  |
| $\sigma_x, \sigma_y, \sigma_z$                                       | normal stress in x-, y-, and z-directions   |
| $\sigma_z, \sigma_r, \sigma_\theta, \tau_{z\theta}$                  | axial, radial, circumferential and shear stresses   |
| $d(\sigma_1'/\sigma_3')/dt$  | principal stress increasing rate  |
| $\phi, \phi'_f$  | friction angle  |
| $\nu_{vh}$   | Poisson's ratio related to the lateral strains that occur in the horizontal direction orthogonal to a vertical direction of compression   |
| $\nu_{hh}, \nu^*$  | Poisson's ratio related to the lateral strains that occur in the horizontal direction orthogonal to a horizontal direction of compression |

# CHAPTER I

## Introduction

### 1.1 Background

In the past, geotechnical analysis normally focused on strength characteristics of soils. However, recent geotechnical design considers on analyzing of soil-structure interaction. This analysis involves deformations of structures and stresses predictions, both in the surrounding soil mass and also over areas of contacting with the loading boundaries. It can be examined from many researches that the analysis of soil deformation are different from the field measurements and the results of conventional laboratory testing frequently give much lower stiffness than those back calculated from the field measurements. This is because the back calculation analysis usually employs the simple soil models which can not explain the real soil behavior.

The stress-strain behavior of soil is nonlinear with increasing in strain level. Strain levels can be categorized into 3 zones, namely small, intermediate and large. At small-strain level, the stiffness is very high and can be assumed as a constant. Each of strain levels in 3 zones is distinguished based on characteristics of stress-strain curve.

1. Small strain: it corresponds to the range of strain generally less than 0.001% (for low-plasticity soils) or less than 0.01% (for plasticity clays) where the small-strain shear modulus is almost constant with the strain (Georgiannou et al., 1991).
2. Intermediate strain: it corresponds to the range of strain from 0.001% or 0.01% to 1% where the stress-strain relationship is highly non-linear and the shear stiffness depends on the strain.
3. Large strain: it corresponds to the range of strain generally larger than 1% where the behavior of soil is approaching failure and the shear modulus becomes small.

Prediction of ground deformation and well knowledge on the stress-strain behavior of soil are required for the design of geotechnical structures. There are a lot of researches concerned about this topic and suggested that under working load condition, the strains occurred in the ground surrounding foundation and excavation may be relatively small (Simpson et al., 1979; Jardine et al., 1986). Summary of various field data by Burland (1989) showed that large ground masses beneath and around structure experience direct strains of less than 0.1%. For example, the deformation in case of wave loading, earthquake, deep excavation working near the geotechnical structures, dynamic foundation is very small, approximately 0.05% or less. Therefore, it can be concluded that the stress-strain behavior of soils at small- to intermediate-strain levels is essential input to obtain more accurate prediction (Burland, 1989).

In the past two decades, a number of researchers investigated the behavior of many soils at small and intermediate strain ranges. However, there are a lot of features which still remain poorly understood, for example: anisotropy, non-linearity, time-effect and yielding characteristics. This information has a significant effect on the results of numerical analysis and improvement of the soil model.

In addition, the development of soil model for Bangkok clay is limited by few data of wide strain range behavior. Effects of principal stress rotation and intermediate principal stress are also the features which are poorly investigated. These data can be obtained from the laboratory experiment. This information is achieved accurately; they should be useful for improving the soil model to better represent the real Bangkok clay behavior.

## **1.2 Objectives**

The objectives of this research are:

- 1.2.1 To develop a triaxial apparatus with a local strain measuring system and bender element system for studying the Bangkok clay behavior at wide strain range.

- 1.2.2 To examine the anisotropic characteristic Bangkok clay in undrained and drained condition.
- 1.2.3 To study the effects of principal stress rotation and intermediate principal stress on undrained behavior.

### **1.3 Scope**

According to fulfill the objectives, this research is almost related to the laboratory works separated into two main parts. The detail of each part can be described as follows.

- 1.3.1 The triaxial apparatus incorporated with local strain measuring system and bender element system are developed to analyze the behavior of Bangkok clay in a wide strain range. The experimental study aims to investigate the non-linear behavior, anisotropic characteristics and yielding characteristics in undrained and drained condition.
- 1.3.2 Using a torsional shear hollow cylinder apparatus to study the effect of major principal stress rotation and intermediate principal stress on undrained behavior of Bangkok clay.

The data from these experimental studies are useful for providing additional database to better explain and model the Bangkok clay behavior.

### **1.4 Layout**

This thesis consists of 7 chapters. The content of each chapter is briefly summarized as follows.

Chapter 2 summarized the review of the literatures about non-linearity, factor affecting the small-strain behavior, measurement of stress-strain characteristic, anisotropy of soil.



Chapter 3 explains triaxial testing apparatus, testing procedures and testing program used in this study. Details of development of triaxial apparatus with local strain measuring system and bender element system are also presented.

Chapter 4 presents the results of triaxial undrained and drained compression shearing tests on Bangkok Clay. The investigation focuses on the non-linearity, anisotropy and strength characteristics. The complete set of cross-anisotropic elastic parameters are also derived.

Chapter 5 described torsional shear hollow cylinder testing apparatus, testing procedures and testing program used in this study. Principal of torsional shear hollow cylinder test and stress and strain calculation are also presented in this chapter.

Chapter 6 presents the results of torsional shear hollow cylinder test of Bangkok Clay. The investigation mainly focuses on effects of major principal stress rotation and the magnitude of intermediate principal stress on undrained behavior of Bangkok Clay. Failure surface and plastic potential in deviatoric plane of Bangkok Clay are proposed.

Chapter 7 shows the summary and conclusion of this research.

## CHAPTER II

### Literature Review

#### 2.1 Introduction

In recent year, there are a lot of experimental researches investigated the mechanical behavior of soils at small-strain level. They showed that the stress-strain behavior of soils is highly non-linear and the soil stiffness varies significantly over the strains range. Figure 2.1 presents a typical stiffness degradation curve in terms of shear modulus ( $G$ ) or Young's modulus ( $E$ ) with strain levels observed in geotechnical structures and measuring abilities of various techniques (Atkinson, 2000; Mair, 1993). As shown in Figure 2.1, the ranges of small-to intermediate-strain level of interest is beyond the capability of the conventional triaxial apparatus, which is the most popular technique to study the stress-strain behavior of soil in the laboratory. Consequently, improvements of the triaxial system in order to be able to accurately measure this non-linear behavior, especially at small-strain level are required. The recently researches on small-strain investigation are briefly summarized here.

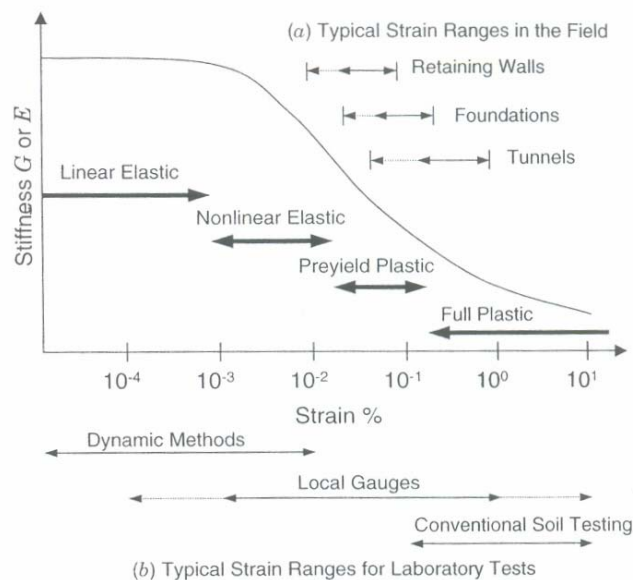


Figure 2.1 Stiffness degradation curve (a) the strain levels observed during the typical geotechnical structures construction (after Mair, 1993) and (b) the strain levels that can be observed by various techniques (after Atkinson, 2000).

## 2.2 Factors affecting small-strain behavior

The behavior of soils at small-strain level is essential information to understand the soil response in earthquake and other types of dynamic loading. Most of the published experimental data focusing on the small-strain stiffness of soils are usually derived from dynamic laboratory tests on both natural and reconstituted samples. Review of literature shows that there are a number of factors affecting the estimation of soil stiffness at small-strain level. These factors are not only related to the nature and soil inherent structure (gradation size and particle shape etc) but also to its geological history (stress state, stress history, aging, chemical processes, etc.).

A normally empirical equation of normalized small-strain shear modulus is proposed as Eq. (2.1) presented by Rampello et al. (1997). The small-strain stiffness depends on the current stress state expressed by the mean effective stress, the current void ratio and the previous stress history experienced by the soil.

$$\frac{G_{\max}}{p_a} = Sf(e) \left( \frac{p'}{p_a} \right)^n \quad (2.1)$$

where  $G_{\max}$  is the small-strain shear modulus,  $f(e)$  is an empirically defined function of the void ratio,  $p'$  is the mean effective stress,  $p_a$  is the reference stress (usually the atmospheric pressure, 100 kPa),  $S$  and  $n$  are dimensionless experimentally determined parameters.

The relationships in the form of Eq. (2.1) are presented by several researchers to fit the experimental data in different types of soil and some of them are summarized in Table 2.1.

In the following sections, the effects of various factors on the small-strain behavior of soils are presented.

Table 2.1 Constants of proposed equations of small-strain stiffness in the form of  $\frac{G_{\max}}{p_a} = Sf(e) \left( \frac{p'}{p_a} \right)^n$  ( $G_{\max}$ ,  $p'$  and  $p_a$  are in kPa) (Yimsiri and Soga, 2000)

| Soil type                               | Test method | $S$       | $f(e)$                        | $n$  | Void ratio range | reference                     |
|---|-------------|-----------|-------------------------------|------|------------------|-------------------------------|
| Sand:                                   |             |           |                               |      |                  |                               |
| Round-grain Ottawa Sand                 | RC          | 690       | $\frac{(2.174 - e)^2}{1 + e}$ | 0.5  | 0.3-0.8          | Hardin and Richart (1963)     |
| Angular-grain crushed quartz            | RC          | 327       | $\frac{(2.973 - e)^2}{1 + e}$ | 0.5  | 0.6-1.3          | Hardin and Richart (1963)     |
| Several sands                           | RC          | 563       | $\frac{(2.17 - e)^2}{1 + e}$  | 0.4  | 0.6-0.9          | Iwasaki et al. (1978)         |
| Reconstituted Toyoura Sand              | Cyclic TX   | 840       | $\frac{(2.17 - e)^2}{1 + e}$  | 0.5  | 0.6-0.8          | Kokusho (1980)                |
| Several cohesionless and cohesive soils | RC          | 450-14000 | $(0.3 + 0.7e^2)^{-1}$         | 0.5  | N.A.             | Hardin and Blandford (1989)   |
| Reconstituted Ticino Sand               | RC & TS     | 507       | $\frac{(2.27 - e)^2}{1 + e}$  | 0.43 | 0.6-0.9          | Lo Presti <i>et al</i> (1993) |
| Clay:                                   |             |           |                               |      |                  |                               |
| Reconstituted NC kaolin                 | RC          | 327       | $\frac{(2.973 - e)^2}{1 + e}$ | 0.5  | 0.5-1.5          | Hardin and Black (1968)       |
| Several undisturbed clays (NC range)    | RC          | 327       | $\frac{(2.973 - e)^2}{1 + e}$ | 0.5  | 0.5-1.7          | Hardin and Black (1968)       |

Table 2.1 (cont.) Constants of proposed equations of small-strain stiffness in the form of  $\frac{G_{\max}}{p_a} = Sf(e) \left( \frac{p'}{p_a} \right)^n$  ( $G_{\max}$ ,  $p'$  and  $p_a$  are in kPa)

| Soil type                                      | Test method | $S$       | $f(e)$   | $n$       | Void ratio range | reference                      |
|--|-------------|-----------|--|-----------|------------------|--------------------------------|
| Reconstituted NC kaolin                        | RC          | 450       | $\frac{(2.973 - e)^2}{1 + e}$                              | 0.5       | 1.1-1.3          | Marcuson and Wahls (1972)      |
| Reconstituted NC bentonite                     | RC          | 45        | $\frac{(4.4 - e)^2}{1 + e}$                                | 0.5       | 1.6-2.5          | Marcuson and Wahls (1972)      |
| Several undisturbed silts and clays (NC range) | RC          | 74-288    | $\frac{(2.973 - e)^2}{1 + e}$                              | 0.46-0.61 | 0.4-1.1          | Kim and Novak (1981)           |
| Undisturbed NC clay                            | Cyclic TX   | 14        | $\frac{(7.32 - e)^2}{1 + e}$                               | 0.6       | 1.7-3.8          | Kokusho et al. (1982)          |
| Six undisturbed Italian clays                  | RC & BE     | 275-1174  | $e^{-1.3}$ (average from $e^{-x}$ : $x = 1.11$ to $1.43$ ) | 0.40-0.58 | 0.6-1.8          | Jamiolkowski et al. (1995)**   |
| Several soft clays                             | SCPT        | 500       | $e^{-1.5}$   | 0.5       | 1-5              | Shibuya and Tanaka (1996)***   |
| Several soft clays                             | SPCT        | 1800-3000 | $(1 + e)^{-2.4}$   | 0.5       | 1-6              | Shibuya <i>et al</i> (1997)*** |

\* RC: resonant column test, TX: triaxial test, TS: torsional shear test, BE: bender element test, SCPT: seismic cone test

\*\* from anisotropic stress condition

\*\*\* use  $\sigma'_v$  instead  $p'$

### 2.2.1 Effective stress state

According to many studies, the soil stiffness is normally proportional to the mean effective stress or the principal effective stress. Figure 2.2 shows examples of the effect of stress level on small-strain shear modulus of many geomaterials (Coop and Jovicic, 1999).

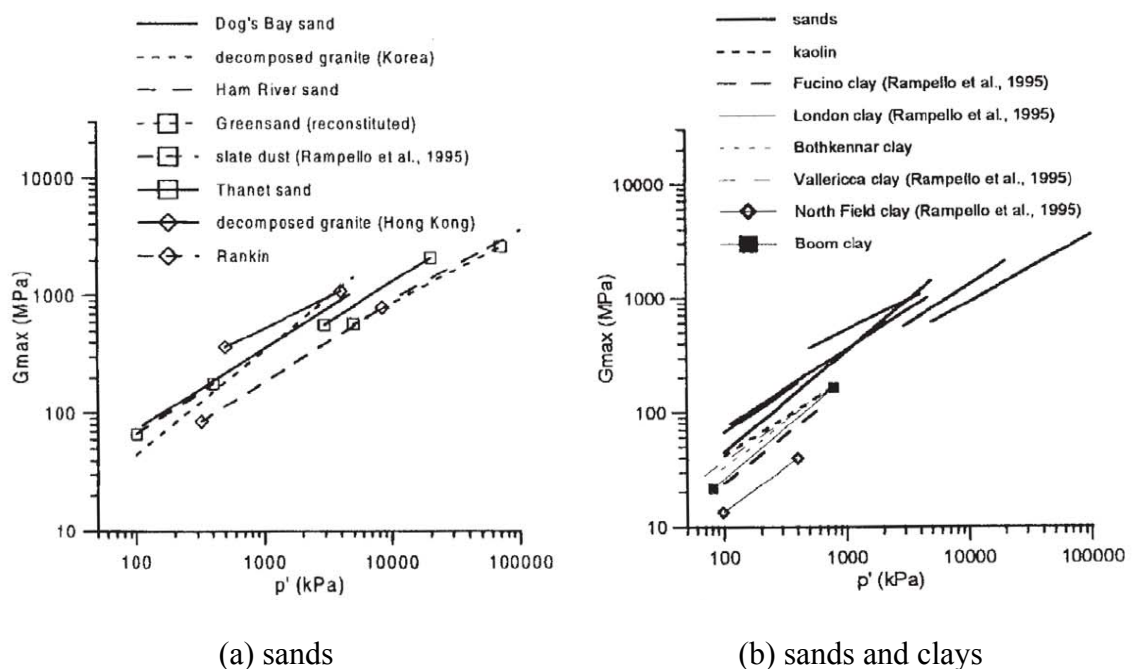


Figure 2.2 Effect of stress level on small-strain shear modulus of many geomaterials (Coop and Jovicic, 1999 )

The relationship shown in Eq. (2.1) is derived assuming isotropic stress condition. However, it is well known that anisotropic stress conditions and anisotropic soil fabric produce stiffness values depended on the loading direction. Roesler (1979) studied the effect of anisotropic stress condition on shear modulus. The shear modulus was measured from shear wave velocity on cubical sand specimen. The principal effective stresses on the cubical specimen can be independently controlled. The results showed that the shear modulus depends on the principal effective stresses in the direction of wave propagation and the particle motion. However, it is relatively independent of the direction out of plane principal stress. This observation has been later confirmed by many researchers (e.g. Yu and Richart, 1984; Stokoe et al., 1985, 1991, 1995).

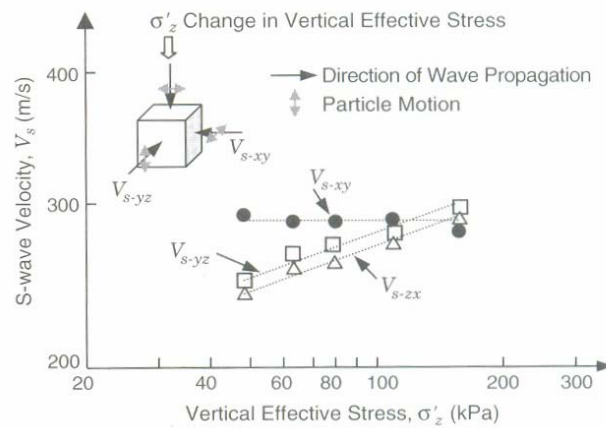


Figure 2.3 Shear wave velocities variation in different directions as a function of anisotropic stress (Stokoe et al., 1995)

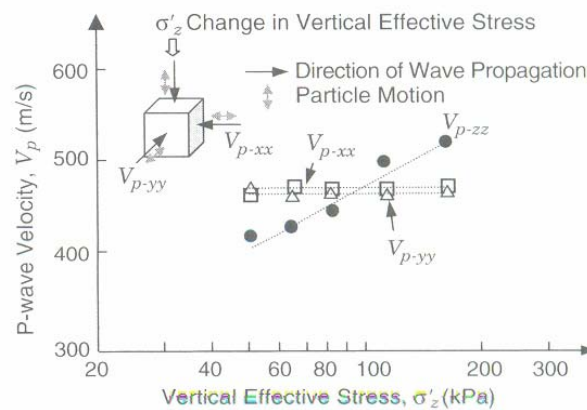


Figure 2.4 P-wave velocities variation in different directions as a function of anisotropic stress (Stokoe et al., 1995)

Figure 2.3 displays shear wave velocities propagating measured in three different directions ( $V_{s-xy}$ ,  $V_{s-yz}$  and  $V_{s-zx}$ ). The vertical effective stress ( $\sigma'_z$ ) was increased, whereas the horizontal effective stresses ( $\sigma'_x$  and  $\sigma'_y$ ) were held constant (Stokoe et al., 1995). The result showed that the shear wave velocities of  $V_{s-xy}$ , which the wave propagation and the particles motion are in the out-of-plane directions, has no change in its velocities. The similar result can be observed on P-wave velocity. As shown in Figure 2.4, P-wave velocity depends only a function of the effective stress in the coaxial direction (Stokoe et al., 1995).

### 2.2.2 Stress history

The stress history and current state are another of the effects on the stress-strain behavior of soils at small-strain level. Generally, the stress history is usually described by the overconsolidation ratio. It is simply defined in terms of effective stress and mean effective stress as  $OCR = \frac{\sigma'_{v\max}}{\sigma'_v}$  and  $R = \frac{p'_c}{p'}$ , respectively.

Rampello et al. (1997) proposed additional terms of the influence of  $OCR$  and  $R$  into the empirical equation explained in term of normalized equation by  $p_a$  as shown in Eqs. (2.2) & (2.3).

$$\frac{G_{\max}}{p_a} = Sf(e) \left( \frac{p'}{p_a} \right)^n OCR^k \quad (2.2)$$

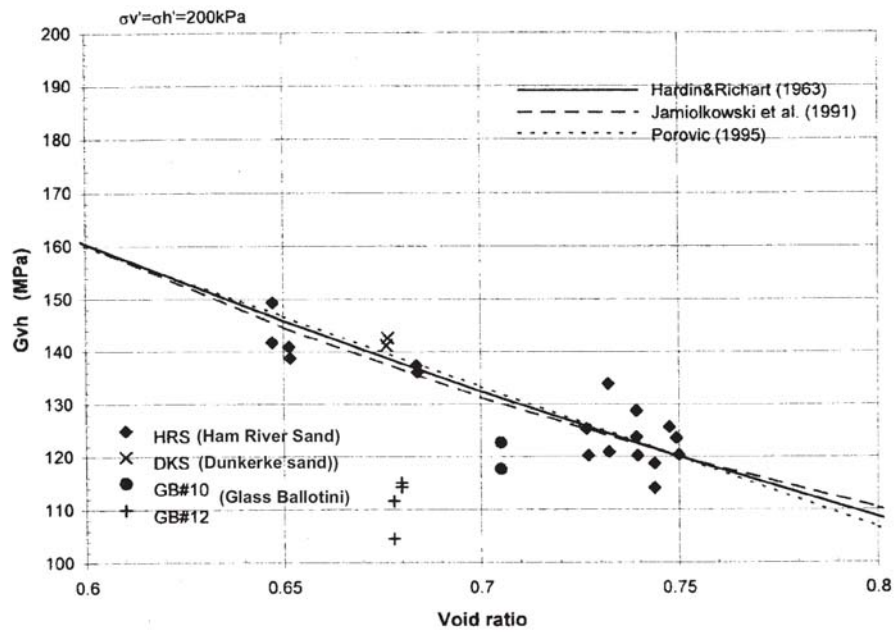
$$\frac{G_{\max}}{p_a} = Sf(e) \left( \frac{p'}{p_a} \right)^n R^k \quad (2.3)$$

However, it was confirmed from many researches that  $OCR$  had insignificant effects on the small-strain stiffness of undisturbed clays if the change in void ratio has been accounted for (Jamiolkowski et al., 1994) but some of them showed no effect on the small-strain modulus of sand (Tatsuoka and Shibuya, 1991 and Lo Presti, 1994)

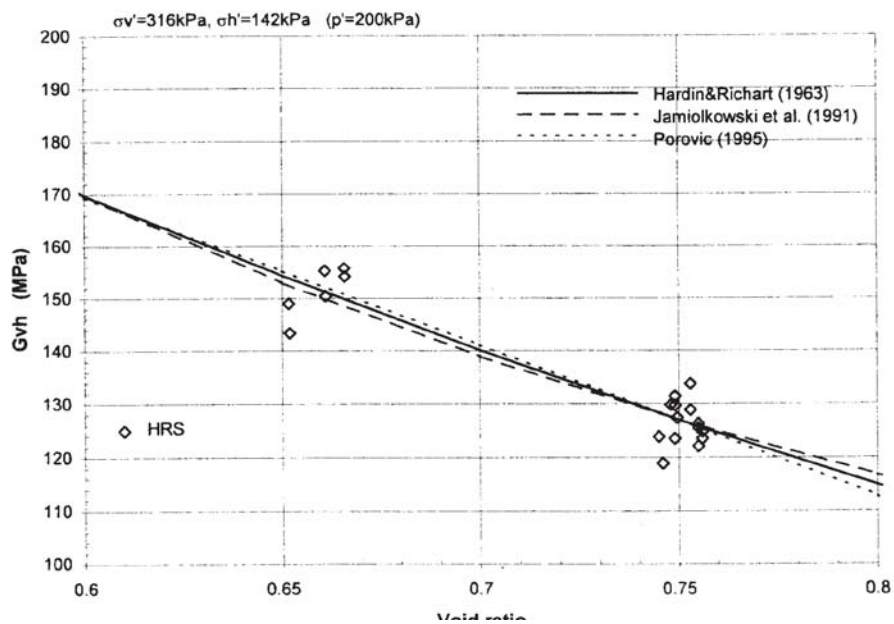
### 2.2.3 Void ratio

The small-strain shear modulus of soils increases systematically as density increases and void ratio reduces. Figure 2.5 shows some examples of the variation of shear stiffness with void ratio for many materials (Kuwano, 1999). In order to compare the shear modulus measured at different densities of many materials, several normalized function ( $f(e)$ ) have been proposed by many researchers as summarized in Table 2.1. Because the function of void ratio is derived from the empirical study in different testing techniques and materials. Therefore, carefully care should be taken when adopting any of them.





(a) isotropic effective stress state



(b) anisotropic effective stress state

Figure 2.5 Effect of void ratio on shear stiffness of HRS for (a) isotropic effective stress state and (b) anisotropic effective stress state (Kuwano, 1999)

However, several experimental and theoretical studies (Weiler, 1988; Houlsby and Wroth, 1991; Rampello et al., 1994 and 1997) have supported that the function of

void ratio in empirical equation of the small-strain shear modulus for overconsolidated clay is a redundant factor. It is because the void ratio is already a function of the stress state and stress history. The small-strain shear modulus of soil can be expressed as a function of two out of three variables  $f(e)$ ,  $p'$  and  $OCR$ . In particular, Eqs (2.2) & (2.3) is altered to Eq. (2.4).

$$\frac{G_{\max}}{p_a} = S^* \left( \frac{p'}{p_a} \right)^{n^*} R^{k^*} \quad (2.4)$$

where the notation of  $*$  is for distinguishing the  $S$ ,  $n$  and  $k$

#### 2.2.4 Stress ratio

Stress ratio is another effect on the soil behavior. It was found from Yu and Richart (1984) that the equation as shown in Eq. (2.2) could not fit the experimental data at high stress ratios ( $\eta=q/p'$ ). From resonant column test results, it was found that the shear stiffness decreased when stress ratio increased. If the stress ratio was smaller than 2.5-3.0, the effect of shearing stress ratio on shear stiffness was less than 10%, and this can be considered within the experimental error in evaluating shear stiffness.

This finding has been confirmed by many researchers. Rampello et al. (1997) conformed that the small-strain shear modulus of reconstituted clay during the drained constant stress ratio test was dependent on  $\eta$ . The shear modulus increased by about 20% when the ratio of  $\eta$  increased from 0 to 0.7. Moreover, Rampello et al. (1997) proposed an expression for clays modified by Eq. (2.4) as shown in Eq. (2.5). In contrast, Pennington et al. (1997) studied in a similar testing set up, that the stress difference did not affect on the small-strain shear modulus, except that measured in horizontal direction.

$$\frac{G_{\max}}{p_a} = S_{\eta}^* \left( \frac{p'}{p_a} \right)^{n^*} R_{\eta}^{k^*} \quad (2.5)$$

where  $R_{\eta}$  is the overconsolidation ratio under the anisotropic stress condition

### 2.2.5 Aging and time effect

The effect of time on stiffness has been observed to be a significant factor in both clay and sand. Many researches show that the small-strain shear modulus increases with time at constant stresses (e.g. Marcuson and Wahls, 1972; Afifi and Richart, 1973; Seed, 1979 and Daramola, 1980). The possible reasons of increasing in stiffness are creep, a movement of soil grain and increased interlocking and cementation phenomenon around soil grain during aging.

Figure 2.6 illustrates the variations of  $G$  with creep time obtained from many tests of low density and poorly graded Dogs Bay sand proposed by Jovicic and Coop (1997). Any values of  $G$  are normalized by the initial  $G$  value at time zero. Figure 2.6 (a) and (b) present the influence of aging/creep for different isotropic effective stress levels and loading directions, respectively. The result showed that the time shows more significantly effect at low stress levels. Increasing in shear stiffness up to 15% is observed within a period of three days. Jovicic and Coop (1997) proposed that increasing in stiffness of soil samples subjected to subsequent stages of isotropic loading and unloading could be attributed to ageing phenomena since creep was already negligible (near-zero volume strains).

### 2.2.6 Recent stress history (immediate stress path)

The small-strain stiffness of soils is influenced by recent stress history. Suddenly change in stress path direction or the time period at a constant stress state has a major effect on subsequent stiffness.

Changing in loading path on the stiffness of overconsolidated soil were investigated by Atkinson et al. (1990). The tests controlled of constant mean effective stress ( $p'$ ) and deviatoric stress ( $q$ ) during drained condition were carried out on overconsolidated London Clay samples and other soils with a range of plasticity. All experiments were started from the same state but differed only in the preceding paths approaching the different starting point. As the different results of stiffness degradation curves illustrated in Figure 2.7, it can be explained that the recent stress history has a major influence on the subsequent soil behavior. Different stiffness

degradation curves were obtained even though the samples sheared along the same stress path as represented in Figure 2.7 (a). This is because the specimens had different stress path histories prior to shearing (*AO*, *BO*, *CO* and *DO*). The stiffer response was obtained when the stress path was reversed (*D* → *O* → *X*) as represented in Figure 2.7 (b).

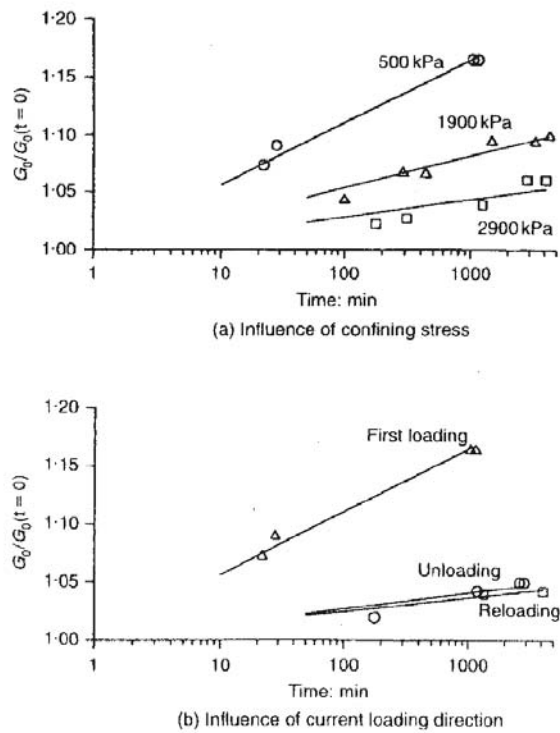
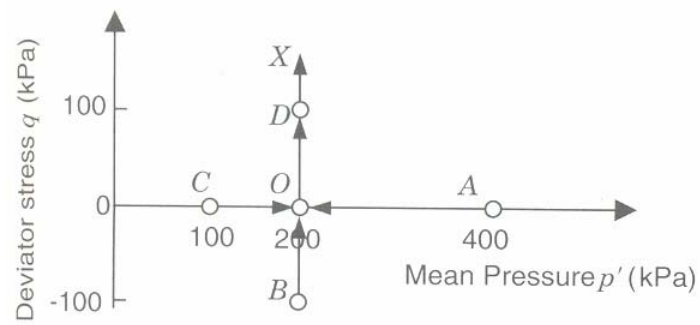
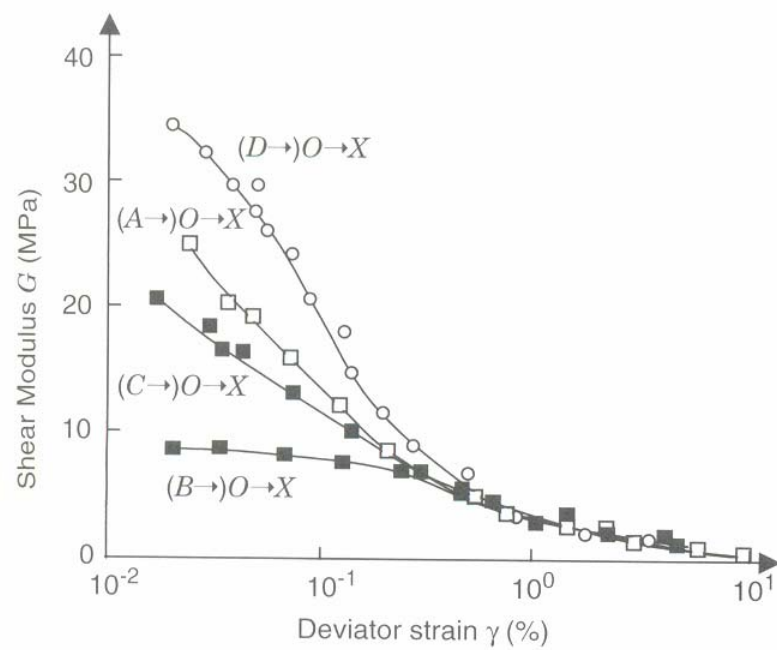


Figure 2.6 Time (creep) effect on the shear stiffness of calcareous sand samples (Jovicic and Coop, 1997)



(a)



(b)

Figure 2.7 Effect of recent stress history on stiffness degradation; (a) stress paths and (b) stiffness degradation on  $OX$  stress path (Atkinson et al., 1990)

### **2.3 Measurement of stress-strain characteristic at wide strain range**

The stiffness and stress-strain characteristic of soil are an important knowledge for analyzing of geotechnical engineering problems. For this purpose, a number of investigation techniques evaluating the stress-strain behavior and stiffness of soils both in the laboratory and in the field are discussed.

Methods of measuring the stiffness of soil vary and depend on the strain level at which the stiffness is required. Figure 2.8 presents strain ranges achieved from various techniques (Ishihara, 1996). The conventional destructive tests like triaxial, direct shear and unconfined compression test are better suitable for large-strain conditions. In case of intermediate- to small-strain are represented by the wave propagation techniques such as resonant column test and bender element test carried out from laboratory. The field tests are in situ shear wave velocity tests, cross-hole seismic test, pressuremeter test. Because the stiffness of soils can be obtained from various methods which have different boundary conditions, a number of factors affecting on behavior of soil should be considered. These factors are summarized below.

- strain level
- stress state
- sample disturbance
- mode of shearing
- strain rate/rate of loading
- drainage condition
- discontinuity

In the following sections, the laboratory tests which obtain the stiffness and stress-strain characteristic of soil at intermediate- to small-strain levels are briefly described.

| Magnitude of strain        |                               | $10^{-6}$                               | $10^{-5}$                       | $10^{-4}$ | $10^{-3}$                       | $10^{-2}$                            | $10^{-1}$ |
|----------------------------|-------------------------------|---|---------------------------------|-----------|---------------------------------|--------------------------------------|-----------|
| Phenomena                  |                               | Wave propagation, vibration             | Cracks, differential settlement |           | Slide, compaction, liquefaction |                                      |           |
| Mechanical characteristics |                               | Elastic                                 | Elasto-plastic                  |           | Failure                         |                                      |           |
| Effect of load repetition  |                               | ←—————→                                 |                                 |           |                                 |                                      |           |
| Effect of rate of loading  |                               | ←—————→                                 |                                 |           |                                 |                                      |           |
| Constants                  |                               | Shear modulus, Poisson's ratio. Damping |                                 |           |                                 | Angle of internal friction, cohesion |           |
| In-situ measurement        | Seismic wave method           | ←—————→                                 |                                 |           |                                 |                                      |           |
|                            | In-situ vibration test        | ←—————→                                 |                                 |           |                                 |                                      |           |
|                            | Repeated loading test         | ←—————→                                 |                                 |           |                                 |                                      |           |
| Laboratory measurement     | Wave propagation precise test | ←—————→                                 |                                 |           |                                 |                                      |           |
|                            | Resonant column precise test  | ←—————→                                 |                                 |           |                                 |                                      |           |
|                            | Repeated loading test         | ←—————→                                 |                                 |           |                                 |                                      |           |

Figure 2.8 Strain ranges achieved from various tests (Ishihara, 1996).

### 2.3.1 Advanced triaxial test

The triaxial test is the most common technique used to study the stress-strain behavior of soil in the laboratory. Because there are a lot of researchers have encouraged that the small-strain stiffness of soil is very important for analysis of the boundary value problems. Accurate prediction of ground movements depends on the variation of stiffness obtained from small-strain level. Recently, the development of triaxial test is the advent to measure behavior of small-strain on the soil sample locally. The monotonic triaxial test developed by local strain measurement device becomes a popular technique to measure behavior of soil in a wide strain range. The advantages of the monotonic triaxial are ability of controlling strain rate, measuring over a wide strain range, controlling the stress path, and obtaining the strength. However, its limitation is impossible to measure damping ratio except for cyclic test.

### **2.3.2 Bender Element test**

The bender element method, developed by Shirley and Hampton (1978), is a simple technique to obtain the small-strain stiffness. The small-strain shear modulus of soil can be derived from the velocity of propagation of a shear wave through the sample. Bender element systems are set up in most laboratory apparatus, especially in the triaxial test as described by Dyvik and Madshus (1985). Less than 0.001% of strain can be estimated in this technique.

The small-strain stiffness observed by the bender element test is necessary for any dynamic or small-strain cyclic loading analysis. Moreover it is usually required as an input parameter for non-linear numerical analyses at larger strain level (Jardine et al., 1991; Stallebarass et al., 1997). More details of this section have been explained in Chapter 3.

### **2.3.3 Shear-plate transducer**

Figure 2.9 displays the schematic diagram of shear-plate transducer. The electrodes are applied to two faces of shear-plate transducer that are parallel to the polarization direction. The movement of the shear-plate transducer is perpendicular to the shear wave propagation direction. The set-up of the shear-plate transducer is similar to the bender element system.

In order to overcome limitations of bender element, the shear plate was considered to be alternative technique (Ismail and Rammah, 2005). Results obtained from shear plate and bender element have an average error less than 2.5% agreeing with the results obtained by Brignoli et al.,(1996). Moreover, the shear-plate transducer is more superior to bender element in the tests of undisturbed stiff soils and soils with large aggregate (sandy sample) because of its non-invasive characteristic. However, the bender element is suited to that of the shear plate for the soft clay.



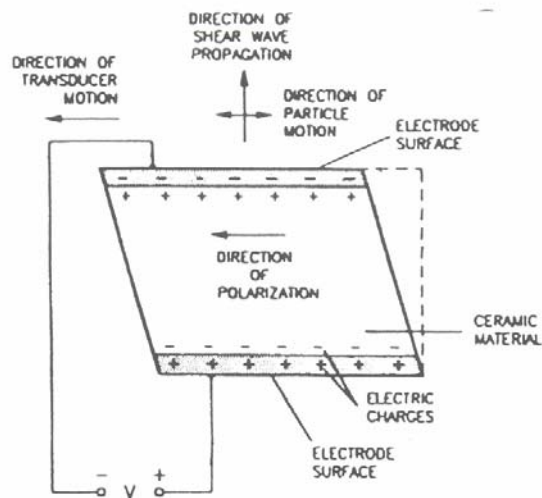


Figure 2.9 Shear-plate transducer (Brignoli et al., 1996)

### 2.3.4 Resonant column test

Another technique for measuring the dynamic soil properties in the laboratory is resonant column test. The theory and procedure of this technique have been explained by Hardin and Music (1965). Theoretical solutions of this technique corresponded to the shear modulus of the soil column to its resonant frequency. During measurement of the resonant frequency, the axial load is allowed to apply to the specimen set up in an enclosed triaxial cell. The general shear modulus determined in this apparatus is in the range of small-strain amplitudes (about  $10^{-3}\%$  to  $10^{-1}\%$ ).

### 2.3.5 Torsional shear hollow cylinder test

The torsional shear hollow cylinder apparatus is a popular technique in order to study the entire anisotropic characteristic of soils. This is because this experiment can control not only the magnitudes of principal stresses but also the inclination of the major principal stress axis by subjected to 4 parameters such as axial load, torque and outer and inner pressure. Moreover, it is also possible to control and measure back pressure and study both of drained and undrained conditions. Therefore, when each of the boundary stress is controlled, effects of the direction of the major principal stress and the magnitude of the intermediate principal stress can be studied (see Chapter 5).

## **2.4 Anisotropy**

Because the soil sediments are under gravity in one-dimension, natural soils are believed that they possess anisotropic response which refers to a dependency on the direction of the applied changes in stress or strain respond. Anisotropic behavior can be conceptually expressed into “Inherent” and “Stress induced”. Inherent anisotropy develops as a result of depositional processes and grain characteristics. Subsequent particle redistribution and orientation during consolidation or other stress processes can result stress induced anisotropy. In reality, most soil sediments are simultaneously subjected to both processes which are usually referred to as initial anisotropy.

Collapse of geotechnical structures can be induced by imposing different modes of shearing. From several studies it is noted that shear strength measured in the compression mode can be significantly higher than in the extension mode. This difference suggests that the stress condition, such as the direction of the principal stress and the magnitude of the intermediate principal stress have some effects on the soil behavior. Furthermore, changing the inclination of the major principal stress critically increase the collapse potential in most case. Consequently, the designs of geotechnical structures namely foundations for deep excavations, dams and multi-stage construction embankments should thoughtfully considerate not only the magnitudes but also the directions the principal stress axes.

In order to examine the entire anisotropic characteristics of soils, it is necessary to use a device which allows the monitoring and independent control not only of the magnitude of the three principal stresses but also the rotation of the major principal stress direction. Torsional shear hollow cylinder device used in this research can be well suited for soil anisotropy study (see Section 2.5.2).

### **2.4.1 Inherent anisotropy**

Inherent anisotropy comes from the anisotropic nature soil fabric. It is likely attributed to the sediment process and grain characteristics of soil mass. Vaid et.al (1995) studied about inherent anisotropic on Syncrude sand by performing a series of

simple shear test on an NGI type simple shear device and a torsional shear hollow cylinder device. Reconstituted samples were prepared by different techniques. The moist taming and water pluviation and/or air pluviation techniques were used in order to prepare for hollow cylinder samples and simple shear specimens, respectively. The results showed the different response on the different preparing techniques. The softest and most brittle response was observed on the moist tamped specimens. The air pluviated samples represented a less brittle response, whereas the samples prepared by the water pluviation technique exhibited a strain hardening behavior as shown in Figure 2.10.

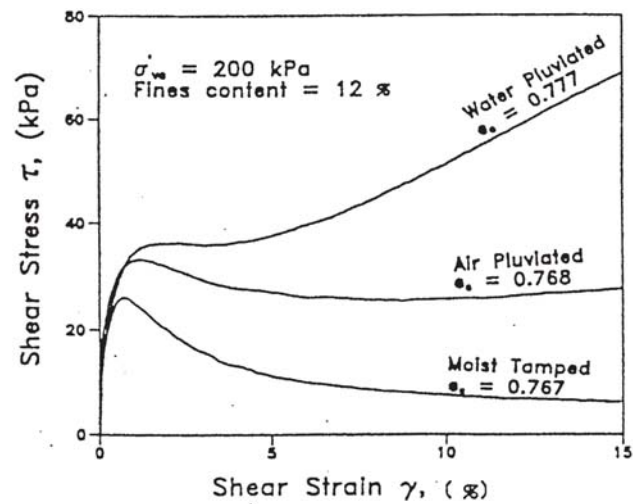


Figure 2.10 Effect of Syncrude sand sample formation on undrained simple shear response (Vaid et al., 1995)

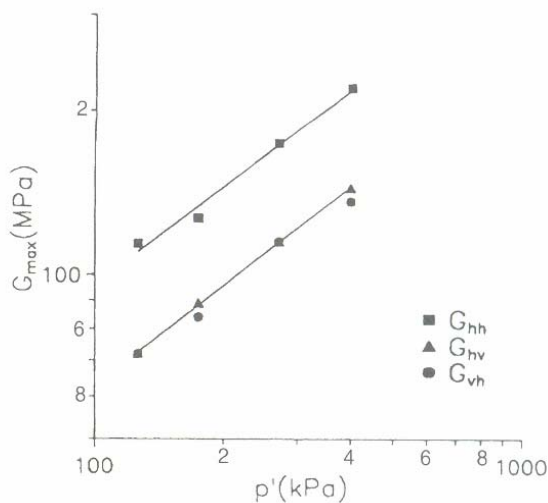


Figure 2.11 Anisotropic stiffness of London clay under isotropic stress conditions (Jovicic and Coop, 1998)

The effect of soil fabric on small-strain stiffness of reconstituted London clay specimen was studied by measuring the shear wave velocities in different directions under the same confining pressures (Jovicic and Coop, 1998). As the result in Figure 2.11, three different values of stiffness ( $G_{vh}$ ,  $G_{hv}$  and  $G_{hh}$ ) could be observed. The values of  $G_{hh}$  shows a larger values than those of  $G_{vh}$  and  $G_{hv}$  ( $G_{vh} \approx G_{hv}$ ) for a given confining pressure. Therefore, it can be indicated that the reconstituted London clay is inherently stiffer in horizontal direction than vertical direction due to its soil fabric.

Jamiolkowski et al. (1995) summarized the ratio of anisotropy of shear wave velocity from several in-situ tests as shown in Table 2.2.

Table 2.2 The ratio of anisotropy of shear wave velocity from in-situ tests (Jamiolkowski et al., 1995)

| Site                                      | Soil type                               | $V_{hh}^s / V_{vh}^s$  | References                           |
|---|---|------------------------|--------------------------------------|
| Montalto di Castro (Italy)                | Silty sand and silty clay strata        | 1.00-1.10              | Jamiolkowski and Lo Presti (1994)    |
| S.Francisco-Oakland Bay Bridge Toll Plaza | Sand and gravel                         | 0.88-1.10              | Mitchell et al. (1994)               |
| Alameda Bay Farm Island (Dike)            | Sand with fines                         | 0.85-1.04              | Mitchell et al. (1994)               |
| Alameda Bay Farm Island (South Loop Road) | Sand and clay strata                    | 0.86-1.16              | Mitchell et al. (1994)               |
| Port of Richmond (Hall Avenue)            | Sandy clay, silty clay, and clay strata | 0.93-1.12              | Mitchell et al. (1994)               |
| Port of Richmond (POR2)                   | Sandy clay, silty clay, and clay strata | 0.93-1.08              | Mitchell et al. (1994)               |
| Port of Richmond (POO7)                   | Poorly graded sand                      | 0.82-1.00              | Mitchell et al. (1994)               |
| Pence Ranch Idaho                         | Silty sand and gravel to sandy gravel   | 0.85-1.03              | Andrus (1994)                        |
| Anderson Bar Idaho                        | Sandy gravel from loose to medium dense | 0.85-1-15              | Andrus (1994)                        |
| Larter Ranch Idaho                        | Silty sand to sandy gravel              | 0.85-1.20              | Andrus (1994)                        |
| Gilroy No.2 Treasure Island               | Quaternary Alluvium Bay Mud             | 0.91-1.14<br>0.90-1.11 | Fuhriman (1993)                      |
| Site A<br>Site B Fort Honkock (Texas)     | Bolson fill                             | 0.75-1.41<br>0.57-1.08 | Stokoe et al. (1992)<br>Nasir (1992) |

#### 2.4.2 Stress induced anisotropy

Stress induced anisotropy refers to the anisotropy due to changing of soil fabric induced by the anisotropic stress state.

Wong and Arthur (1985) studied the effect of anisotropy induced in the inherently isotropic planes of samples of dense Leighton Buzzard sand using the directional shear cell under undrained shear condition. All specimens prepared by vertical raining of sand into the moulds were proved experimentally not to possess any inherent anisotropy in horizontal planes (see Figure 2.12). During shearing stage

$\sigma'_2$  was controlled at  $b=0.4$ . The imposed stress paths during subsequent shearing could be divided into two stages. During stage A, the specimens were loaded to a predetermined effective stress ratio  $\sigma'_3/\sigma'_1$  (with the major principal stress direction  $=\psi_A$ ) and then unloaded back to  $\sigma'_3/\sigma'_1=1$ . In stage B, the specimens were reloaded with the rotated major principal stress of  $\psi_B$ . The different directions are  $\Delta\psi=0^\circ$  and  $70^\circ$  ( $\Delta\psi=\psi_A-\psi_B$ ) as Figure 2.12. Stage A involved a axial strains range being developed before unloading.

The obvious effect of induced anisotropy on stiffness and dilatancy can be observed in Figure 2.13. The dense Leighton Buzzard sand response depended strongly on the strains applied during stage A, where the anisotropy was occurred. As the pre-strain level increased, the specimens tended more contractile and less stiff. This response was reinforced by  $\Delta\psi=70^\circ$ , the specimens became contract more and the stress-strain response was much more ductile. These results showed the degree of anisotropy induced during stage A.

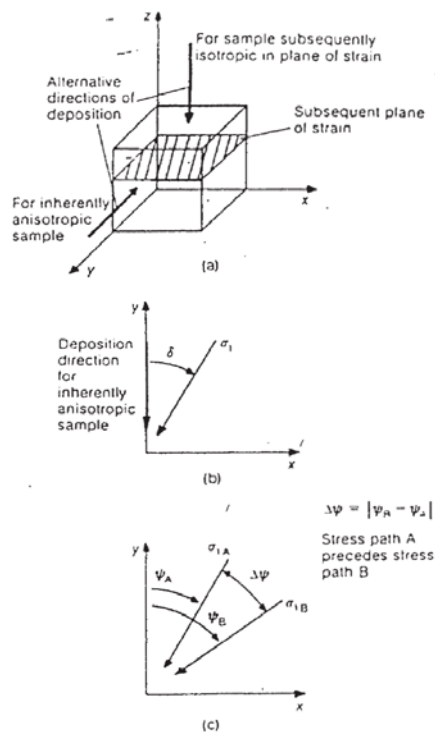


Figure 2.12 Sample orientation, stress paths and definition of measurement of anisotropy in the DSC (Wong and Arthur, 1985)

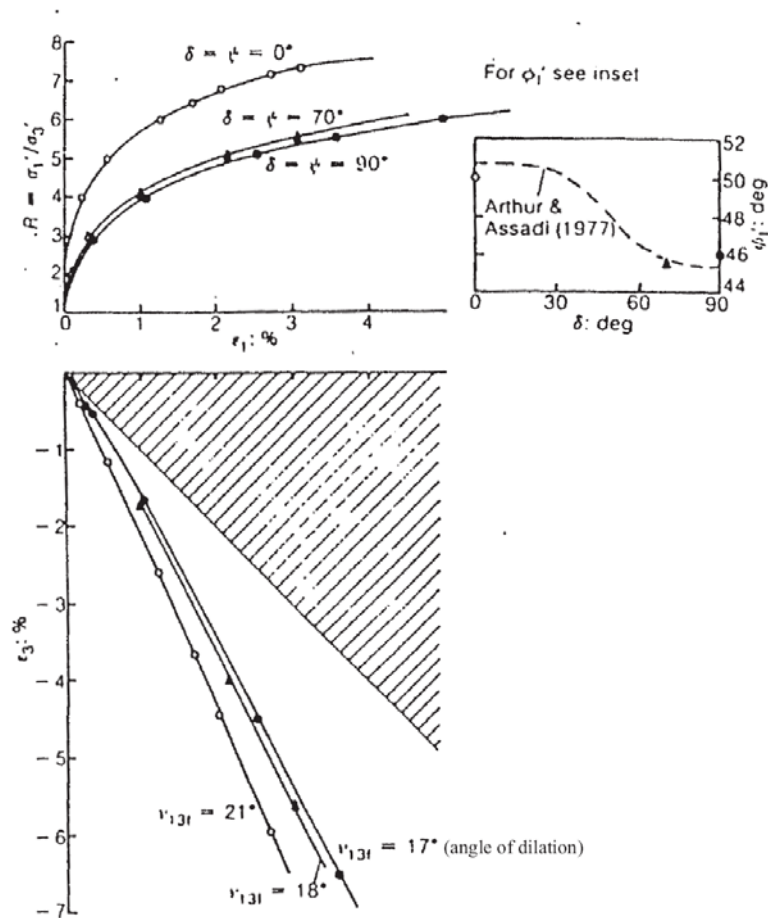


Figure 2.13 Stress-strain relationship of inherently anisotropic dense sand (Wong and Arthur, 1985)

### 2.4.3 Practical implications of soil anisotropy

Rotation of the principal stress direction is a common phenomenon in the geotechnical structures. Figure 2.14 represents the contours of the principal stress rotation ( $\alpha$ ) of the embankment analyzing from a non-linear isotropic finite element method (Yeats, 1983). The embankment was constructed on highly overconsolidated soft clay. These results explained that under the center line of embankment, the structure was namely subjected to an increase in axial stress. On the other hand, the soil at the toe of the foundation was supported in the state of unloading. This could be represented by a variation of  $\alpha$  from  $0^\circ$  to  $90^\circ$  respectively. From finite element analyzed by Hight and Higgins (1994), Jardine (1994) plotted the inclination of  $\alpha$  in a strutted deep excavation in Figure 2.15. This strutted deep excavation was built in a

thin deposition of Thames gravel ( $K_0 \approx 0.5$ ) overlaying on a thicker deposit of overconsolidated London Clay ( $K_0 \approx 2$ ). They also found that the rotation of  $\alpha$  were between  $30^\circ$  and  $90^\circ$  in the clay deposit.

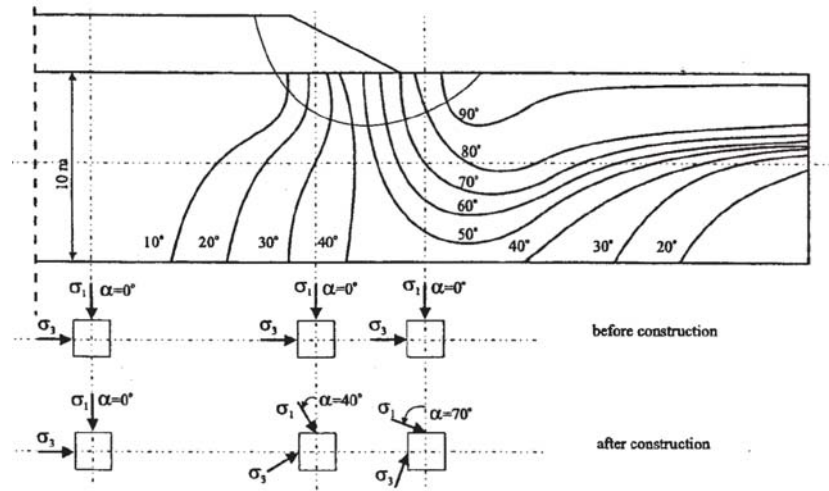


Figure 2.14 Contours of  $\sigma_1$  under embankment on soft clay from non-linear numerical analysis (Yeats, 1983)

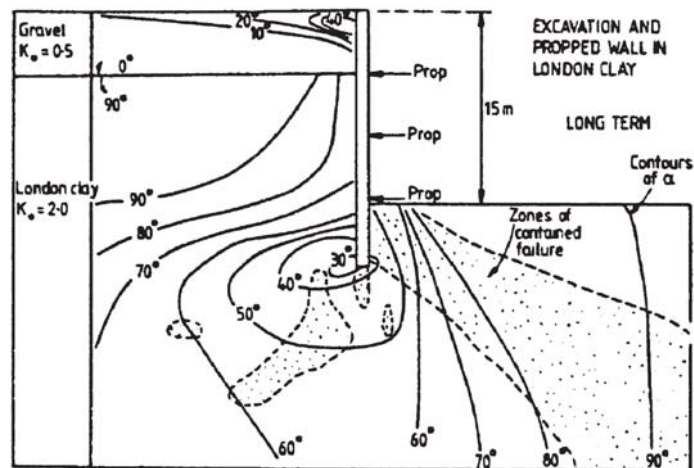


Figure 2.15 Contours of  $\sigma_1$  directions close to an excavation in Thames gravel overlaying on London clay (Jardine, 1994)

Most of the practical analysis in geotechnical design usually assumes the soil as isotropic behavior. In an attempt to quantify the relevance of this assumption, Zdravkovic et al. (2001) studied the effects of anisotropic on the behavior of soft clay embankment. They carried out finite element analysis using both an isotropic (Modified Cam-Clay) and anisotropic (MIT-E3) soil models. Moreover, these finite



element predictions were compared with the data from a full-scale test embankment brought to failure. Observed data was proposed by La Rochelle et al. (1974) and Tavenas et al. (1979). The plan view and cross section of the embankment are presented in Figure 2.16.

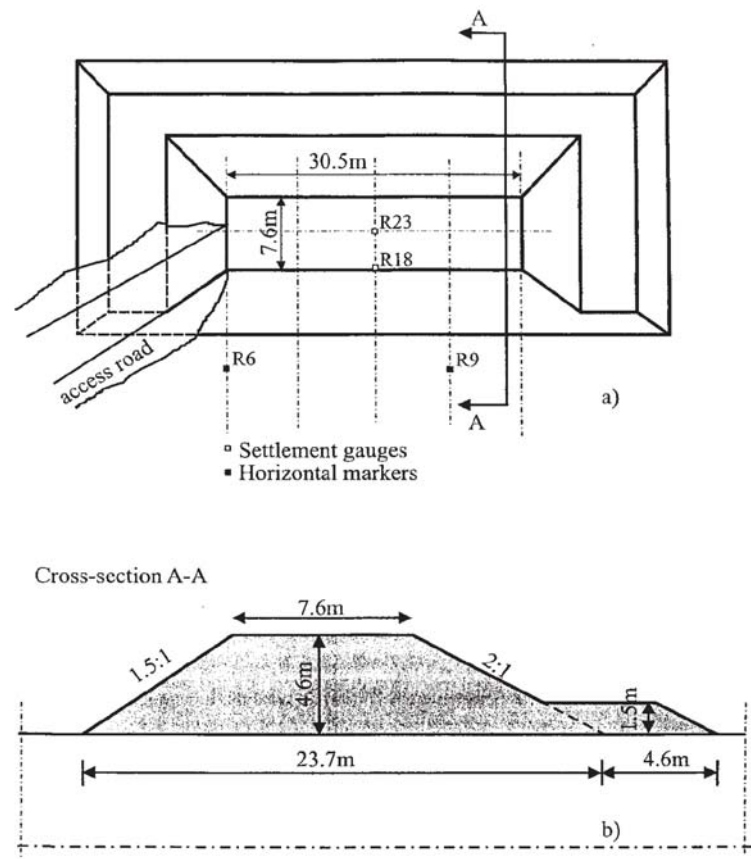


Figure 2.16 (a) Plane view and (b) Cross-section of the Saint-alban test embankment (Zdravkovic et al., 2001)

Figure 2.17 shows the development of horizontal displacement at the toe of the embankment. The horizontal displacement was normalized by the maximum horizontal displacement predicted just before the embankment failed. This result confirmed that anisotropic model represented a reasonable prediction. The failure height predicted by both anisotropic soil model and in-situ observation was 3.9 m. Moreover, the anisotropic approach fitted to the undrained shear strength data observed from direct simple shear (DSS) and triaxial compression and extension on isotropically consolidated samples. On the other hand, the isotropic approach fitted to only the undrained triaxial compression strength and the prediction embankment

height was 4.9 m, full 1 m more than the others. The reason for the overestimation was the large variation of the major principal stress to the vertical occurred along the failure surface.

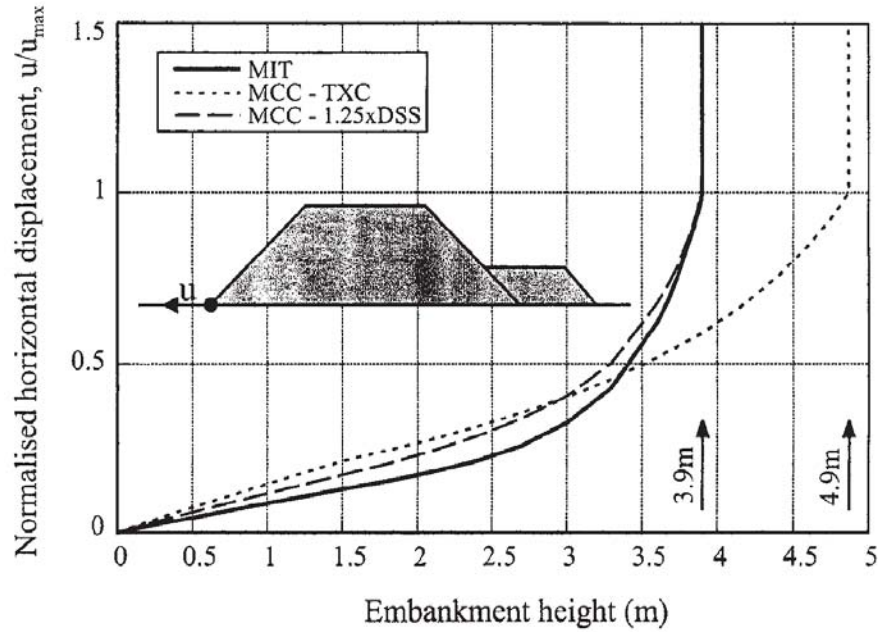


Figure 2.17 Comparison of failure heights from different analyzes (Zdravkovic et al., 2001)

## 2.5 Study of anisotropy using torsional shear hollow cylinder test

### 2.5.1 Definitions of $\alpha$ and $b$

The state of stress can be fully defined by stress tensor as shown in Eq. (2.6). From equilibrium consideration, the relationships are  $\tau_{zy} = -\tau_{yz}$ ,  $\tau_{xy} = -\tau_{yx}$  and  $\tau_{zx} = -\tau_{xz}$ . Therefore, the six independent stress components are required so as to define the state of stresses on the element. Moreover, it also can be defined by specifying the magnitude of the principal stresses ( $\tau = 0$ ). The direction of these principal stresses acting on three planes are defined by  $\alpha$ ,  $\beta$  and  $\gamma$  as shown in Figure 2.18.

$$T_{\sigma} = \begin{bmatrix} \sigma_z & \tau_{zy} & \tau_{zx} \\ \tau_{yz} & \sigma_y & \tau_{yx} \\ \tau_{xz} & \tau_{xy} & \sigma_x \end{bmatrix} \quad (2.6)$$

$$T_{\sigma}^* = \begin{bmatrix} \sigma_1 & 0 & 0 \\ 0 & \sigma_2 & 0 \\ 0 & 0 & \sigma_3 \end{bmatrix} \quad (2.7)$$

In geotechnical environments, the sedimentation of soil normally occurs in the direction of gravity. The angle  $\alpha=\beta=\gamma=0^\circ$  is expected in this condition. For normally consolidated sedimentation, the vertical stress is higher than the horizontal stresses ( $\sigma_v > \sigma_h$ ). Therefore,  $\sigma_v = \sigma_1$  and  $\sigma_h = \sigma_2 = \sigma_3 < \sigma_v$ . On the other hand, for heavily overconsolidated sedimentation, the vertical stress is lower than the horizontal stresses ( $\sigma_h > \sigma_v$ ),  $\sigma_h = \sigma_1 = \sigma_2$  and  $\sigma_v = \sigma_3$ . In order to express these changes in the relative magnitude of the intermediate principal stress, the intermediate principal stress parameter ( $b$ ) is informed (Bishop, 1966).

$$b = \frac{\sigma'_2 - \sigma'_3}{\sigma'_1 - \sigma'_3} \quad (2.8)$$

By using this relationship,  $b=0$  and  $\alpha=0^\circ$  in case of normally consolidated soils and  $b=1$  and  $\alpha=90^\circ$  in case of overconsolidated soils. It is also widely observed that the  $b$  value for plane strain condition lies within a range of  $b=0.3-0.5$ .

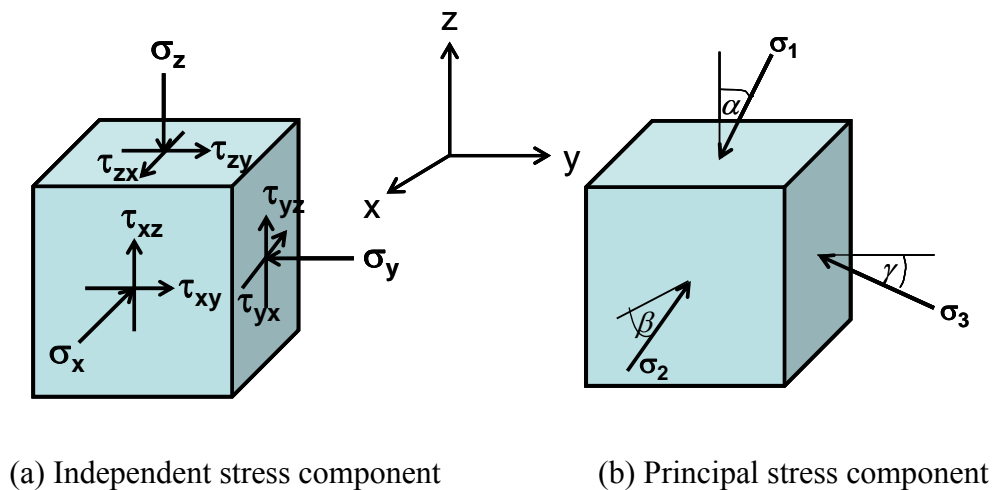


Figure 2.18 Stress components acting on a soil element (a) Independent stress component (b) Principal stresses component

### **2.5.2 Suitability of torsional shear hollow cylinder apparatus to study soil anisotropic behavior**

In order to study anisotropic characteristics of soils, the laboratory device which allows the ability to control both the magnitudes and the directions of the principal stress during shear is required. Moreover, the control of drainage condition is also the important qualification for performing both drained and undrained tests.

The torsional shear hollow cylinder apparatus becomes a popular device in geotechnical research. Because of their versatility to control not only the magnitudes of these principal stresses but also the inclination of the major principal stress axis by subjected to axial load, torque and outer and inner pressure. It is also possible to control and measure back pressure and study both of drained and undrained conditions. Therefore, when each of the stress boundaries is independently controlled, the direction of the major principal stress and the magnitude of the intermediate principal stress can be controlled.

The conventional triaxial apparatus has been used commonly in the laboratory. This device offers only two stress states at failure. The non-continuous change of  $\alpha$  from  $0^\circ$  to  $90^\circ$  in compression and extension modes is coupled with a jump of  $b$  from 0 to 1. Although  $b$  can be controlled in plane strain and true triaxial apparatus, the limitation in  $\alpha$  rotation is still remained in these tests. A directional shear cell is another technique which offers attractive capabilities to examine of strength anisotropy. Because it can impose subjectively normal and shear stress on the cubical specimen sides, three degree of freedom ( $\sigma_1$ ,  $\sigma_3$  and  $\alpha$ ) can be controlled. The stress component of directional shear cell is displayed in Figure 2.19. However, there are some problems in this test such as the presence of the edges to non-uniformities in the stress and stress distributions and the side membranes do not allow large differences in stress. The applicable stress states at failure by some of the advanced laboratory strength devices are summarized in Figure 2.20.

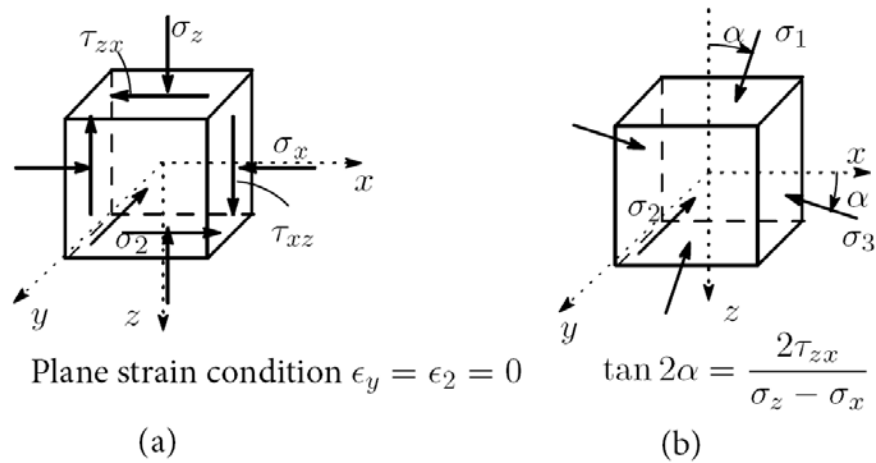
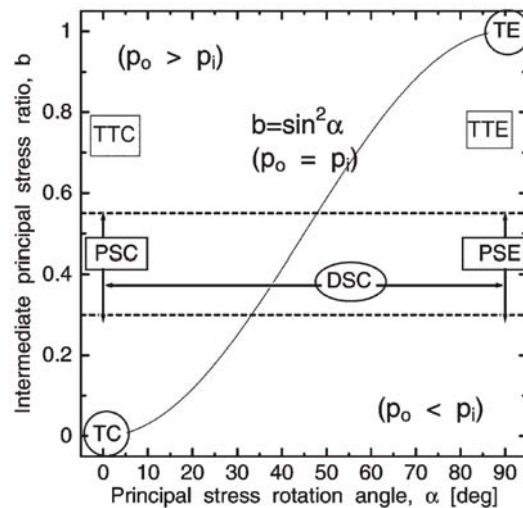


Figure 2.19 Directional shear cell (a) Stress components (b) Principal stresses and their directions (Nguyen, 2006)



Legends:

TC, TE: Triaxial compression ( $\alpha = 0^\circ, b = 0$ ) and extension ( $\alpha = 90^\circ, b = 1$ )

PSC, PSE: Plane strain compression and extension (under condition of  $\epsilon_2 = 0$ )

TTC, TTE: true triaxial compression and extension (Range  $0 \leq b \leq 1$ ;  $\alpha = 0$  or  $90^\circ$ )

DSC: Directional shear cell ( $0^\circ \leq \alpha \leq 90^\circ$  under condition of  $\epsilon_2 = 0$ )

HCA: Hollow cylinder apparatus at all possible regions ( $p_o, p_i$  are outer and inner cell pressure)

Figure 2.20 Applicable stress states at failure in some of the advanced laboratory strength devices (Nguyen, 2006)

### 2.5.3 Non-uniformity on hollow cylinder specimen

Although the hollow cylinder devices can offer highly capabilities for studying the behavior of soil, there are some disadvantages due to the non-uniform distribution of stresses and strains within the specimens. The combinations of normal and torsional shear stresses lead to the major principal stress rotation from the vertical direction in the hollow cylinder sample. The applied torque can develop shear stresses both in the vertical and horizontal directions. The gradients of radial stress and circumferential stress are established by the difference between the inner and outer pressure. Because of the application of inner and outer pressure through the flexible membranes, the shear stress (vertical and circumferential) will not be developed on this boundary. Therefore,  $\sigma_r$  is always a principal stress ( $\sigma_r = \sigma_2$ ). In some case, it is usually to control equal inner and outer pressure. The gradient of radial stress across the wall is zero and consequently  $\sigma_r = \sigma_\theta$ . For this condition, the direction of the major principal stress is related to  $b = \sin^2 \alpha$ . From the test principal as explained above, there are 2 main causes can lead to stress and strain non-uniformity. The first cause is stress non-uniformities arising from curvature of the hollow cylinder specimen. When the uniform boundary stresses are applied and there is no end restraint, variations of stress and strain can be occurred across the wall of the specimen, either torque or different inner and outer pressures which are applied leads to non-uniform stress across the wall of the specimen. Difference between internal and external pressure causes rise to variation in  $\sigma_r$  and  $\sigma_\theta$  across the wall. Even when the case of  $p_o$  and  $p_i$  are equal, torque leads to variations in shear stress across the wall. This condition may cause non-uniformities in normal stress  $\sigma_z$ ,  $\sigma_r$  and  $\sigma_\theta$ . For this reason it is necessary to analyze in terms of average stresses. Therefore, the distribution of stresses and strains remains a function of the specimen geometry and the stress and strain properties of the materials. This topic will be discussed future in the following sections.

The other cause is strain non-uniformities arising from end restraint. As a result of the restraining effect which is happened by the function between the platens and the specimen, the developments of radial shear stresses  $\tau_{zr}$  are arisen at the top and bottom ends of the specimen. Although it is possible to reduce the frictional

restraint but this friction is necessary for transmission of torque to the sample. These shear stresses result in additional circumferential stress, in bending moment which affect the distribution of vertical stress and in rotations of principal stress out of the plane of the cylinder wall. A non-uniform distribution of axial stress is illustrated in Figure 2.21. The stress distribution developing from these effects is clearly dependent on specimen geometry, the specimen's constitutive law and the applied pressure and load combinations.

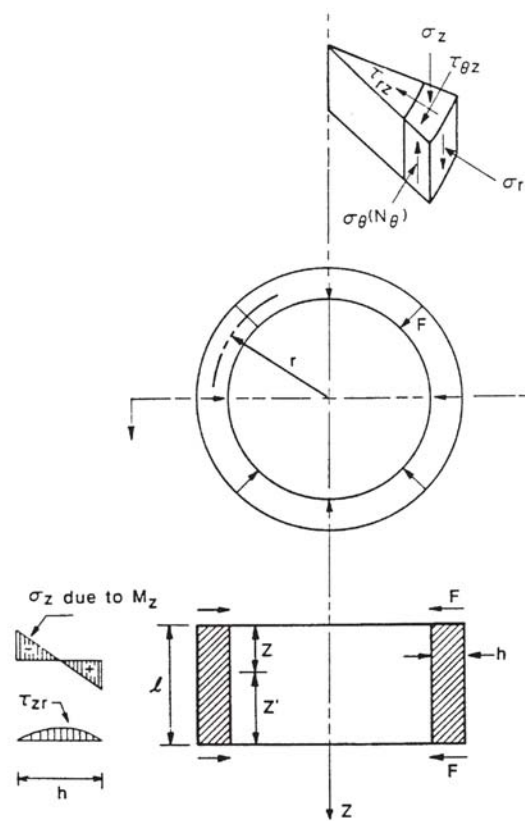


Figure 2.21 Stress component in hollow cylinder samples including end-effects (after Saada and Townsend, 1981)

#### 2.5.4 Previous studies of stress and strain non-uniformity

From the combinations of wall curvature and end restraint effect, the stresses and strains on the hollow cylinder specimen are not uniform. This restriction is related to boundary conditions namely; sample dimensions, end platen effects and stress path. There are a number of results from numerical analyzes on hollow cylindrical sample by different authors. These studies will be summarized in the following section.

Two-dimensional axisymmetric models with linear elastic and strain hardening Modified Cam-Clay (MCC) constitutive laws were used in finite element analysis of the non-uniformities in the large ICHCA proposed by Hight et al. (1983). In order to quantify the level of non-uniformity of stresses across the wall of hollow cylinder samples, the parameter as shown bellow was expressed by Hight et al. (1983):

$$\beta_3 = \frac{\int_a^b |\sigma(r) - \bar{\sigma}^*| \cdot dr}{(b-a) \cdot \sigma_L} \quad (2.9)$$

where  $\sigma(r)$  is the distribution of the stress across the wall of the specimen.

$\bar{\sigma}^*$  is the real average stress from the distribution of stress across the wall.

$\sigma_L$  is a measure of the stress level which was derived as  $\frac{|\bar{\sigma}_\theta| + |\bar{\sigma}_r|}{2}$ .

$a$  and  $b$  are inner and outer radius respectively.

Figure 2.22 shows the definitions used for stress non-uniformity and accuracy. A line of  $\bar{\sigma}$  in Figure 2.22 represents the average stress value obtained using the experimental interpretation. Moreover, similar can be used for differences in average strain and for strain non-uniformity.



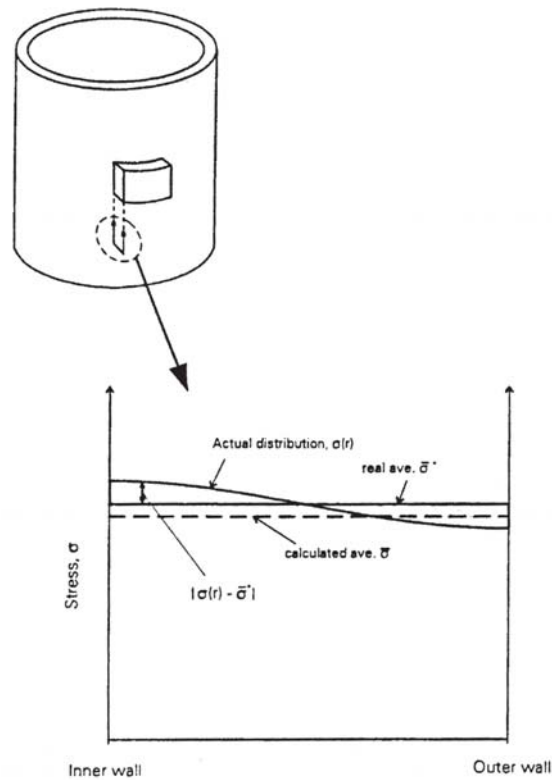


Figure 2.22 Definitions used for stress non-uniformity (Hight et al., 1983)

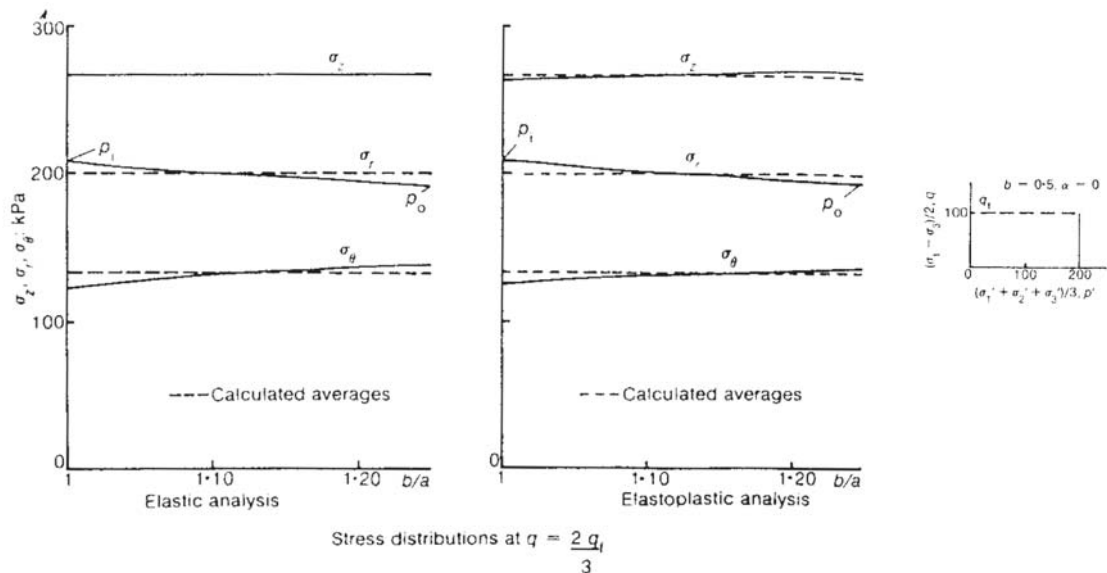


Figure 2.23 Stress distributions across the hollow cylinder specimen wall (Hight et al., 1983)

From the study, the non-uniformity effects were investigated by using the various dimensions of the hollow cylinder specimen. The specimens were fixed in the wall thickness at 25 mm. Outer and inner diameters were 250 and 200 mm,

respectively. The specimen heights were changed. The example of stress distributions at 2/3 of failure stress across the wall of sample is shown in Figure 2.23. The sample was isotropically consolidated to  $p'=200$  kPa and followed by drained shearing to 100 kPa of shear stress level at constant  $p'$  and with  $b=0.5$ . As a result of different inner and outer pressures, non-uniform distributions of radial and circumferential stresses across the wall were observed. Moreover, in the elasto-plastic case, the normal stress became non-uniform as well.

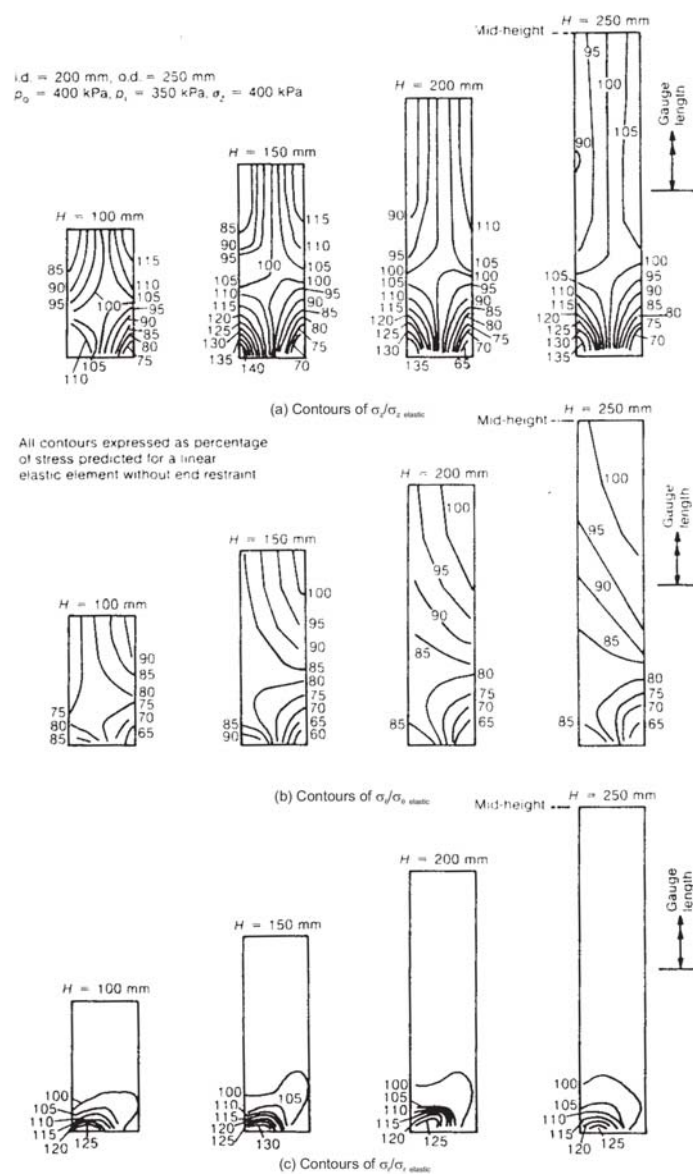


Figure 2.24 Linear elastic analysis of stress distribution in fixed-end hollow cylinder elements of different heights (Hight et al., 1983)

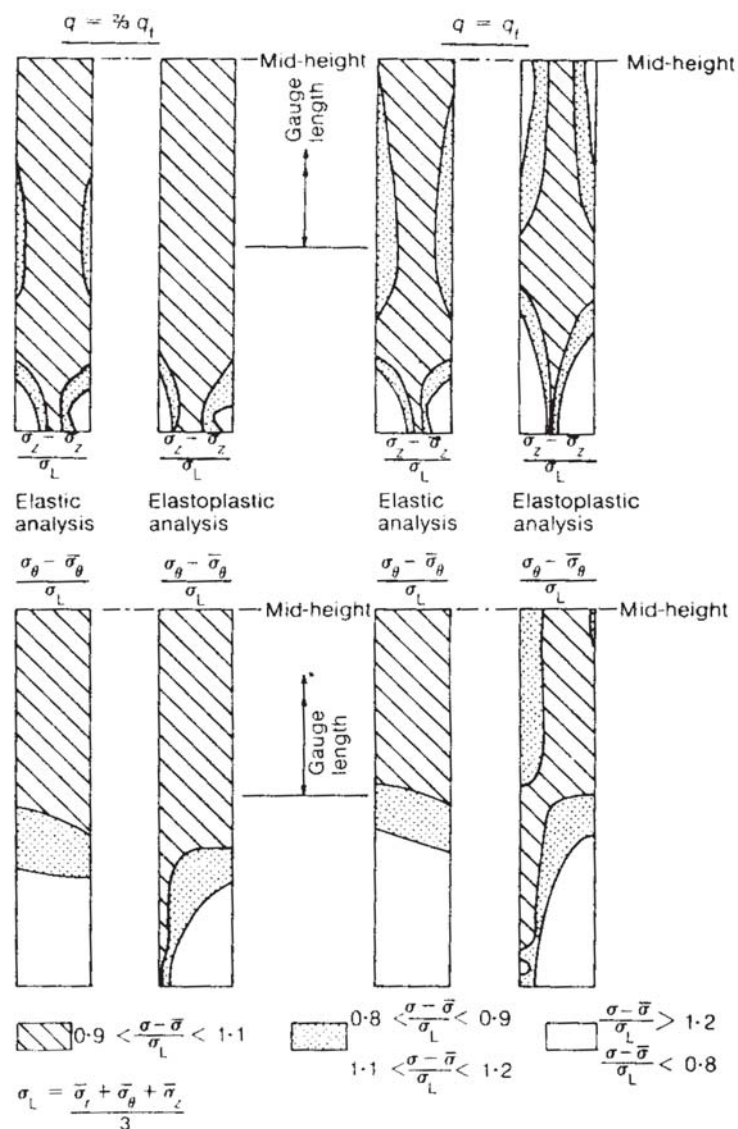


Figure 2.25 Elastoplastic and elastic analyses of fixed-end 200 mm height hollow cylinder samples (Hight et al., 1983)

As an illustration of the effects of end restraint, Figure 2.24 shows the results from a series of linear elastic analyses of fixed-end sample of 4 different heights and inner and outer diameter of 200 mm and 250 mm, respectively. The combination of applied stresses comprised an axial stress of 400 kPa, inner pressure of 350 kPa and outer pressure of 400 kPa but the torque was omitted. Analyzes are represented as contours of percentages of linear elastic analyses. Poisson's ratio of 0.499 and unrestrained hollow cylinder were assumed. The concentrations of non-uniformities

between the ends of samples were observed. The most concentration was evidently in the axial stress.

Figure 2.25 displays the result from the analysis of a complete hollow plastic with end restraint. The behavior was assumed to be strain-hardening plastic. The average stress path is displayed in Figure 2.23 ( $b=0.5$  and  $\alpha=0^\circ$ ). The dimension of sample is 200 mm inner diameter, 250 mm outer diameter and a height of 250 mm. Distributions of normalized  $\sigma_z$  and  $\sigma_\theta$  are illustrated in 2 stress levels namely; at failure ( $q_f$ ) and  $2/3$  of  $q_f$ . It can be obviously observed that the stress non-uniformity become larger as failure is approached. However, the uniform stress distributions are reasonably obtained in the central portion of the sample.

From the study of Hight et al. (1983), they considered acceptable the level of stress non-uniformities in the ICHCA if the value of  $\beta_3 < 0.11$ . The ratio of outer to inner cell pressure was restricted to the range of  $0.9 < \frac{p_o}{p_i} < 1.2$ . As this reason the regions of “no-go” stress state which stress non-uniformities were considered unacceptable were proposed. A schematic view of “no-go” areas corresponding in  $q - b - \alpha$  space is presented in Figure 2.26.

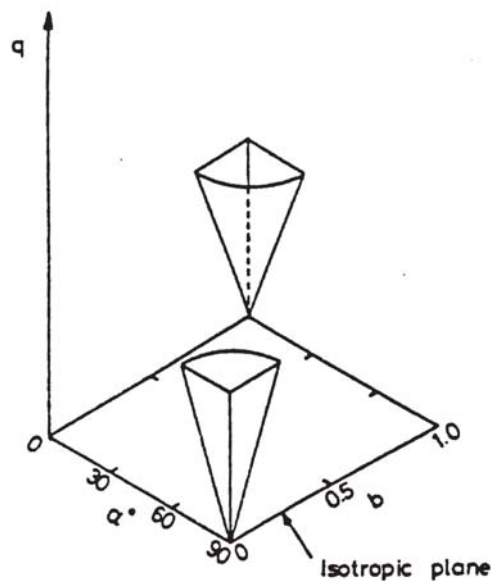


Figure 2.26 Schematic diagram of “no-go” areas proposed by Hight et al. (1983)

Sayão and Vaid (1991) suggested that using of  $\beta_3$  parameter proposed by Hight et al. (1983) can lead to an exaggerated view of excessive non-uniformities in hollow cylinder specimen. They also proposed a different stress non-uniformity coefficient across the wall based on the difference in the effective stress ratio ( $R = \frac{\sigma_1'}{\sigma_3}$ ). This coefficient was defined below.

$$\beta_R = \frac{R_{\max} - R_{\min}}{R_{av}} \quad (2.10)$$

where  $R_{\max}$  and  $R_{\min}$  are maximum and minimum stress ratio respectively.

$R_{av}$  is the average stress ratio.

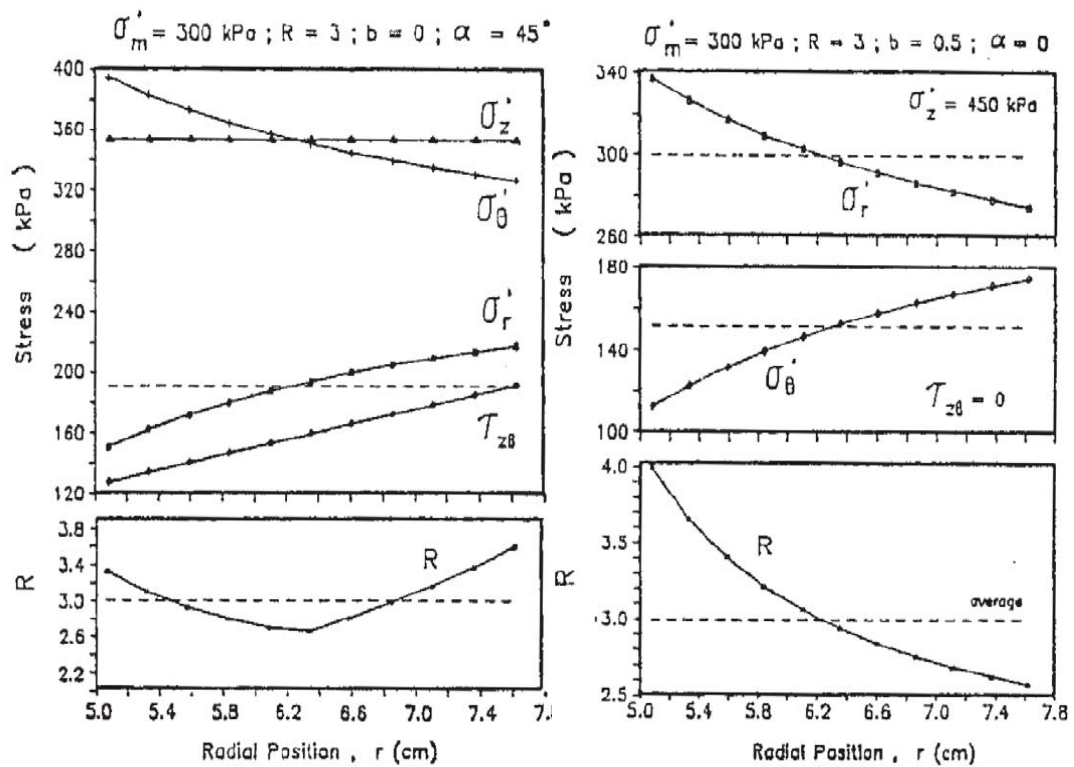


Figure 2.27 Elastic stresses across the wall of hollow cylinder specimens (Sayão and Vaid, 1991)

Figure 2.27 illustrates an example of the elastic stress distribution across the wall of specimen. The inner and outer diameters of the sample were 120 mm and 152 mm respectively. The wall thickness was 25 mm. There were two sets of stress states namely;  $p'=300$  kPa,  $R=3$ ,  $b=0$  and  $\alpha=45^\circ$  and  $p'=300$  kPa,  $R=3$ ,  $b=0.5$  and  $\alpha=0^\circ$ . The stress non-uniformity coefficients ( $\beta_3$ ) proposed by Hight et al. (1983) of both stress states were 0.07. This value was acceptable to the criteria of  $\beta_3 \leq 0.11$ . However, when considering in the stress ratio distributions, the stress non-uniformity coefficients ( $\beta_R$ ) of the first and second stress states were 0.32 and 0.46. These values were not acceptable by Sayão and Vaid (1991) because these could imply a difference of up to  $10.5^\circ$  in mobilized shear resistance angle in triaxial condition.

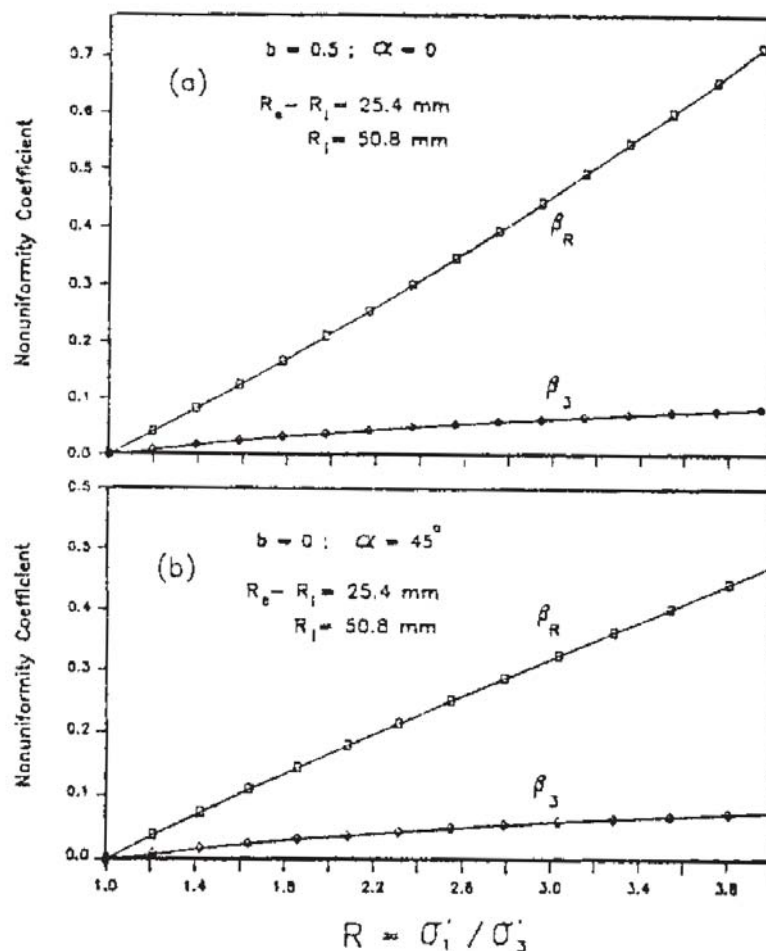


Figure 2.28 Effect of stress ratio on non-uniformity coefficients (Sayão and Vaid, 1991)

As shown in Figure 2.28 (Sayão and Vaid, 1991), stress non-uniformities increased with stress ratio ( $R$ ). They also recommended that the stress non-uniformities were considered acceptable when the value was  $\beta_R \leq 0.2$ . This value was corresponded to the maximum difference between  $R_{max}$  and  $R_{min}$  was below 20%. Therefore, it was recommended that the stress ratio should to be controlled below 2.5 so as to maintain acceptable levels of non-uniformities. Moreover, they also presented that increase in the wall thickness, increase the stress non-uniformity and inner radii exceed 40-50 mm could decrease degree of non-uniformities.

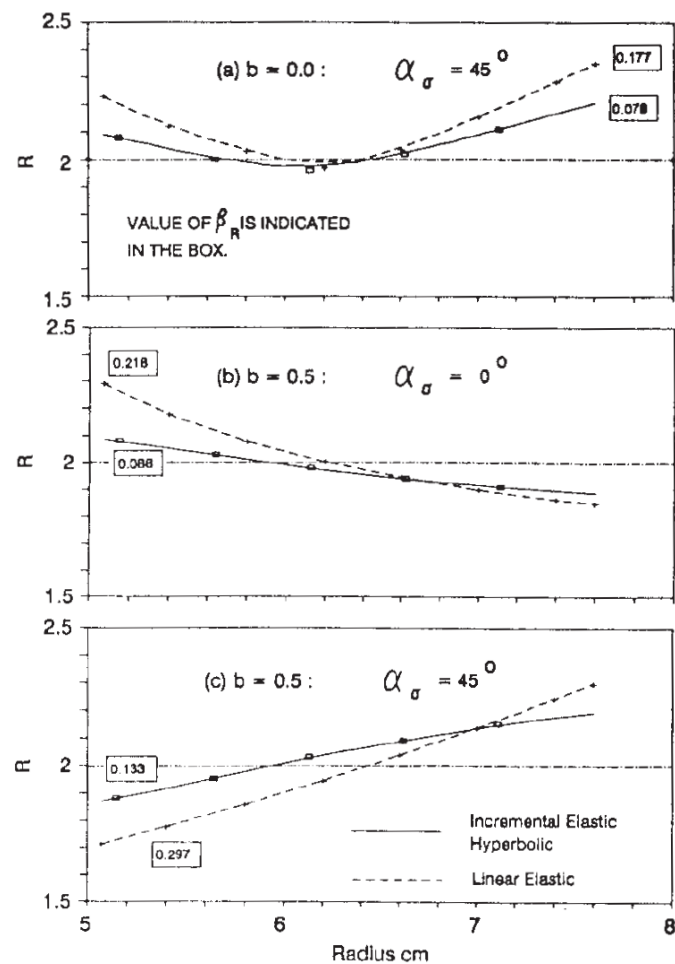
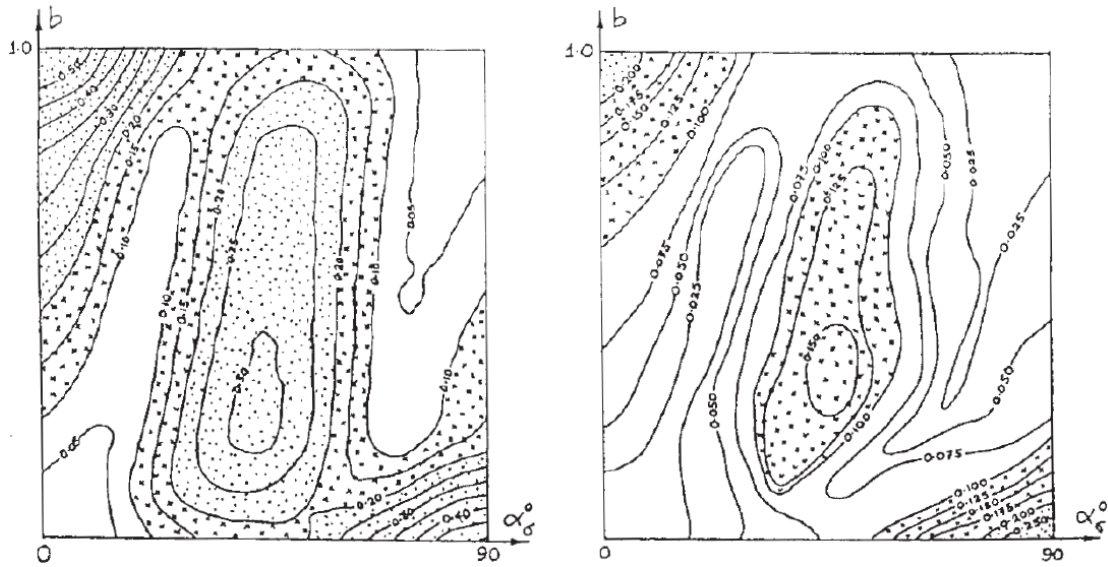


Figure 2.29 Distribution of stress ratio across the wall of a hollow cylinder sample at  $p' = 300$  kPa,  $R = 2.0$  and  $Dr = 30\%$  (Wijewickreme and Vaid, 1991)

Wijewickreme and Vaid (1991) observed non-uniformities of stress due to the hollow cylinder curvature using linear-elastic and non-linear (elastic) hyperbolic soil models. Figure 2.29 displays the distribution of stress ratio across the wall of sample

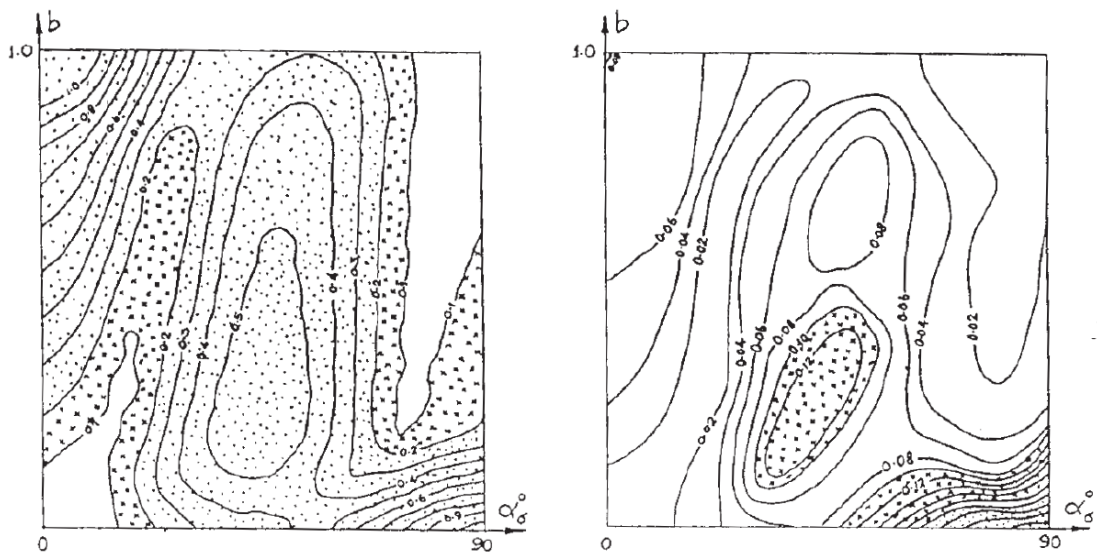
with values of  $\alpha=0^\circ$  and  $45^\circ$  and  $b=0$  and  $0.5$  at  $R=2$ . Linear elastic analyze consistency overestimates non-uniformity level when compared to the value obtained by the non-linear model.



(a) Linear elastic (Sayão, 1989)

(b) Incremental elastic hyperbolic

Figure 2.30 Contours of  $\beta_R$  at  $p' = 300$  kPa,  $R = 2.0$  and  $Dr = 30\%$  (Wijewickreme and Vaid, 1991)



(a) Linear elastic (Sayão, 1989)

(b) Incremental elastic hyperbolic

Figure 2.31 Contours of  $\beta_R$  at  $p' = 300$  kPa,  $R = 3.0$  and  $Dr = 30\%$  (Wijewickreme and Vaid, 1991)



When non-linear consideration, Wijewickreme and Vaid (1991) also observed that non-uniformity of stress increase with stress ratio at low levels of  $R$  but they tend to reduce as failure is approached. Figure 2.30 and 2.31 show contours of  $\beta_r$  for the entire  $b - \alpha$  space for the stress state namely  $R=2$  and  $R=3$ . The decrease in the level of non-uniformity with effective stress ratio can be observed (represented by the smaller shaded area in Figure 2.31).

### **2.5.5 Previous studies of effects of $\alpha$ and $b$ on soil response**

From the literature review, the shear strength and stiffness of soils depend significantly on the magnitude of the intermediate principal stress usually represented in term of  $b$  parameter and the rotation of the major principal stress with respect to the vertical direction ( $\alpha$ ). Most geotechnical structures are subjected to complex stress regimes where  $\alpha \neq 0$  and  $b \neq 0$  and  $\neq 1$ , which is not normally simulated adequately in routine laboratory investigations.

In this section the literature reviews of soil anisotropic features are described. These reviews are focused on the features of both undrained and drained condition of several soils subjected to the stress stages with different orientations of  $\alpha$  and magnitudes of  $b$ .

#### **2.5.5.1 Effect of $\alpha$**

##### **i. Drained condition**

To investigate the effect of initial anisotropy, torsional shear tests carried out on medium-loose Ham River sand, HRS (formed by water pluviated technique) under drained shear condition were studied by Symes (1983). All specimens were isotropically consolidated to a mean effective stress ( $p'$ ) of 200 kPa with a back pressure of 400 kPa in order to ensure saturation. Specimens were sheared with the various values of  $\alpha$  and  $b$  so as to investigate the effects of anisotropic behavior under drained condition. The shear stress was increased monotonically until failure carried out under stress control, while  $p=600$  kPa and  $b$  were kept constant. The inclination of  $\alpha$  related to the vertical direction was varied between  $0^\circ$  and  $90^\circ$ .

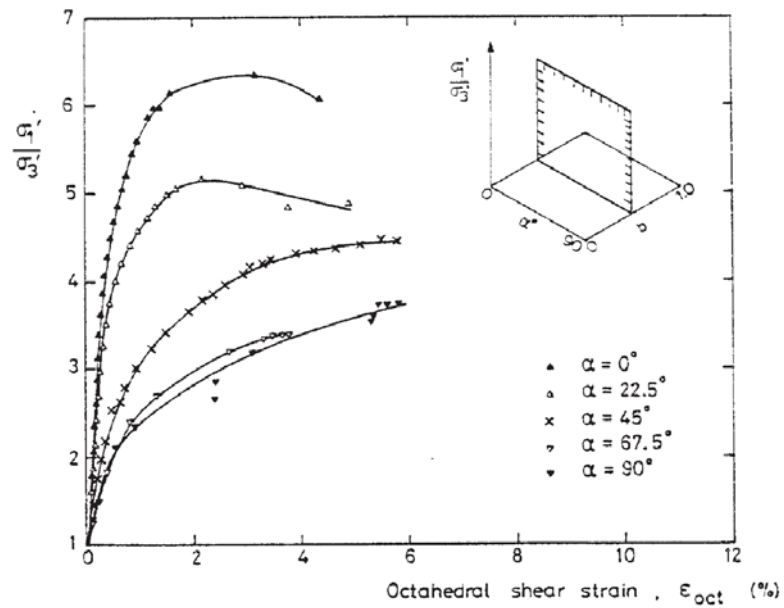


Figure 2.32 Stress ratio versus octahedral shear strain from HCA tests on isotropically consolidated medium-loose HRS sheared drained with  $b=0.5$  (Symes, 1983)

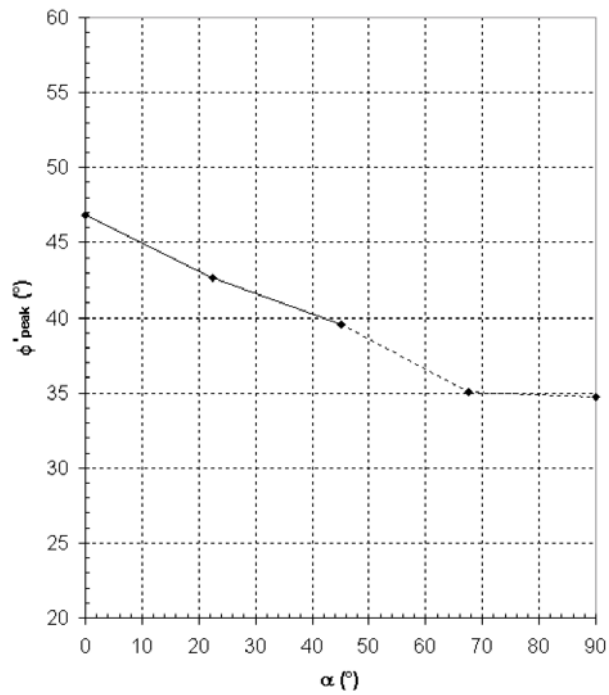


Figure 2.33 Mobilised  $\phi'_{peak}$  at peak stress ratio from HCA tests on isotropically consolidated HRS sheared drained with  $b=0.5$  (Symes, 1983)

Figure 2.32 shows the relationship between stress ratio ( $\sigma'_1/\sigma'_3$ ) versus octahedral shear strain, ( $\varepsilon_{oct}$ ) from a series of HCA tests with  $b=0.5$  and values of  $\alpha$  ranging between  $0^\circ$  and  $90^\circ$ .  $\varepsilon_{oct}$  is defined by 
$$\varepsilon_{oct} = \frac{2}{\sqrt{6}} \sqrt{(\varepsilon_1 - \varepsilon_2)^2 + (\varepsilon_2 - \varepsilon_3)^2 + (\varepsilon_3 - \varepsilon_1)^2}$$
. The result shows that the stiffness of soil reduced with increasing values of  $\alpha$ . Volumetric compression also tended to increase with increasing  $\alpha$ . Stress ratios at peak and ultimate state reduced dramatically as  $\alpha$  was rotated from the vertical direction. Figure 2.33 shows a significant variation in friction angle at the maximum stress ratio, ( $\phi'_{peak}$ ). The value of  $\phi'_{peak}$  values showed a dramatic decrease of nearly  $12^\circ$  when  $\alpha$  was rotated from  $0^\circ$  to  $90^\circ$ . Moreover, similar trends were occurred at the fixed  $b=0, 0.14$  and  $1$ , although the larger effects observed when  $b=0.5$ .

Wong and Arthur (1985) sheared the dry samples of dense Leighton Buzzard sand using the directional shear cell, DSC at constant  $b$  value ( $b=0.4$ ). The directions of the major principal stress respected to deposit direction were controlled at  $\delta=0^\circ, 70^\circ$  and  $90^\circ$ . It is noted that  $\delta$  in this case refers to  $\alpha$  in this research. These specimens were formed by pouring in moulds designed to allow plane shearing either parallel to the direction of deposition or in orthogonal directions as shown in Figure 2.12. The stress-strain curves for tests with three different sample bedding plane orientations ( $\delta=0^\circ, 70^\circ$  and  $90^\circ$ ) are illustrated in Figure 2.13. The drained shear strength, as represented by the maximum stress ratio  $\sigma'_1/\sigma'_3$ , was observed to change with the angle  $\delta$ . Stiffness decreased with increasing  $\delta$  resulted in the value of friction angle at failure ( $\phi'_f$ ). The values of  $\phi'_f$  decreased nearly  $5^\circ$  when  $\delta$  varied from  $0^\circ$  to  $70\sim 90^\circ$ . These results represented similar observation to those obtained from Symes (1983) which is described above.

The experiment by Oda et al. (1978) was carried out on Toyoura sand in a plane strain device under drained shearing condition. The different orientations with respect to the vertical shearing direction ( $\delta$ ) were controlled between  $0^\circ$  and  $90^\circ$ . It is noted that  $\delta$  direction in this study is different from that proposed by Wong and

Arthur (1985) as discussed above. However, it is reciprocal of  $\alpha$  defined by Symes (1983) as  $\alpha=90-\delta$ . Specimens were isotropically consolidated to  $p$  of 50, 100, 200 and 400 kPa. Then specimens were sheared by increasing the vertical stress until failure, while keeping  $\sigma'_3$  constant and controlling  $\sigma'_2$  to maintain plane strain conditions ( $b \approx 0.2 \sim 0.3$ ).

The stress-strain relationship between of  $\sigma'_1 - \sigma'_3$  versus  $\epsilon_1$  in case of shearing with  $\sigma'_3 = 200$  kPa is shown in Figure 2.34. It is exhibited that the stress-strain responses became softer as  $\delta$  reduced (increasing  $\alpha$ ). The stress ratio at peak deviator stress also decreased when decreasing in  $\delta$  (with a minimum found when  $\delta \approx 24^\circ$ ). Moreover, the volumetric strains ( $V$  in the figure), showed less dilatant for lower  $\delta$  value. Similar trends in the stress-strain response were obtained for the samples sheared at other stress levels.

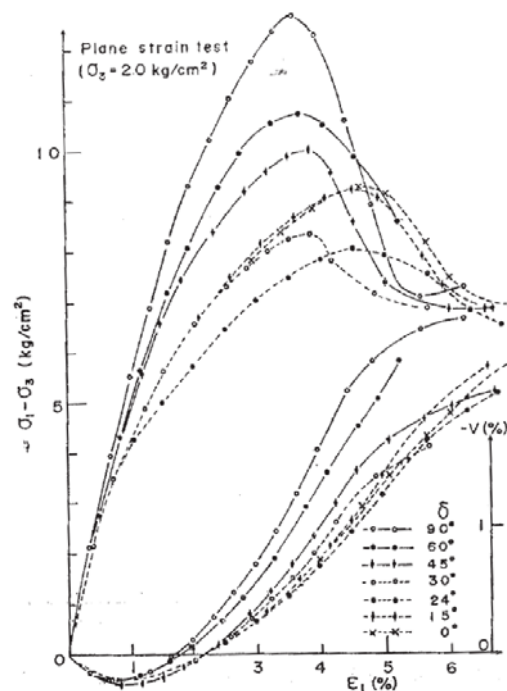


Figure 2.34 Stress-strain relationship from plane strain tests on isotropically consolidated dense Toyoura sand (Oda et al., 1978)

The result of changing in  $\phi'_{peak}$  with  $\delta$  for tests at initial stress levels of 50 and 200 kPa is presented in Figure 2.35. The drained strength increased with increasing  $\delta$ .

The minimum  $\phi'_{peak}$  could be observed between  $\delta=15^\circ$  and  $30^\circ$ . The maximum difference in  $\phi'_{peak}$  was around  $6^\circ$ - $7^\circ$ . Interestingly this observation represents different trend with Symes (1983) and Wong and Arthur (1985) described above. However, there are a lot of drained plane strain and true triaxial and torsional shear test carried on Toyoura sand confirmed the same stress-strain and strength trends with the observation reported by Oda et al. (1978) (Tatsuoka et al.,1986; Lam and Tatsuoka, 1988a; Miura et al.,1986).

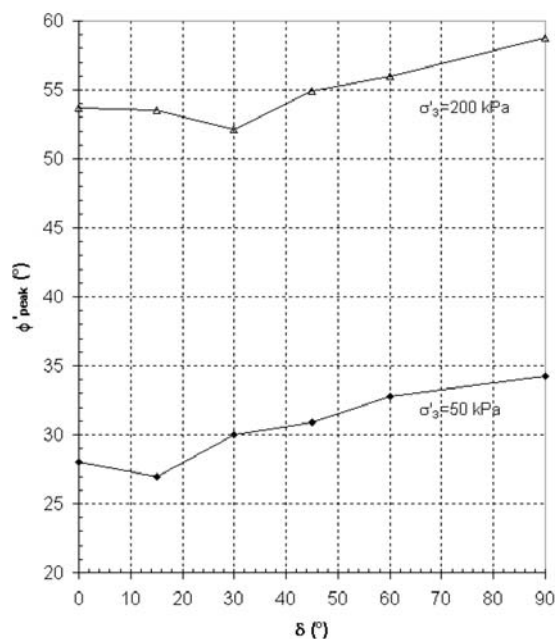


Figure 2.35 Anisotropy of mobilised  $\phi'$  at peak from plane strain tests on isotropically consolidated dense Toyoura sand (data from Oda et al., 1978); Note that  $\alpha = 90 - \delta$

It is important to emphasize that  $\phi'$  depends highly on the material types. Predominately granular soils tend to suffer reductions in  $\phi'$  when increasing in  $\alpha$ , whereas fine-grained soils can show marginal reductions or even increases in this parameter (Menkiti, 1995; Porovic, 1995; Hight et al., 1997).

## ii. Undrained condition

Shibuya (1985) studied the effect of  $\alpha$  on undrained shear strength ( $s_u$ ) of water pluviated loose Ham River sand (HRS) using a hollow cylinder device. A series

of hollow cylindrical specimen were isotropically consolidated to  $p \approx 200$  kPa. During shearing,  $p$  was controlled at the constant value of 600 kPa under stress control. The predetermined loading paths were followed with different values of  $\alpha$  and  $b$ .

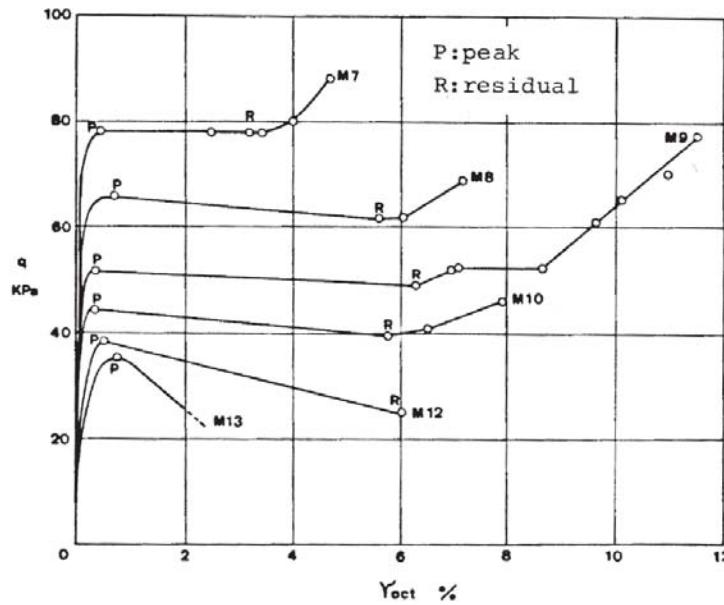


Figure 2.36 Development of octahedral shear strain in HCA tests on isotropically consolidated, medium-loose HRS with  $b=0$  and various values of  $\alpha$  (Shibuya, 1985)

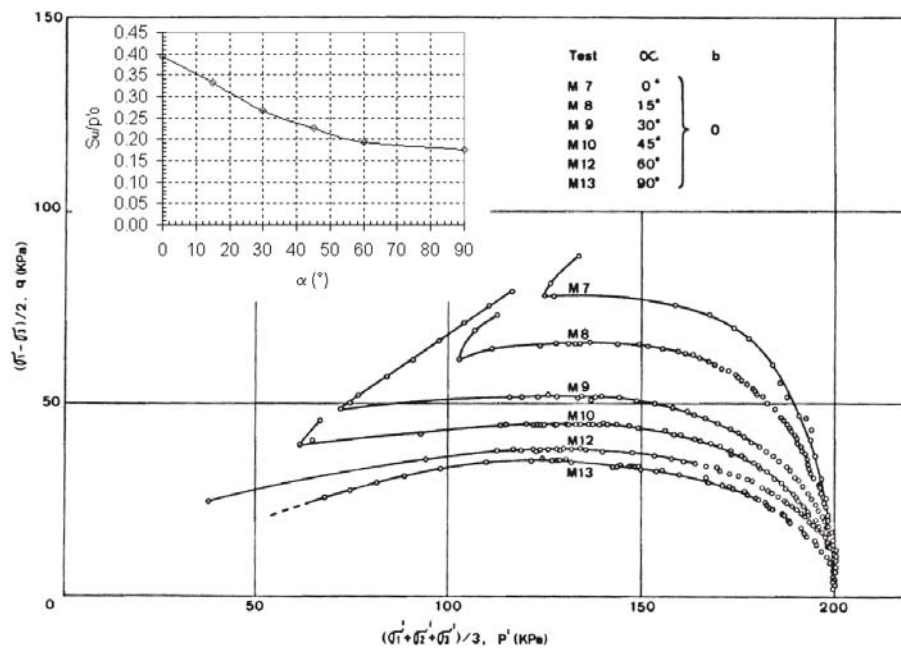


Figure 2.37 Effective stress paths from HCA tests on isotropically consolidated HRS with  $b=0$  and various values of  $\alpha$  (Shibuya, 1985). Insert corresponds to the

normalised undrained shear strength

Figure 2.36 represents a typical shear stress ( $q=(\sigma'_1-\sigma'_3)/2$ ), versus octahedral shear strain ( $\gamma_{oct}=\frac{2}{\sqrt{6}}\sqrt{(\varepsilon_1-\varepsilon_2)^2+(\varepsilon_2-\varepsilon_3)^2+(\varepsilon_3-\varepsilon_1)^2}$ ) for the series of tests where samples were sheared with  $b=0$ , and  $\alpha$  ranging between  $0^\circ$  and  $90^\circ$ . The stress-strain showed softer response at higher values of  $\alpha$ . The value of  $q_{peak}$  was reached at larger strains as increasing in  $\alpha$  as shown in Figure 2.37. The distribution of  $s_u$  normalised by the mean effective stress before shearing ( $p_0 \approx 200$  kPa) with  $\alpha$  is summarized in the insert of Figure 2.37. The value of  $s_u$  exhibited a dramatic fall particularly between  $\alpha=0^\circ$  and  $60^\circ$ . The value of  $s_u$  was nearly 2.3 times larger at  $\alpha=0^\circ$  than at  $\alpha=90^\circ$ . Similar trends were observed at  $b=0.5$  and  $1.0$ . It is noted that similar effects of the undrained test series of pluviated loose HRS were widely investigated in the hollow cylinder device reported by many researchers such as Symes (1983); Symes et al. (1984); Shibuya et al. (2002a).

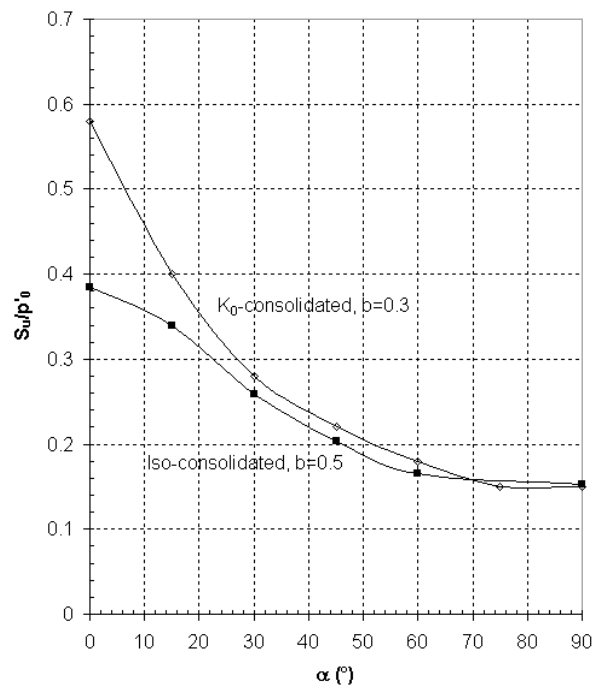


Figure 2.38 Anisotropy of undrained shear strength from isotropically and  $K_0$ -consolidated HRS sand HCA samples (data from Shibuya 1985 and Shibuya and Hight 1996)

Shibuya and Hight (1996) and Shibuya et al. (2002b) studied similar tests on  $K_0$ -consolidated ( $K_0=0.5$ ) loose HRS. The loose HRS specimens were prepared in the same way and tested with the same apparatus used by Symes (1983) and Shibuya (1985). All specimens were also consolidated to  $p_0 \approx 200$  kPa, and  $b=0.3$  during undrained shearing due to plane strain condition. A similar result could be observed. Softer and weaker responses were noticed with increasing in the value of  $\alpha$ . The value of  $s_u$  at  $\alpha=0^\circ$  was 3.8 times larger than at  $\alpha=90^\circ$ . Figure 2.38 shows the distributions of  $s_u/p_0'$  for isotropically consolidated samples sheared with  $b=0.5$  (from Shibuya, 1985), and the  $K_0$ -consolidated ones (with  $b=0.3$ ).

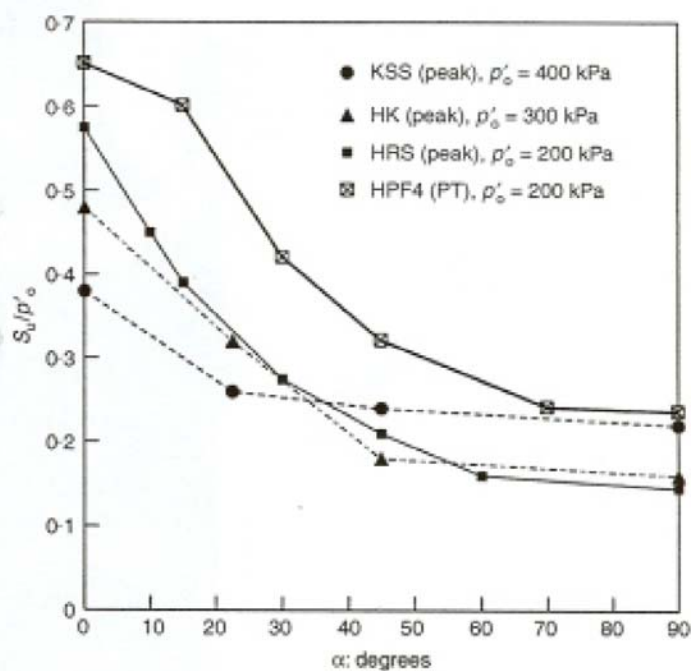


Figure 2.39 Anisotropy of undrained shear strength at  $b = 0.5$  of normally  $K_0$ -consolidated soils ( $OCR = 1$ ) from the Imperial College database (Jardine et al., 1997). Values of  $s_u$  taken at peak shear stress, and at phase transformation point (PT) for HPF4 specimens

Anisotropic behavior of many soils was widely studied at Imperial College. Table 2.3 presents the testing program researched at Imperial College for reconstituted clayey soils and silts using HCA. Figure 2.39 summarizes a general decreasing trend at  $b=0.5$  with increasing  $\alpha$  of the normalized  $s_u/p_0'$ , of some  $K_0$  normally consolidated reconstituted soils.



Table 2.3 HCA tests on reconstituted  $K_0$  recompression clayey soils and non-plastic silt at Imperial College London

| Soils | Author<br>(Year)  | $CF$<br>[%] | $p'_0$<br>[kPa] | $K_0$ | $b$ -ratios<br>considered | Inclinations at shear<br>$\alpha$ [°] |
|-------|-------------------|-------------|-----------------|-------|---------------------------|---------------------------------------|
| HK    | Menkiti (1995)    | 7           | 400             | 0.49  | 0, 0.5, 1                 | 0, 22.5, 45, 90                       |
| KSS   | Menkiti (1995)    | 44          | 300             | 0.585 | 0, 0.5, 1                 | 0, 22.5, 45, 90                       |
| HPF4  | Zdravkovic (1996) | 0           | 200             | 0.5   | 0, 0.3, 0.5, 1            | 0, 15, 30, 45, 60, 90                 |
| HK15  | Rolo (2003)       | 15          | 200             | 0.5   | 0, 0.3, 0.5, 1            | 0, 45, 90                             |

**Notes:**

HK = a mixture of kaolin and sand (Ham River Sand)

KSS = a mixture of kaolin, sand and silt

HPF4 = non-plastic quart-based silt

HK15 = a mixture of kaolin and HPF4 silt

Zdravkovic (1996) also performed series inclined-consolidation tests, which are not reported here.

$CF$ : Clay fraction

$p'_0$ : Mean effective pressure at the end of anisotropic  $K_0$  consolidation

Figure 2.40 illustrates the effective stress paths and stress-strain curves of Toyoura sand subjected to rotation of  $\alpha_\sigma$  ( $b=0.5$ ,  $p=300$  kPa) developed in torsional shear test (Nakata et al., 1998). The material became softer with increasing  $\alpha_\sigma$  in all the experiments (although the stress-strain response at small strains is not clear). The influence of void ratio (relative density) in the response of the material is immediately apparent. The denser samples (higher relative density) exhibited a mainly dilation response at all rotations of  $\alpha_\sigma$  whereas, the responses of looser samples became markedly collapsible and brittle when  $\alpha$  rotated from the vertical.

Figure 2.41 illustrates the distribution of maximum  $s_u$  versus  $\alpha_\sigma$  for the sample of Toyoura sand ( $Dr=30\%$ ). A drop of  $s_u$  by a factor of 2 between  $\alpha_\sigma=15^\circ$  and  $75^\circ$  was observed.

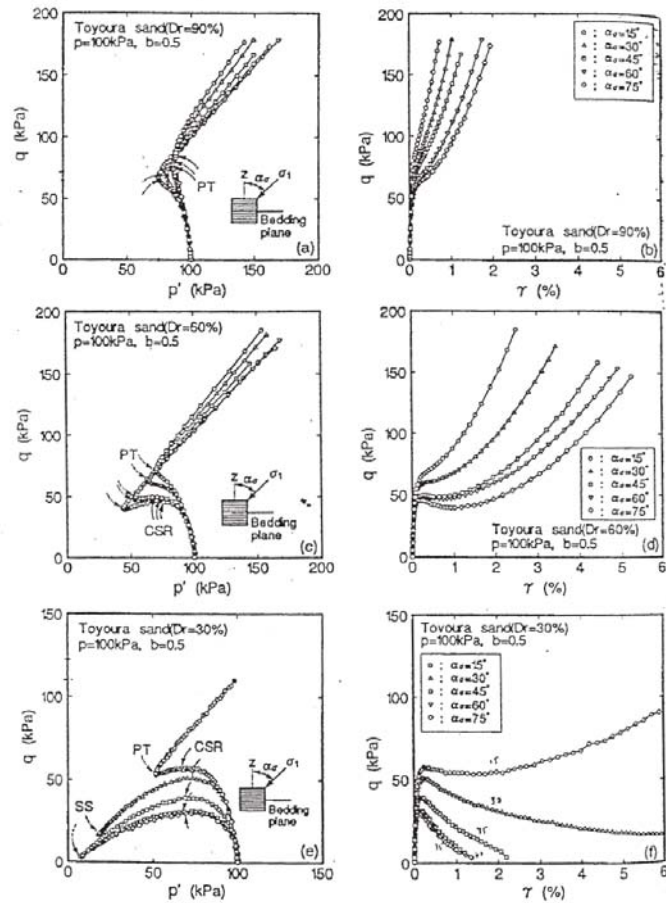


Figure 2.40 Effect of the principal stress direction on the ESP of isotropically consolidated Toyoura sand (Nakata et al., 1998)

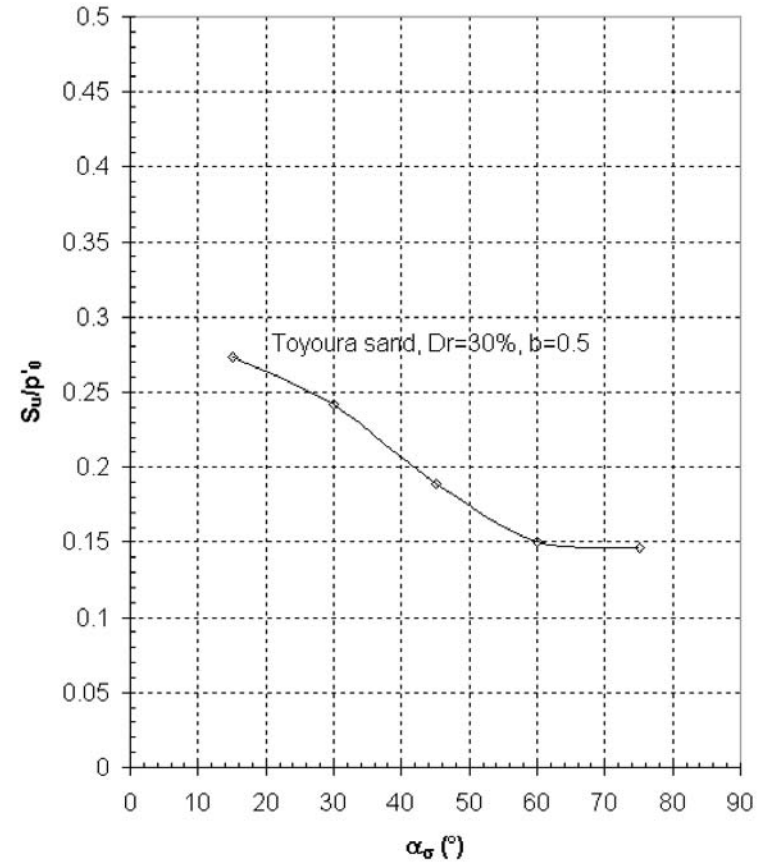


Figure 2.41 Anisotropy of normalised undrained shear strength of isotropically consolidated Toyoura sand (data from Nakata et al., 1998)

### 2.5.5.2 Effect of $b$

#### i. Drained condition

As described in section 2.5.5.1, the study proposed by Symes (1983) investigated separately effects of  $\alpha$  and  $b$  on isotropically consolidated medium-loose HRS ( $OCR=1$ ) by means of a stress-controlled hollow cylinder device. Series of hollow cylinder specimens were performed with  $b=0, 0.14, 0.5$  and  $1.0$ , while  $\alpha$  was set at some predetermined value between  $0^\circ$  and  $90^\circ$  during shearing.

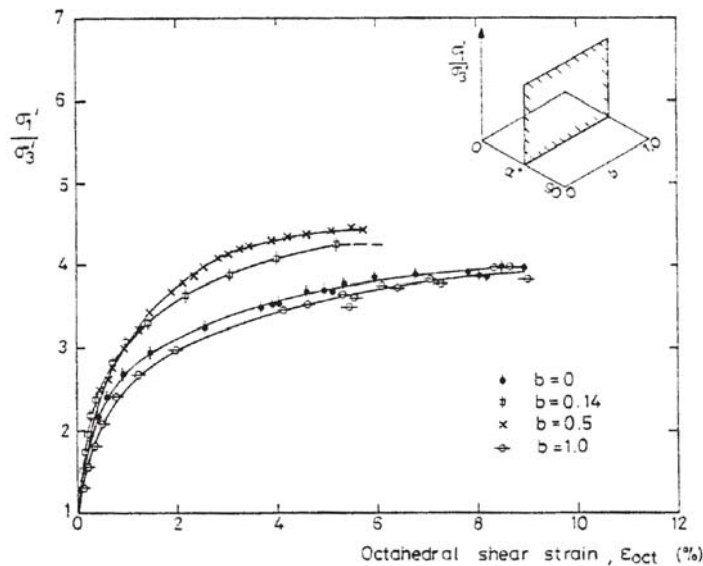


Figure 2.42 Effect of  $b$  on the stress-strain response of isotropically consolidated medium-loose HRS ( $OCR=1$ ); (Symes, 1983)

The stress ratio versus octahedral shear strain curves observed from tests sheared with  $\alpha=45^\circ$  are displayed in Figure 2.42. The result showed that the tests of  $b=0.14$  and  $0.5$  was highest initial stiffness and largest stress ratios. These two tests also presented the least volumetric strains to failure. The result of  $\phi'$  obtained at the failure points are presented in the Figure 2.43. It can be observed that slight variations in  $\phi'$  could effect from changes in  $b$ . The highest stiffness was observed when shearing with  $b \approx 0.3 \sim 0.5$  closes to plane strain conditions whereas, the lowest stiffness and strength was observed when  $b=0.1$ .

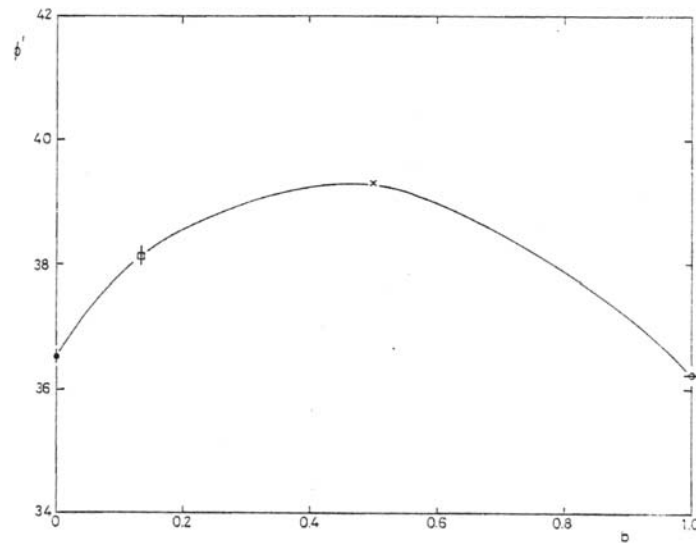


Figure 2.43 Effect of  $b$  on the ultimate  $\phi'$  of isotropically consolidated medium-loose HRS ( $OCR=1$ ); (Symes, 1983)

Investigation on Medium-loose Ottawa sand using hollow cylinder apparatus was studied by Sayão and Vaid (1996). Hollow cylindrical samples formed by pluviated through water were isotropically consolidated to the effective mean stress,  $p \approx 300$  kPa. Then samples were sheared to failure under drained conditions with  $b = 0, 0.3, 0.5$  and  $0.8$ , while  $\alpha$  was fixed at  $45^\circ$ . The shear and volumetric response of these tests are presented in Figure 2.44. The stiffest shear response was obtained in the test associated with near plane strain condition ( $b=0.3$ ). The softest response and the largest volumetric strains were occurred when  $b=0$ . This is consistent with the observation proposed by Symes (1983) as described above.

Drained strength data investigated by many researchers on isotropically consolidated samples ( $OCR=1$ ) is summarized in Figure 2.45 (Ochiai and Lade, 1983; Lade and Duncan, 1973; Lam and Tatsuoka, 1988b). The important observations are that drained strength increased when  $b$  increased up to around  $0.6$  and then remained reasonably constant or decreased slightly thereafter. Moreover it is also clear that the degree of anisotropy decreased as the direction of  $\alpha$  rotated to coincide with the bedding plane.

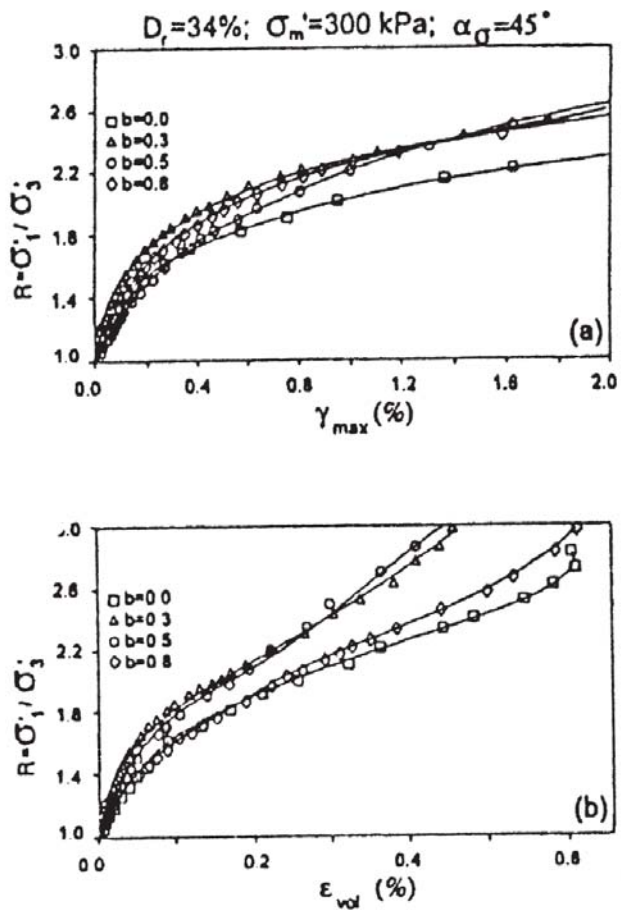


Figure 2.44 Effect of  $b$  on strain response of Syncrude sand (Sayão and Vaid, 1996)

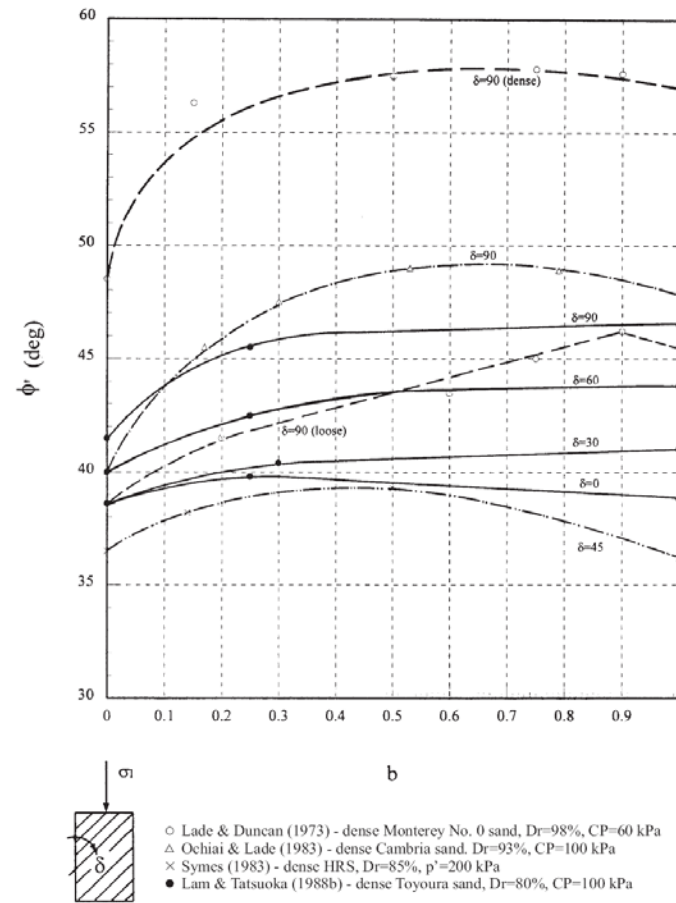


Figure 2.45 Effect of  $b$  on the anisotropy of peak  $\phi'$  (adapted from Zdravkovic, 1996)

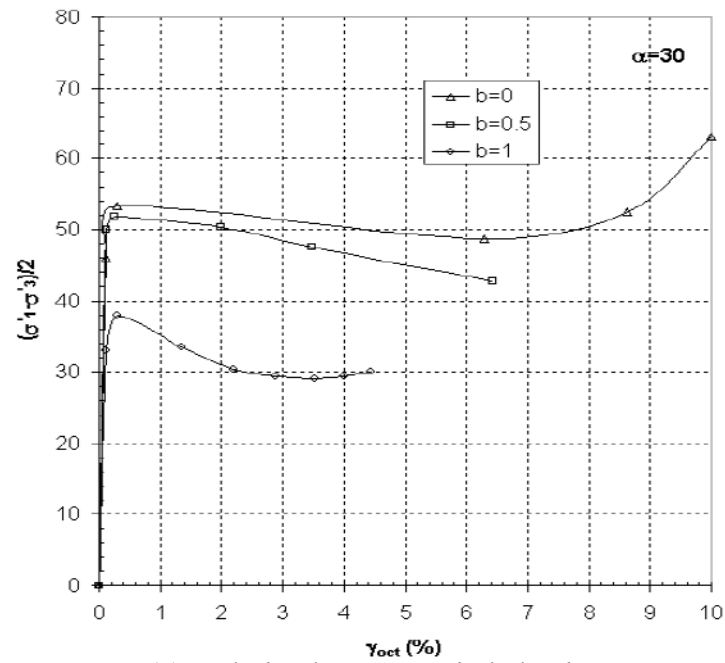
## ii. Undrained condition

The effects of  $b$  values on the undrained response of medium-loose, isotropically consolidated HRS proposed by Shibuya (1985), Shibuya and Hight (1987), and Shibuya et al. (2002a and 2002b) were investigated by means of hollow cylinder device. The detail of test was already briefly described in section 2.3.5.1. The tests were sheared with various  $b=0, 0.5$  and  $1$  and  $\alpha$  between  $0^\circ$  and  $90^\circ$ .

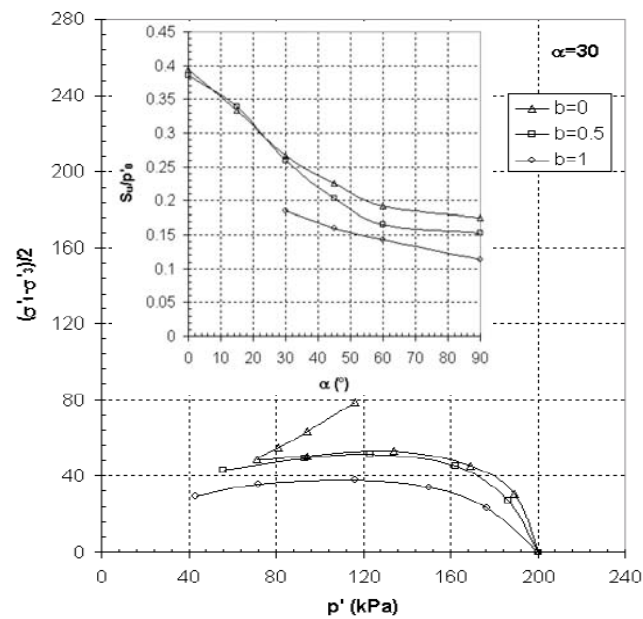
The example result ( $\alpha=30^\circ$ ) of stress-strain curve and effective stress paths are shown in Figure 2.46. A softer, weaker and more brittle undrained behavior seemed to result when shearing with larger values of  $b$ . This response was also depended on the direction of  $\alpha$  as summarized in the insert of Figure 2.46 (b). The undrained shear strength was normalized by the effective stress before shearing ( $p_0 \approx 200$  kPa). For  $\alpha < 45^\circ$ , negligible undrained shear strength anisotropy could be obtained when  $b < 0.5$ . However, the differences in  $s_u$  occurred close to 40% arise at higher values of  $b$ . There was a more marked effect of  $b$  after  $\alpha=45^\circ$ , with  $s_u$  about 1.5 times larger when  $b=0$  than when  $b=1$ .

Similar results have been proposed by Yoshimine et al. (1998) on loose Toyoura sand (TS). Hollow cylindrical specimens were prepared by air-pluviation with subsequent vibration before saturation. The specimens were isotropically consolidated to  $p \approx 100$  kPa and then undrained sheared under strain control with different  $b$  value ( $b=0, 0.25, 0.5, 0.75$  and  $1$ ), while keeping constant  $\alpha=45^\circ$  and  $p$ .

As shown in Figure 2.47, the similar trend of stress-strain and effective stress paths with above was observed. Weaker and more compressible response occurred when  $b$  increases. However, it is noted that these effects seemed to be more dramatic at earlier values of  $b$  than for HRS. The variation of  $s_u$  for HRS at the same value of  $\alpha=45^\circ$  is shown in Figure 2.48. The result seemed to explain that TS was more dependent on  $b$  value than HRS, at least for this particular value of  $\alpha$ . The  $b$  value of TS drops by a factor of 1.8 between  $b=0$  and  $b=1$ , a fall 28% larger than that experienced by HRS.



(a) undrained stress-strain behaviour



(b) effective stress path and undrained strength anisotropy

Figure 2.46 Effect of  $b$  on the response of isotropically consolidated HRS ( $OCR=1$ ); data from Shibuya, 1985

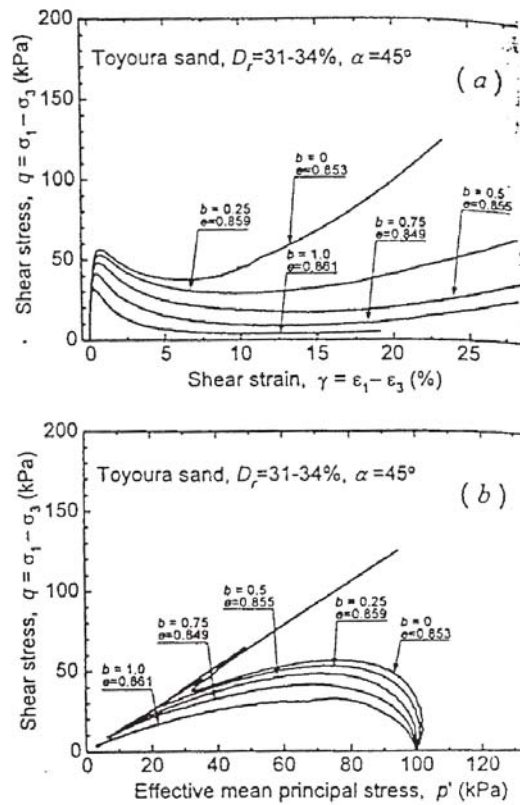


Figure 2.47 Effect of  $b$  on the undrained behaviour of isotropically consolidated Toyoura sand (Yoshimine et al, 1998)

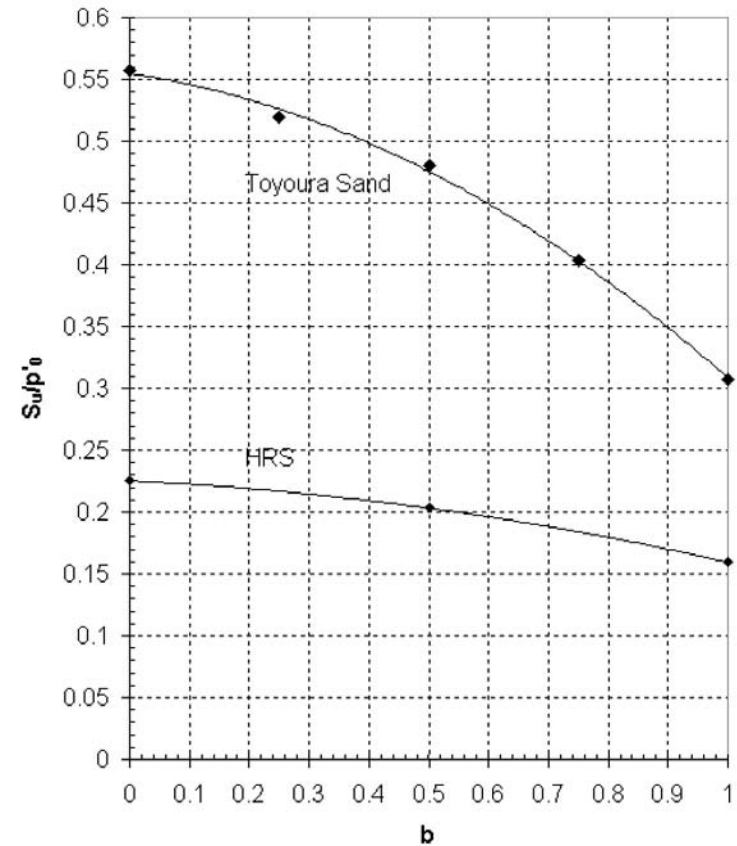


Figure 2.48 Effect of  $b$  on the undrained strength of two isotropically consolidated sands sheared with  $\alpha = 45^\circ$  (data from Yoshimine et al., 1998 and Shibuya, 1985)



## **CHAPTER III**

### **Triaxial Testing Apparatus, Testing Procedures and Testing Program**

#### **3.1 Introduction**

In order to be able to evaluate the behavior of soil at intermediate to small strain level, a conventional triaxial apparatus was developed by incorporating the new local strain measuring devices and bender element system. Then 20 undisturbed samples of Bangkok Clay were performed on the triaxial test in both undrained and drained conditions so as to examine the effect of anisotropy on the stress-strain behavior in a wide strain ranges. Details of triaxial testing apparatus, testing procedure and triaxial testing program were explained in this chapter.

#### **3.2 Triaxial test**

In this part, the research methodology was designed to investigate both of isotropically consolidated undrained compression (CIUC) and isotropically consolidated drained compression (CIDC) test of the vertically and horizontally cut specimens for studying about the effect of anisotropy on the stress-strain behavior in small to intermediate strain level.

##### **3.2.1 Conventional triaxial testing system**

Although a conventional triaxial apparatus is the most common testing device for observing the stress-strain behavior of soil in the laboratory, the result obtained from this equipment does not always reflect the real stress-strain behavior of soils. It is usually observed that the stiffness of soil which is obtained from the conventional triaxial apparatus is far below the stiffness of soil which is derived from back calculation using the measured displacement occurred in the field. There are a lot of factors believed that be the causes of the error, for example, the sample disturbance, the overestimation of axial strain from the external measurement in triaxial apparatus and the boundary condition of the experiment. However, the main of factor may be the obtaining stiffness value at the different of the strain level from any test.

A number of recent research works have suggested that the study of stress-strain behavior of soil is highly non-linear and the small-strain stiffness of soil is very important for the analysis of the boundary value problems. However, the small-strain level of interest is beyond the capability of the conventional triaxial apparatus. Consequently, there are developments of the conventional triaxial system to be able to accurately measure this non-linear behavior, especially at small-strain range. Several local strain measurement systems are introduced. Bender element system is also utilized to obtain the small-strain stiffness.

### 3.2.2 Triaxial system set-up

The triaxial testing in this research comprised a triaxial cell, two pressure controllers (DPCs), some instrumentation such as cell pressure, back/pore pressure transducer and a controlling microcomputer. The modification of this device included incorporation of the local axial and radial strain measurement system and the pulse transmission by bender element system. The triaxial testing system in this study is presented in Figure 3.1. Each component of the system is described below.

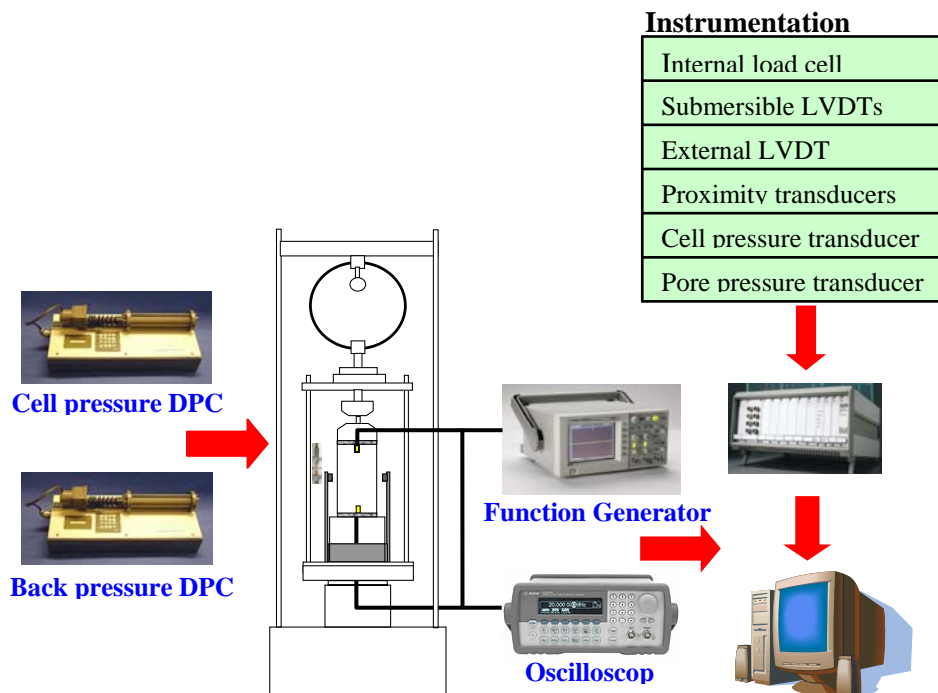


Figure 3.1 Triaxial system

### i. Triaxial cell

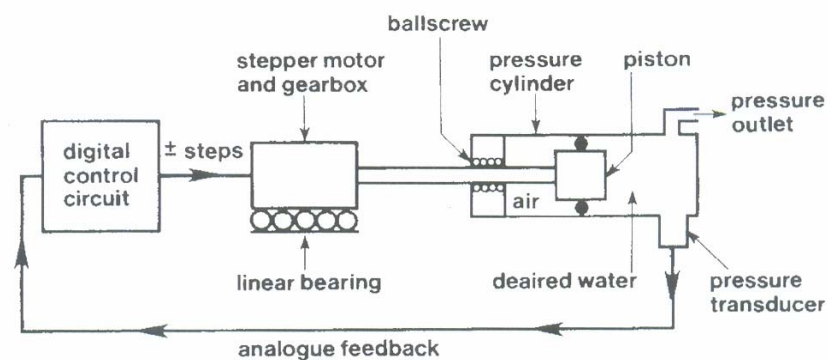
The EL25-4157 triaxial cell was used in this test. Axial force was exerted on the specimen by a load frame. The triaxial cell (EL25-4157) was manufactured for using with a 50 mm-diameter specimen. The triaxial chamber allowed a maximum pressure of 1700 kPa and could be subjected 45 kN load frame.

### ii. Digital pressure controller

Figure 3.2 (a) presented the digital pressure controller (DPC) used in this research. This equipment was a microprocessor controlled hydraulic actuator for precise regulation and measurement of liquid pressure and liquid volume change. Its schematic diagram was presented in Figure 3.2 (b). The principle of operation has been detailed by Menzies (1988). Two DPCs were controlled manually for controlling of back pressure and cell pressure. The resolutions of the measurement and control were 1 kPa and  $1\text{mm}^3$  for pressure and volume change, respectively. The volume capacity was  $200\text{ cm}^3$ .



(a) Photo



(b) Schematic diagram

Figure 3.2 Digital pressure controller (Menzies, 1988)

### **iii. Data logger**

The ELE data logger box with 11 channels was used to provide the voltage excitation to the transducers and amplify and filter the output signals from the transducers before passing them to the microcomputer.

### **iv. Microcomputer**

The microcomputer was used to collect the output signal data from all instruments through the data logger and also control function generator and obtain waveform from oscilloscope.

### **v. Instrument**

The instrumentation employed in the triaxial testing system included internal load cell, proximity transducer, submersible LVDT, external LVDT, volume change transducer, cell pressure transducer pore, pressure transducer, back pressure transducer.

## **3.3 Development of conventional triaxial apparatus**

### **3.3.1 Local strain measurement system**

In order to develop the conventional triaxial system, the submersible LVDTs and proximity transducers were used for the local axial and radial strain measurement in this research.

#### **i. Submersible LVDT**

The linear variable differential transformer (LVDT) is the displacement transducer of inductive type (Cuccovillo and Coop, 1997). In order to develop the conventional triaxial system, the submersible LVDT was used for measuring the local axial strain occurred on the soil specimen. It was because it was strengthness. Figure 3.3 displayed the floating-type LVDT used in this research. Two transducers were set up diametrically opposite each other on the specimen using the mount and glued to the membrane using cyanoacrylate instant cement.

The strain readings accuracy at large-strain level would be controlled by the accuracy of the calibration and any tilting of the transducer. However, the most important factor on small-strain level was the electric noise. This error was minimized by carefully earthing the shields of the transducer cables and using a transducer power supply of sufficient stability. The remaining noise for the internal LVDTs was reduced by programming the data logger to integrate each reading over a relatively long period (Cuccovillo, 1997).

### **Advantages and limitation of submersible LVDTs**

The advantages of the LVDT are: (i) Easy analysis due to linear calibration curve, (ii) good resolution in the order of less than 0.001% and (iii) good stability (Yimsiri and Soga, 2002). On the other hand, its limitations are: (i) high cost, (ii) large in size, except for miniature LVDT, and (iii) prone to jamming of the inner rod because of the tilting of the core, especially when the sample approaches failure (Yimsiri and Soga, 2002).

### **ii. Proximity transducer**

The proximity transducer is an inductive displacement transducer. The operation of this device is on the principle of loss of magnetic field as a result of the circulation of eddy currents within the metallic target. The loss of field is proportional to the distance between the probe and the target. In this research, proximity transducer was used as the local radial strain measurement device because of its non-contacting nature and ease of set-up. The setting-up of the proximity transducer was displayed in Figure 3.4. The proximity transducers were held in place at mid-height of the specimen in diametrically opposite direction by the column. The bottom of the column was connected to the bottom base pedestal of the triaxial cell by screws. A  $5 \times 5 \text{ cm}^2$  square aluminium foil was attached on the rubber membrane by silicone sealant as a target of the proximity transducer. Changing in the specimen diameter could be derived from the movements of the aluminium foil targets in the radial direction monitored by the proximity transducer.

### Advantages and limitation of proximity transducer

The advantages of the proximity transducer are: (i) Easy analysis due to linear calibration, (ii) good resolution in the order of less than 0.001% and (iii) good accuracy in the order of 0.008% (Yimsiri and Soga, 2002). On the other hand, its limitations are: (i) difficulties in the set-up procedure (ii) high cost, (iii) usually not water-submersible (except some special-built ones) and (iv) usually susceptible to change in pressure (except some special-built ones) (Yimsiri and Soga, 2002).



Figure 3.3 Floating-type LVDT



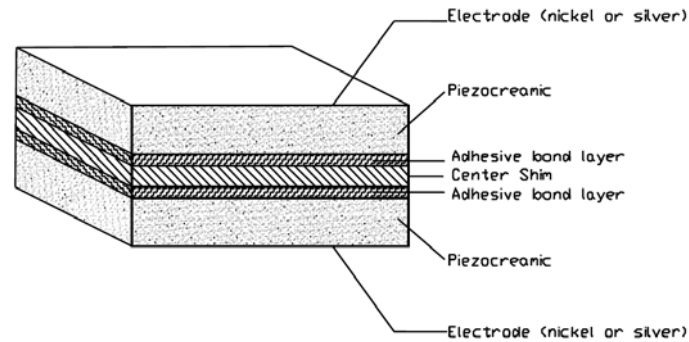
Figure 3.4 Proximity transducer

### 3.3.2 Pulse transmission by bender element system

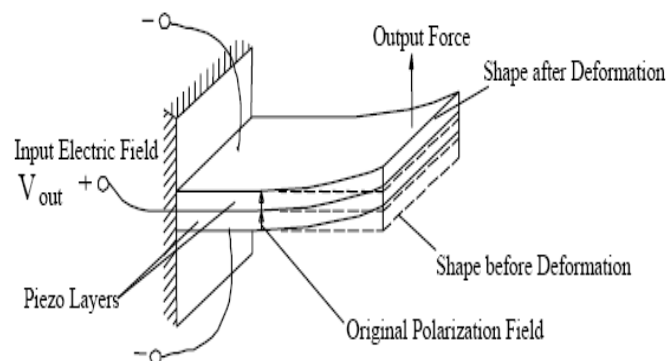
#### i. Bender element preparation and set-up

The bender element is an electro-mechanical transducer which capable of converting the mechanical energy to electrical energy or vice-versa. Two piezo-ceramic plates rigidly are bonded together as sandwich connected in series and parallel when it functions as a receiver and transmitter, respectively. The bender elements used in this research were T226-A4-303X/Y poled. Figure 3.5 illustrated the piezo-ceramic bender element connected in parallel and series respectively. When a voltage is applied to the element, it will either contract or expand, and similarly when it expands or contracts it produced a voltage. Therefore, if a voltage is applied to both sides of the bender element, one side will lengthen while the other will shorten as shown Figure 3.6 (a). Moreover, the bender element is a high impedance device. It is

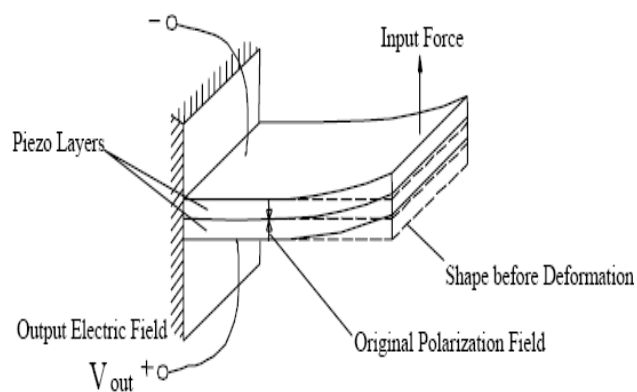
necessary to have a proper protection by using epoxy to protect electrically short circuits the transducer. Figure 3.6 (b) displayed the bender element prepared for mounting into soil testing device.



(a) Structure of a 2-Layer piezoceramic element



(b) Y - poled with parallel connection ( 3 wires )



(c) X - poled with series connection ( 2 wires )

Figure 3.5 Piezoceramic bender element connected in series and parallel

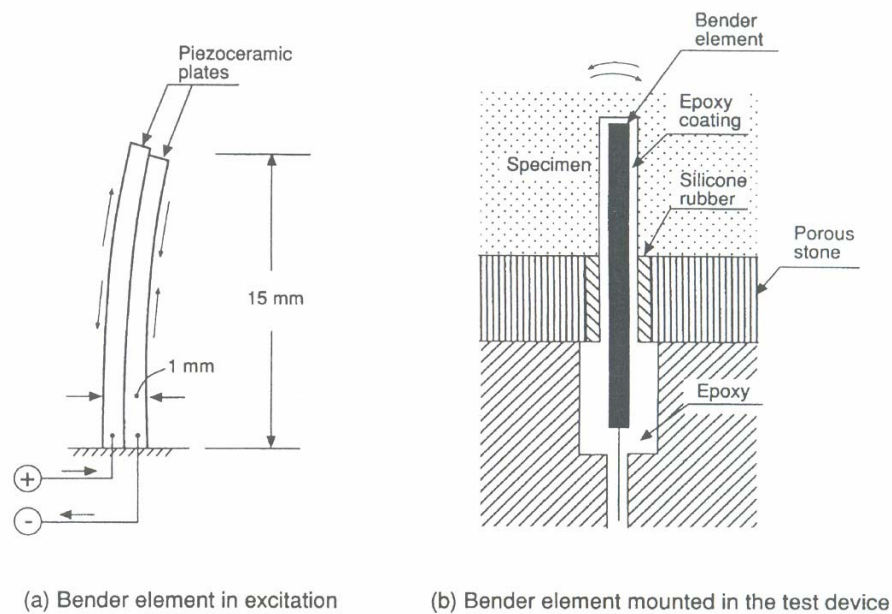


Figure 3.6 Bender element (Dyvik and Madshus, 1985)

The bender element is used for incorporating into several laboratory apparatus. The most typical apparatus is triaxial and oedometer apparatus. Figure 3.7 showed the set up of bender element in triaxial apparatus. The transmitter was mounted on the top cap, whereas the receiver was mounted on the bottom base pedestal. The wire outputs are taken away as to connect the accessories equipment such as, function generator and oscilloscope.

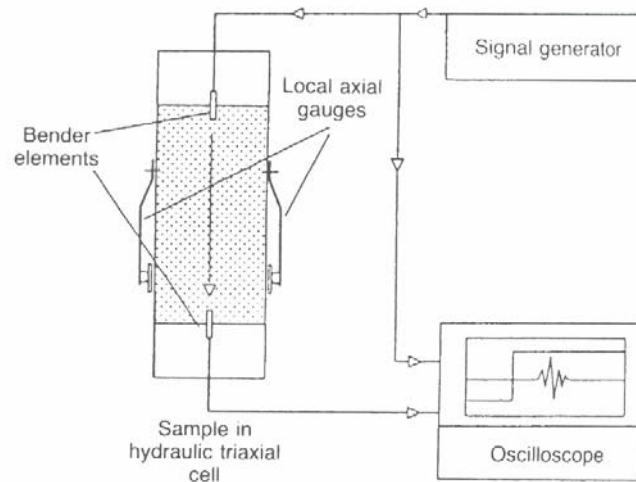


Figure 3.7 Set-up of bender element test (Viggiani and Atkinson, 1995)



## ii. Interpretations of arrival time

The small-strain shear modulus ( $G_{\max}$ ) is calculated from the velocity of the shear wave traveling through the sample ( $V_s$ ) as shown below.

$$G_{\max} = \rho V_s^2 \quad (3.1)$$

where  $\rho$  is the mass density of the sample

Viggiani and Atkinson (1995) recommended that the correct length ( $L$ ) used in the calculation of  $V_s$  is the length between tip to tip of two bender elements. Figure 3.8 represented typical signals obtained from oscilloscope in bender element test. The transmission signal of the shear wave is clearly defined, but the arrival signal at the receiving element is not. The first deflection of the signal occurs at point 0.

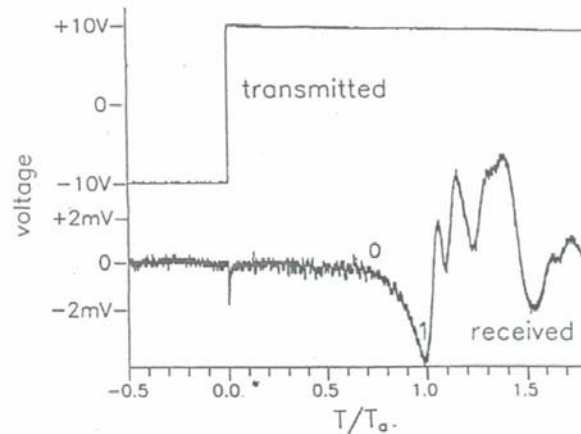


Figure 3.8 Typical oscilloscope signals from a bender element test Viggiani and Atkinson (1995)

Theoretical studies by Salinero et al., (1986) established that the first signal may not correspond to the arrival of the shear wave but it may be the arrival of the so-called near-field component traveling with the velocity of compression wave. Viggiani and Atkinson (1995) observed that this can be caused the maximum overestimation of  $G_{\max}$  by 14%. Nevertheless, Salinero et al., (1986) proposed that the presence of the near-field effect not only depends on the distance between source

and receiver ( $L$ ) but also on the wavelength ( $\lambda$ ) of the sine wave and hence on its frequency ( $f$ ) and travel velocity. They also defined the number of wavelength between the source and receiver ( $R_d$ ) as being the controlling parameter.

$$R_d = \frac{L}{\lambda} = \frac{fL}{V_s} \quad (3.2)$$

Providing the value of  $R_d$  is kept above about 5, the near-field effect will not be observed. The general technique can be achieved by keeping the frequency of the transmitted wave sufficiently high as to fulfill this criterion.

### iii. Function generator

The function generator Agilent 33220A was used to generate pulse to the transmitting transducer and the oscilloscope through the exciter. The pulses could be generated by function generator had a minimum-maximum frequency of 500 -5 MHz .

### iv. Oscilloscope

Agilent 3000 series oscilloscope was used in this research. The receiver transducer receives the signal from the transmitter through the soil specimen also connected to the oscilloscope. The oscilloscope was connected to the microcomputer by USB interface to enable control and data transfer.

## 3.4 Triaxial testing program

The program was designed to investigate the effect of non-linearity and anisotropy on the stress-strain behavior of Bangkok clay. Both of isotropically consolidated undrained compression (CIUC) and isotropically consolidated drained compression (CIDC) test of the vertically and horizontally cut specimens were studied in this research. The test procedures of each stage are described in the following sections.

### 3.4.1 Sampling

The samples used in this research were undisturbed Bangkok clay taken from Ramkhamheng area, Bangkok from 10-14.5 m. The undisturbed samples were

collected by piston sampler (diameter of 5 in). All tube samples were immediately waxed from both sides for preventing the loss of moisture and then were safely carried to the laboratory without jerks.

### 3.4.2 Sample preparation

After removing the wax layer and cling-film from the tube samples extruded from the sampling tubes, they were carefully inspected to ascertain its condition and suitability for testing. If there were any unusual evidence or detrimental features, namely opened fissured, those samples were discarded. Before placed in the soil lathe, the ends of the samples were flattened by trimming knife. Then the samples were trimmed down by trimming knife to reduce its diameter to 50 mm and height to 100 mm. The layouts of both vertical and horizontal cut specimens were shown in Figure 3.9. Trimming immediately was used for moisture content determination.

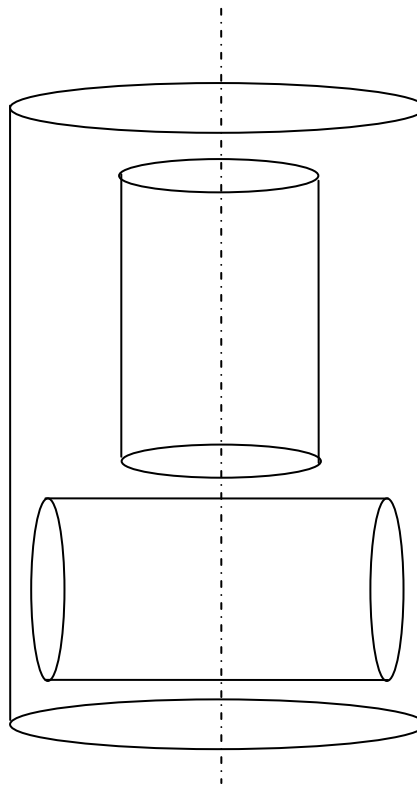


Figure 3.9 Layout of vertical and horizontal specimen

### **3.4.3 Specimen set-up**

The specimen was placed on the base pedestal of the triaxial cell. Both ends of the specimen were used the porous stones for easy drainage. During the mounting of the specimen on the base pedestal, the bender element was pushed into both end of the specimen. In order to minimize the possible severe damage caused during pushing bender element into the specimen, pre-bored slot was manually prepared at each end of the specimen by the shape knife.

Then the samples were enclosed with rubber membrane. The side of the top cap and base pedestal were coated with silicon grease in order to prevent leakage through the sealing. O-rings were used to seal the rubber membrane.

Finally, the triaxial cell chamber was assembled and filled with de-air water. The valves to the back pressure system were closed to prevent the specimen from sucking the water and swelling during specimen set-up process.

### **3.4.4 Saturation**

The back pressure was applied to ensure the specimen fully saturated. A typical back pressure used was 200 kPa. The terminated time for the saturation process was typically 24 hours. The drainage valves were opened during the saturation of the specimen. The theoretical and experimental studies of the saturation of the specimen using back pressure were described by Black and Lee (1973). To avoid error in the measurement of specimen volume changes, the full saturation of the specimen was required. The typical value of Skempton B-value (Skempton, 1954) was 0.90-0.95, which correspond to the degree of saturation of 100% for soft to stiff clays (Black and Lee, 1973).

### **3.4.5 Isotropic consolidation**

The rate of stress consolidation to ensure fully drainage was 1 kPa per 20 minutes in constant rate of stress. During consolidated time, the water was allowed to drain through the drainage valve, while the excess pore pressure was observed from the pore pressure transducer at the top of the specimen to ensure fully drainage.

Moreover, during isotropic consolidation, the shear wave velocity of bender element was also measured to obtain the relationship between the small-strain shear modulus and consolidation stress.

#### **3.4.6 Rest period**

In order to decrease effect of recent stress history, more than 24 hrs of rest period was necessary in all tests.

#### **3.4.7 Compression shearing**

In this study, the undrained and drained were performed. The test involved axial loading under strain-controlled condition and keeping the cell pressure constant. The nominal external strain rate employed was 0.15 mm per hour and the excess pore pressure response was monitored for undrained shearing. For drained shearing, the nominal external strain rate employed was 0.02 mm per hour and the water was allowed to drain through drainage valve, while the excess pore pressure response was monitored.

#### **3.4.8 Data processing**

The outputs from all the transducers during the triaxial test were taken by the computer. For the small-strain region, the data logging was very crucial at the start of compression shearing. Therefore, the data was logged at a very frequent interval with a maximum speed of reading of every 15 and 30 seconds for undrained and drained shearing respectively. The following readings were taken simultaneous:

- Time
- Axial load
- Cell pressure
- Pore water pressure
- Back pressure

- Volume change
- Local axial displacement
- Local radial displacement
- External axial displacement
- Proving ring

Characteristics of the transducers used in this experiment are summarized in Table3.1.

Table 3.1 Characteristics of the transducers used

| Channel | Transducers              | Capacity           | Vin (V) | Vout        | Gain No. | Offset | Calibration factor        | Resolution                |
|---------|--------------------------|--------------------|---------|-------------|----------|--------|---------------------------|---------------------------|
| 1       | Submersible load cell    | 3 kN               | +5/-5   | 0 to -10 V  | 1        | 0      | -0.051904 kN/V            | $5.894 \times 10^{-4}$ kN |
| 2       | External LVDT            | 5 cm               | +5/-5   | 0 to 10 V   | 3        | 0      | 5.486 mm/V                | $6.679 \times 10^{-2}$ mm |
| 3       | Cell pressure transducer | 1500 kPa           | +5/-5   | 0 to 143 mV | 2        | 0      | -124.050570 kPa/V         | 0.706 kPa                 |
| 4       | Pore pressure transducer | 700 kPa            | +5/-5   | 0 to 143 mV | 1        | 0      | -51.020386 kPa/V          | 0.581 kPa                 |
| 5       | Back pressure transducer | 1000 kPa           | +5/-5   | 0 to 143 mV | 1        | 1      | -48.490658 kPa/V          | 0.575 kPa                 |
| 6       | Volume change transducer | 60 cm <sup>3</sup> | +5/-5   | 0 to 1.25 V | 4        | 0      | 39.373 cm <sup>3</sup> /V | 12.016 mm <sup>3</sup>    |
| 7       | Local LVDT 1             | 10 mm              | outside | ±10 V       | 1        | 0      | 0.473061 mm/V             | $1.216 \times 10^{-3}$ mm |
| 8       | Local LVDT 2             | 10 mm              | outside | ±10 V       | 1        | 0      | 0.437756 mm/V             | $1.213 \times 10^{-3}$ mm |
| 9       | Proximity transducer 1   | 5 mm               | outside | 0 to 5 V    | 1        | 0      | 0.942 mm/V                | $1.150 \times 10^{-3}$ mm |
| 10      | Proximity transducer 2   | 5 mm               | outside | 0 to 5 V    | 1        | 0      | 0.957 mm/V                | $1.168 \times 10^{-3}$ mm |
| 11      | Proving ring             | 2 kN               | +5/-5   | 0 to 2 V    | 4        | 0      | -0.775 kN/V               | $2.365 \times 10^{-4}$ kN |

## CHAPTER IV

### Results of Triaxial Test

#### 4.1 Introduction

The experimental study results of the stress-strain behavior of Bangkok Clay are presented in this chapter. The study intends to examine the stress-strain characteristic at wide strain range, non-linearity and anisotropic behavior of Bangkok Clay. The Bangkok Clay behavior is discussed based on the results from triaxial compression test in both undrained and drained conditions. These experimental results should provide further understanding about Bangkok Clay behavior and be useful for the development of new constitutive models for Bangkok Clay as well.

In this study, both of isotropically consolidated undrained compression (CIUC) and isotropically consolidated drained compression (CIDC) tests were performed on undisturbed Bangkok Clay specimens by triaxial apparatus incorporated with local strain measurement systems (LVDTs and proximity transducers) and bender element system. In order to study the anisotropy behavior, the specimens were cut in two directions, both vertical and horizontal. Details of triaxial testing apparatus, testing procedures and testing program have already presented in Chapter 3. The undisturbed Bangkok Clay specimens used in this study were collected from Lad Prao area in Bangkok between the depths of 10.5-14.5 m. All specimens were performed on medium stiff clay to stiff clay layer. The specimen characteristics are presented in Table 4.1.

#### 4.2 Isotropic consolidation

##### 4.2.1 Consolidation parameters

The undisturbed Bangkok Clay samples were isotropically consolidated to the in-situ mean vertical effective stress. The measured isotropic consolidation curves of Bangkok Clay samples are presented in Figure 4.1. Figure 4.1 shows the relationship of void ratio ( $e$ ) versus the natural log of mean effective stress ( $\ln p'$ ). From Figure



4.1, the average Cam-Clay swelling parameter ( $\kappa$ ) derived from  $\kappa = \Delta e / \Delta \ln p'$  is around 0.093. This value corresponds to the average recompression ratio,  $RR = 2.7$  calculated from  $RR = \Delta \varepsilon_{vol} / \Delta \log \sigma_v'$ . This result is close to the typical value of  $RR$  of 2.77 from the oedometer test reported by Shibuya and Tamrakar (2001).

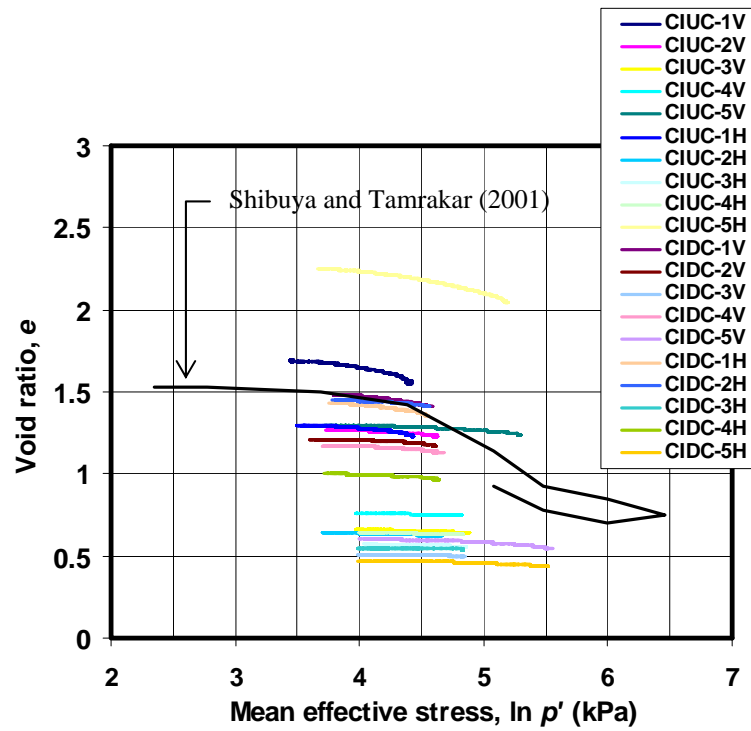


Figure 4.1 Isotropic consolidation curves

Table 4.1 Specimen characteristics for detailed study

| Test No. | Depth (m) | $p'_0$ (kPa) | Void ratio $e_0$ | Water content, $w_n$ (%) | $LL$ (%) | $PL$ (%) | Specimen direction |
|----------|-----------|--------------|------------------|--------------------------|----------|----------|--------------------|
| CIUC-1V  | 10.9      | 80           | 1.69             | 59.62                    | -        | -        | Vertical           |
| CIUC-1H  | 11.7      | 90           | 1.30             | 48.40                    | 73.5     | 27.29    | Horizontal         |
| CIUC-2V  | 13.1      | 100          | 1.27             | 44.72                    | -        | -        | Vertical           |
| CIUC-2H  | 12.9      | 100          | 0.64             | 23.25                    | 42.25    | 15.63    | Horizontal         |
| CIUC-3V  | 14.5      | 130          | 0.66             | 27.67                    | -        | -        | Vertical           |
| CIUC-3H  | 13.7      | 120          | 0.57             | 23.49                    | 51.00    | 17.60    | Horizontal         |
| CIUC-4V  | 13.7      | 120          | 0.76             | 29.33                    | -        | -        | Vertical           |
| CIUC-4H  | 13.7      | 120          | 0.64             | 24.99                    | 51.00    | 17.60    | Horizontal         |
| CIUC-5V  | 13.1      | 200*         | 1.30             | 48.33                    | -        | -        | Vertical           |
| CIUC-5H  | 12.3      | 180*         | 2.25             | 81.56                    | 53.30    | 17.91    | Horizontal         |
| CIDC-1V  | 11.7      | 90           | 1.48             | 51.92                    | 61.10    | 32.26    | Vertical           |
| CIDC-1H  | 11.7      | 90           | 1.43             | 55.99                    | 73.50    | 27.92    | Horizontal         |
| CIDC-2V  | 13.1      | 100          | 1.21             | 45.80                    | 51.75    | 25.00    | Vertical           |
| CIDC-2H  | 12.3      | 90           | 1.45             | 43.75                    | 53.30    | 17.91    | Horizontal         |
| CIDC-3V  | 13.9      | 120          | 0.51             | 17.77                    | 39.10    | 15.66    | Vertical           |
| CIDC-3H  | 13.9      | 120          | 0.55             | 19.27                    | 50.35    | 18.38    | Horizontal         |
| CIDC-4V  | 12.9      | 100          | 1.17             | 41.62                    | -        | -        | Vertical           |
| CIDC-4H  | 12.9      | 100          | 1.00             | 32.96                    | 42.25    | 15.63    | Horizontal         |
| CIDC-5V  | 13.7      | 240*         | 0.60             | 21.02                    | -        | -        | Vertical           |
| CIDC-5H  | 13.9      | 240*         | 0.47             | 18.09                    | 50.35    | 18.38    | Horizontal         |

Remark: \* isotropically consolidated to  $p'_0 = 2p'_{in-situ}$  where  $p'_0$  = isotropic consolidation pressure and  $p'_{in-situ}$  = in-situ mean effective stress.

#### 4.2.2 Anisotropic deformation during isotropic consolidation

Because both local axial and radial strain measurement systems incorporated in triaxial apparatus were independently monitored, it is possible to directly study the

anisotropic deformation of the specimens during the isotropic consolidation stage. Both submersible LVDTs and proximity transducers were set in place at mid-height of the specimen in diametrically opposite direction. The set-up of the local strain measurement systems for vertical- and horizontal-cut specimens is displayed in Figure 4.2. For vertical-cut specimen, the axial strain ( $\varepsilon_a$ ) measured by LVDTs is coincident with the in-situ vertical direction and perpendicular with bedding plane, whereas the radial strain ( $\varepsilon_r$ ) measured by proximity transducers is coincident with the in-situ horizontal direction and parallel to the bedding plane as shown in Figure 4.2 (a). For horizontal-cut specimen, the axial strain ( $\varepsilon_a$ ) measured by LVDTs is coincident with the in-situ horizontal direction and parallel with bedding plane, whereas the radial strain ( $\varepsilon_r$ ) measured by proximity transducers is coincident with the in-situ vertical direction and perpendicular to the bedding plane as shown in Figure 4.2 (b).

The typical relationships between axial and radial strain are summarized in Figure 4.3. The result shows that the deformation under isotropic consolidation is anisotropic.  $\Delta\varepsilon_a > \Delta\varepsilon_r$  is observed for the vertical-cut specimen corresponding with  $\Delta\varepsilon_a < \Delta\varepsilon_r$  for the horizontal-cut specimen. Summary of measured ratios of  $\Delta\varepsilon_a/\Delta\varepsilon_r$  for the vertical-cut specimens and ratios of  $\Delta\varepsilon_r/\Delta\varepsilon_a$  for the horizontal-cut specimens are shown in Table 4.2. The ratios of  $\Delta\varepsilon_a/\Delta\varepsilon_r$  and the inverts of them for the vertical- and horizontal-cut specimens are plotted with depth in Figure 4.4. The result represents that the specimens are stiffer in the horizontal direction. The ratios of  $\Delta\varepsilon_a/\Delta\varepsilon_r$  vary between 1 and 4.5 and the average ratio is around 2.14. This result agrees with the result of anisotropic deformation characteristic of Bangkok Clay reported by Kuwano and Bhattarai (1989). A series of drained test was carried out on soft Bangkok Clay by using a true triaxial apparatus. The clay specimens were sheared along different radial stress paths on the octahedral plane in order to study anisotropic deformation characteristic. They recommended that the result showed the anisotropic deformation characteristic of Bangkok Clay. The Bangkok Clay sample was more compressible in the vertical direction than in the horizontal direction.

Table 4.2 Ratios of  $\Delta\varepsilon_a/\Delta\varepsilon_r$  during isotropic consolidation

| Test No. | Isotropic consolidation |          |   |
|----------|-------------------------|----------|---|
|          | Consolidation pressure  |          | Average $\Delta\varepsilon_a / \Delta\varepsilon_r$ |
|          | From (kPa)              | To (kPa) |   |
| CIUC-1V  | 230                     | 280      | 1.03  |
| CIUC-1H  | 240                     | 290      | 3.65 <sup>*</sup>                                   |
| CIUC-2V  | 240                     | 300      | 1.73  |
| CIUC-2H  | 240                     | 300      | 2.04 <sup>*</sup>                                   |
| CIUC-3V  | 250                     | 330      | 1.20  |
| CIUC-3H  | 250                     | 320      | 0.96 <sup>*</sup>                                   |
| CIUC-4V  | 250                     | 320      | 0.80  |
| CIUC-4H  | 250                     | 320      | 3.60 <sup>*</sup>                                   |
| CIUC-5V  | 240                     | 400      | 1.21  |
| CIUC-5H  | 240                     | 380      | 2.17 <sup>*</sup>                                   |
| CIDC-1V  | 240                     | 290      | 0.94  |
| CIDC-1H  | 240                     | 290      | 2.41 <sup>*</sup>                                   |
| CIDC-2V  | 240                     | 300      | 1.30  |
| CIDC-2H  | 240                     | 290      | 3.14 <sup>*</sup>                                   |
| CIDC-3V  | 250                     | 320      | 1.50  |
| CIDC-3H  | 250                     | 320      | 1.95 <sup>*</sup>                                   |
| CIDC-4V  | 240                     | 300      | 1.69  |
| CIDC-4H  | 240                     | 300      | 4.54 <sup>*</sup>                                   |
| CIDC-5V  | 250                     | 440      | 1.00  |
| CIDC-5H  | 250                     | 440      | 1.02 <sup>*</sup>                                   |

Remark: <sup>\*</sup>  $\Delta\varepsilon_r/\Delta\varepsilon_a$  for the horizontal-cut specimens

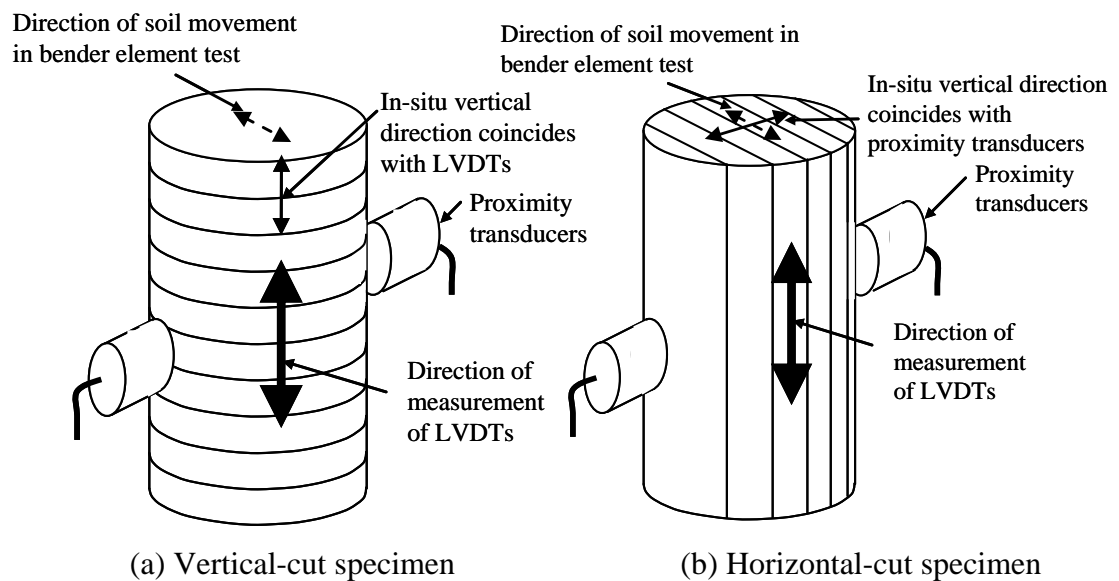
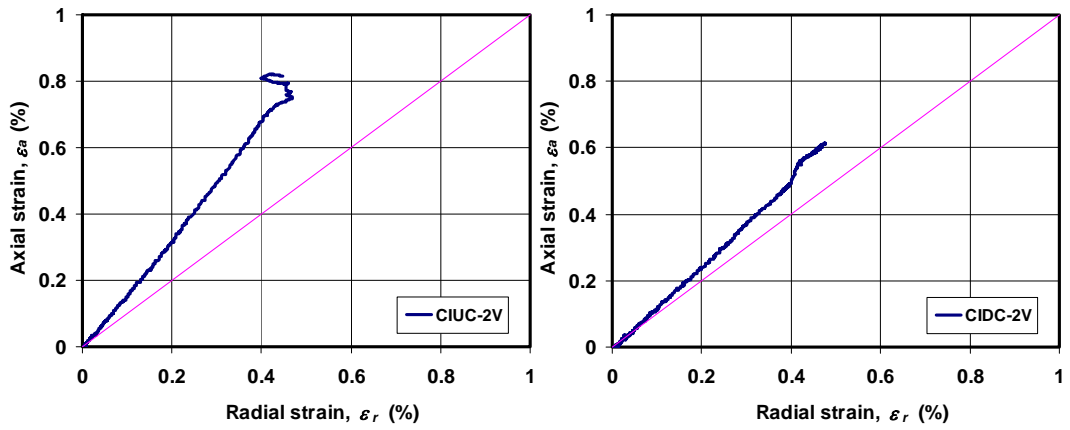
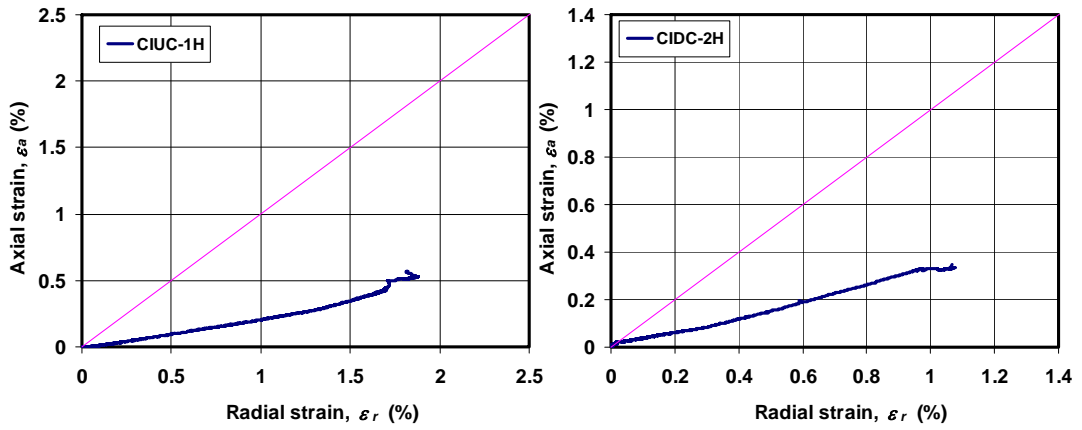


Figure 4.2 Set-up of local strain measurements and bender element system



(a) Vertical-cut specimen (Test CIUC-2V and CIDC-2V)



(b) Horizontal-cut specimen (Test CIUC-1H and CIDC-2H)

Figure 4.3 Anisotropic deformations during isotropic consolidation

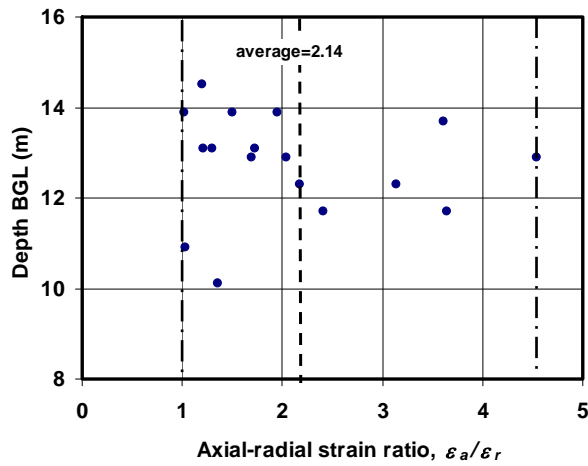


Figure 4.4 Ratios of  $\Delta\epsilon_d/\Delta\epsilon_r$  with depth during isotropic consolidation

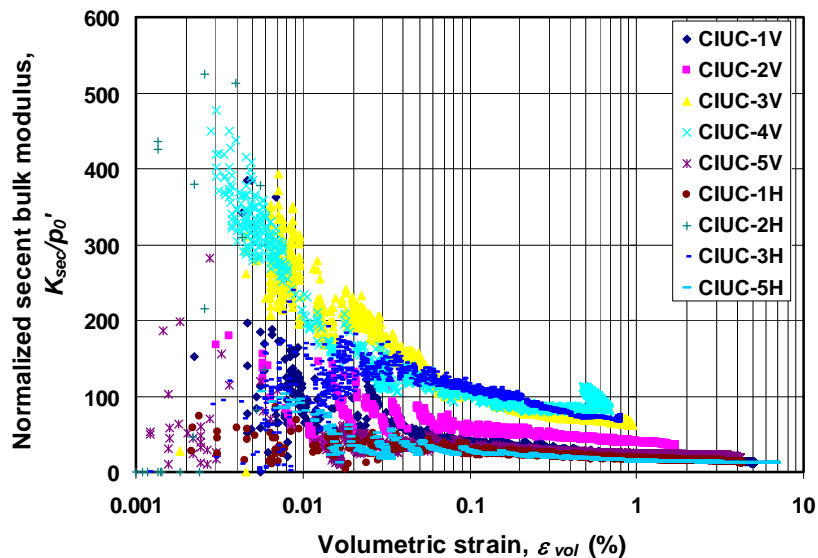
### 4.2.3 Bulk modulus during isotropic consolidation

Due to the constant rate of stress consolidation, the secant bulk modulus and its degradation with volumetric strain can be observed. The secant bulk modulus is derived from Eq. (4.1).

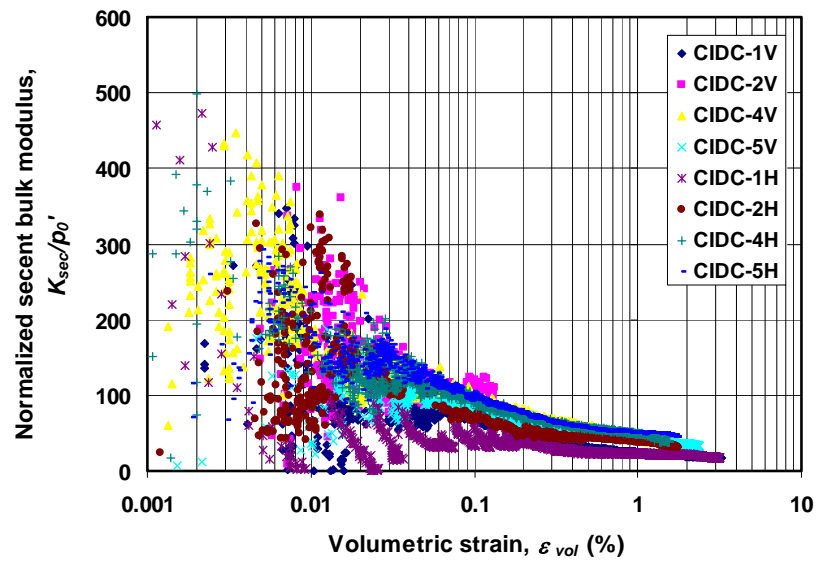
$$K_{sec} = \frac{\Delta p'}{\Delta \varepsilon_{vol}} \quad (4.1)$$

where  $K_{sec}$  is the secant bulk modulus,  $\Delta p'$  is the change in mean effective confining pressure and  $\Delta \varepsilon_{vol}$  is the change in volumetric strain.

Figure 4.5 shows normalized secant bulk modulus degradation curves of Bangkok Clay. The results show that the secant bulk moduli can be derived to as small as 0.002% of volumetric strain. However, there are some tests that are quite scattered and less reliable for volumetric strains less than 0.01%. The estimated small-strain bulk moduli at  $\varepsilon_{vol}$  of 0.001% are summarized in Table 4.3. The small-strain bulk moduli at  $\varepsilon_{vol}$  of 0.001% can be calculated to  $\kappa$  using the relationship of  $K=(1+e_0)p_0'/\kappa$ . The average  $\kappa$  calculated from this relationship is about 0.015.



(a) CIUC tests



(b) CIDC tests

Figure 4.5 Secant bulk modulus degradation curve

Table 4.3 Small-strain bulk modulus during isotropic consolidation

| Test No. | Isotropic consolidation      |     |  |                                   |
|----------|------------------------------|-----|--|-----------------------------------|
|          | Consolidation pressure (kPa) |     | Small-strain bulk modulus $K_{\epsilon_{vol}=0.001\%}$ (kPa) | $K_{\epsilon_{vol}=0.001\%}/p'_0$ |
|          | From                         | To  |  |                                   |
| CIUC-1V  | 230                          | 280 | 7000   | 88                                |
| CIUC-1H  | 240                          | 290 | 6000   | 75                                |
| CIUC-2V  | 240                          | 300 | 9700   | 97                                |
| CIUC-2H  | 240                          | 300 | 13500  | 135                               |
| CIUC-3V  | 250                          | 330 | 40000  | 307                               |
| CIUC-3H  | 250                          | 320 | 14300  | 119                               |
| CIUC-4V  | 250                          | 320 | 45500  | 379                               |
| CIUC-4H  | 250                          | 320 | 50000  | 417                               |
| CIUC-5V  | 240                          | 400 | 10000  | 50                                |
| CIUC-5H  | 240                          | 380 | 16750  | 93                                |
| CIDC-1V  | 240                          | 290 | 10000  | 111                               |
| CIDC-1H  | 240                          | 290 | 6000   | 67                                |
| CIDC-2V  | 240                          | 300 | 15000  | 150                               |
| CIDC-2H  | 240                          | 290 | 16000  | 183                               |
| CIDC-3V  | 250                          | 320 | N/A  | N/A                               |
| CIDC-3H  | 250                          | 320 | 17300  | 144                               |
| CIDC-4V  | 240                          | 300 | 15800  | 158                               |
| CIDC-4H  | 240                          | 300 | 16000  | 160                               |
| CIDC-5V  | 250                          | 440 | 25000  | 104                               |
| CIDC-5H  | 250                          | 440 | 36000  | 150                               |

Remark: N/A = Not Available

### 4.3 Small-strain stiffness characteristics

The small-strain stiffness of undisturbed Bangkok Clay samples in this study was measured from two techniques, triaxial test with local strain measurement and bender element test. In this section, small-strain stiffness are presented and compared. The anisotropic of the small-strain shear modulus is also discussed.

#### 4.3.1 Small-strain shear modulus obtained from bender element test

During isotropic consolidation, the small-strain shear modulus was measured by a wave propagation technique via bender element system. The details of this technique are described in section 3.3.2. The shear wave velocity is calculated by identifying the arrival time of the transmitted shear wave. The small-strain shear modulus can be derived from Eq. (4.2).

$$G_{\max} = \rho V_s^2 = \rho \frac{L^2}{t_s^2} \quad (4.2)$$

where  $\rho$  is the total density of the soil and  $V_s$  is the shear wave velocity, which is determined from the effective length  $L$  which the shear wave travels and the travel time  $t_s$ .

The relationship between the small-strain shear modulus and isotropic confining stress was measured during isotropic consolidation. In this study,  $G_{\max}$  measured from the vertical- and horizontal-cut specimen are  $G_{vh}$  and  $G_{hh}$ , respectively. In Figure 4.6, the relationship between normalized  $G_{\max}/F(e)$  and  $p'$  of Bangkok Clay specimen is displayed. The empirical equation of Bangkok Clay in the form suggested by Hardin and Black (1968) is used to fit the relationship between  $G_{\max}$  and  $p'$  as:

$$G_{vh} = 1700F(e)p'^{0.4} \quad (4.3)$$

$$G_{hh} = 1450F(e)p'^{0.4} \quad (4.4)$$

where  $G_{\max}$  and  $p'$  are in kPa and  $F(e) = (2.937 - e)^2 / (1 + e)$  (Hardin and Black (1968))



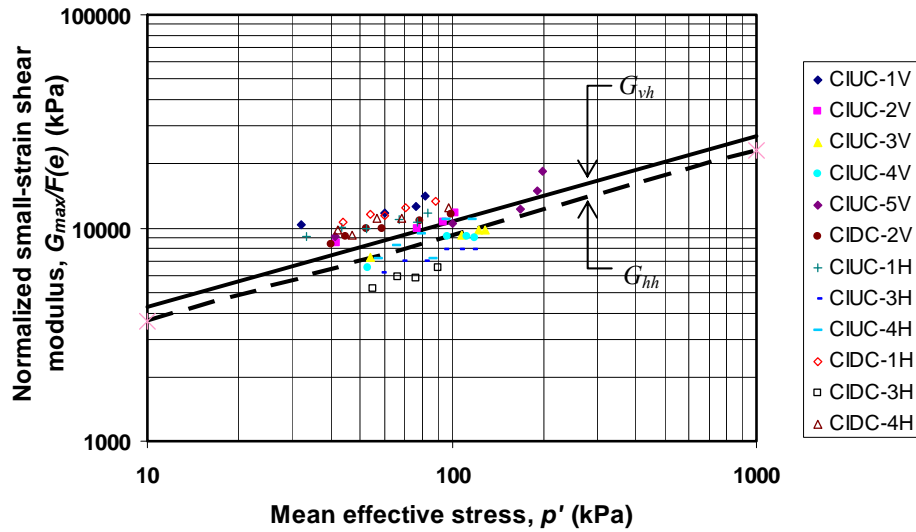


Figure 4.6 Relationship between small-strain shear modulus and isotropic confining stress

#### 4.3.2 Small-strain Young's modulus obtained from triaxial test

The small-strain Young's modulus  $E_v$  and  $E_h$  under isotropic confining stress condition can be derived from the drained triaxial compression tests of the vertical- and horizontal-cut specimens. The relationship between the small-strain Young's modulus  $E_{max}/F(e)$  and  $p'$  of Bangkok Clay specimen are summarized in Figure 4.7.

The relationship of  $E_{max}/F(e)$  and  $p'$  is assumed to have the same exponent of  $p'$  as the relationship of  $G_{max}/F(e)$  and  $p'$  because of the limited number of data. The relationships between  $E_v$ ,  $E_h$  and  $p'$  are represented by Eqs. (4.5) and (4.6) as follow (See Figure 4.7).

$$E_v = 2850F(e)p^{0.4} \quad (4.5)$$

$$E_h = 2250F(e)p^{0.4} \quad (4.6)$$

where  $E_v$ ,  $E_h$  and  $p'$  are in kPa and  $F(e) = (2.937 - e)^2 / (1 + e)$  (Hardin and Black (1968))

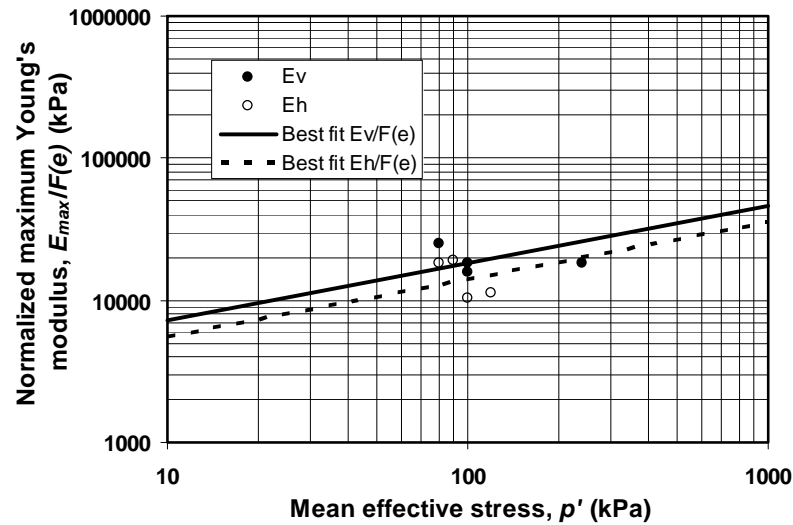


Figure 4.7 Relationship between small-strain Young's modulus and isotropic confining stress

Table 4.4 Small-strain Young's modulus

| Test No. | Isotropic consolidation      |     |  |                |
|----------|------------------------------|-----|--|----------------|
|          | Consolidation pressure (kPa) |     | Small-strain Young's modulus $E_{max}$ (kPa) | $E_{max}/p'_0$ |
|          | From                         | To  |  |                |
| CIUC-1V  | 230                          | 280 | 7000   | 88             |
| CIUC-1H  | 240                          | 290 | 6000   | 75             |
| CIUC-2V  | 240                          | 300 | 9700   | 97             |
| CIUC-2H  | 240                          | 300 | 13500  | 135            |
| CIUC-3V  | 250                          | 330 | 40000  | 307            |
| CIUC-3H  | 250                          | 320 | 14300  | 119            |
| CIUC-4V  | 250                          | 320 | 45500  | 379            |
| CIUC-4H  | 250                          | 320 | 50000  | 417            |
| CIUC-5V  | 240                          | 400 | 10000  | 50             |
| CIUC-5H  | 240                          | 380 | 16750  | 93             |
| CIDC-1V  | 240                          | 290 | 10000  | 111            |
| CIDC-1H  | 240                          | 290 | 6000   | 67             |
| CIDC-2V  | 240                          | 300 | 15000  | 150            |
| CIDC-2H  | 240                          | 290 | 16000  | 183            |
| CIDC-3V  | 250                          | 320 | N/A  | N/A            |
| CIDC-3H  | 250                          | 320 | 17300  | 144            |
| CIDC-4V  | 240                          | 300 | 15800  | 158            |
| CIDC-4H  | 240                          | 300 | 16000  | 160            |
| CIDC-5V  | 250                          | 440 | 25000  | 104            |
| CIDC-5H  | 250                          | 440 | 36000  | 150            |

### 4.3.3 Anisotropy of small-strain shear modulus

In order to derive anisotropic behavior of small-strain modulus under isotropic confining stress condition, the best-fit equations of the small-strain modulus in the vertical and horizontal directions are used. The result shows that the undisturbed Bangkok Clay samples are stiffer in the vertical direction under isotropic confining stress. The ratios of  $G_{hh}/G_{vh}$  and  $E_h/E_v$  are shown below.

$$G_{hh}/G_{vh} = 0.85$$

$$E_h/E_v = 0.80$$

### 4.3.4 Determination of cross-anisotropic elastic parameters

The cross-anisotropic elastic matrix under isotropic confining stress condition of the undisturbed Bangkok Clay is represented in this section. This model assumes the soil to be cross-anisotropic elastic behavior with shear modulus and Young's modulus depending on the stress-state. The Poisson's ratios are practically constant.

#### 4.3.4.1 Small-strain modulus

Summary of small-strain shear modulus and Young's modulus derived in Section 4.3.1 and 4.3.2 are shown below.

$$G_{vh}=1700F(e)p^{0.4} \quad (4.3b)$$

$$G_{hh}=1450F(e)p^{0.4} \quad (4.4b)$$

$$E_v=2850F(e)p^{0.4} \quad (4.5b)$$

$$E_h=2250F(e)p^{0.4} \quad (4.6b)$$

#### 4.3.4.2 Small-strain Poisson's ratios

The small-strain Poisson's ratios  $\nu_{vh}$  and  $\nu_{hv}$  can be directly derived from the vertical- and horizontal-cut specimens in the drained triaxial compression tests, respectively. It is because the local strain measurement systems both axial and radial

directions were arranged during the tests. The results of small-strain Poisson's ratio are presented in Table 4.5. The Poisson's ratio  $\nu_{hh}$  is calculated from the condition of isotropic in the horizontal direction as shown in Eq. (4.7).

$$G_{hh} = \frac{E_h}{2(1 + \nu_{hh})} \quad (4.7)$$

The average of  $\nu_{vh}$  and  $\nu_{hv}$  used for the derived elastic compliance matrix are shown below.

$$\nu_{vh} = 0.088$$

$$\nu_{hv} = 0.084$$

$$\nu_{hh} = -0.224$$

Table 4.5 Small-strain Poisson's ratios

| Test No. | Mean effective confining stress $p'_0$ (kPa) | Poisson's ratio $\nu_{vh}$ | Poisson's ratio $\nu_{hv}$ |
|----------|--|----------------------------|----------------------------|
| CIDC-1V  | 80   | 0.115                      | -                          |
| CIDC-2V  | 100  | 0.038                      | -                          |
| CIDC-3V  | 120  | 0.100                      | -                          |
| CIDC-4V  | 100  | 0.058                      | -                          |
| CIDC-5V  | 120  | 0.127                      | -                          |
| CIDC-1H  | 80   | -                          | 0.309                      |
| CIDC-2H  | 90   | -                          | 0                          |
| CIDC-3H  | 120  | -                          | 0                          |
| CIDC-4H  | 100  | -                          | 0.057                      |
| CIDC-5H  | 120  | -                          | 0.055                      |
| Average  |  | 0.088                      | 0.084                      |

#### 4.3.4.3 Original elastic compliance matrix

The original elastic compliance matrix derived from the experimental results is summarized in this section.

$$G_{vh} = 1700F(e)p^{0.4} \quad (4.8)$$

$$G_{hh} = 1450F(e)p^{0.4}$$

$$E_v = 2850F(e)p^{0.4}$$

$$E_h = 2250F(e)p^{0.4}$$

$$\nu_{vh} = 0.088$$

$$\nu_{hv} = 0.084$$

$$\nu_{hh} = -0.224$$

From the summary of the derived elastic parameters as shown above, there are two problems on unreliable parameters. The first one is non-symmetrical compliance. The result shows the relation of  $E_v/\nu_{vh} \neq E_h/\nu_{hv}$ . Another problem is minus value of  $\nu_{hh}$ . The modification of the derived elastic parameters is discussed in the next section.

#### 4.3.4.4 Modified elastic compliance matrix

In order to satisfy the symmetrical compliance matrix ( $E_v/\nu_{vh} = E_h/\nu_{hv}$ ),  $\nu_{hv}$  is adjusted because it is considered to have an error more than  $\nu_{vh}$ . The modified  $\nu_{hv}$  becomes 0.070 compared to the original value of 0.084.

Hardin (1978) suggested that Poisson's ratio for soils lie somewhere between 0 to 0.2 and that any value within this range is accurate enough for most application. Therefore,  $\nu_{hh}$  is adjusted to 0.15 as suggested by Hardin (1978)

The modified elastic compliance matrix is summarized below.

$$G_{vh} = 1700F(e)p^{0.4} \tag{4.9a}$$

$$G_{hh} = 1450F(e)p^{0.4}$$

$$E_v = 2850F(e)p^{0.4}$$

$$E_h = 2250F(e)p^{0.4}$$

$$\nu_{vh} = 0.088$$

$$\nu_{hv} = 0.070$$

$$\nu_{hh} = 0.15$$

Although, the isotropic of the horizontal plane is violated, it is considered to be acceptable because this model is used to predict the behavior only in triaxial stress condition in section 4.3.5.

### 4.3.5 Application of cross-anisotropic elastic parameters

In this section, the undrained shear stress path direction and the undrained small-strain Young's modulus are predicted from the cross-anisotropic compliance matrices analyzed from result of drained triaxial test as shown in section 4.3.4. The prediction is compared with the undrained experimental results.

#### 4.3.5.1 Prediction of undrained stress path direction and undrained small-strain Young's modulus of vertical-cut specimen

For the vertical-cut specimen, the cross-anisotropic elastic constitutive equation is shown below.

$$\begin{bmatrix} \delta\varepsilon_a \\ \delta\varepsilon_r \\ \delta\varepsilon_r \\ \delta\gamma_{ar} \\ \delta\gamma_{ra} \\ \delta\gamma_{rr} \end{bmatrix} = \begin{bmatrix} \frac{1}{E_v} & -\frac{\nu_{hv}}{E_h} & -\frac{\nu_{hv}}{E_h} & 0 & 0 & 0 \\ -\frac{\nu_{vh}}{E_v} & \frac{1}{E_h} & -\frac{\nu_{hh}}{E_h} & 0 & 0 & 0 \\ -\frac{\nu_{vh}}{E_v} & -\frac{\nu_{hh}}{E_h} & \frac{1}{E_h} & 0 & 0 & 0 \\ 0 & 0 & 0 & \frac{1}{G_{vh}} & 0 & 0 \\ 0 & 0 & 0 & 0 & \frac{1}{G_{hv}} & 0 \\ 0 & 0 & 0 & 0 & 0 & \frac{1}{G_{hh}} \end{bmatrix} \begin{bmatrix} \delta\sigma'_a \\ \delta\sigma'_r \\ \delta\sigma'_r \\ \delta\tau_{ar} \\ \delta\tau_{ra} \\ \delta\tau_{rr} \end{bmatrix} \quad (4.10)$$

where  $a$  and  $r$  are the vertical and horizontal directions of a triaxial specimen, whereas  $v$  and  $h$  are the original in-situ vertical and horizontal directions.

From Eq. (4.10); 
$$\delta\varepsilon_a = \frac{\delta\sigma'_a}{E_v} - 2\nu_{hv} \frac{\delta\sigma'_r}{E_h}$$

$$\delta\varepsilon_r = -\nu_{vh} \frac{\delta\sigma'_a}{E_v} + \frac{\delta\sigma'_r}{E_h} - \nu_{hh} \frac{\delta\sigma'_r}{E_h}$$

For undrained condition;  $\delta\varepsilon_{vol} = \delta\varepsilon_a + 2\delta\varepsilon_r = 0$

$$0 = \frac{\delta\sigma'_a}{E_v} - 2\nu_{hv} \frac{\delta\sigma'_r}{E_h} + 2 \left[ -\nu_{vh} \frac{\delta\sigma'_a}{E_v} + \frac{\delta\sigma'_r}{E_h} - \nu_{hh} \frac{\delta\sigma'_r}{E_h} \right]$$

$$\frac{\delta\sigma'_r}{\delta\sigma'_a} = \frac{E_v}{E_h} \left[ \frac{-1 + 2\nu_{vh}}{2(1 - \nu_{hv} - \nu_{hh})} \right] \quad (4.11)$$

Stress path direction;

$$\frac{\delta q}{\delta p'} = \frac{3(\delta\sigma'_a - \delta\sigma'_r)}{\delta\sigma'_a + 2\delta\sigma'_r} = \frac{3 \left( 1 - \frac{\delta\sigma'_r}{\delta\sigma'_a} \right)}{1 + 2 \frac{\delta\sigma'_r}{\delta\sigma'_a}} \quad (4.12)$$

By substituting the parameters of the original and modified elastic compliance matrix in Eqs. (4.8) and (4.9) into Eqs. (4.11) and (4.12), the undrained stress path direction can be derived. The calculated values are presented in Table 4.6.

Undrained small-strain Young's modulus;

$$\begin{aligned} (E_a)_u &= \frac{\delta q}{\delta\varepsilon_a} = \frac{\delta\sigma'_a - \delta\sigma'_r}{\delta\varepsilon_a} \\ &= \frac{\delta\sigma'_a - \delta\sigma'_r}{\frac{\delta\sigma'_a}{E_v} - 2\nu_{hh} \frac{\delta\sigma'_r}{E_h}} = \frac{1 - \frac{\delta\sigma'_r}{\delta\sigma'_a}}{\frac{1}{E_v} - \frac{2\nu_{hh}}{E_h} \frac{\delta\sigma'_r}{\delta\sigma'_a}} \end{aligned} \quad (4.13)$$

By substituting the parameters of the original and modified elastic compliance matrix in Eqs. (4.8) and (4.9) into Eq. (4.13), the predicted undrained small-strain Young's modulus are;

$$\text{Original:} \quad (E_a)_u = 3459F(e)p^{\rho,4} \quad (4.14)$$

$$\text{Modified:} \quad (E_a)_u = 3762F(e)p^{\rho,4} \quad (4.15)$$

where  $(E_a)_u$  and  $p'$  are in kPa and  $F(e)=(2.973-e)^2/(1+e)$

#### 4.3.5.2 Prediction of undrained stress path direction and undrained small-strain Young's modulus of horizontal-cut specimen

For the horizontal-cut specimen, the cross-anisotropic elastic constitutive equation is shown below.

$$\begin{bmatrix} \delta\varepsilon_{r1} \\ \delta\varepsilon_{r2} \\ \delta\varepsilon_a \\ \delta\gamma_{rr} \\ \delta\gamma_{ar} \\ \delta\gamma_{ra} \end{bmatrix} = \begin{bmatrix} \frac{1}{E_v} & -\frac{\nu_{hv}}{E_h} & -\frac{\nu_{hv}}{E_h} & 0 & 0 & 0 \\ -\frac{\nu_{vh}}{E_v} & \frac{1}{E_h} & -\frac{\nu_{hh}}{E_h} & 0 & 0 & 0 \\ -\frac{\nu_{vh}}{E_v} & -\frac{\nu_{hh}}{E_h} & \frac{1}{E_h} & 0 & 0 & 0 \\ 0 & 0 & 0 & \frac{1}{G_{vh}} & 0 & 0 \\ 0 & 0 & 0 & 0 & \frac{1}{G_{hv}} & 0 \\ 0 & 0 & 0 & 0 & 0 & \frac{1}{G_{hh}} \end{bmatrix} \begin{bmatrix} \delta\sigma'_r \\ \delta\sigma'_r \\ \delta\sigma'_a \\ \delta\tau_{rr} \\ \delta\tau_{ar} \\ \delta\tau_{ra} \end{bmatrix} \quad (4.16)$$

where  $a$  is the vertical directions of a triaxial specimen,  $r_1$  is the radial direction perpendicular to the bedding plane,  $r_2$  is the radial direction parallel to the bedding plane and  $v$  and  $h$  are the original in-situ vertical and horizontal directions.

Form Eq. (4.16);

$$\delta\varepsilon_a = -\frac{\nu_{vh}}{E_v} \delta\sigma'_r - \frac{\nu_{hh}}{E_h} \delta\sigma'_r + \frac{\delta\sigma'_a}{E_h}$$

$$\delta\varepsilon_{r1} = \frac{\delta\sigma'_r}{E_v} - \frac{\nu_{hv}}{E_h} \delta\sigma'_r - \frac{\nu_{hv}}{E_h} \delta\sigma'_a$$

$$\delta\varepsilon_{r2} = -\frac{\nu_{vh}}{E_v} \delta\sigma'_r + \frac{\delta\sigma'_r}{E_h} - \frac{\nu_{hh}}{E_h} \delta\sigma'_a$$



For undrained condition;  $\delta\varepsilon_{vol} = \delta\varepsilon_a + \delta\varepsilon_{r1} + \delta\varepsilon_{r2} = 0$

$$0 = -\frac{\nu_{vh}}{E_v} \delta\sigma'_r - \frac{\nu_{hh}}{E_h} \delta\sigma'_r + \frac{\delta\sigma'_a}{E_h} + \frac{\delta\sigma'_r}{E_v} - \frac{\nu_{hv}}{E_h} \delta\sigma'_r - \frac{\nu_{hv}}{E_h} \delta\sigma'_a - \frac{\nu_{vh}}{E_v} \delta\sigma'_r + \frac{\delta\sigma'_r}{E_h} - \frac{\nu_{hh}}{E_h} \delta\sigma'_a$$

$$\frac{\delta\sigma'_r}{\delta\sigma'_a} = \frac{E_v}{E_h} \left[ \frac{-(1 - \nu_{hv} - \nu_{hh})}{(1 - \frac{E_v}{E_h} \nu_{hv} - \nu_{vh} + \frac{E_v}{E_h} - \nu_{vh} - \frac{E_v}{E_h} \nu_{hh})} \right] \quad (4.17)$$

By substituting the parameters of the original and modified elastic compliance matrix in Eqs. (4.8) and (4.9) into Eqs. (4.17) and (4.12), the undrained stress path direction can be derived. The calculated values are presented in Table 4.6.

Undrained small-strain Young's modulus;

$$(E_a)_u = \frac{\delta q}{\delta\varepsilon_a} = \frac{\delta\sigma'_a - \delta\sigma'_r}{\frac{\delta\sigma'_a}{E_h} - \frac{\nu_{vh}}{E_v} \delta\sigma'_r - \frac{\nu_{hh}}{E_h} \delta\sigma'_r}$$

$$= \frac{1 - \frac{\delta\sigma'_r}{\delta\sigma'_a}}{\frac{1}{E_h} - \frac{\nu_{vh}}{E_v} \frac{\delta\sigma'_r}{\delta\sigma'_a} - \frac{\nu_{hh}}{E_h} \frac{\delta\sigma'_r}{\delta\sigma'_a}} \quad (4.18)$$

By substituting the parameters of the original and modified elastic compliance matrix in Eqs. (4.8) and (4.9) into Eq. (4.18), the predicted undrained small-strain Young's modulus are;

$$\text{Original:} \quad (E_a)_u = 4087F(e)p^{0.4} \quad (4.19)$$

$$\text{Modified:} \quad (E_a)_u = 3106F(e)p^{0.4} \quad (4.20)$$

where  $(E_a)_u$  and  $p'$  are in kPa and  $F(e) = (2.973 - e)^2 / (1 + e)$

The undrained small-strain Young's moduli are predicted by Eq. (4.14), (4.15), (4.19) and (4.20) are compared with the undrained experimental results in Figure 4.8 and Table 4.6. It is noted that the positive percent of error means the predicted value is higher than the measured value, whereas the negative means the predicted value is lower than the measured value. The results show that the predicted values from the original and modified elastic compliance matrixes are within  $\pm 60\%$  and  $\pm 40\%$  from the measured values, respectively.

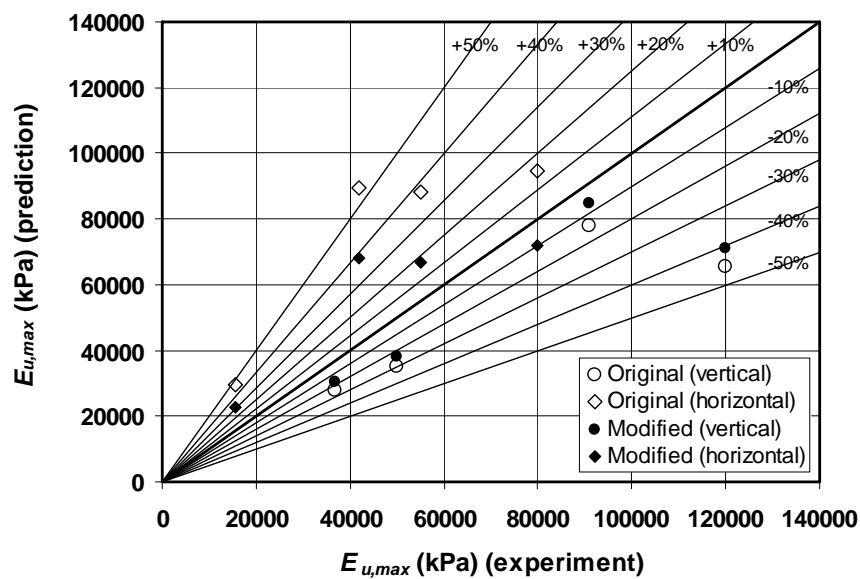


Figure 4.8 Predictions of undrained small-strain Young's modulus

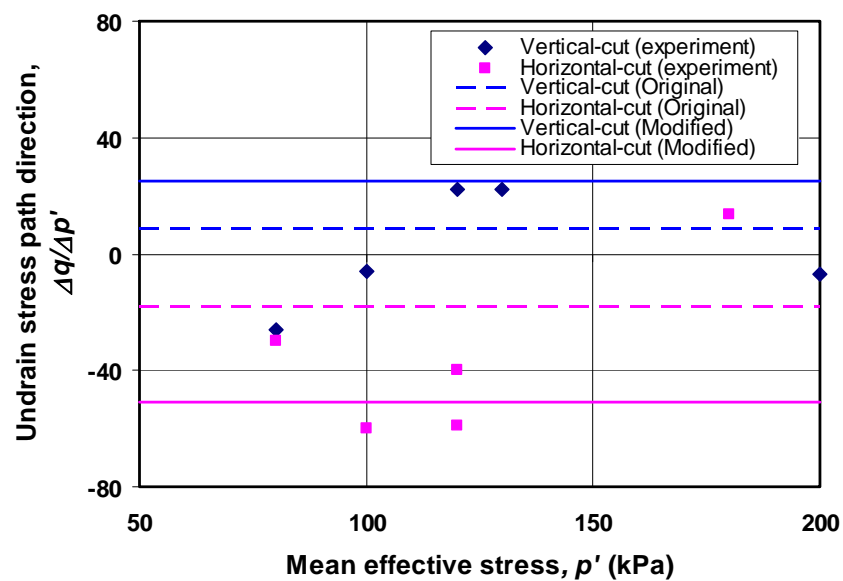


Figure 4.9 Predictions of undrained stress path direction

Table 4.6 Predictions of undrained small-strain Young's modulus

| Test No. | Specimen orientation | Effective mean confining pressure $p'$ (kPa) | Void ratio $e$ | Undrained stress path direction ( $\Delta q/\Delta p'$ ) (experiment) | Undrained stress path direction ( $\Delta q/\Delta p'$ ) (prediction) |          | Undrained small-strain Young's modulus $E_u$ (experiment) (kPa) | Undrained small-strain Young's modulus $E_u$ (prediction) (kPa) |          |
|----------|----------------------|--|----------------|---|---|----------|---|---|----------|
|          |                      |  |                |   | Original  | Modified |   | Original  | Modified |
| CIUC-1V  | Vertical             | 80   | 1.69           | -26.1   | 9   | 25       | 27900   | 12215   | 13284    |
| CIUC-2V  | Vertical             | 100  | 1.27           | -6  | 9   | 25       | 36800   | 27884   | 30325    |
| CIUC-3V  | Vertical             | 130  | 0.66           | 22.2  | 9   | 25       | 91000   | 78121   | 84959    |
| CIUC-4V  | Vertical             | 120  | 0.76           | 22.2  | 9   | 25       | 120000  | 65323   | 71042    |
| CIUC-5V  | Vertical             | 200  | 1.3            | -6.7  | 9   | 25       | 50000   | 35045   | 38112    |
| CIUC-1H  | Horizontal           | 80   | 1.28           | -30   | -18   | -51      | 15500   | 29648   | 22529    |
| CIUC-2H  | Horizontal           | 100  | 0.62           | -60   | -18   | -51      | 55000   | 88128   | 66966    |
| CIUC-3H  | Horizontal           | 120  | 0.62           | -40   | -18   | -51      | 80000   | 94795   | 72032    |
| CIUC-4H  | Horizontal           | 120  | 0.66           | -59   | -18   | -51      | 42000   | 89392   | 67927    |
| CIUC-5H  | Horizontal           | 180  | 2.16           | 13.4  | -18   | -51      | 65000   | 6823  | 5185     |

#### 4.4. Stress-strain behavior in a wide strain range

In this section, the non-linearity in undrained and drained conditions is presented. The stress-strain behavior of soil is non-linear and the stiffness for both undrained and drained loading conditions decays with strain level. In order to consider about the non-linear stress-strain relationship, the normalized stiffness degradation curves are summarized.

##### 4.4.1 Non-linearity in undrained and drained condition

From the deviatoric stress-axial strain relationship, undrained and drained secant Young's modulus,  $E_{u,sec}$  and  $E'_{sec}$  are derived. The normalized stiffness degradation curves,  $E_{u,sec}/p_0'$  and  $E'_{sec}/p_0'$  from undrained and drained triaxial compression tests are summarized in Figure 4.10 (a) and (b). It can be observed that the normalized stiffness degradation curves from the drained tests are more scattered than those from the undrained test. However, there is no distinction between the normalized stiffness degradation curves from the vertical- and horizontal-cut specimens in both two loading conditions. Moreover, the result shows the difference in the non-linearity in undrained and drained conditions. The average normalized stiffness degradation value of the drained tests at small-strained level is less than that of the undrained tests.

In order to study of non-linearity of normalized secant Young's modulus in both undrained and drained conditions. The ratios of secant Young's modulus at any axial strain level and secant Young's modulus at small-strain level of axial strain are presented. For undrained condition, the ratios of  $E_{u,(eq=0.01\%)} / E_{u,(eq=0.001\%)}$ ,  $E_{u,(eq=0.1\%)} / E_{u,(eq=0.001\%)}$  and  $E_{u,(eq=1\%)} / E_{u,(eq=0.001\%)}$  are 0.85, 0.50 and 0.19, respectively, whereas the ratios of  $E'_{(eq=0.01\%)} / E'_{(eq=0.001\%)}$ ,  $E'_{(eq=0.1\%)} / E'_{(eq=0.001\%)}$  and  $E'_{(eq=1\%)} / E'_{(eq=0.001\%)}$  are 0.6, 0.45 and 0.20 for drained condition (see Figure 4.11). This can be seen that undrained condition shows more non-linearity behavior than drained condition.

#### **4.4.2 Anisotropy of stress-strain relationship**

In order to study anisotropic behavior of stress-strain relationship, stress-strain behaviors of the vertical- and horizontal-cut specimens which were located in almost the same depth, same stress history and at the same initial effective confining stress are compared. In this section, anisotropy of the undrained and drained behavior is considered separately

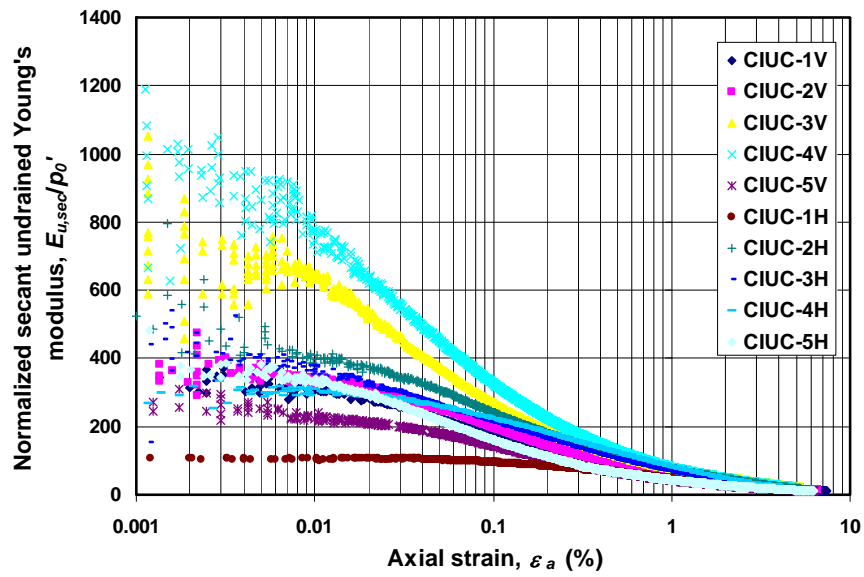
##### **4.4.2.1 Anisotropy in undrained behavior**

The experimental data of undrained tests CIUC-1V and CIUC-1H are chose to consider. The deformation characteristics of both vertical- and horizontal-cut specimens are illustrated in Figure 4.12. The results show that the undrained effective stress path of the vertical-cut specimen slightly tends to the left more than that of horizontal-cut specimen due to the generation of a little more excess pore pressure.

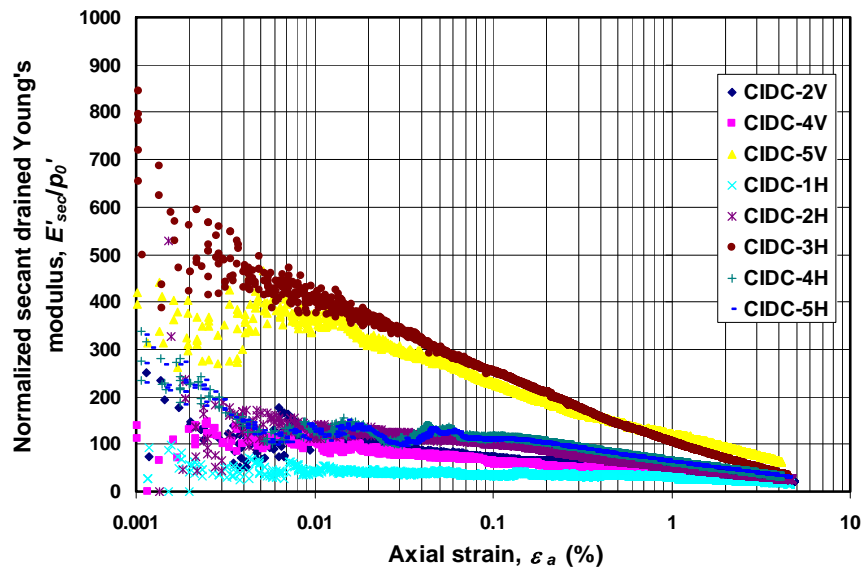
The results of the stress-strain curve represented in the deviatoric stress-axial strain relationship and the normalized secant undrained Young's modulus degradation curves support that the vertical-cut specimen is stiffer than the horizontal-cut specimen.

##### **4.4.2.2 Anisotropy in drained behavior**

The anisotropic characteristics in drained conditions are presented in Figure 4.13. These results are derived from the experiment data of tests CIDC-2V and CIDC-1H. It can observe from the stress-strain curves and the normalized stiffness degradation curves that the vertical-cut specimen is stiffer than the horizontal-cut specimen. The volumetric strain curves of both condition is almost similar until  $\varepsilon_v=1\%$ . Then a little higher volumetric strain of vertical-cut specimen is observed.

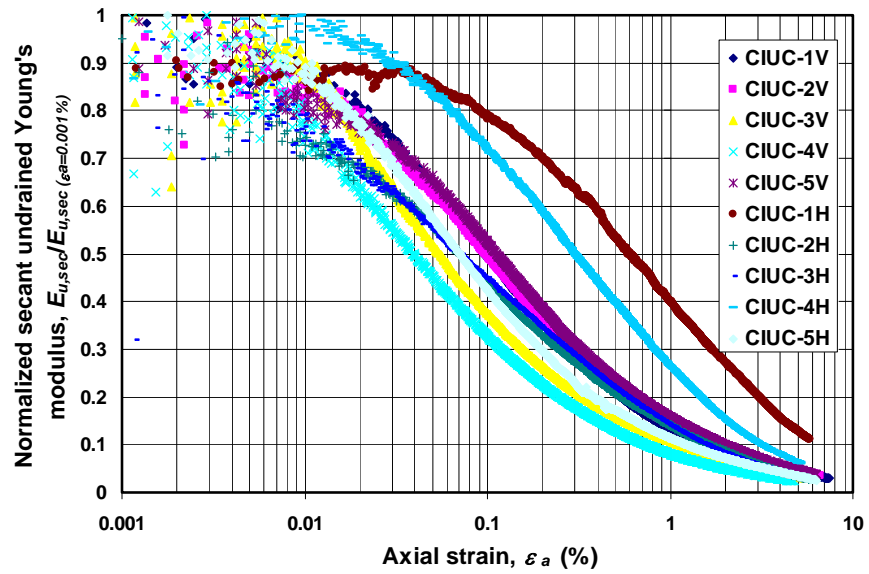


(a) Undrauned condition

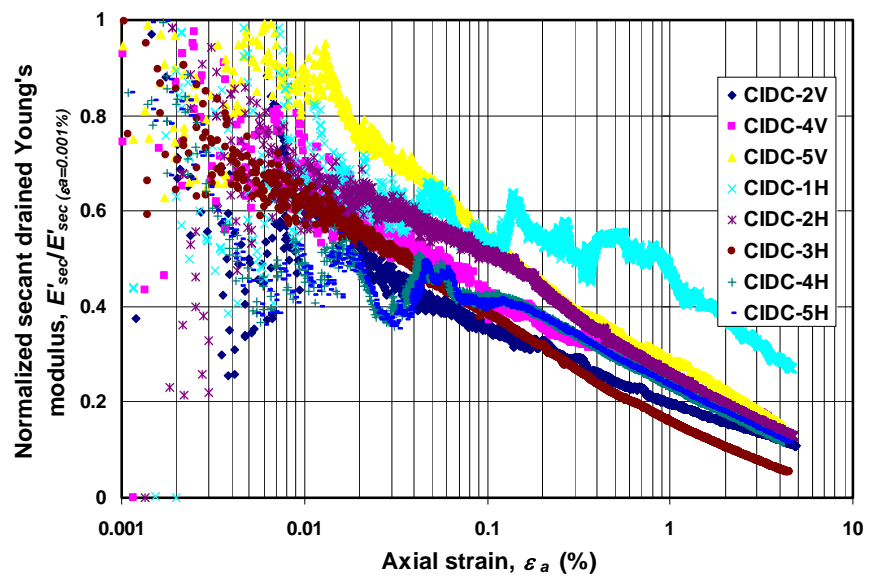


(b) Drain condition

Figure 4.10 Normalized stiffness degradation curves



(a) Undrained condition



(b) Drain condition

Figure 4.11 Normalized stiffness degradation curves by small-strained Young's modulus

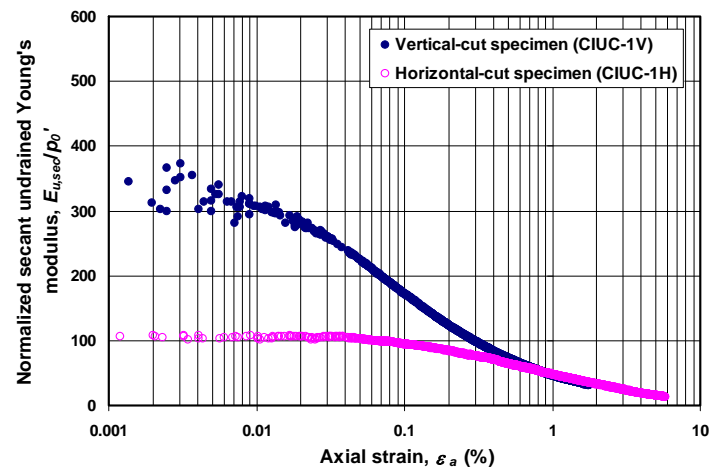
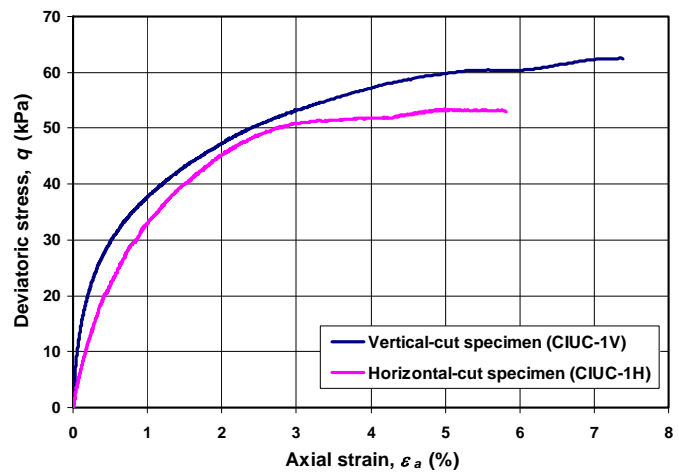
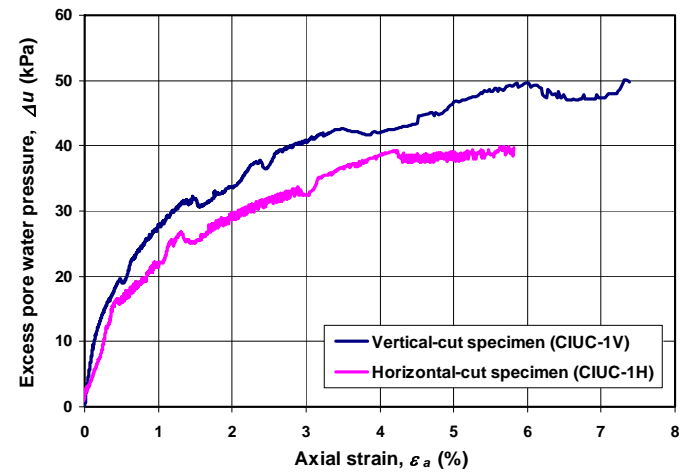
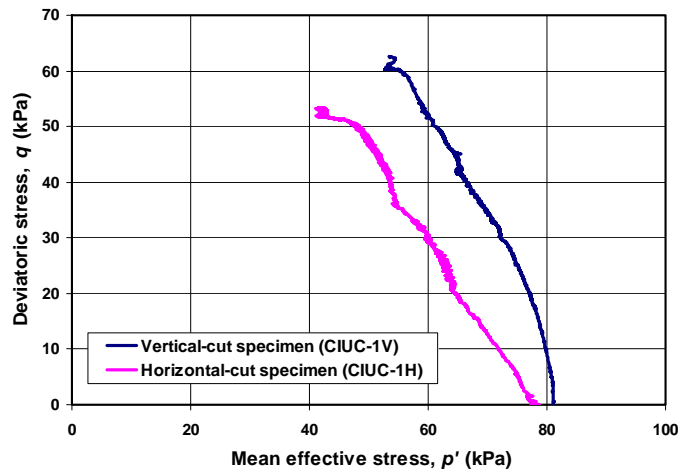


Figure 4.12 Anisotropy in undrained behavior



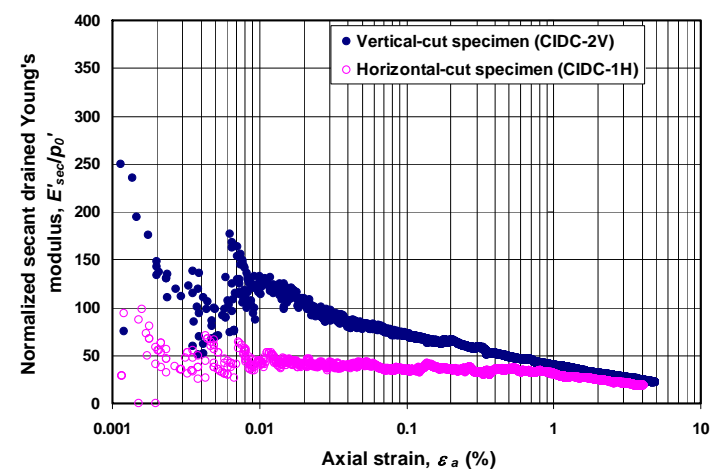
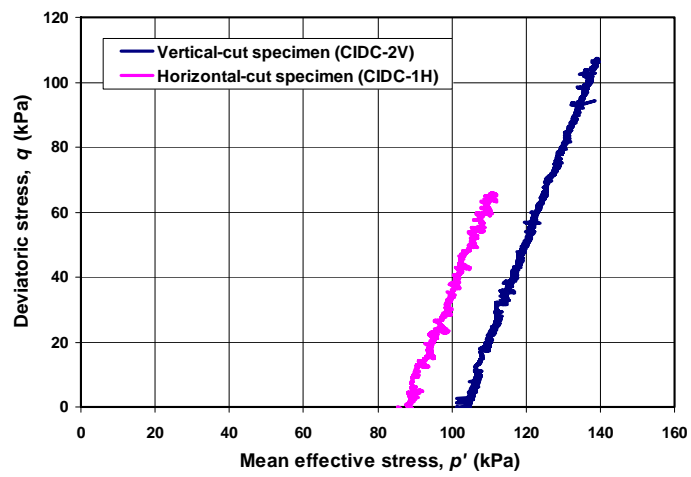
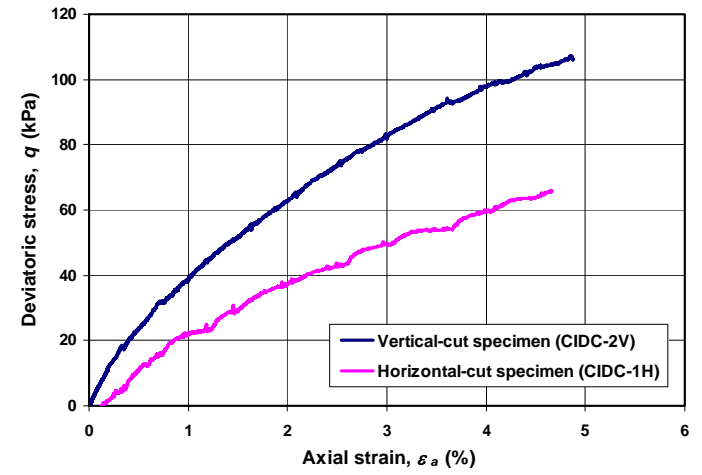
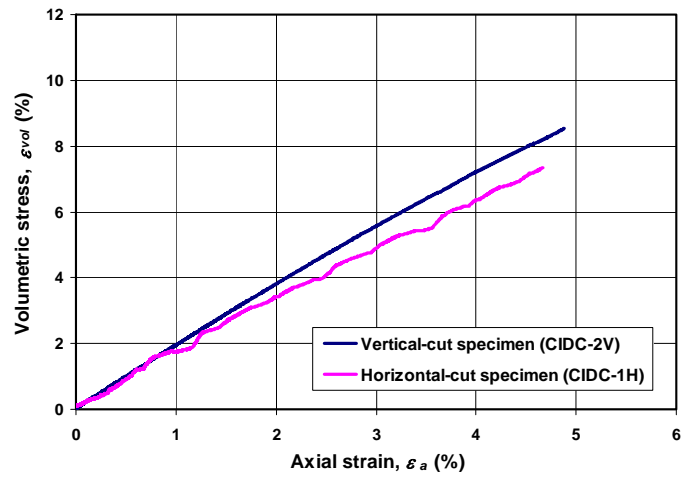


Figure 4.13 Anisotropy in drained behavior

## 4.5 Optimization of cross-anisotropic elastic parameters

This section presents the investigation of cross-anisotropic elastic parameters of Bangkok Clay using the least-square method optimization. The anisotropic stiffness parameters obtained from both undrained and drained triaxial tests are assumed to follow the three-parameter cross-anisotropic elastic model proposed by Graham & Houlsby (1983).

### 4.5.1 Three-parameter cross-anisotropic elastic model proposed by Graham & Houlsby (1983)

Due to cross-anisotropic of the soils, the relationship between stress and strain increments can be expressed by 5 independent parameters ( $E_v$ ,  $E_h$ ,  $G_{vh}$ ,  $\nu_{vh}$ , and  $\nu_{hv}$ ). Graham & Houlsby (1983) proposed a simplified cross-anisotropic elastic model that required only three independent parameters ( $E^*$ ,  $\alpha$  and  $\nu^*$ ), instead of five parameters. The simplified equation is shown in Eq (4.21).

$$\begin{Bmatrix} d\varepsilon_v \\ d\varepsilon_h \\ d\varepsilon_h \\ d\gamma_{vh} \\ d\gamma_{hv} \\ d\gamma_{hh} \end{Bmatrix} = \frac{1}{E^*} \begin{bmatrix} 1 & -\frac{\nu^*}{\alpha} & -\frac{\nu^*}{\alpha} & 0 & 0 & 0 \\ -\frac{\nu^*}{\alpha} & \frac{1}{\alpha^2} & -\frac{\nu^*}{\alpha^2} & 0 & 0 & 0 \\ -\frac{\nu^*}{\alpha} & -\frac{\nu^*}{\alpha^2} & \frac{1}{\alpha^2} & 0 & 0 & 0 \\ 0 & 0 & 0 & \frac{2(1+\nu^*)}{\alpha} & 0 & 0 \\ 0 & 0 & 0 & 0 & \frac{2(1+\nu^*)}{\alpha} & 0 \\ 0 & 0 & 0 & 0 & 0 & \frac{2(1+\nu^*)}{\alpha^2} \end{bmatrix} \begin{Bmatrix} d\sigma'_v \\ d\sigma'_h \\ d\sigma'_h \\ d\tau_{vh} \\ d\tau_{hv} \\ d\tau_{hh} \end{Bmatrix} \quad (4.21)$$

where the three independent parameters are defined in Equations (4.22) to (4.24).

$$\text{Modified Young's modulus,} \quad E^* = E_v \quad (4.22)$$

$$\text{Anisotropy factor,} \quad \alpha = \sqrt{\frac{E_h}{E_v}} \quad (4.23)$$

Modified Poisson's ratio, 
$$\nu^* = \nu_{hh} \quad (4.24)$$

From the symmetry of the compliance matrix and the isotropy in the horizontal plane, the other parameter linkages are forced as  $\nu_{hv}/\nu_{vh} = E_h/E_v = \alpha^2$ ,  $\nu_{vh} = \nu_{hh}/\alpha$  and  $G_{vh} = G_{hh}/\alpha = \alpha E^*/2(1 + \nu^*)$ . Therefore, the all cross-anisotropic elastic parameters can be computed by three independent parameters as listed in Equation (4.25).

$$E_v = E^* \quad (4.25a)$$

$$E_h = \alpha^2 E^* \quad (4.25b)$$

$$G_{vh} = \alpha E^*/2(1 + \nu^*) \quad (4.25c)$$

$$G_{hh} = \alpha^2 E^*/2(1 + \nu^*) \quad (4.25d)$$

$$\nu_{hh} = \nu^* \quad (4.25e)$$

$$\nu_{vh} = \nu^*/\alpha \quad (4.25f)$$

$$\nu_{hv} = \alpha \nu \quad (4.25g)$$

These are automatically adopted the assumption that the anisotropic factor ( $\alpha$ ) can be determined from  $\alpha = \nu_{hv}/\nu_{hh}$  or  $\alpha = G_{hh}/G_{vh}$ .

The elastic constitutive equation can also be rewritten in terms of triaxial stress-strain parameters (Muir Wood, 1990): mean effective stress  $p' = (\sigma'_a + 2\sigma'_r)/3$ , deviator stress  $q = \sigma'_a - \sigma'_r$ , volumetric strain  $\varepsilon_p = \varepsilon_a + 2\varepsilon_r$  and deviator strain  $\varepsilon_q = 2(\varepsilon_a - \varepsilon_r)/3$ . The elastic stiffness matrix becomes

$$\begin{Bmatrix} dp' \\ dq \end{Bmatrix} = \begin{bmatrix} K^* & J \\ J & 3G^* \end{bmatrix} \begin{Bmatrix} d\varepsilon_p \\ d\varepsilon_q \end{Bmatrix} \quad (4.26)$$

where  $G^*$  is a modified shear modulus,  $K^*$  is a modified bulk modulus and  $J$  is a coupling modulus. These elastic parameters can be written in terms of  $E^*$ ,  $\alpha$  and  $\nu^*$  as

$$G^* = E^* \left[ \frac{2 - 2\nu^* - 4\alpha\nu^* + \alpha^2}{6(1 + \nu^*)(1 - 2\nu^*)} \right] \quad (4.27)$$

$$K^* = E^* \left[ \frac{1 - \nu^* + 4\alpha\nu^* + 2\alpha^2}{9(1 + \nu^*)(1 - 2\nu^*)} \right] \quad (4.28)$$

$$J = E^* \left[ \frac{1 - \nu^* + \alpha\nu^* - \alpha^2}{3(1 + \nu^*)(1 - 2\nu^*)} \right] \quad (4.29)$$

The compliance matrix (i.e. the inversion of stiffness matrix) can also be defined as

$$\begin{Bmatrix} d\varepsilon_p \\ d\varepsilon_q \end{Bmatrix} = \frac{1}{\det} \begin{bmatrix} 3G^* & -J \\ -J & K^* \end{bmatrix} \begin{Bmatrix} dp' \\ dq \end{Bmatrix} \quad (4.30)$$

where  $\det = 3K^*G^* - J^2$ . For isotropic material, there is no coupling between volumetric and distortional behaviour or the  $J$  terms are zero.

#### 4.5.2 Optimization

In this study, all moduli are assumed to be power function of mean confining stress (Rampello et al., 1997). Therefore, the drained vertical Young's modulus can be assumed as in Equation (4.31).

$$\frac{E_v}{p_a} = A \left( \frac{p'_0}{p_a} \right)^n \quad (4.31)$$

where  $A$  and  $n$  are dimensionless parameters and  $p_a$  is the atmospheric pressure (approximately 100 kPa).

Based on the assumptions of Graham & Houlsby (1983), the constitutive law in Equation (4.21) is adopted and other drained elastic parameters can be calculated according to Equations (4.25a) – (4.25g). It can be seen that all parameters from drained test can be written as functions of four parameters  $A$ ,  $n$ ,  $\alpha$ , and  $\nu^*$ .

On the other hand, due to the constraint of no volume change in undrained test, the undrained Young's moduli measured from the vertically- and horizontally-cut specimens are functions of other elastic parameters. For vertically-cut specimen, the

directions of soil deposition are identical to the triaxial directions therefore, the constitutive relationship in Equation (4.21) can be reduced to Equation (4.32). Taking into account of the undrained condition,  $d\varepsilon_p = d\varepsilon_a + 2d\varepsilon_r = 0$ ; the vertical undrained Young's modulus can be derived as Equation (4.33).

$$\begin{Bmatrix} d\varepsilon_a \\ d\varepsilon_r \end{Bmatrix} = \frac{1}{E^*} \begin{bmatrix} 1 & -\frac{2v^*}{\alpha} \\ -\frac{v^*}{\alpha} & \frac{(1-v^*)}{\alpha^2} \end{bmatrix} \begin{Bmatrix} d\sigma'_a \\ d\sigma'_r \end{Bmatrix} \quad (4.32)$$

$$E_v^u = \frac{d\sigma'_a}{d\varepsilon_a} = E^* \left[ \frac{\alpha v^* + v^* - 1}{2v^{*2} + v^* - 1} \right] \quad (4.33)$$

For horizontally-cut specimen, the directions of soil deposition do not coincide with the triaxial directions therefore, the compliance matrix can be written as in Equation (4.34).

$$\begin{Bmatrix} d\varepsilon_a \\ d\varepsilon_{r,v} \\ d\varepsilon_{r,h} \end{Bmatrix} = \frac{1}{E^*} \begin{bmatrix} \frac{1}{\alpha^2} & -\frac{v^*}{\alpha} & -\frac{v^*}{\alpha^2} \\ -\frac{v^*}{\alpha^3} & 1 & -\frac{v^*}{\alpha^3} \\ -\frac{v^*}{\alpha^2} & -\frac{v^*}{\alpha} & \frac{1}{\alpha^2} \end{bmatrix} \begin{Bmatrix} d\sigma'_a \\ d\sigma'_r \\ d\sigma'_r \end{Bmatrix} \quad (4.34)$$

where  $d\varepsilon_{r,v}$  and  $d\varepsilon_{r,h}$  are the increment of radial strains associated to vertical and horizontal direction of soil deposition, respectively. Considering the undrained condition,  $d\varepsilon_p = d\varepsilon_a + d\varepsilon_{r,v} + d\varepsilon_{r,h} = 0$ ; the horizontal undrained Young's modulus can be expressed as shown in Equation (4.35). The measured shear moduli in case of undrained tests still follow Graham & Houlsby (1983) assumptions, i.e.,  $G_{vh} = G_{hh}/\alpha = \alpha E^*/2(1+v^*)$ . Again, it can be seen that all parameters from undrained test can also be written as a function of four parameters  $A$ ,  $n$ ,  $\alpha$ , and  $v^*$ .

$$E_h^u = \frac{d\sigma'_a}{d\varepsilon_a} = \alpha^2 E^* \left[ \frac{2\alpha^2 v^* + \alpha v^* + v^* - \alpha - \alpha^3}{\alpha^2 v^{*2} + 2\alpha v^{*2} + v^{*2} + \alpha^2 v^* + v^* - \alpha - \alpha^3} \right] \quad (4.35)$$

The four independent parameters:  $A$ ,  $n$ ,  $\alpha$  and  $v^*$  were determined from totally 20 tests of CIUC and CIDC tests based on least-square method (shown in Table 4.7).

The obtained optimized parameters are  $A = 460$ ,  $n = 0.52$ ,  $\alpha = 0.98$  and  $\nu^* = 0.086$ . Consequently, the cross-anisotropic elastic parameters of Bangkok Clay can be derived from Equations (4.25) as shown in Equations (4.36).

$$\frac{E_v}{p_a} = 460 \left( \frac{p'_0}{p_a} \right)^{0.52} \quad (4.36a)$$

$$\frac{E_h}{p_a} = 442 \left( \frac{p'_0}{p_a} \right)^{0.52} \quad (4.36b)$$

$$\frac{G_{vh}}{p_a} = 208 \left( \frac{p'_0}{p_a} \right)^{0.52} \quad (4.36c)$$

$$\frac{G_{hh}}{p_a} = 203 \left( \frac{p'_0}{p_a} \right)^{0.52} \quad (4.36d)$$

$$\nu_{hh} = 0.086 \quad (4.36e)$$

$$\nu_{vh} = 0.088 \quad (4.36f)$$

$$\nu_{hv} = 0.084 \quad (4.36g)$$

Table 4.8 shows the elastic parameters of all tests calculated by Equations (4.25). The experimental results (Table 4.7) are compared with the calculated values (Table 4.8) in terms of Young's moduli, shear moduli, and Poisson's ratios as presented in Figures 4.14, 4.15 and 4.16, respectively. The results show that the calculated values are within  $\pm 60\%$  of the measured values. It is noted that the positive percent of error means the calculated value is higher than the measured value, whereas the negative means the calculated value is lower than the measured value.

Table 4.7 Measured values of elastic parameters

| Test No. | $p'_0$<br>(kPa) | Measured values     |                   |                |                |                   |                   |
|----------|-----------------|---------------------|-------------------|----------------|----------------|-------------------|-------------------|
|          |                 | Consolidation stage |                   | Shearing stage |                |                   |                   |
|          |                 | $G_{vh}$<br>(kPa)   | $G_{hh}$<br>(kPa) | $E_v$<br>(kPa) | $E_h$<br>(kPa) | $\nu_{vh}$<br>(-) | $\nu_{hv}$<br>(-) |
| CIUC-1V  | 80              | 10001               |                   | 30000*         |                | -                 | -                 |
| CIUC-2V  | 100             | 15018               |                   | 42000*         |                | -                 | -                 |
| CIUC-3V  | 130             | 32592               |                   | 92500*         |                | -                 | -                 |
| CIUC-4V  | 120             | 26203               |                   | 110000*        |                | -                 | -                 |
| CIUC-5V  | 200             | 24642               |                   | 50000*         |                | -                 | -                 |
| CIUC-1H  | 90              |                     | 15528             |                | 15500**        | -                 | -                 |
| CIUC-2H  | 100             |                     | -                 |                | 55000**        | -                 | -                 |
| CIUC-3H  | 120             |                     | 30614             |                | 80000**        | -                 | -                 |
| CIUC-4H  | 120             |                     | 37120             |                | 42000**        | -                 | -                 |
| CIUC-5H  | 180             |                     | -                 |                | 65000**        | -                 | -                 |
| CIDC-1V  | 90              | -                   |                   | 23100          |                | 0.115             | -                 |
| CIDC-2V  | 100             | 16520               |                   | 25550          |                | 0.038             | -                 |
| CIDC-3V  | 120             | -                   |                   | 32900          |                | 0.100             | -                 |
| CIDC-4V  | 100             | -                   |                   | 23500          |                | 0.058             | -                 |
| CIDC-5V  | 24              | -                   |                   | 65000          |                | 0.127             | -                 |
| CIDC-1H  | 90              |                     | 14282             |                | 18000          | -                 | 0.309             |
| CIDC-2H  | 90              |                     | -                 |                | 18000          | -                 | 0                 |
| CIDC-3H  | 120             |                     | 27598             |                | 43000          | -                 | 0                 |
| CIDC-4H  | 100             |                     | 25762             |                | 20028          | -                 | 0.057             |
| CIDC-5H  | 240             |                     | -                 |                | 30000          | -                 | 0.055             |

**Remarks:** \*  $E_v = E_v^u$  for CIUC tests on vertical-cut specimens; \*\*  $E_h = E_h^u$  for CIUC tests on vertical-cut specimens

Table 4.8 Calculated values of elastic parameters

| Test No. | $p'_0$<br>(kPa) | Calculated values   |                   |                |                |                   |                   |
|----------|-----------------|---------------------|-------------------|----------------|----------------|-------------------|-------------------|
|          |                 | Consolidation stage |                   | Shearing stage |                |                   |                   |
|          |                 | $G_{vh}$<br>(kPa)   | $G_{hh}$<br>(kPa) | $E_v$<br>(kPa) | $E_h$<br>(kPa) | $\nu_{vh}$<br>(-) | $\nu_{hv}$<br>(-) |
| CIUC-1V  | 80              | 18481               |                   | 37795*         |                | -                 | -                 |
| CIUC-2V  | 100             | 20755               |                   | 42445*         |                | -                 | -                 |
| CIUC-3V  | 130             | 23789               |                   | 48649*         |                | -                 | -                 |
| CIUC-4V  | 120             | 22819               |                   | 46666*         |                | -                 | -                 |
| CIUC-5V  | 200             | 29762               |                   | 60865*         |                | -                 | -                 |
| CIUC-1H  | 90              |                     | 19256             |                | 38477**        | -                 | -                 |
| CIUC-2H  | 100             |                     | -                 |                | 40644**        | -                 | -                 |
| CIUC-3H  | 120             |                     | 22363             |                | 44686**        | -                 | -                 |
| CIUC-4H  | 120             |                     | 22363             |                | 44686**        | -                 | -                 |
| CIUC-5H  | 180             |                     | -                 |                | 55175**        | -                 | -                 |
| CIDC-1V  | 90              | -                   |                   | 43548          |                | 0.088             | -                 |
| CIDC-2V  | 100             | 20755               |                   | 46000          |                | 0.088             | -                 |
| CIDC-3V  | 120             | -                   |                   | 50575          |                | 0.088             | -                 |
| CIDC-4V  | 100             | -                   |                   | 46000          |                | 0.088             | -                 |
| CIDC-5V  | 240             | -                   |                   | 72522          |                | 0.088             | -                 |
| CIDC-1H  | 90              |                     | 19256             |                | 41823          | -                 | 0.084             |
| CIDC-2H  | 90              |                     | -                 |                | 41823          | -                 | 0.084             |
| CIDC-3H  | 120             |                     | 22363             |                | 48572          | -                 | 0.084             |
| CIDC-4H  | 100             |                     | 20340             |                | 44178          | -                 | 0.084             |
| CIDC-5H  | 240             |                     | -                 |                | 69650          | -                 | 0.084             |

**Remarks:** \*  $E_v = E_v^u$  for CIUC tests on vertical-cut specimens; \*\*  $E_h = E_h^u$  for CIUC tests on vertical-cut specimens



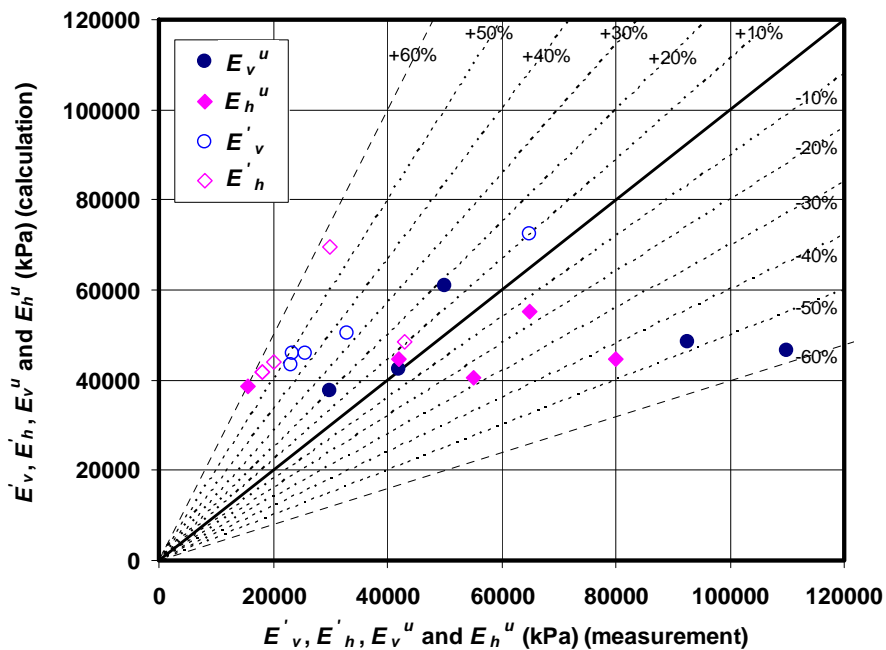


Figure 4.14 Comparison between measured and calculated values of Young's moduli

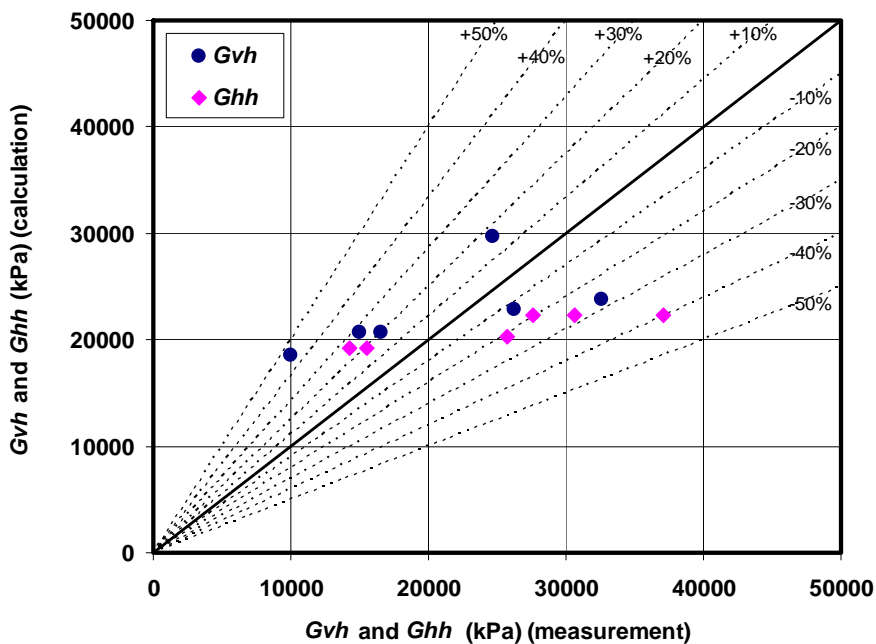


Figure 4.15 Comparison between measured and calculated values of shear moduli

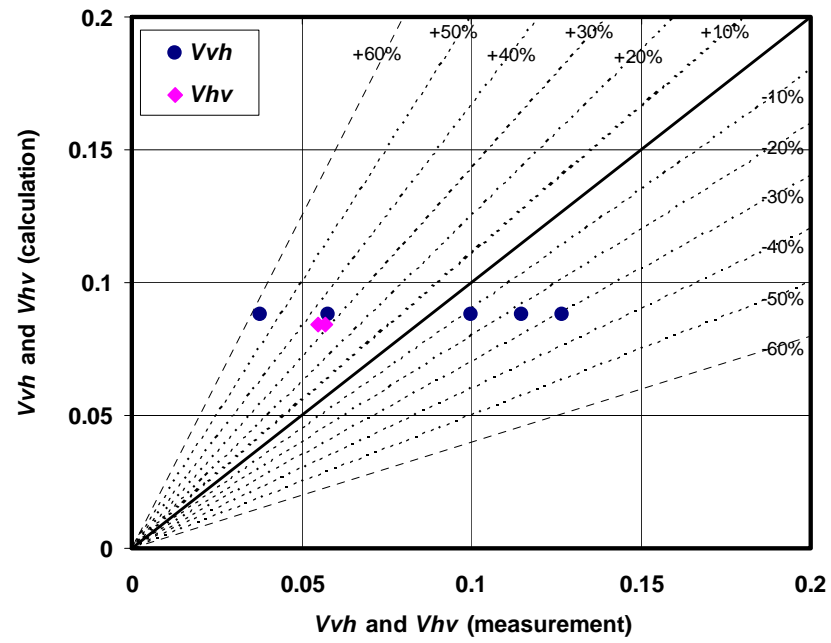


Figure 4.16 Comparison between measured and calculated values of Poisson's ratios

## CHAPTER V

### Torsional Shear Hollow Cylinder Testing Apparatus, Testing Procedures and Testing Program

#### 5.1 Introduction

Anisotropy behavior of Bangkok Clay and effects of directions of major principal stress rotation ( $\alpha$ ) and magnitude of intermediate principal stress ( $b$ ) on undrained behavior of Bangkok Clay were investigated. These effects were observed by means of torsional shear hollow cylinder apparatus. In each test, the directions of major principal stress and the magnitude of the intermediate principal stress were controlled at  $\alpha=0^\circ$ ,  $45^\circ$  and  $90^\circ$  and  $b=0$ ,  $0.5$  and  $1$ , respectively. There are 9 tests in total. Torsional shear hollow cylinder test and testing program were discussed in details in this chapter.

#### 5.2 Torsional shear hollow cylinder testing system

The layout of the torsional shear apparatus was shown in Figure 5.1. The main components were informed below.

1. A stationary, large 256 mm diameter stainless steel was sealed by large O-ring. The removable cell chamber, having 15 mm thick perspex, was designed to be fixed by stiffening ring which has 3 bolts.

2. A loading shaft incorporated with two-component load cell was aligned along the frame's central axis. The shaft carried the top cap was connected to the inner cell pressure line, the suction and the back pressure line. The inner and outer cells were filled with de-aired water from the main water supply.

3. A system of actuators was connected to the loading shaft. The axial load and torque were applied via a rigid end platen. The application of both axial load ( $W$ ) and torque ( $M_T$ ) was achieved by means of Bellofram cylinder and step motor respectively.

4. A loading system was set by stress control mode. The system included electro-pneumatic controllers acted through de-aired water interfaces to control the inner pressure, outer pressure and back pressure. The electro-pneumatic controllers were connected to a computer-controlled system in order to control operations.

5. A systems of stress and strain measuring transducers. The outer pressure, inner pressure and pore water pressure were measured by means of pressure gauges (P.G.). A dial gauge transducer was used for gauging the axial displacement. The torsional shear deformation of the specimen was measured at the top cap by a potentiometer. Volume changes of specimen and inner cell were measured by differential pressure transducers (D.P.T.). These transducers were connected to the computer for automatic data acquisition and closed-loop control. The characteristics of the transducers were summarized in Table 5.1.

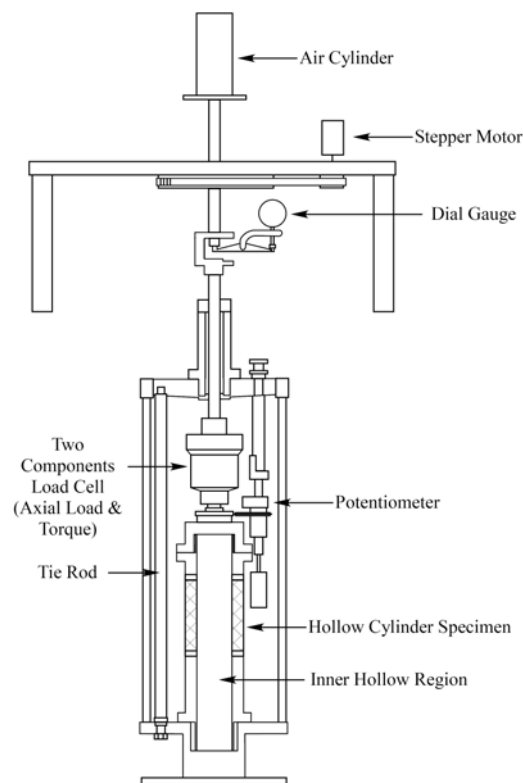


Figure 5.1 Torsional shear apparatus

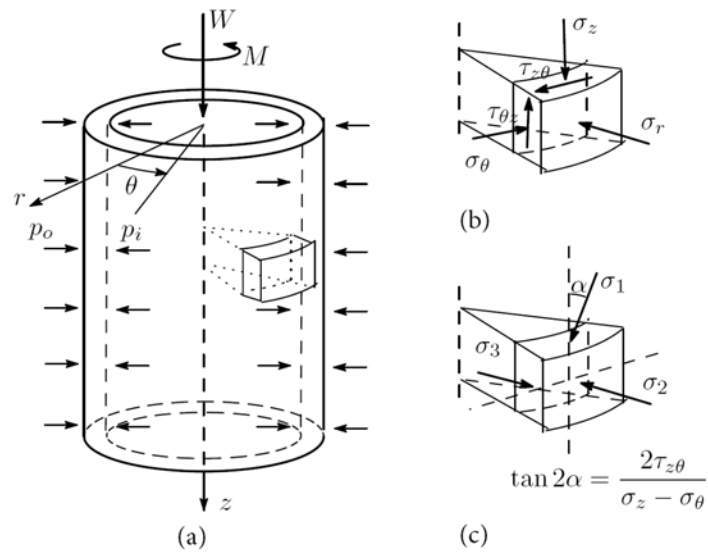


Figure 5.2 Hollow cylinder testing (a) Boundary loads (b) Individual stress components and (c) Principal stresses and their directions (Reinaldo, 2003)

Table 5.1 Characteristics of the transducers used

| Channel | Transducers               | Model No. | Serial Number | Offset | Gain<br>(mV/(mV/V)) | Calibration factor           | R <sup>2</sup> |
|---------|---------------------------|-----------|---------------|--------|---------------------|------------------------------|----------------|
| 1       | Axial Load                | TS300     | 576301        | 0      | 4000                | 0.7378 N/mV                  | -              |
| 2       | Torque                    | TS300     | 576301        | 0      | 4000                | 0.007354 N.m/mV              | -              |
| 3       | Axial Displacement        | DT-20D    | YD9415        | 0      | 4000                | 0.004981 mm/mV               | 0.99998        |
| 4       | Rotation                  | CP-2ut    | -             | 0      | 4000                | 0.019487 Deg/mV              | 0.99994        |
| 5       | Outer pressure transducer | PG-10KU   | EE9360020     | 0      | 2255                | 0.2186 kPa/mV                | .0999998       |
| 6       | Inner pressure transducer | PG-10KU   | YT0060050     | 0      | 2268                | 0.21589 kPa/mV               | 0.999999       |
| 7       | Pore pressure transducer  | PG-5KU    | AF-5913       | 0      | 2263                | 0.10889 kPa/mV               | 0.999998       |
| 8       | Volume change transducer  | BP15-24   | 74114         | 0      | ZERO 4.46 SPAN 3.92 | 0.005608 cm <sup>3</sup> /mV | 0.999968       |

### 5.3 Principal of torsional shear hollow cylinder test

Figure 5.2 represented the boundary loads which are imposed on the hollow cylinder specimen and the stress state which can be simulated on an imaginary element at the specimen wall. Four stress components on the hollow cylinder specimen ( $\sigma_z$ ,  $\sigma_r$ ,  $\sigma_\theta$ ,  $\tau_{\theta z}$ ) can be adjusted by applying and controlling the inner pressure ( $p_i$ ), the outer pressure ( $p_o$ ), the axial load ( $W$ ) and the torque ( $M_T$ ). The torque generates torsional shear stresses ( $\tau_{\theta z}$  and  $\tau_{z\theta}$ ) in both vertical and horizontal planes. The axial load can contribute to a vertical stress ( $\sigma_z$ ). Differences between inner pressure and outer pressure establish gradients of radial stress ( $\sigma_r$ ) and circumferential stress ( $\sigma_\theta$ ) across the cylinder wall. As the boundary loads can be applied independently, the magnitude of the three principal stresses and the inclination of the major and minor principal stress directions can be controlled. The Mohr circle represented of stress in the wall of the specimen and the major principal stress rotation angle was shown in Figure 5.3. In case of inner pressure and outer pressure are equal ( $p_i=p_o$ ), the radial stress and circumferential stress are also equal to both outer and inner pressures. For this condition, it can be seen that the direction of the major principal stress is related to the intermediate principal stress as  $b=\sin^2\alpha$ .

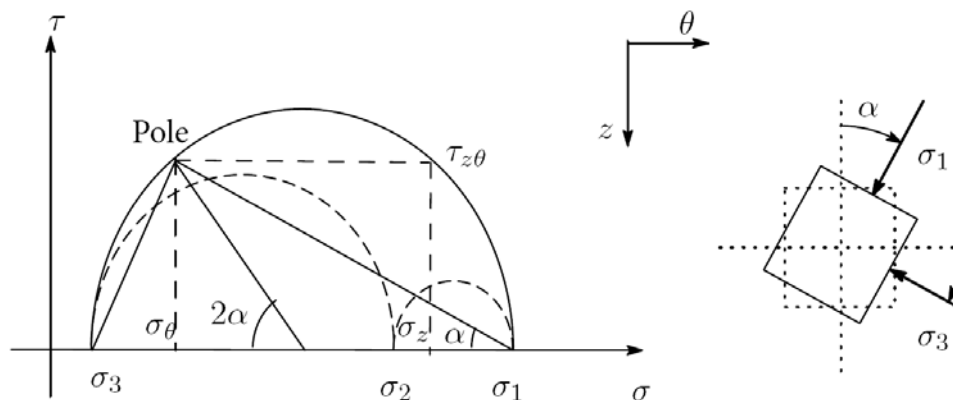


Figure 5.3 Definition of the major principal stress rotation angle  $\alpha$  (Reinaldo, 2003)

#### 5.4 Stress and strain calculation

The stress and strain components in hollow cylindrical specimens are calculated with reference to the work by Hight et al. (1983). In order to interpretations of the stress and strain components, considering the specimen as a single element is required for analyzing. Because the stresses vary across the wall of the hollow cylindrical specimen the calculation is in term of average stresses and strains. The expressions for calculating average stresses proposed by Hight et al. (1983) are shown below.

$$\sigma_z = \frac{W}{\pi(r_o^2 - r_i^2)} + \frac{p_o r_o^2 - p_i r_i^2}{r_o^2 - r_i^2} \quad (5.1)$$

$$\sigma_r = \frac{p_o r_o + p_i r_i}{r_o + r_i} \quad (5.2)$$

$$\sigma_\theta = \frac{p_o r_o - p_i r_i}{r_o - r_i} \quad (5.3)$$

$$\tau_{\theta z} = \frac{3M_T}{2\pi(r_o^3 - r_i^3)} \quad (5.4)$$

where  $\sigma_z$ ,  $\sigma_r$ ,  $\sigma_\theta$  and  $\tau_{\theta z}$  are the average axial, radial, circumferential and shear stresses respectively.  $M_T$  is the applied torque,  $W$  is the axial force and  $p_o$  and  $p_i$  are the outer and inner cell pressure. The current outer and inner radii of specimen are denoted by  $r_o$  and  $r_i$  respectively.

The average axial and circumferential normal stresses are derived from equilibrium consideration so that they are valid irrespective of the material's constitutive law (Hight et al., 1983).

Strain components, defined in the same coordinate system as stress components, were also calculated in the same manner as described in Hight et al. (1983).

$$\varepsilon_z = \frac{w}{H_0} \quad (5.5)$$



$$\varepsilon_r = -\frac{u_o - u_i}{r_{oz} - r_{iz}} \quad (5.6)$$

$$\varepsilon_\theta = -\frac{u_o + u_i}{r_{oz} + r_{iz}} \quad (5.7)$$

$$\gamma_{\theta z} = \frac{2\theta(r_o^3 - r_i^3)}{3H_0(r_o^2 - r_i^2)} \quad (5.8)$$

where  $\varepsilon_z$ ,  $\varepsilon_r$ ,  $\varepsilon_\theta$  and  $\gamma_{\theta z}$  are the average axial, radial, circumferential and shear strains respectively.  $H_0$  is the initial height of specimen.  $w$  is the axial deformation of the initial height.  $\theta$  is the circumferential angular deformation (measured in radians).  $u_o$  and  $u_i$  are radial deformations of the outer and inner wall with initial radii of  $r_{oz}$  and  $r_{iz}$  respectively.

The expressions as shown above can be used to obtain the principal stress as follows. The intermediate principal stress is always fixed to the horizontal direction and equal to the radial stress. The maximum and minimum principal stresses are mobilized on the  $z - \theta$  plane.

$$\sigma_1 = \frac{\sigma_z + \sigma_\theta}{2} + \sqrt{\left(\frac{\sigma_z - \sigma_\theta}{2}\right)^2 + \tau_{\theta z}^2} \quad (5.9)$$

$$\sigma_2 = \sigma_r \quad (5.10)$$

$$\sigma_3 = \frac{\sigma_z + \sigma_\theta}{2} - \sqrt{\left(\frac{\sigma_z - \sigma_\theta}{2}\right)^2 + \tau_{\theta z}^2} \quad (5.11)$$

The principal strains are shown below. It is noted that the equations assume that the principal stress and strain axes are coincidence.

$$\varepsilon_1 = \frac{\varepsilon_z + \varepsilon_\theta}{2} + \sqrt{\left(\frac{\varepsilon_z - \varepsilon_\theta}{2}\right)^2 + \left(\frac{\gamma_{\theta z}}{2}\right)^2} \quad (5.12)$$

$$\varepsilon_2 = \varepsilon_r \quad (5.13)$$

$$\varepsilon_3 = \frac{\varepsilon_z + \varepsilon_\theta}{2} - \sqrt{\left(\frac{\varepsilon_z - \varepsilon_\theta}{2}\right)^2 + \left(\frac{\gamma_{\theta z}}{2}\right)^2} \quad (5.14)$$

In geotechnical engineering, it is often convenient to consider the principal stresses in the 3-dimensional principal effective stress space. The invariant of stresses can be expressed by:

$$p' = \frac{\sigma'_1 + \sigma'_2 + \sigma'_3}{3} \quad (5.15)$$

$$J = \frac{1}{6} \sqrt{(\sigma'_1 - \sigma'_2)^2 + (\sigma'_2 - \sigma'_3)^2 + (\sigma'_3 - \sigma'_1)^2} \quad (5.16)$$

$$\theta = \arctan \frac{[(2b-1)]}{\sqrt{3}} \quad (5.17)$$

$$b = \frac{\sigma'_2 - \sigma'_3}{\sigma'_1 - \sigma'_3} \quad (5.18)$$

Note that the normal stresses are in terms of effective stress ( $\sigma' = \sigma - u$ ) and  $b$  is the intermediate principal stress parameter. The value of  $b$  is  $0 \leq b \leq 1$ . For symmetric loading,  $b$  parameter equals to either 0 (triaxial compression) or 1 (triaxial extension). In case of plane strain condition,  $b$  equals to 0.3-0.5.

As shown in Figure 5.4, the mean effective stress ( $p'$ ) is corresponded to the distance along the space diagonal of the current deviatoric plane from the origin ( $\overline{OA}$ ). In the deviatoric plane, the invariant of the stress deviator ( $J$ ) is calculated of the current stress state from the space diagonal or  $\pi$ -plane ( $\overline{AN}$ ). The Lode's angle ( $\theta$ ) represents the orientation of the stress state within this plane.

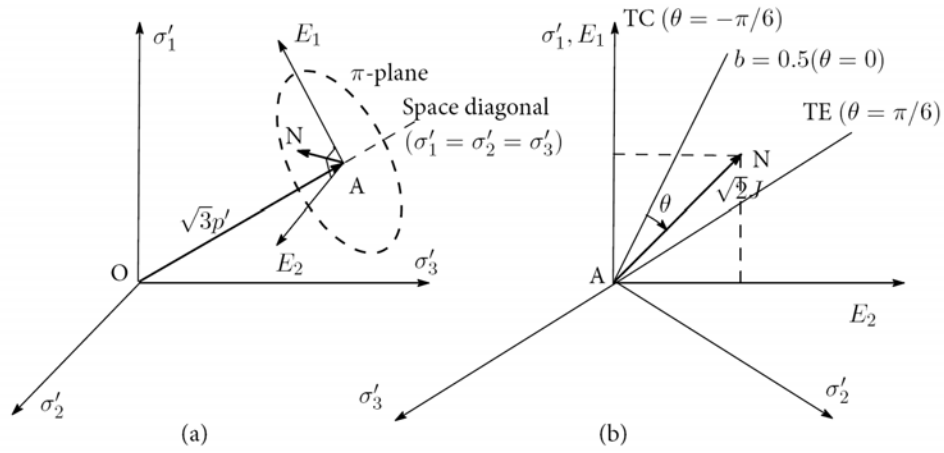


Figure 5.4 Generalized stress state:

(a) Principal stresses; (b) Deviatoric plane (Reinaldo, 2003)

### 5.5 Computer control and data acquisition

The personal computer was used to control the independent parameters of torsional shear hollow cylinder apparatus. The control software was written in a basic language. The program allowed to control of four stresses ( $\sigma_z, \sigma_r, \sigma_\theta$  and  $\tau_{\theta z}$ ) and therefore enabled independent controls of the direction of major principal stress ( $\alpha$ ) from the vertical direction and the magnitude of intermediate principal stress coefficient ( $b$ ). The controls parameters used to follow the desired stress path are displayed.

$$p = \frac{(\sigma_z + \sigma_r + \sigma_\theta)}{3} \quad (5.19)$$

$$b = \frac{\sigma_r - \left(\frac{\sigma_z + \sigma_\theta}{2}\right) + \frac{1}{2}\sqrt{(\sigma_z - \sigma_\theta)^2 + 4\tau_{\theta z}^2}}{\sqrt{(\sigma_z - \sigma_\theta)^2 + 4\tau_{\theta z}^2}} \quad (5.20)$$

$$R(t) = \frac{\sigma_z + \sigma_\theta + \sqrt{(\sigma_z - \sigma_\theta)^2 + 4\tau_{\theta z}^2}}{\sigma_z + \sigma_\theta - \sqrt{(\sigma_z - \sigma_\theta)^2 + 4\tau_{\theta z}^2}} \quad (5.21)$$

$$\alpha = \frac{1}{2} \arctan\left(\frac{2\tau_{\theta z}}{\sigma_z - \sigma_\theta}\right) \quad (5.22)$$

where  $p$ ,  $b$ ,  $R$  and  $\alpha$  are the mean stress, intermediate principal stress ratio, total stress ratio (in function of stress rate) and the angle of the major principal stress from the vertical direction respectively.

From the above control parameters, the target stresses can be calculated as:

$$\sigma_z(t) = \frac{(R(t)+1) + (R(t)-1)\cos 2\alpha}{2b(R(t)-1) + 2(R(t)+2)} 3p \quad (5.23)$$

$$\sigma_r(t) = \frac{b(R(t)-1) + 1}{b(R(t)-1) + (R(t)+2)} 3p \quad (5.24)$$

$$\sigma_\theta(t) = \frac{(R(t)+1) - (R(t)-1)\cos 2\alpha}{2b(R(t)-1) + 2(R(t)+2)} 3p \quad (5.25)$$

$$\tau_\alpha(t) = \frac{(R(t)-1)\sin 2\alpha}{2b(R(t)-1) + 2(R(t)+2)} 3p \quad (5.26)$$

A small incremental change of the loading parameters was specified and the rests of the target stresses were theoretically recalculated in order that the control system could apply the necessary changes to the desired stresses until the final state of the desired path was reached. The loading parameters can be calculated by Eq. (5.1-5.4) and are performed below.

$$W = \pi(r_o^2 - r_i^2)\sigma_z(t) - \pi(p_o r_o^2 - p_i r_i^2) \quad (5.27)$$

$$M_t = \frac{2}{3} \pi(r_o^3 - r_i^3)\tau_\alpha(t) \quad (5.28)$$

$$p_o = \frac{\sigma_r(t)(r_o - r_i) + \sigma_\theta(t)(r_o - r_i)}{2r_o} \quad (5.29)$$

$$p_i = \frac{\sigma_r(t)(r_o - r_i) - \sigma_\theta(t)(r_o - r_i)}{2r_i} \quad (5.30)$$

Table 5.2 Specimen characteristics for detailed study

| Test No. | $\alpha$<br>( $^{\circ}$ ) | $b$ | Borehole<br>No. | Depth<br>(m) | Natural water<br>content ( $w_n$ )<br>(%) | Liquid<br>Limit ( $LL$ )<br>(%) | Plastic<br>Limit ( $PL$ )<br>(%) | Plastic<br>Index ( $PI$ )<br>(%) |
|----------|----------------------------|-----|-----------------|--------------|---|---------------------------------|----------------------------------|----------------------------------|
| A00B00   | 0                          | 0   | BH-5            | 14.0-14.6    | 20.16                                     | 64.8                            | 16.31                            | 48.49                            |
| A00B05   | 0                          | 0.5 | BH-5            | 13.3-13.8    | 22.16                                     | 53.6                            | 17.97                            | 35.63                            |
| A00B10   | 0                          | 1   | BH-5            | 13.2-13.8    | 25.26                                     | 59.6                            | 17.65                            | 41.95                            |
| A45B00   | 45                         | 0   | BH-6            | 11.8-12.4    | 54.29                                     | 85.18                           | 32.97                            | 52.21                            |
| A45B05   | 45                         | 0.5 | BH-5            | 10.6-11.2    | 61.83                                     | -                               | -                                | -                                |
| A45B10   | 45                         | 1   | BH-5            | 12.0-12.6    | 49.4                                      | 85.8                            | 27.39                            | 58.41                            |
| A90B00   | 90                         | 0   | BH-6            | 11.5-12.0    | 53.36                                     | 87.6                            | 31.85                            | 55.75                            |
| A90B05   | 90                         | 0.5 | BH-7            | 9.8-10.4     | 79.33                                     | 114.2                           | 40.04                            | 74.16                            |
| A90B10   | 90                         | 1   | BH-7            | 7.0-7.6      | 55.58                                     | 62.80                           | 22.31                            | 40.49                            |

Remark  $u$  = under drainage to lower and stratum  
 $K_o = 0.7$   
 $\gamma_t = 17 \text{ kN/m}^2$

## **5.6 Torsional shear hollow cylinder program**

The detail of testing program was planned to assess the behavior of anisotropy of Bangkok Clay. Effects of the major principal stress rotation and the difference magnitude of intermediate principal stress were observed by means of the torsional shear hollow cylinder apparatus. Three different directions of the major principal stress, namely  $\alpha=0^\circ$ ,  $45^\circ$  and  $90^\circ$ , were evaluated corresponding with the intermediate principal stress ratio  $b=0$ ,  $0.5$  and  $1.0$  at each  $\alpha$  in undrained condition (CIUC). The torsional shear hollow cylinder testing programs and the specimen properties were expressed in Table 5.2.

### **5.6.1 Sampling**

The specimens which were used in these tests were undisturbed Bangkok Clay from Nakniwas, Ladprao. The depths of these samples were from 7.5-15 m. The undisturbed samples were collected by 12 cm diameter piston sampler. The tube samples were immediate waxed from both sides to prevent the loss of moisture and then was safety carried to the laboratory in Hokkaido University.

### **5.6.2 Sample preparation**

After the wax layer and cling-film were removed from the tube samples, they were carefully inspected to convince that their condition were suitable for testing. If there were some opened fissured or any evidences of unusual features, those samples were discarded. Before placing the samples in the soil lathe, the ends of the samples were flattened by trimming knife. The samples were gradually trimmed down by means of the wire saw to reduce its diameter to 70 mm.

The cylinder specimens were then encased within a two-part steel mould (inside diameter of 120 mm). The ends of the specimen were smooth chopped into the height of 120 mm. After that the steel mould were tied by 4 screw bolts at the end of caps, ready for the next step of forming the inner cylinder cavity. In order to prevent the cling between steel mold and specimen, a thin plastic film was used to cover the specimen before putting on. At the centers of the end caps of the steel mould, one side

had a 30 mm diameter hole, whereas the other side had 10 mm diameter hole. The picture of the steel mould was shown in Figure 5.5.

The inner hole was produced and enlarged by using successive drill (nominal diameter of 3/8 inch) as shown in Figure 5.5. The 10 mm diameter end cap of steel mould was then replaced by the 30 mm diameter end cap. Moreover, the drill was substituted by the wire saw and the remaining was performed. The completed inner diameter was 30 mm. The process of forming the hollow cylinder specimen illustrated in Figure 5.6.

For each specimen, water content measurements were made to check any change experienced before and after sample testing. The specimen's dimension ( $H$ ,  $D_i$  and  $D_o$ ) were measured at 4 positions. The specimen's dimensions were recorded and average values were input into the controlling program as the initial conditions. The specimen's weight was also measured.



(a) Outside trimming: soil lathe and wire saw



(b) Inside drilling: drill and steel mould

Figure 5.5 Tools used for the preparation of hollow cylinder specimen



(a) A tube sample



(b) Outside trimming in the soil lathe



(c) Flattening the ends of sample



(d) Drilling inner cavity by a drill



(e) Drilling inner cavity to 30 mm

(f) A hollow cylinder specimen diameter by the wire saw ( $D_i = 30$  mm,  $D_o = 70$  mm and  $H_i = 120$ mm)

Figure 5.6 Stage of preparation of hollow cylinder specimen



### 5.6.3 Specimen set up

The main step of set up was explained in the following section. Each of stages of hollow cylinder specimen set-up was displayed in Figure 5.7.



(a) Installing base pedestal, bottom porous stone and inner membrane in the position



(b) Placing a specimen on the bottom porous stone



(c) Attaching 8 damp trip filter papers on the specimen wall



(d) Setting the top cap and enclosing inner and outer membrane



(e) Connection between load cell and top cap and potentiometer installation



(f) Filling cell water and connection between the set of stationary and load frame

Figure 5.7 Stage of hollow cylinder specimen set-up

### - Installation of the specimen

The specimen was placed on the base pedestal which was located with the porous stone and the inner membrane in the position. The porous stones were embedded radially with 6 thin brass blades to allow torsion failure to develop without any end slips as shown in Figure 5.8.



Figure 5.8 Top and bottom porous stones with radial brass blades

### - Side drain

8 damp strip of 1 cm-wide filter papers were attached to the outer specimen wall to facilitate the consolidation.

### - Inner and outer membrane enclosure

After placing the specimen on the pedestal and attaching filter papers on the specimen wall, the top cap was set in place. The inner and outer rubber membranes were placed over the specimen with care to expel locally trapped air. After that 4 O-ring, two at each specimen end, were applied to seal the specimen from the outer cell. One inner O-ring was used to seal with the top cap.

### - Connection between load cell and top cap

After enclosing the membrane, the potentiometer was installed. The frame and the outer cell chamber were lifted into the position. The cell chamber was fixed by stiffening ring which had 3 bolts. Finally, the set of stationary was connected with the load frame. Two bolts at the base were hold firmly.

### - Filling the cell water

The level of water in the chamber was separated into 3 levels. At first, the outer cell chamber was filled with de-aired water to the first level. Once completed, the inner cell chamber was also poured with de-aired water to the same level. After that, the next levels of the water in both of outer and inner cell were filled by the same procedure until the final level. In order to extract the trapped air within the space between the inner membrane and the specimen, the de-aired water was additionally applied.

### **5.6.4 Saturation**

After completing the specimen set up, a suction of 100 kPa was applied in the cell and suction line to extract the trapped air within the system. After 15 minutes, the air within the drainage lines was flushed with de-aired during decreasing the suction pressure to zero. The back pressure method was used to improve the saturation. The cell pressure and the back pressure were simultaneously increased in several steps while keeping their difference constant and were equal to initial effective stress. The typical applied back pressure was 200 kPa. During this process, saturation checking could be made by applying cell pressure increment and closing the drainage valve. The Skempton  $B$ -value was calculated. The typical values of  $B$  were greater than 0.95, which correspond to the degree of saturation of 100% for soft to stiff clay.

### **5.6.5 Isotropic consolidation**

The specimens were applied the pressure to the in-situ effective stress. The details of in-situ effective stress of any tests were summarized in Table 5.3. During consolidation time, the water was allowed to drain through the drainage valves.

A standard period to stop consolidation could be determined by 3-time method in the following manner. Plot the measured values between the volume change ( $\Delta V$ ) and time ( $t$ ) on a semi-logarithmic scale and obtain the steepest slope line on the curve. Draw a straight line parallel to this line on the semi-logarithmic graph with the distance of  $3t$ . This line is called as “3t-line”. When the  $\Delta V$ - $\log t$

curve reaches the 3-time, the consolidation should be terminated (The Japanese Geotechnical Society, 1999).

Table 5.3 Details of stress during saturation

| Test No. | $\alpha$<br>( $^{\circ}$ ) | $b$ | In-situ<br>effective<br>pressure $\sigma'_{v,0}$<br>(kPa) | Consolidati<br>on pressure<br>$p'_0$<br>(kPa) | Initial<br>effective<br>stress $p'_i$<br>(kPa) | Back<br>pressure<br>$u_b$<br>(kPa) |
|----------|----------------------------|-----|---|---|--|------------------------------------|
| A00B00   | 0                          | 0   | 128.1   | 105   | 50   | 200                                |
| A00B05   | 0                          | 0.5 | 126.2   | 100   | 50   | 200                                |
| A00B10   | 0                          | 1   | 124.5   | 100   | 50   | 200                                |
| A45B00   | 45                         | 0   | 104   | 85  | 50   | 200                                |
| A45B05   | 45                         | 0.5 | 92.3  | 75  | 50   | 200                                |
| A45B10   | 45                         | 1   | 109.1   | 90  | 50   | 200                                |
| A90B00   | 90                         | 0   | 105   | 85  | 50   | 200                                |
| A90B05   | 90                         | 0.5 | 79.7  | 65  | 50   | 200                                |
| A90B10   | 90                         | 1   | 54.1  | 45  | 45   | 200                                |

### 5.6.6 Checking of excess pore water pressure

Because of the permission of drainage, the excess pore water pressure could not be observed during consolidation. The post observation of the excess pore water pressure after the consolidation time reached to the standard period to stop consolidation by 3-time method was performed by closing the drainage valves. If the excess pore water pressure can be dissipated, the specimen will be ready to conduct to the undrained shearing. On the other hand, if the excess pore water pressure can not be dispersed, the rest period will be allowed to the specimen. The termination of the isotropic consolidation stage is judged by the dissipation of the excess pore water pressure ( $\Delta u < 1$  kPa).

### 5.6.7 Undrained shearing

In this study, the undrained shearing was performed. In case of compression and extention mode, samples were undrained sheared until failure. However, a series of sample controlled at  $\alpha=45^{\circ}$ , the final undrained shearing state was terminated when either excessive deformation was observed or the degree of rotation was  $30^{\circ}$ . The water contents of the specimen after undrained shearing were observed.

## CHAPTER VI

### Results of Torsional Shear Hollow Cylinder Test

#### 6.1 Introduction

In this chapter the experimental results obtained from torsional shear hollow cylinder tests are described and discussed in detail. The results of these tests are used to evaluate the anisotropic response of Bangkok Clay in terms of stress-strain and strength parameters. The independent effects of  $\alpha$  and  $b$  are separated and their influence on the stress-strain behavior, stiffness and strength characteristic of Bangkok Clay are evaluated.

Nine torsional shear tests on hollow cylindrical Bangkok Clay samples were carried out each with a different  $b$  values at 0, 0.5 and 1 in undrained condition. The  $\alpha$  values were fixed at  $0^\circ$ ,  $45^\circ$  and  $90^\circ$ . The back pressure of 200 kPa was applied to ensure the specimen saturation. After the saturation, with a Skempton's  $B$  parameter greater than 0.95, all specimens were isotropically consolidated to the pressure which is equivalent to the in-situ effective vertical stress ( $p_0'$ ). The termination of the isotropic consolidation stage is judged by the dissipation of the excess pore water pressure ( $\Delta u < 1$  kPa).

Undrained shearing was then applied (after termination of the isotropic consolidation stage) under constant  $\alpha$ ,  $b$  and  $p$  conditions. A total of nine torsional shear tests performed with different fixed values of  $\alpha$  values at  $0^\circ$ ,  $45^\circ$  and  $90^\circ$  and  $b$  at 0, 0.5 and 1 is shown in Table 6.1. The symbols of A and B stand for  $\alpha$  and  $b$ , respectively. The number beside A and B letters indicates the values of each of the parameters (e.g. A00B05 corresponds to the test which was undrained sheared with  $\alpha=0^\circ$  and  $b=0.5$ ). The total mean stress was also kept constant during this stage.

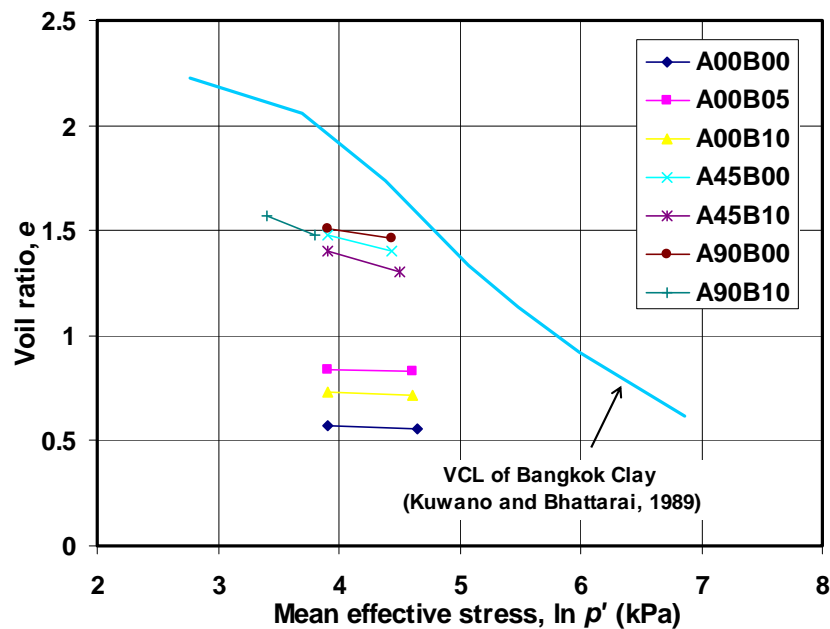
Table 6.1 Values of  $\alpha$  and  $b$  in the torsional shear testing program

| Value of $b$ during undrained shearing | Direction of the major principal stress ( $\alpha$ ) |        |        |
|--|--|--------|--------|
|  | 0°   | 45°    | 90°    |
| 0                                      | A00B00   | A45B00 | A90B00 |
| 0.5                                    | A00B05   | A45B05 | A90B05 |
| 1                                      | A00B10   | A45B10 | A90B10 |

## 6.2 Isotropic consolidation

### 6.2.1 Compressibility of isotropically consolidated Bangkok Clay

The undisturbed Bangkok Clay samples were isotropically consolidated the pressure being equal to their in-situ effective vertical stresses. Relationships of  $e$ - $\ln p'$  of Bangkok Clay under torsional shear hollow cylinder tests are summarized in Figure 6.1.  $e$  is void ratio and  $p'$  is mean effective stress. Because all of Bangkok Clay specimens were consolidated to  $p_0'$ , the trends of  $e$ - $\ln p'$  lie under virgin consolidation line of Bangkok Clay recommended by Kuwano and Bhattarai (1989).

Figure 6.1 Compression curve in  $e$ - $\ln p'$  plane

### 6.2.2 Anisotropic deformation during isotropic consolidation

During the test, a continuous record of deformation of hollow cylindrical specimens was measured independently by two transducers. A dial gauge transducer is used for reading the axial displacement. Volume changes of specimen and inner cell are measured using differential pressure transducers (D.P.T.). Since all strain components in the hollow cylindrical specimens were measured by transducers, it is possible to directly study the anisotropic deformation of the specimens during the isotropic consolidation stage.

The typical relationships between vertical and horizontal strain during isotropic consolidation are summarized in Figure 6.2. The strain in the vertical direction ( $\varepsilon_v$ ) was measured from axial strain ( $\varepsilon_z$ ), whereas the strain in the horizontal direction ( $\varepsilon_h$ ) was averaged two values of radial ( $\varepsilon_r$ ) and circumferential ( $\varepsilon_\theta$ ) strain. The result shows that the deformation response under isotropic consolidation is different in two directions. The specimens are stiffer in the horizontal direction. The ratios of  $\Delta\varepsilon_v/\Delta\varepsilon_h$  vary between 1.55 and 4.29 and the average ratio is around 2.34 (see Figure 6.3). The measure ratios of  $\Delta\varepsilon_v/\Delta\varepsilon_h$  in all tests are summarized in Table 6.2. It is noted that at the end of isotropic consolidation, shear strain was occurred slightly. Records of strain at the end of the tests are also summarized in Table 6.2. This result agrees with the result from triaxial test as reported in chapter 4. The average ratio is around 2.14. The average ratio of anisotropic deformation in torsional shear hollow cylinder test shows slightly higher than those obtained from triaxial test. The different might be caused by the different properties of specimen. This result also agrees with the result of anisotropic deformation characteristic of Bangkok Clay reported by Kuwano and Bhattarai (1989) which were conducted using true triaxial test under drained conditions.

Table 6.2 Ratios of  $\Delta\varepsilon_1/\Delta\varepsilon_3$  during isotropic consolidation

| Test No. | $\alpha$<br>( $^\circ$ ) | $b$ | $p'_0$<br>(kPa) | End of consolidation   |                        |                             |                            | Average<br>$\Delta\varepsilon_v/\Delta\varepsilon_h^*$ |
|----------|--------------------------|-----|-----------------|------------------------|------------------------|-----------------------------|----------------------------|--|
|          |                          |     |                 | $\varepsilon_z$<br>(%) | $\varepsilon_r$<br>(%) | $\varepsilon_\theta$<br>(%) | $\gamma_{\theta z}$<br>(%) |  |
| A00B00   | 0                        | 0   | 105             | -                      | -                      | -                           | -                          | -  |
| A00B05   | 0                        | 0.5 | 100             | 0.27                   | 0.23                   | 0.12                        | -0.09                      | 1.76   |
| A00B10   | 0                        | 1   | 100             | 0.26                   | 0.13                   | 0.06                        | -0.09                      | 4.29   |
| A45B00   | 45                       | 0   | 85              | 1.34                   | 1.17                   | 0.64                        | 0.07                       | 1.88   |
| A45B05   | 45                       | 0.5 | 75              | -                      | -                      | -                           | -                          | -  |
| A45B10   | 45                       | 1   | 90              | 1.71                   | 1.70                   | 1.01                        | -0.07                      | 1.71   |
| A90B00   | 90                       | 0   | 85              | 1.53                   | 0.08                   | 0.44                        | -0.07                      | 6.00   |
| A90B05   | 90                       | 0.5 | 65              | 2.53                   | 0.81                   | 0.86                        | 0                          | 1.55   |
| A90B10   | 90                       | 1   | 45              | 1.85                   | 0.39                   | 1.01                        | -0.05                      | 2.86   |

Note:  $\Delta\varepsilon_v/\Delta\varepsilon_h^* = \Delta\varepsilon_z / (\Delta\varepsilon_r + \Delta\varepsilon_\theta) / 2$

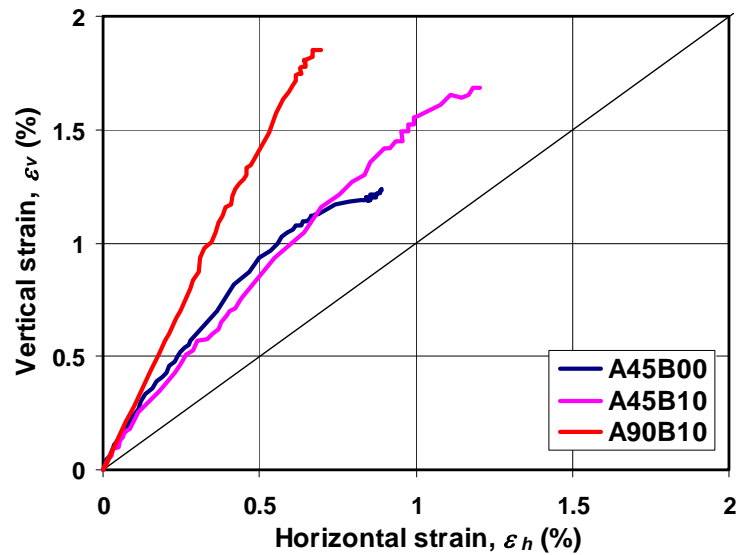


Figure 6.2 Anisotropic deformations during isotropic consolidation



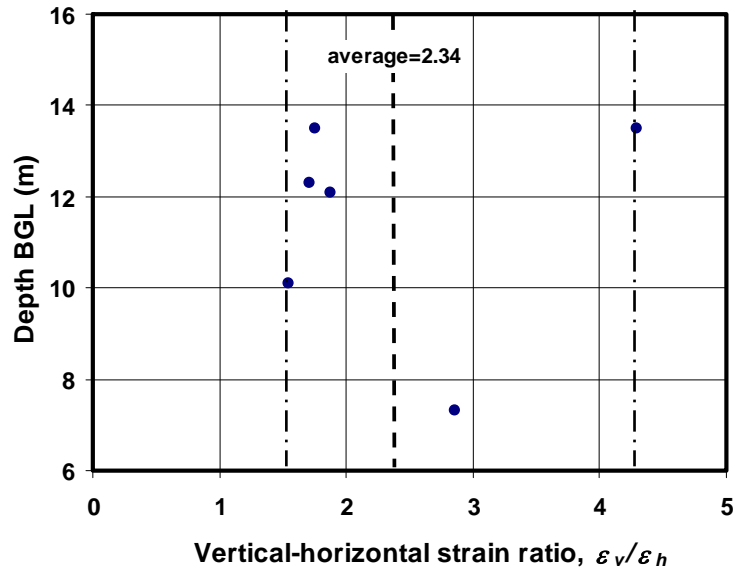


Figure 6.3 Ratios of  $\Delta\varepsilon_v/\Delta\varepsilon_h$  with depth during isotropic consolidation

### 6.3 Stress-strain and pore pressure behavior

#### 6.3.1 Effects of $\alpha$ on stress-strain and pore pressure behavior

The main results of stress-strain characteristics from a series of tests with different inclinations of  $\alpha$  are presented and discussed in this section. The deviator stress and strain invariants in these experimental results are calculated using the general invariant expressions as shown in Eqs. (6.1) & (6.2).

$$q = \sqrt{3J_2} = \frac{1}{\sqrt{2}} \sqrt{(\sigma'_1 - \sigma'_2)^2 + (\sigma'_2 - \sigma'_3)^2 + (\sigma'_3 - \sigma'_1)^2} \quad (6.1)$$

$$\varepsilon_q = \frac{\sqrt{2}}{3} \sqrt{[(\varepsilon_1 - \varepsilon_2)^2 + (\varepsilon_2 - \varepsilon_3)^2 + (\varepsilon_3 - \varepsilon_1)^2]} \quad (6.2)$$

Figure 6.4 shows the stress-strain relationship between  $q/p_o'$  versus  $\varepsilon_q$  (Figure 6.4(a)), effective stress paths ( $q/p_o'$ -  $p'/p_o'$  space) (Figure 6.4(b)) and normalized excess pore water pressure ( $\Delta u/p_o'$ ) versus  $\varepsilon_q$  (Figure 6.4(c)) of a test series in which

the  $b$  parameter was fixed at 0, 0.5 and 1, whereas the direction of the major principal stress was varied from  $\alpha=0^\circ$  to  $90^\circ$ .

The results show the influence of the direction of major principal stress on the undrained behavior of Bangkok Clay. At any  $b$ , Bangkok Clay tends to exhibit a softer response when the major principal stress becomes more horizontal ( $\alpha$  increases) with more pronounced effects when  $\alpha$  increases from  $0^\circ$  to  $45^\circ$ . The effects of  $\alpha$  on stress-strain curves found in this study are similar to TSHC data reported by Zdravkovic & Jardine (2000) on quartzitic silt and Kumruzzaman & Yin (2010) on sandy silt.

The effective stress paths shown in Figure 6.4(b) for constant  $b$  tests do not show clearly effect of  $\alpha$  on the stress path characteristic. The stress path at  $\alpha=0^\circ$  (A00B00) shows dilative behavior after reaching maximum excess pore pressure which makes the stress path turns right with increasing deviatoric stress. The dilation behavior was also observed in  $CK_0UC$  results performed on Bangkok Clay at the depth of 18.5 m studied by Shibuya et al. (2001). The tests correspond to  $\alpha = 0^\circ$  and  $b = 0$ . The specimens used in both tests were conducted on stiff clay layer.

At any  $b$ , the curves of excess pore water pressure tends to exhibit a more contractive response when major principal stress becomes more horizontal ( $\alpha$  increases); however, the effect is more pronounced when  $\alpha$  increases from  $0^\circ$  to  $45^\circ$ . The effects of  $\alpha$  on excess pore pressure found in this study are similar to TSHC data reported by Kumruzzaman & Yin (2010) on sandy silt, and TTX data reported by Kuwano & Bhattarai (1989) on undisturbed Bangkok Clay and Prashant & Penumadu (2005) on reconstituted kaolin.

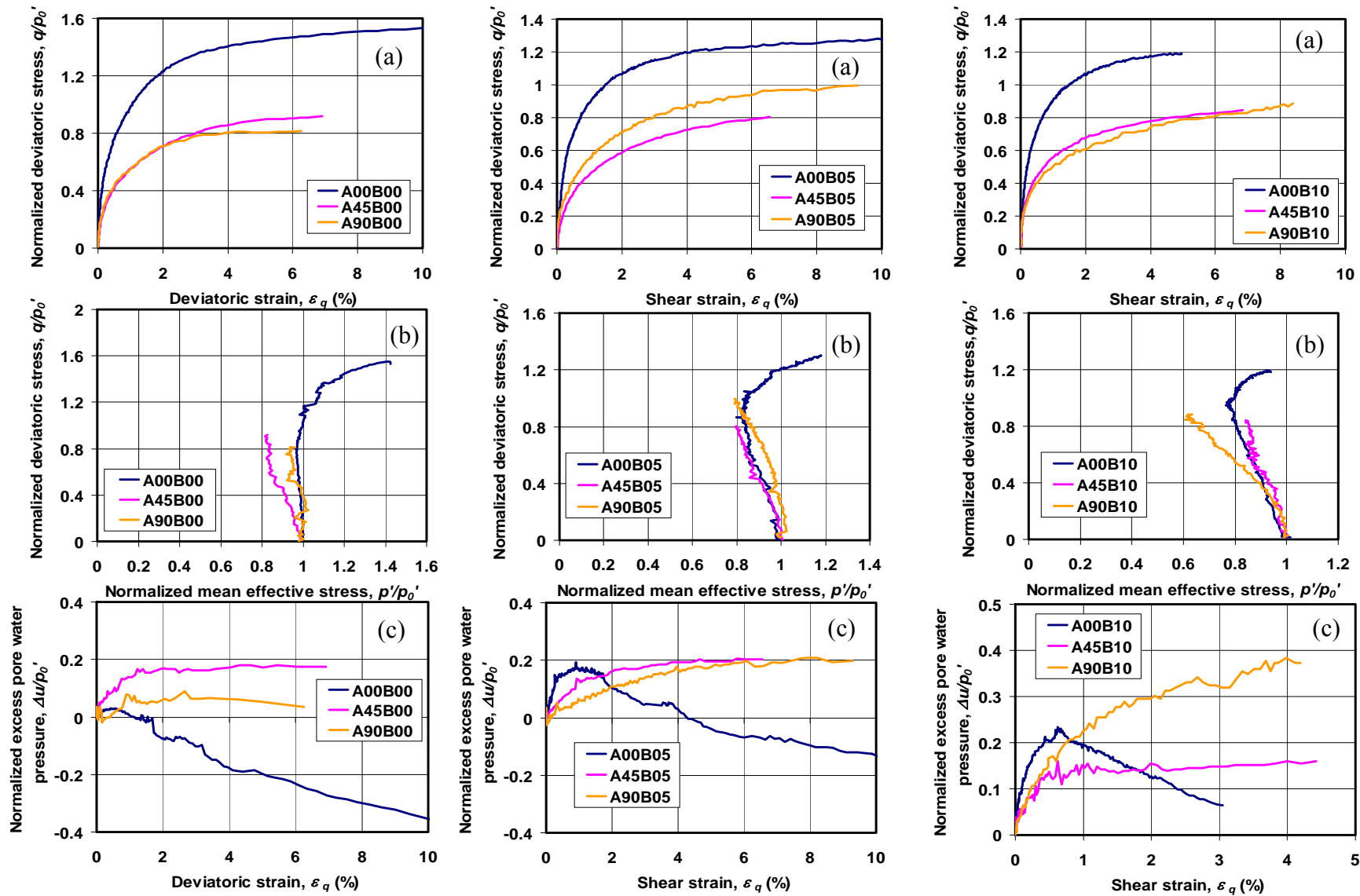


Figure 6.4 Curves of (a) stress-strain relationship (b) effective stress path (c) normalized excess pore water pressure for  $\alpha=0^\circ$ ,  $45^\circ$  and  $90^\circ$

### 6.3.2 Effects of $b$ on stress-strain and pore pressure behavior

Figure 6.5 shows the stress-strain relationship between  $q/p_o'$  versus  $\varepsilon_q$  (Figure 6.5(a)), effective stress paths ( $q/p_o'$ -  $p'/p_o'$  space) (Figure 6.5(b)) and normalized excess pore water pressure ( $\Delta u/p_o'$ ) versus  $\varepsilon_q$  (Figure 6.5(c)) of a test series in which the direction of the major principal stress was fixed at  $\alpha=0^\circ$  and the values of  $b$  parameter were varied from 0 to 1.

From Figure 6.5(a), The value of  $b$  has relatively less effects on the stress-strain curves. The effects of  $b$  on stress-strain curves found in this study are similar to TTX data reported by Prashant & Penumadu (2005, 2007) on reconstituted kaolin clay.

The normalized undrained effective stress path for the tests sheared with constant  $\alpha$  values and  $b$  parameters were varied at 0, 0.5 and 1 is summarized in Figure 6.5(b). The results clearly exhibit that the stress path has tendency to move to the left due to the generation of more excess pore pressure except for the case of  $\alpha=45^\circ$ . Moreover, it is noted that the results showed the dilation behavior when  $\alpha$  values were fixed at  $0^\circ$ . The tests of  $\alpha=0$  and  $b=0, 0.5$  and 1 showed a nearly vertical path with almost constant mean effective stress,  $p'/p_o' \approx 1$  until  $q/p_o'=0.4, 0.9$  and 0.95, respectively. Then the curve of effective stress path tended to the right to show the dilation behavior. The effects of  $b$  on stress path found in this study are similar to TSHC data reported by Kumruzzaman & Yin (2010) on sandy silt.

Bangkok Clay also becomes more contractive as the value of  $b$  increases (see Figure 6.5(c)) but the effects of  $b$  cannot be observed at  $\alpha=45^\circ$ . The effects of  $b$  on excess pore pressure found in this study are similar to TSHC data reported by Zdravkovic & Jardine (2000) on quartzitic silt and Kumruzzaman & Yin (2010) on sandy silt, and TTX data reported by Prashant & Penumadu (2004, 2007) on reconstituted kaolin clay.

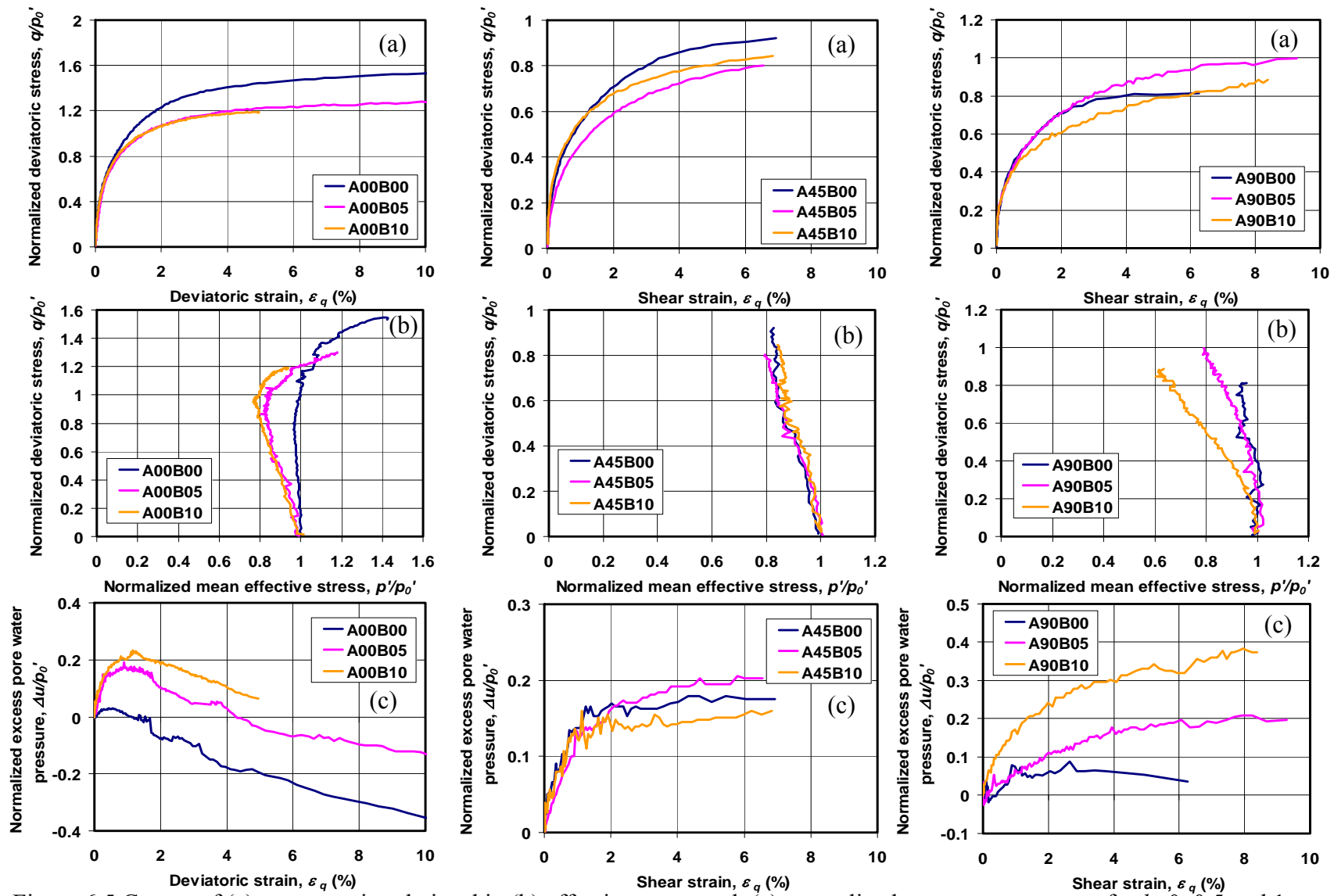


Figure 6.5 Curves of (a) stress-strain relationship (b) effective stress path (c) normalized pore water pressure for  $b=0, 0.5$  and  $1$

## 6.4 Strength behavior

### 6.4.1 Undrained shear strength

#### 6.4.1.1 Effects of $\alpha$ on undrained shear strength

The effects of  $\alpha$  on normalized peak undrained shear strength ( $s_u/p_o'$ ) (where  $s_u=q_{max}/2$ ) at different  $b$  values are summarized in Figure 6.6 and Table 6.3. The result shows that as major principal stress becomes more horizontal ( $\alpha$  increases), Bangkok Clay has lower  $s_u/p_o'$ , however, the effect is less when  $\alpha$  changes from  $45^\circ$  to  $90^\circ$ . The values of  $s_u/p_o'$  from TX seem to be less affected by  $\alpha$  (more isotropic). The CK<sub>0</sub>UC data of stiff Bangkok Clay reported by Shibuya et al. (2001) and CK<sub>0</sub>UC/E data of medium Bangkok Clay reported by Seah & Lai (2003) also show relatively consistent results with this study.

Comparisons of effects of  $\alpha$  on undrained shear strength of Bangkok Clay with other soils are summarized in Figure 6.7. The variation of  $s_u/p_o'$  with an slightly increase in the direction of  $\alpha$  found for Bangkok Clay  $b=0.5$  series shows nearly similar from that found in London Clay which were carried on hollow cylinder apparatus in order to investigate the anisotropic behavior reported by Nishimura et al. (2007). The variation in  $s_u/p_o'$  tend to decrease when  $\alpha$  increases from  $0^\circ$  to  $45^\circ$ , then increase when  $\alpha$  increases from  $45^\circ$  to  $90^\circ$ . However, the lower rate of increase of  $s_u/p_o'$  values obtained from Bangkok Clay samples is observed, when comparing with the rate obtained from London Clay. When  $\alpha$  increases from  $0^\circ$  to  $45^\circ$ , the decrease rate of the values of  $s_u/p_o'$  obtained from this study is similar to decomposed granite when the direction of  $\alpha$  increases from  $0^\circ$  to  $45^\circ$  reported by Kumruzzaman and Yin (2010).

The results obtained in this experiment are also compared with the anisotropy of other  $K_0$ -consolidated materials investigated in the Imperial College hollow cylinder apparatus: Ham River sand (HRS) (Porovic and Jardine, 1994); clay-silt-sand (KSS) and clay-sand (HK) mixtures (Menkiti, 1995; Jardine and Menkiti, 1999); and a dense silt (HPF4) (Zdravkovic and Jardine, 1997, 2000). The values of undrained

shear strength are normalized by initial mean effective stress at a range of  $\alpha$  values, while keeping  $b$  parameters fixed at 0.5 in order to achieve near plain strain condition. It is also found that soils become weaker when tested at higher values of  $\alpha$ . The reductions of normalized undrained shear strength of Bangkok Clay are most nearly similar to clay-silt-sand (KSS) mixtures which has the highest percentage of clay material (50% of kaolin – 25% of silt – 25% of sand).

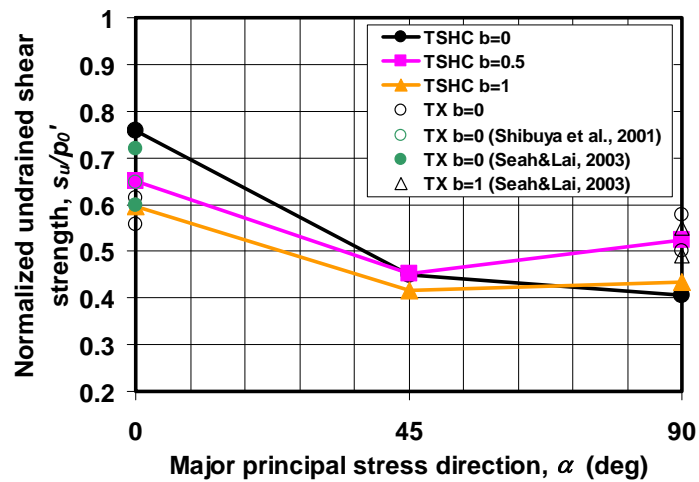


Figure 6.6 Effects of  $\alpha$  on normalized undrained shear strength of Bangkok Clay

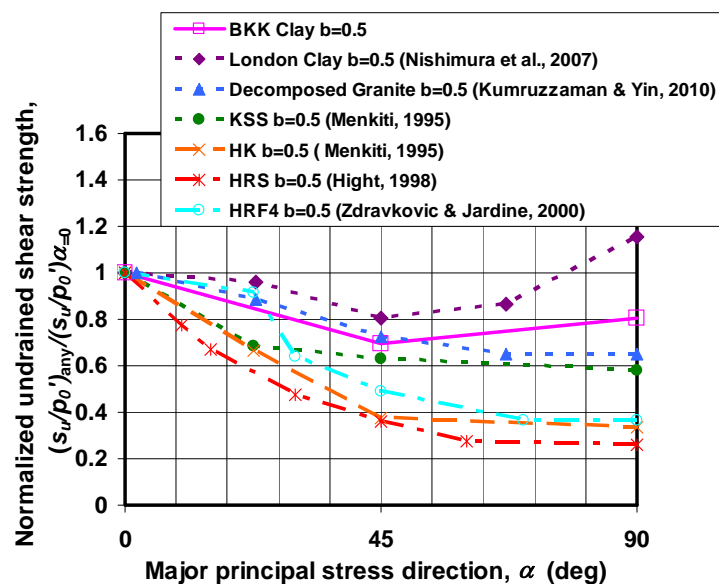


Figure 6.7 Effects of  $\alpha$  on normalized peak undrained shear strength

Table 6.3 Values of  $s_u/p_o'$  at varies  $b$  and  $\alpha$ 

| $b \backslash \alpha$ | $0^\circ$ | $45^\circ$ | $90^\circ$ |
|-----------------------|-----------|------------|------------|
| <b>0</b>              | 0.76*     | 0.45       | 0.41       |
| <b>0.5</b>            | 0.65*     | 0.45       | 0.52*      |
| <b>1</b>              | 0.60      | 0.42       | 0.43*      |

Remark; \*  $s_u/p_o'$  is derived at  $\varepsilon_q=8.5\%$ .

#### 6.4.1.2 Effects of $b$ on undrained shear strength

The effects of magnitude of  $b$  on normalized peak undrained shear strength ( $s_u/p_o'$ ) at different  $\alpha$  values are summarized in Figure 6.8 and in Table 6.3. The result shows that the tests fixed  $\alpha$  at  $0^\circ$ , the values of  $s_u/p_o'$  tend to decrease when  $b$  parameter increases. The decrease values of  $s_u/p_o'$  series in which  $\alpha$  was fixed at  $0^\circ$  drops by 21% when  $b$  parameter varies from 0 to 1. The main observations on  $s_u/p_o'$  of  $\alpha=45^\circ$  and  $90^\circ$  series show a different results from the series of  $\alpha=0^\circ$ . Variation of  $b$  has relatively no effect because the values of  $s_u/p_o'$  not change when  $b$  increases. The CK<sub>o</sub>UC data of stiff Bangkok Clay reported by Shibuya et al. (2001) and CK<sub>o</sub>UC/E data of medium Bangkok Clay reported by Seah & Lai (2003) also show relatively consistent results with this study.

Figure 6.9 compares the effects of  $b$  parameter on Bangkok Clay compared with other soils. The trend of a decrease in the values of  $s_u/p_o'$  with an increase in  $b$  parameter found from Bangkok Clay series of  $\alpha=45^\circ$  is slightly different from that found in decomposed granite reported by Kumruzzaman and Yin (2010). The completely decomposed granite were carried out using hollow cylinder apparatus maintaining a fixed principal stress directions ( $\alpha=0^\circ, 23^\circ, 45^\circ, 67^\circ$  and  $90^\circ$ ) together a fixed value of  $b=0.5$ . The values of  $s_u/p_o'$  tend to vary a little when increasing in  $\alpha$  from  $0^\circ$  to  $90^\circ$ , whereas they tend to be constant in the present data.



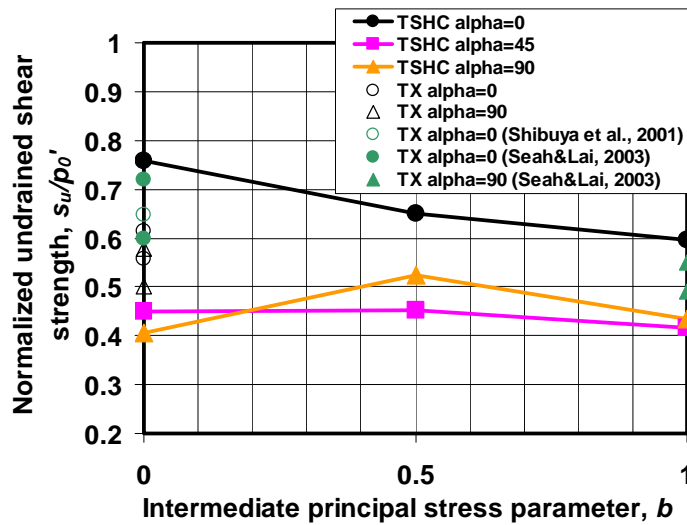


Figure 6.8 Effects of  $b$  on normalized peak undrained shear strength of Bangkok Clay

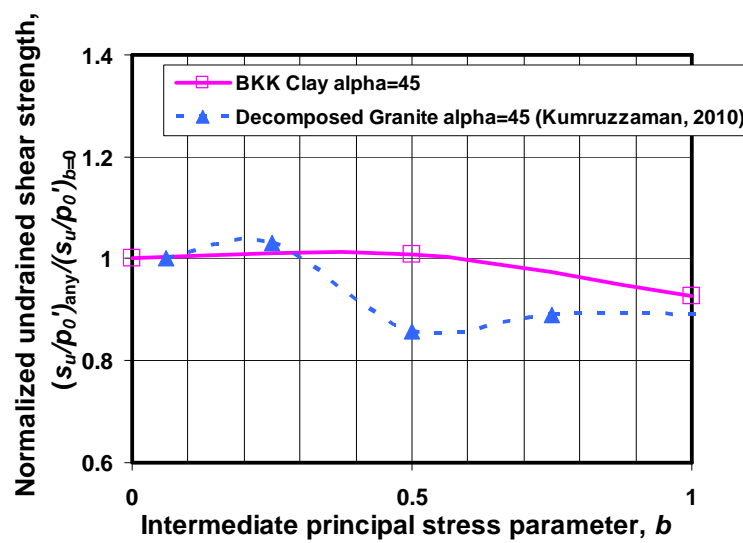


Figure 6.9 Effects of  $b$  on normalized peak undrained shear strength

## 6.4.2 Friction angle

### 6.4.2.1 Effects of $\alpha$ on friction angle

From Mohr-Coulomb failure criterion, the effective friction angle is calculated from the maximum mobilized values of ratios of effective principal stresses from each

test. The equation is formed by  $\phi' = \sin^{-1} \left( \frac{\sigma'_1 - \sigma'_3}{\sigma'_1 + \sigma'_3} \right)$ .

The effects of  $\alpha$  on measured friction angle  $\phi'_{max}$  at different  $b$  values are summarized in Figure 6.10 and Table 6.4. For given of  $b$  fixed at 0, the values of  $\phi'_{max}$  decrease when  $\alpha$  increases from  $0^\circ$  to  $90^\circ$ . The lower rate of the decrease of  $\phi'_{max}$  values is observed when  $\alpha$  increases from  $0^\circ$  to  $45^\circ$ , compared with  $\alpha$  increases from  $45^\circ$  to  $90^\circ$ . The  $\phi'_{max}$  values drop by 10% and 20% when the value  $\alpha$  varies from  $0^\circ$  to  $45^\circ$  and  $45^\circ$  to  $90^\circ$ , respectively.

However, the results of variation of  $\phi'_{max}$  affected by  $\alpha$  when  $b$  were fixed at 0.5 and 1 shows the different trends when compared with the series of  $b=0$ . The curves represent that the tests which the  $b$  parameters were fixed at  $b=0.5$  and 1, the  $\phi'_{max}$  values tend to decrease when  $\alpha$  increases up to  $45^\circ$ . Then the values of  $\phi'_{max}$  veer to increase when  $\alpha$  increases from  $45^\circ$  to  $90^\circ$ . The decrease values of  $\phi'_{max}$  series in which  $b$  parameter was fixed at 1 exhibit a higher rate than the values of  $\phi'_{max}$  series of  $b$  parameter was fixed at 0.5. The lowest of  $\phi'_{max}$  value of Bangkok Clay is observed in the test of  $\alpha=45^\circ$  and  $b=1$ . The results of TX from this study, Shibuya et al. (2001), and Seah & Lai (2003) are consistent with TSHC data but with more isotropic characteristics.

Figure 6.11 compares the effects of  $\alpha$  on  $\phi'_{max}$  of Bangkok Clay compared with other soils. The trend of decrease of  $\phi'_{max}$  values with an increase in  $\alpha$  from 0 to  $45^\circ$  observed from Bangkok Clay at  $b=0.5$  series shows a similar trend from that observed in completely decomposed granite, London Clay and  $K_0$  consolidated silt reported by Kumruzzaman and Yin (2010); Nishimura et al. (2007) and Zdravkovic and Jardine (2000), respectively. The decrease rate in the values of  $\phi'_{max}$  is around 11% which is similar to the rate obtained from decomposed granite and London Clay but it is slightly lower than those obtained from  $K_0$  consolidated silt.

After the direction of  $\alpha$  changes from  $45^\circ$  to  $90^\circ$ , however they show the different trend when compared with decomposed granite. Because the results of  $\phi'_{max}$  values on completely decomposed granite, still exhibit decrease whereas the  $\phi'_{max}$  values on Bangkok Clay show the increase trend when  $\alpha$  increases from  $45^\circ$  to  $90^\circ$ .

The results of  $\phi'_{max}$  on London Clay and  $K_0$  consolidated silt represent a lower increase rate when  $\alpha$  increases from  $45^\circ$  to  $90^\circ$ .

The results obtained in this experiment are also compared with the anisotropy of other  $K_0$ -consolidated materials investigated by the Imperial College hollow cylinder apparatus: Ham River sand (HRS) (Hight, 1998); a mixture of HRS and 10% of kaolin (HK) (Menkiti, 1995; Jardine and Menkiti, 1999); a artificial clay mixture of 50% of kaolin with 25% of silt and 25% of sand (KSS) (Menkiti, 1995; Jardine and Menkiti, 1999) and a dense silt (HPF4) (Zdravkovic and Jardine, 1997, 2000). The reduction rates of  $\phi'_{max}$  of Bangkok Clay are slightly lower than those obtained from HRS and HRF4 when  $\alpha$  changed from  $0^\circ$  to  $45^\circ$ . However, the results of  $\phi'_{max}$  of Bangkok Clay show the slightly higher reduction rate when comparing with those obtained from HK and KKS.

Table 6.4 Values of  $\phi'_{max}$  at varies  $\alpha$  and  $b$

| $b \backslash \alpha$ | $0^\circ$ | $45^\circ$ | $90^\circ$ |
|-----------------------|-----------|------------|------------|
| <b>0</b>              | 30.4      | 27.3       | 21.8       |
| <b>0.5</b>            | 45        | 40.2       | 45.9*      |
| <b>1</b>              | 59        | 34.6       | 45**       |

Remarks; \*  $\phi'_{max}$  is derived at  $\varepsilon_q=8.5\%$ .

\*\*  $\phi'_{max}$  is derived at  $\varepsilon_q=6\%$ .

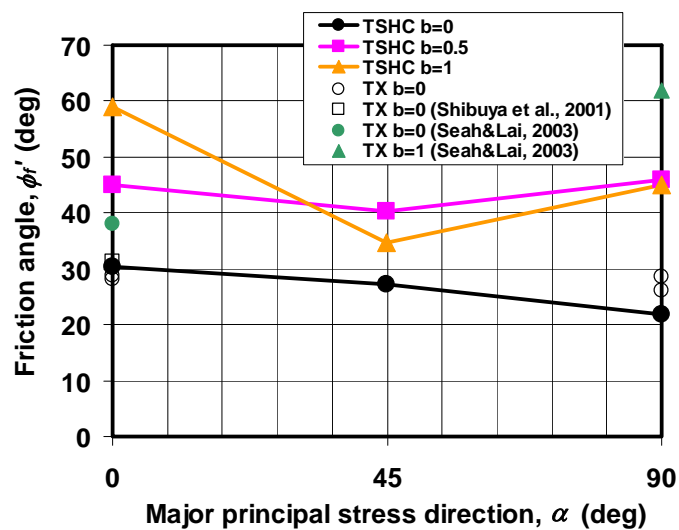


Figure 6.10 Effects of  $\alpha$  on friction angle of Bangkok Clay

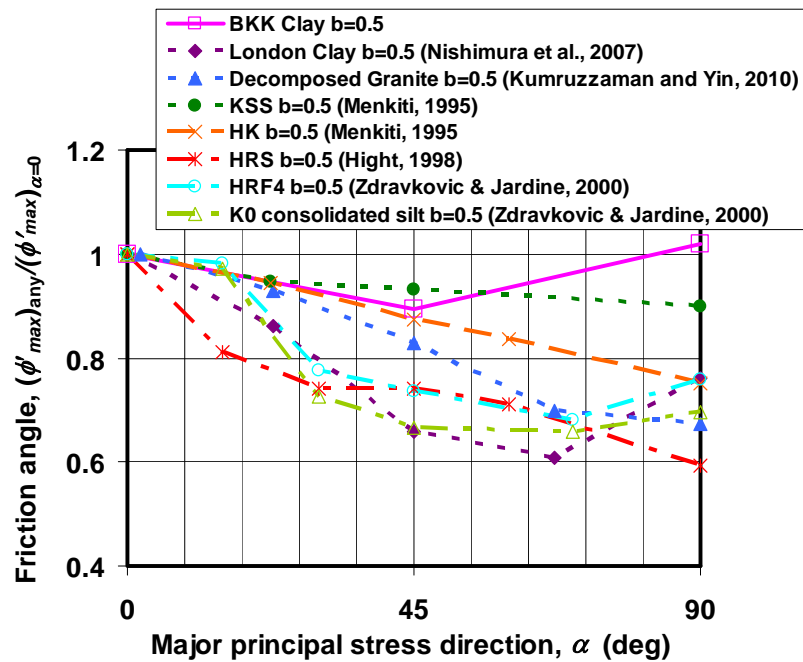


Figure 6.11 Effects of  $\alpha$  on friction angle

#### 6.4.2.2 Effects of $b$ on friction angle

The effects  $b$  on the effective friction angle at different  $\alpha$  values are summarized in Figure 6.12 and Table 6.4. The results show that  $\phi'_{max}$  increases with  $b$ , especially when  $b$  changes from 0 to 0.5 comparing with 0.5 to 1.0. The increase of  $\phi'_{max}$  series in which  $\alpha=90^\circ$  exhibits a higher rate than the  $\phi'_{max}$  series of  $\alpha=0^\circ$  and  $45^\circ$ . The values of  $\phi'_{max}$  increase by factors of 1.5, 1.5 and 2.1 when  $b$  varied from 0 to 0.5 at  $\alpha=0^\circ$ ,  $45^\circ$  and  $90^\circ$ , respectively. When  $b$  parameter changes from 0.5 to 1, the values of  $\phi'_{max}$  still tend to increase in the series of  $\alpha=0^\circ$ , whereas the values of  $\phi'_{max}$  tend to decrease in the series of  $\alpha=45^\circ$  and  $90^\circ$ . Increasing rate of the test  $\alpha=0^\circ$  is 31%. Decreasing rate of the tests  $\alpha=45^\circ$  and  $90^\circ$  are 14% and 2%, respectively. The results of TX from this study, Shibuya et al. (2001), and Seah & Lai (2003) are consistent with TSHC data but with more isotropic characteristics.

Comparisons of effects of  $b$  on friction angle of Bangkok Clay with other soils are summarized in Figure 6.13. The trend of an increase in  $\phi'_{max}$  obtained from Bangkok Clay when  $\alpha=45^\circ$  series is similar to those obtained in decomposed granite when the  $b$  parameter increases from 0 to 1 reported by Kumruzzaman and Yin

(2010). The completely decomposed granite were carried out using hollow cylinder apparatus maintaining a fixed principal stress directions ( $\alpha=45^\circ$ ) together a varied value of intermediate principal stress parameter ( $b=0, 0.25, 0.5, 0.75$  and  $1$ ). Almost similar rate of increasing in the values of  $\phi'_{max}$  can be observed in Figure 6.13.

The result of  $\phi'_{max}$  obtained from Bangkok Clay when  $\alpha=0^\circ$  is compared with the result obtained from Kaolin Clay which was carried out using true triaxial test reported by Prashant and Penumadu (2005). The intermediate principal stress parameters were varied at  $b=0, 0.25, 0.5, 0.75$  and  $1$  when the direction of the major principal stress was fixed at  $\alpha=0^\circ$ . When  $b$  parameter varies from  $0$  to  $0.5$ , the values of  $\phi'_{max}$  of Bangkok Clay increase with a bit higher rate than those obtained in Kaolin Clay. However, the result shows the difference trend that the values of  $\phi'_{max}$  observed from Bangkok Clay still tend to increase when the values of  $b$  change from  $0.5$  to whereas the  $\phi'_{max}$  results of Kaolin Clay tend to be constant.

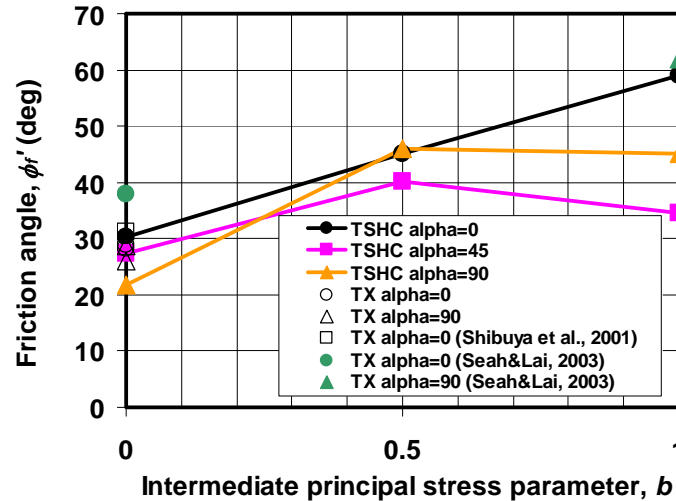


Figure 6.12 Effects of  $b$  on friction angle of Bangkok Clay

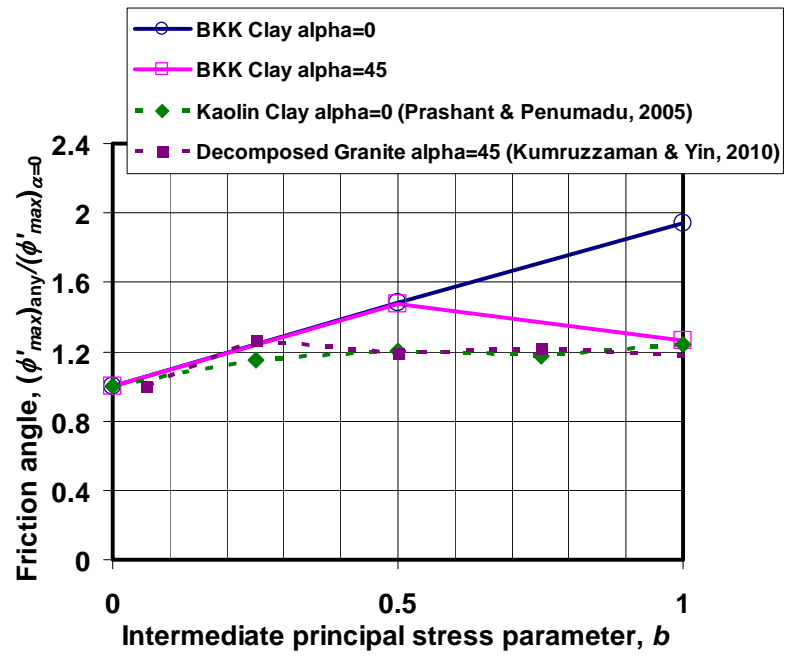


Figure 6.13 Effects of  $b$  on friction angle

### 6.4.3 Excess pore water pressure

#### 6.4.3.1 Effects of $\alpha$ on excess pore water pressure

The effects of  $\alpha$  on excess pore water pressure at different  $b$  values are discussed in this section. Table 6.5 and Figure 6.14 show results of normalized ultimate excess pore water pressure ( $\Delta u_f/p_0'$ ) when the direction of  $\alpha$  varies from  $0^\circ$  to  $90^\circ$ . As major principal stress becomes more horizontal ( $\alpha$  increases),  $\Delta u_f/p_0'$  increases; however, this effect is less when  $\alpha$  changes from  $45^\circ$  to  $90^\circ$ . Increasing excess pore water pressure with increasing in  $\alpha$  is observed in many published researches. (e.g. Nishimura et al., 2007 and Kumruzzaman and Yin, 2010).

#### 6.4.3.2 Effects of $b$ on excess pore water pressure

The effects of  $b$  on excess pore water pressure at different  $\alpha$  values are summarized Table 6.5 and Figure 6.15. The results show that as the value of  $b$  increases,  $\Delta u_f/p_0'$  increases but the effects of  $b$  cannot be observed at  $\alpha=45^\circ$ . The series of  $\alpha=45^\circ$  show almost constant excess pore water pressure.

Table 6.5 Values of  $u_f/p_0'$  at varies  $\alpha$  and  $b$

| $b \backslash \alpha$ | $0^\circ$ | $45^\circ$ | $90^\circ$ |
|-----------------------|-----------|------------|------------|
| <b>0</b>              | -0.24     | 0.18       | 0.04       |
| <b>0.5</b>            | -0.07     | 0.20       | 0.20       |
| <b>1</b>              | 0.02      | 0.16       | 0.36       |

**Remark;**  $u_f/p_0'$  is taken at  $\varepsilon_q=8.5\%$ .

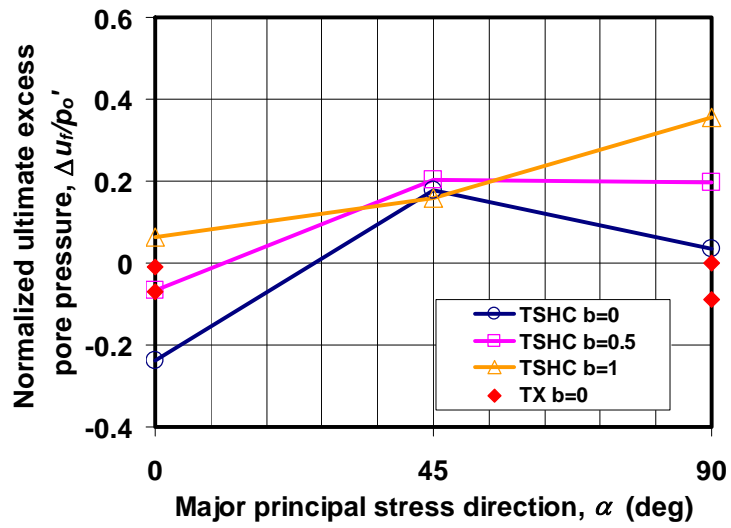


Figure 6.14 Effects of  $\alpha$  on excess pore water pressure

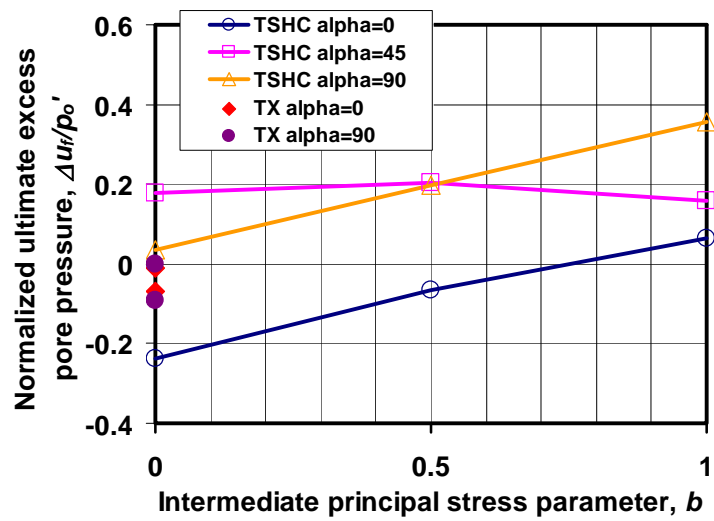


Figure 6.15 Effects of  $b$  on excess pore water pressure



## 6.5 Stiffness characteristics

In the following sections, effects of  $\alpha$  and  $b$  on stiffness degradation curves are presented and discussed. The octahedral shear stiffness ( $G_{oct}$ ) is calculated as:

$$G_{oct} = \frac{1}{3} \frac{q}{\varepsilon_q} \quad (6.3)$$

where  $\Delta q$  and  $\Delta \varepsilon_q$  are inclinations of deviatoric stress and strain invariant in general stress space.

### 6.5.1 Effects of $\alpha$ on stiffness characteristics

Figure 6.16 shows the normalized secant shear stiffness degradation curves of a test series in which  $b$  was fixed at 0, 0.5 and 1, whereas  $\alpha$  was varied from 0° to 90°. The stiffness can be measured to the strain as small as 0.01%. The results show that  $G_{oct}$  gradually decreases as the  $\varepsilon_q$  increases due to the non-linear nature of soil. The octahedral shear response is stiffest along the direction of  $\alpha=0^\circ$  path. Moreover, as major principal stress becomes more horizontal ( $\alpha$  increases), Bangkok Clay becomes softer but this is not so obvious when  $b=0.5$ . The octahedral shear moduli tend to decrease obviously with an increase in  $\alpha$  values from 0°.

Figure 6.17 and Table 6.6 shows the effects of the inclination of  $\alpha$  on normalized octahedral shear stiffness ( $G_{oct}/p_0'$ ) at  $\varepsilon_q=0.01\%$  with different  $b$  values. The result exhibits that the values of  $G_{oct(\varepsilon_q=0.01\%)/p_0'}$  show the maximum values in all  $b$  series when  $\alpha=0^\circ$ . Then the shear modulus immediately decreases when  $\alpha$  changes from 0° to 45°. The  $G_{oct(\varepsilon_q=0.01\%)/p_0'}$  values drop by 41%, 19% and 38% in the series of  $b=0, 0.5$  and 1, respectively. The higher rate of decreasing is observed at  $b=0$ . The effects  $\alpha$  are less when  $\alpha$  changes from 45° to 90°. The  $G_{oct(\varepsilon_q=0.01\%)/p_0'}$  values are almost constant.

In order to study the effect of  $\alpha$  on non-linearity of the normalized stiffness degradation curves, ratios of  $G_{oct(\varepsilon_q=0.1\%)/G_{oct(\varepsilon_q=0.01\%)}$  and  $G_{oct(\varepsilon_q=1\%)/G_{oct(\varepsilon_q=0.01%)}$  called non-linearity index in this study are used for considering the non-linearity on

0.01%-0.1% and 0.1%-1% of strain ranges, respectively. In case the non-linearity index is 1, this means the normalized stiffness degradation curves represents linear behavior. As summarized in Table 6.7 and Figure 6.18 and 6.19, the direction of  $\alpha$  has the effect on the non-linearity index in all test series ( $b=0, 0.5$  and  $1$ ). At 0.01%-0.1% and 0.1%-1% of strain ranges, the non-linearity index decreases when  $\alpha$  changed from  $0^\circ$  to  $90^\circ$ . This means the degradation curve exhibit more non-linear behavior when  $\alpha$  changed from  $0^\circ$  to  $90^\circ$ .

Table 6.6 Values of  $G_{oct(\epsilon_q=0.01\%)/p_0'}$  at varies  $\alpha$  and  $b$

| $b \backslash \alpha$ | $0^\circ$ | $45^\circ$ | $90^\circ$ |
|-----------------------|-----------|------------|------------|
| <b>0</b>              | 255       | 150        | 150        |
| <b>0.5</b>            | 185       | 150        | 125        |
| <b>1</b>              | 200       | 125        | 150        |

Table 6.7 Values of non-linearity index of stiffness degradation curve

| Test No. | $\alpha$<br>( $^\circ$ ) | $b$ | Non-linearity index                                   |   |
|----------|--------------------------|-----|---|---|
|          |                          |     | $G_{oct(\epsilon_q=0.1\%)/G_{oct(\epsilon_q=0.01\%)}$ | $G_{oct(\epsilon_q=1\%)/G_{oct(\epsilon_q=0.01\%)}$ |
| A00B00   | 0                        | 0   | 0.46  | 0.12  |
| A00B05   | 0                        | 0.5 | 0.50  | 0.16  |
| A00B10   | 0                        | 1   | 0.55  | 0.15  |
| A45B00   | 45                       | 0   | 0.41  | 0.12  |
| A45B05   | 45                       | 0.5 | 0.42  | 0.13  |
| A45B10   | 45                       | 1   | 0.43  | 0.13  |
| A90B00   | 90                       | 0   | 0.35  | 0.09  |
| A90B05   | 90                       | 0.5 | 0.40  | 0.11  |
| A90B10   | 90                       | 1   | 0.33  | 0.09  |

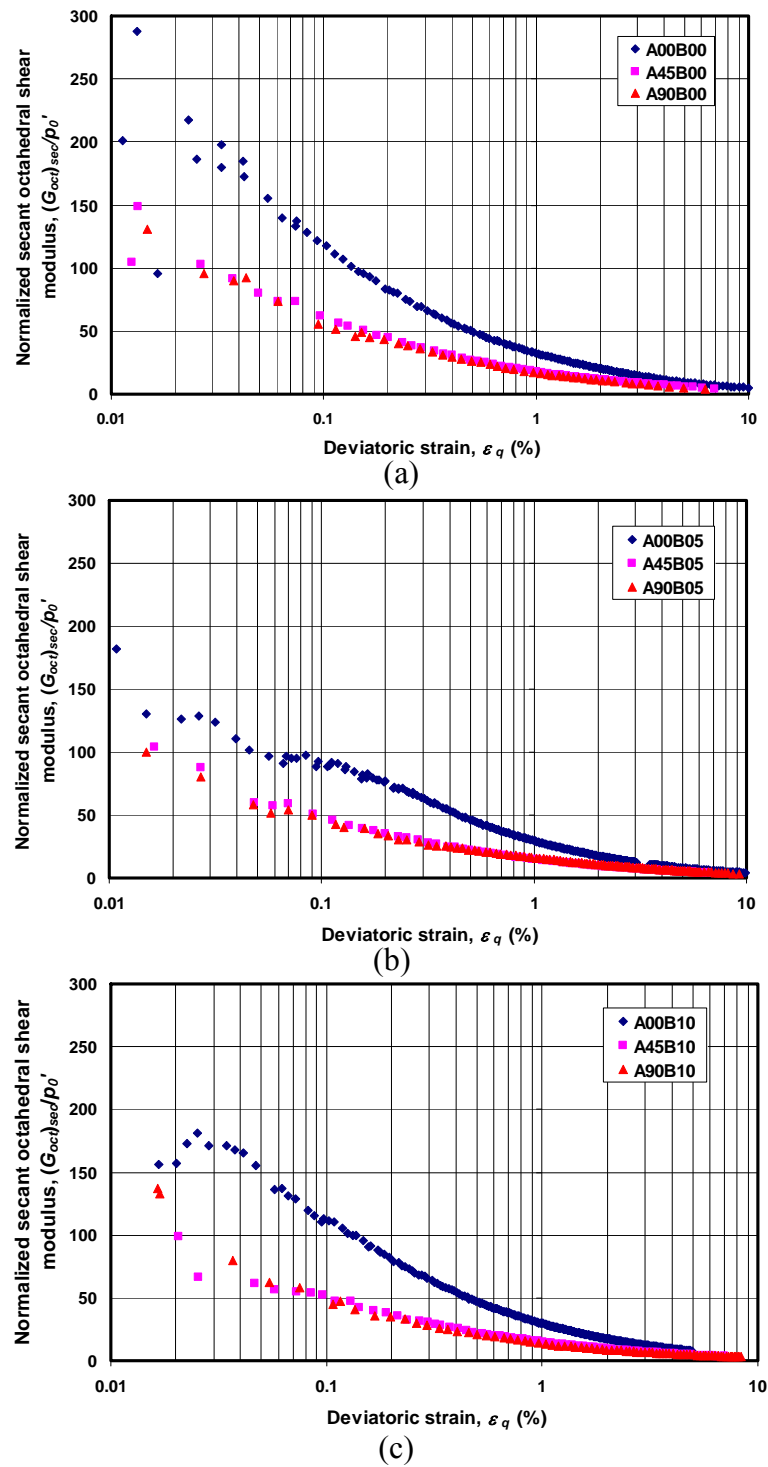


Figure 6.16 Normalized octahedral shear stiffness degradation curves

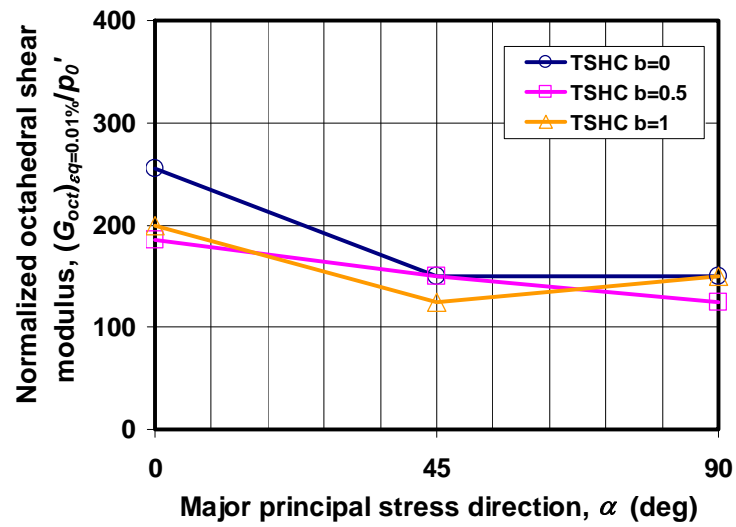


Figure 6.17 Effects of  $\alpha$  on normalized octahedral shear modulus at 0.01% of strain

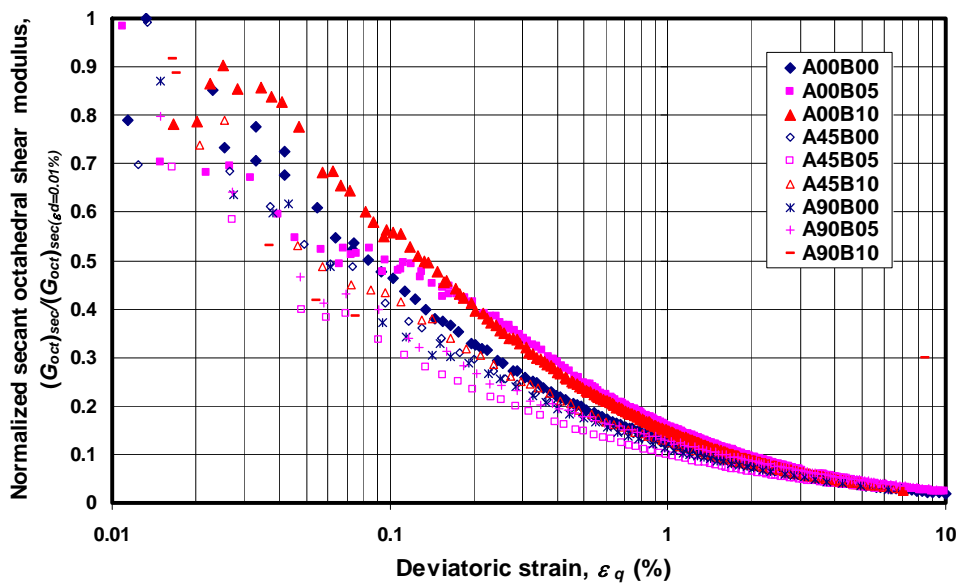


Figure 6.18 Normalized octahedral shear stiffness degradation curves

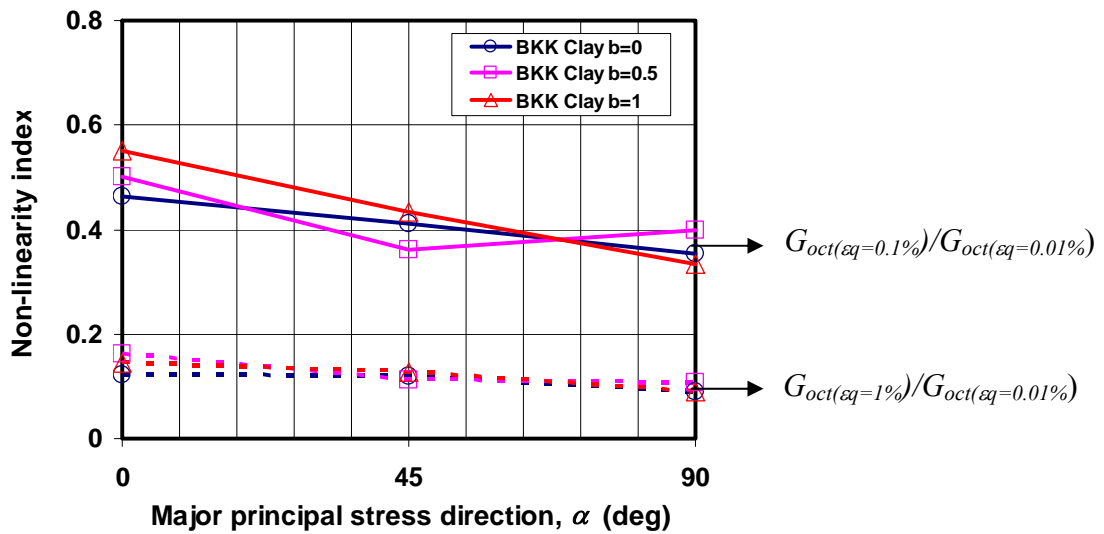


Figure 6.19 Effects of  $\alpha$  on non-linearity index at 0.01% to 0.1% and 0.1% to 1% of strain

### 6.5.2 Effects of $b$ on stiffness characteristics

The normalized secant shear stiffness degradation curves of a test series in which  $\alpha$  was fixed at  $=0^\circ$ ,  $45^\circ$  whereas  $b$  was varied from 0 to 1 are shown in Figure 6.20. The results show that the stiffness characteristic of Bangkok Clay is strongly anisotropic and non-linear. For more clearly observation, the effects of  $b$  parameters on normalized octahedral shear modulus at 0.01% of deviatoric strain at different  $\alpha$  directions are summarized in Figure 6.21 and Table 6.6.  $G_{oct}(\epsilon_q=0.01\%)/p_0'$  seems to decrease with an increase of  $b$  but the effects are rather small. The  $\alpha$  values were fixed at  $0^\circ$  and  $45^\circ$ , changing of  $b$  from 0 to 1 caused  $G_{oct}(\epsilon_q=0.01\%)/p_0'$  values decrease around 21% and 17%, respectively. As the tests which the  $\alpha$  values were fixed at  $90^\circ$ , the  $G_{oct}(\epsilon_q=0.01\%)/p_0'$  values tend to be constant when  $b$  increases from 0 to 1. The small effects of  $b$  on  $G_{oct}$  found in this study are quite different from other researchers who reported that, as  $b$  increases, the stiffness either increases (e.g. Kuwano & Bhatara, 1989; Kirkgard & Lade, 1993; and Prashant & Penumadu, 2004) or decreases (e.g. Zdravkovic & Jardine, 2000).

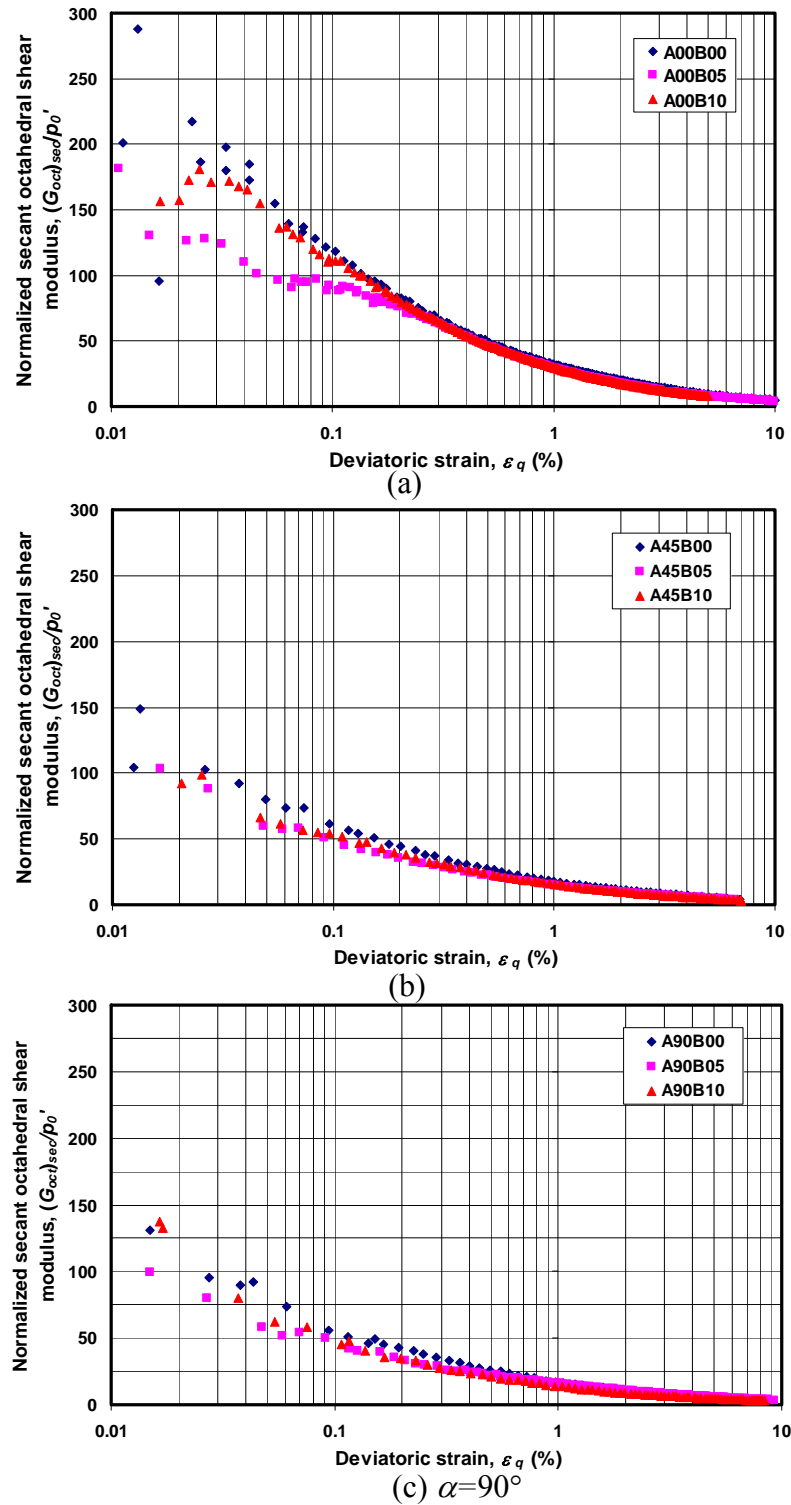


Figure 6.20 Normalized octahedral shear stiffness degradation curve

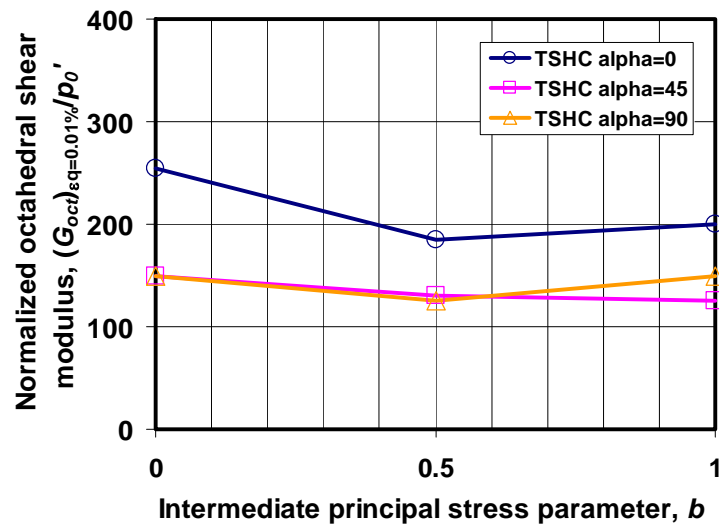


Figure 6.21 Effects of  $b$  on normalized octahedral shear modulus at 0.01% of strain

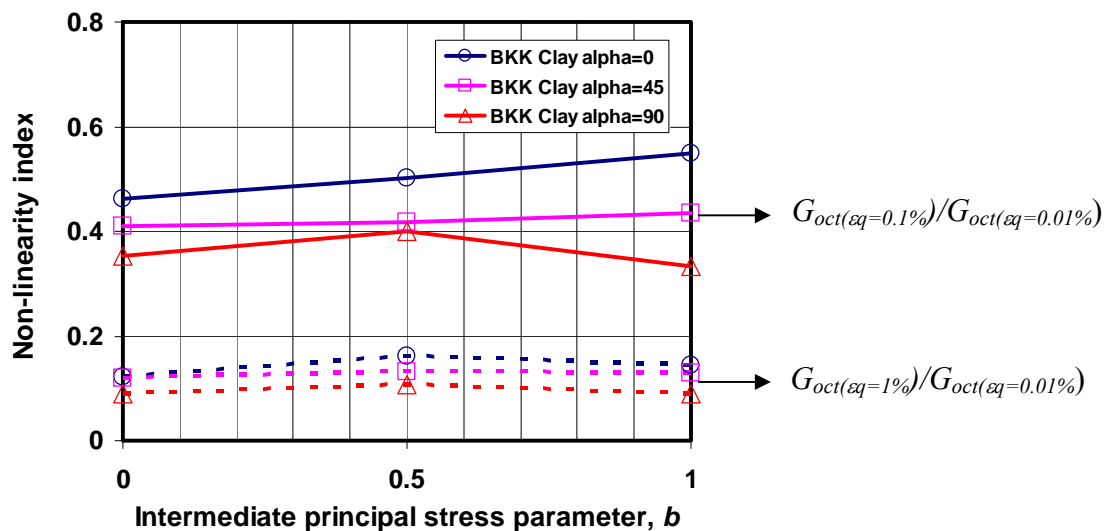


Figure 6.22 Effects of  $\alpha$  on non-linearity index at 0.01% to 0.1% and 0.1% to 1% of strain

Figure 6.18 and 6.22 show the effect of  $b$  parameter on non-linearity of the normalized stiffness degradation curves in 0.01%-0.1% and 0.1%-1% of strain ranges. The result shows almost similar trend in all ranges of strain that the effect of  $b$  parameter has the less influence on the non-linearity index. Changing rates of non-linearity index are small especially at 0.1%-1 of strain ranges. The non-linearity indexes are summarized in Table 6.7.

### 6.5.3 Effects of $\alpha$ on Young's modulus

Figure 6.23 presents normalized secant undrained Young's modulus ( $E_{u,sec}/p_o'$ ) degradation curves calculated from tests with  $b=0$  at  $\alpha=0^\circ$  and  $90^\circ$ . The  $E_{u,sec}$  is calculated as  $\sigma_l/\varepsilon_l$ . It is considered justify for  $\alpha=0^\circ$  and  $90^\circ$  since, in these tests,  $\sigma_l$  and  $\varepsilon_l$  have similar direction. The TSHC results show that, as major principal stress becomes more horizontal ( $\alpha$  increases),  $E$  decreases. The ratio of  $E_{u,90^\circ}/E_{u,0^\circ}$  at  $\varepsilon_q = 0.01\%$  is approximately 0.66. The TX results of comparable conditions are also presented in Figure 6.23. The  $E_{u,sec}$  from TX is larger and the measured strain is smaller due to the use of local strain measurement. The TX results also show similar anisotropic characteristics with the ratio of  $E_{u,90^\circ}/E_{u,0^\circ}$  at  $\varepsilon_q = 0.001\%$  of approximately 0.58.

The small-strain Poisson's ratios ( $\nu$ ) can be directly measured from the Bangkok Clay specimens. Poisson's ratio is derived from the relationships between horizontal and vertical strain. The strain in the vertical direction ( $\varepsilon_v$ ) was measured from axial strain ( $\varepsilon_z$ ), whereas the strain in the horizontal direction ( $\varepsilon_h$ ) was measured the average of radial ( $\varepsilon_r$ ) and circumferential ( $\varepsilon_\theta$ ) strain. Because all tests in this experiment are undrained condition, Poisson's ratios are 0.5.

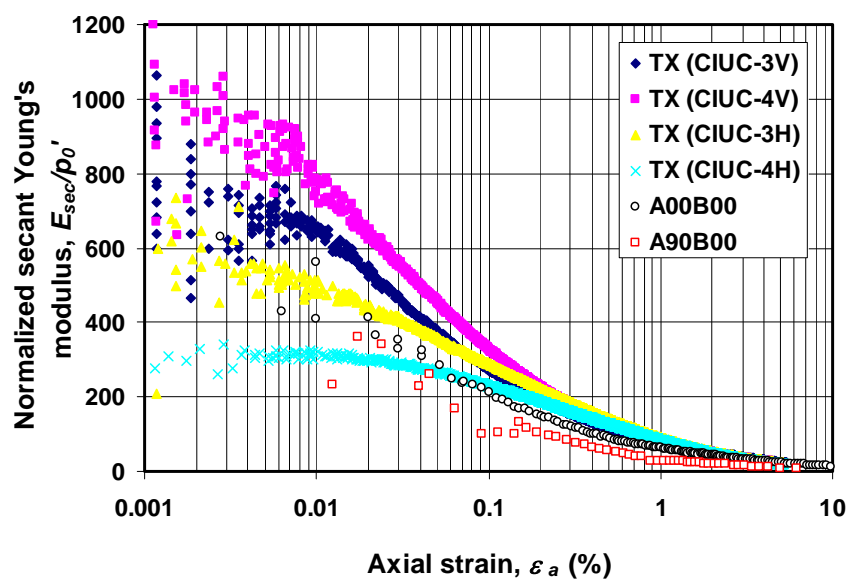


Figure 6.23 Normalized Young's modulus degradation curves



## 6.6 Relationships between individual stress and strain components

### 6.6.1 Cross-coupling terms

Figure 6.24 shows features of strain components of  $\alpha = 45^\circ$  at various  $b$ . It shows that the shear strain component,  $\gamma_{\theta z}$  occurred dominantly during each early stages in all tests. Considering A45B05 test, corresponded to plain strain condition, the small developments of  $\varepsilon_z$ ,  $\varepsilon_\theta$  and  $\varepsilon_r$  are vary small and can be negligible. From the relationship between the strains in this test, it is clearly that the developments of shear stress during the test have no effect on any of the normal strains. This can imply that in case of plane strain and soil has horizontal bedding, the stiffness properties are assumed to be independent with the horizontal plane. Therefore, six of cross-coupling terms in the compliance matrix are taken to be zero. The 16-term compliance matrix is reduced to 10 coefficients as shown in Eq. (6.4).

However, the specimens develop significant axial, radial and circumferential strains from a relatively early stage in case of A45B00 and A45B10 tests. The incremental ratios of  $d\varepsilon_z/d\gamma_{\theta z}$  are 0.18 and -0.12 in A45B00 and A45B10, respectively. Change of the normal stresses during the tests in case of  $\alpha = 45^\circ$  and  $b = 0$  and 1 is one major factor of the development of the normal strains in these tests. Moreover, the developments of shear stress during the tests might have some effects to the normal strains.

$$\begin{pmatrix} \Delta\varepsilon_z \\ \Delta\varepsilon_r \\ \Delta\varepsilon_\theta \\ \Delta\gamma_{z\theta} \end{pmatrix} = \begin{pmatrix} \frac{1}{E_z} & \frac{\nu_{rz}}{E_r} & \frac{\nu_{\theta z}}{E_\theta} & 0 \\ \frac{\nu_{zr}}{E_z} & \frac{1}{E_r} & \frac{\nu_{\theta r}}{E_\theta} & 0 \\ \frac{\nu_{z\theta}}{E_z} & \frac{\nu_{r\theta}}{E_r} & \frac{1}{E_\theta} & 0 \\ 0 & 0 & 0 & \frac{1}{G_{z\theta}} \end{pmatrix} \begin{pmatrix} \Delta\sigma_z \\ \Delta\sigma_r \\ \Delta\sigma_\theta \\ \Delta\tau_{z\theta} \end{pmatrix} \quad (6.4)$$

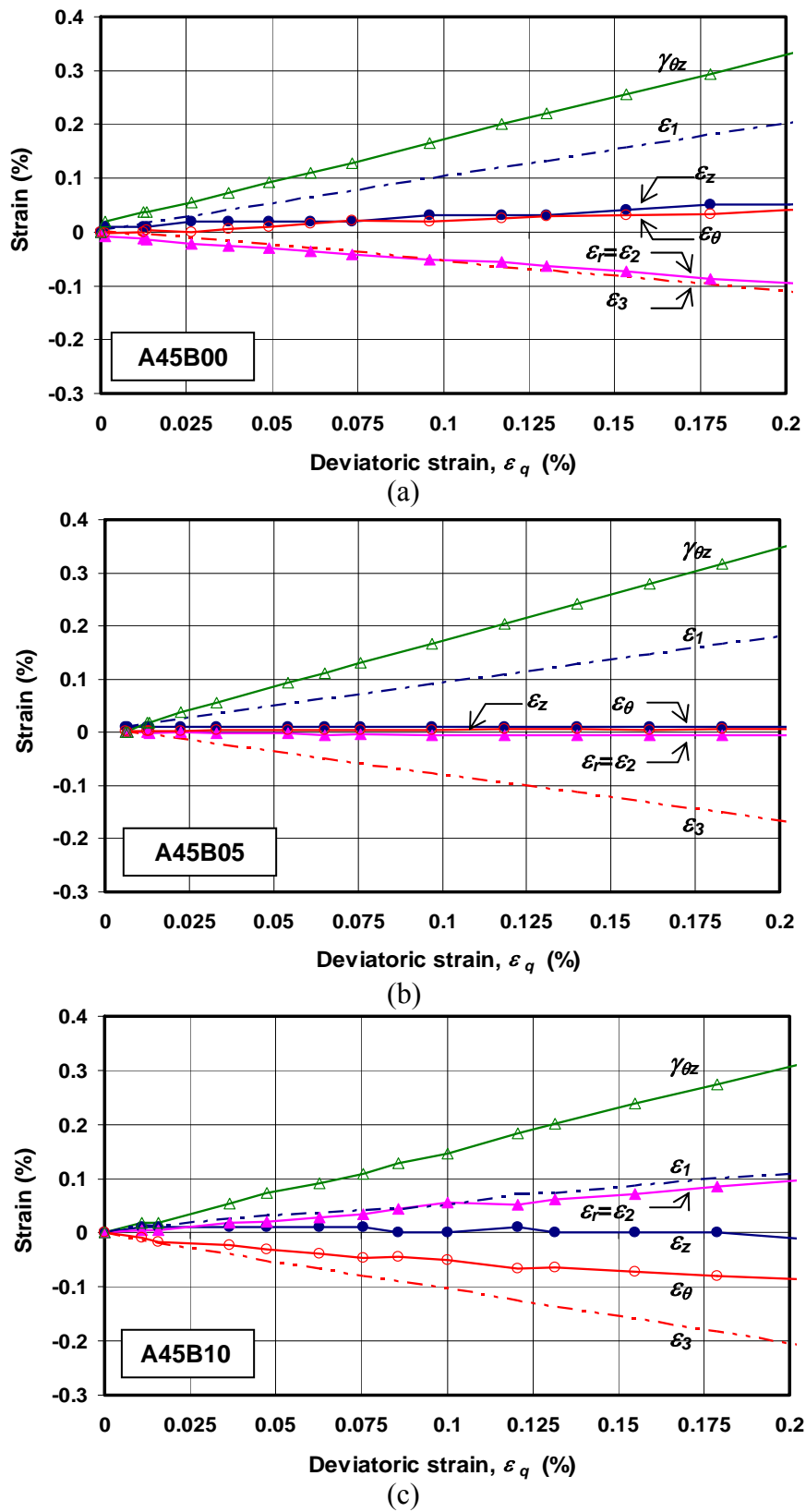


Figure 6.24 Relationships between strains in A45B00, A45B05 and A45B10 tests

### 6.6.2 Plane strain condition

Figure 6.25 shows relationships between strain components of tests with  $b=0.5$ . These tests are performed in order to model plane-strain condition where  $\varepsilon_2$  is supposed to be negligible. In case of A00B05 and A45B05, the development of  $\varepsilon_2$  is negligible. On the other hand, in case of A90B05 test shows some development of  $\varepsilon_2$  toward the final stage of the test. Therefore, the results can imply that the plane-strain condition corresponds to  $b=0.5$  for  $\alpha=0^\circ$  to  $45^\circ$ . However, as  $\alpha$  increases, this condition may correspond to a lower  $b$  value, especially when the soil approaches failure. This finding is consistent with the data of undisturbed Bangkok Clay by Kuwano & Bhatara (1989) who reported the  $b = 0.27-0.5$  for plane-strain condition. Other researches also report  $b = 0.2-0.66$  for plane-strain condition (e.g. Kirkgard & Lade, 1993; Zdravkovic & Jardine, 1997; Prashant & Penumadu, 2004).

### 6.6.3 Directions of principal stress and strain inclination

In order to study directions of principal stress and principal stress and strain inclination relationship, these directions are derived by following equations.

$$\alpha = \frac{1}{2} \tan^{-1} \left( \frac{2 \cdot \tau_{z\theta}}{\sigma_z - \sigma_\theta} \right) \quad (6.5)$$

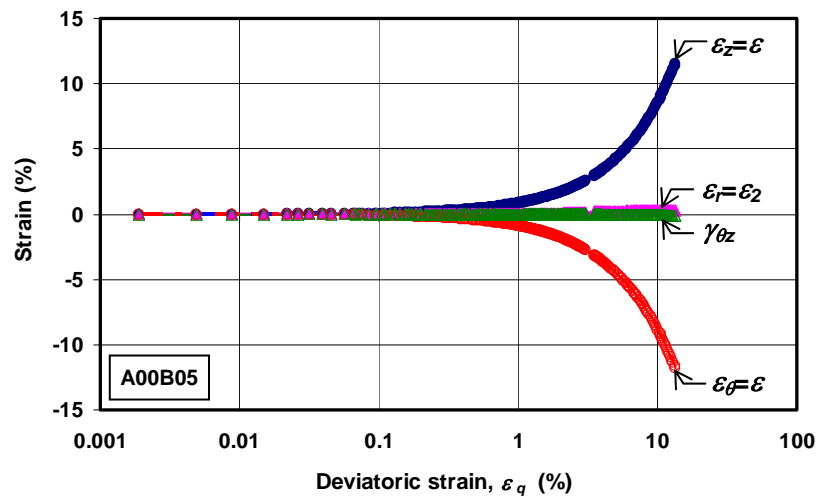
$$\alpha_\sigma = \frac{1}{2} \tan^{-1} \left( \frac{2 \cdot \Delta \tau_{z\theta}}{\Delta \sigma_z - \Delta \sigma_\theta} \right) \quad (6.6)$$

$$\alpha_\varepsilon = \frac{1}{2} \tan^{-1} \left( \frac{2 \cdot \varepsilon_{z\theta}}{\varepsilon_z - \varepsilon_\theta} \right) \quad (6.7)$$

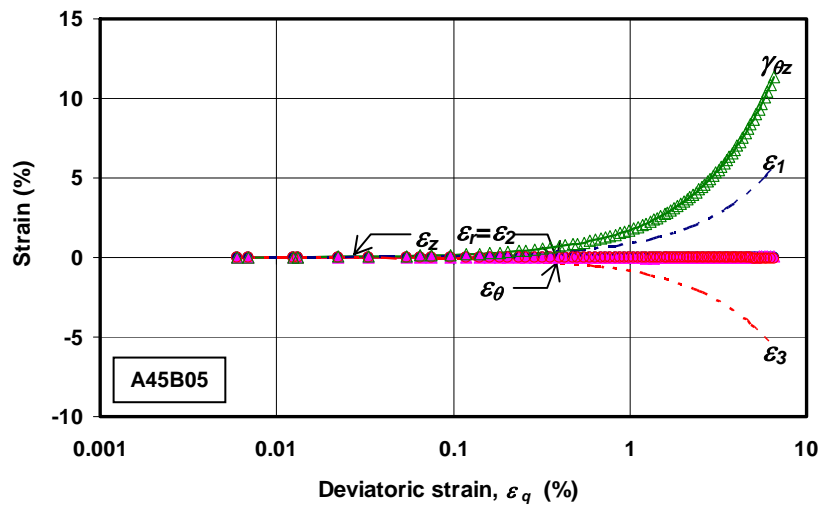
$$\alpha_\varepsilon = \frac{1}{2} \tan^{-1} \left( \frac{2 \cdot \varepsilon_{z\theta}}{\varepsilon_z - \varepsilon_\theta} \right) \quad (6.8)$$

In all tests, the principal stress direction is constant throughout the tests; therefore, the principal stress direction is identical to the principal stress increment direction ( $\alpha = \alpha_\sigma$ ). The results show that all tests with the principal stress directions coincide with the principal axes of the material ( $\alpha=0^\circ$  and  $90^\circ$ ) show coincidence of

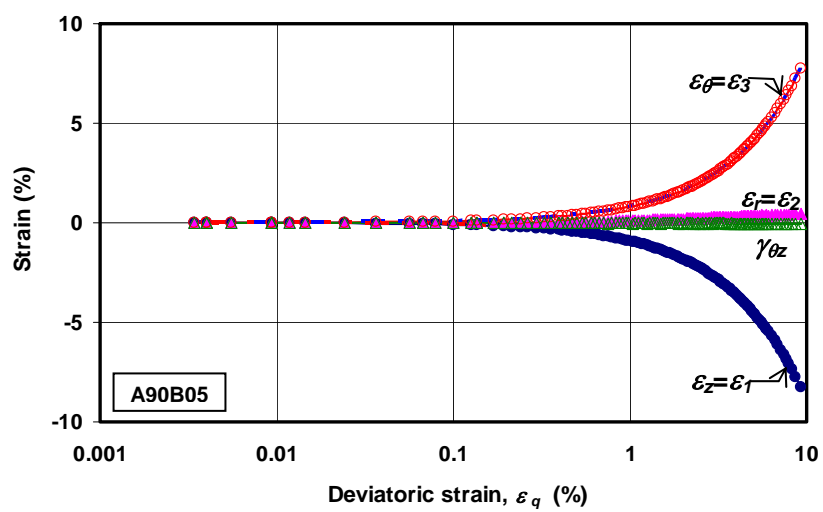
the principal stress increment and principal strain increment directions. The example of these cases is presented in Figure 6.26(a) for test A00B00. The tests which involve rotation of the principal stress direction from the principal axes of the material ( $\alpha=45^\circ$ ) show some deviation between the principal stress increment and principal strain increment directions. For tests A45B00 and A45B05, the principal stress increment and principal strain increment directions show small deviation of up to  $\pm 2^\circ$  at  $\varepsilon_q = 0.06\%$  as shown in Figure 6.26(b). However, test A45B10 shows difference by up to  $\pm 17^\circ$  during the beginning of shearing stage ( $\varepsilon_q = 0.06\%$ ) before gradually converging to remain within  $\pm 1^\circ$  after  $\varepsilon_q$  exceeds  $\sim 3\%$  as shown in Figure 6.26(c). The difference of the observed principal stress increment and principal strain increment directions during the beginning of shearing is due to the cross-anisotropic elastic characteristics of the material. During undrained shearing, both directions are converging due possibly to: (i) the adjustment of principal axes of the material to coincide with the principal stress increment direction and (ii) the evolution of plastic behavior. This observed behavior during undrained shearing is similar to the results during inclined consolidation of quartzitic silt reported by Zdravkovic & Jardine (2001).



(a) A00B05

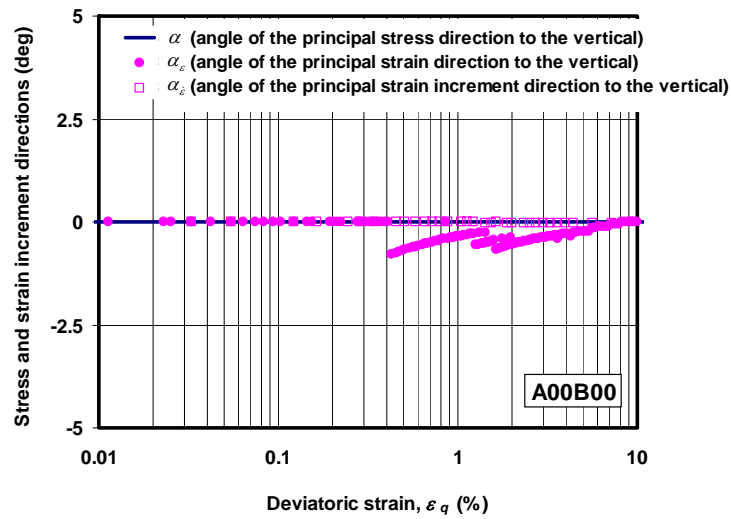


(b) A45B05

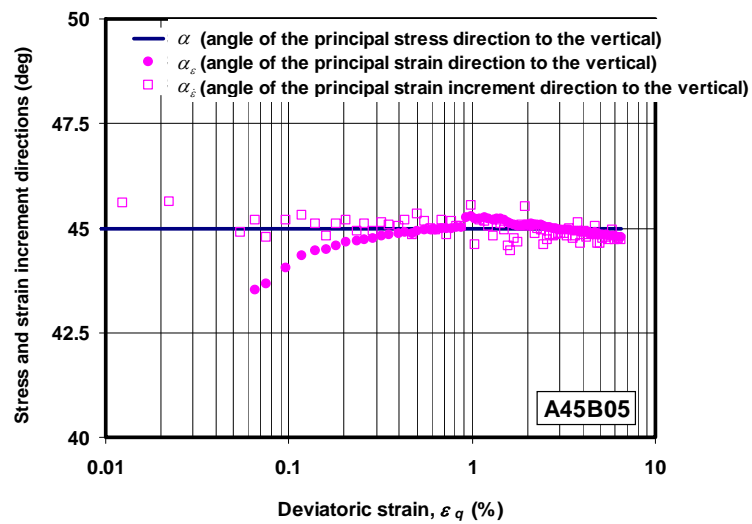


(c) A90B05

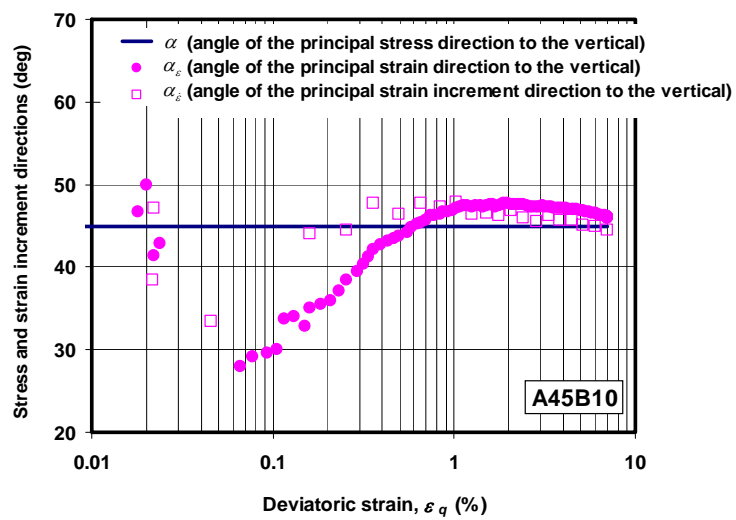
Figure 6.25 Relationships between individual strains



(a) A00B00



(b) A45B05



(c) A45B10

Figure 6.26 Evolutions of principal stress and strain increment directions

## 6.7 Failure surface

Figure 6.27 shows the variations of  $\phi_f'$  and  $M_f$  with  $b$  parameter of 2 cases, i.e. (a)  $\alpha=0^\circ&90^\circ$  and (b)  $\alpha=45^\circ$ . The predictions of  $\phi_f'$  and  $M_f$  by five commonly quoted failure criteria are also superimposed in these figures by fitting the model with the results of triaxial compression conditions. The details of the failure criteria and the parameters used are summarized in Table 6.8. The results show that the variations of  $\phi_f'$  and  $M_f$  can be best approximated by the Drucker-Prager failure criterion. Table 6.9 also shows the summarized  $\phi_f'$  and  $M_f$  in failure surface. Furthermore, the failure conditions of Bangkok Clay are also presented in deviatoric plane for a constant mean effective stress of  $p'=100$  kPa as shown in Figure 6.28 for 2 cases, i.e. (a)  $\alpha=0^\circ&90^\circ$  and (b)  $\alpha=45^\circ$ . Figure 6.28(a) ( $\alpha=0^\circ&90^\circ$ ) shows the failure points symmetrically about the vertical axis ( $\sigma_z'$ ) due to the hypothesis of cross-anisotropy of the specimen obtained from the field. The five commonly quoted failure envelopes, the details of which are shown in Table 6.8, are compared with the experimental data. Again, it can be seen that the Drucker-Prager failure criterion shows best fit to the experimental data. It is noted that the results of A90B00 (on  $\sigma_x'$ - and  $\sigma_y'$ -axis) are smaller and do not fit the proposed failure criterion well. Figure 6.28(b) ( $\alpha=45^\circ$ ) has the experimental data for only 1/6 of the full failure envelope; however, failure points are plotted in six-fold symmetry about the origin due to the hypothesis of isotropy which is postulated from the case of  $\alpha=0^\circ&90^\circ$ . It can be seen that the Drucker-Prager failure criterion still fit the results well. The Drucker-Prager failure criterion found for undisturbed Bangkok Clay from this study is consistent with the data reported earlier by Kuwano & Bhattarai (1989). However, other studies on undisturbed clays report that their failure envelopes are rather similar to Lade-Duncan type and also show anisotropic characteristics (e.g. Kirkgard & Lade, 1993; Callisto & Callabresi, 1998; and Callisto & Rampello, 2002).

Figure 6.28 also presented the plastic strain increment vectors on the principal strain axes which are superimposed on the principal stress axes. The plastic strain increments are taken at  $\varepsilon_q \approx 5\%$  to avoid effects of strain non-uniformity and it assumes that the strains at this stage are fully plastic. The results show that the strain

increment vectors appear to be normal to the Drucker-Prager failure envelope. This indicates that the failure envelope and the plastic potential are identical corresponding to an associated flow rule. The Lode angles of stress and strain increment are summarized in Table 6.10. This finding is also consistent with the data of undisturbed Bangkok Clay reported earlier by Kuwano & Bhattarai (1989). Other studies on undisturbed clays report that their plastic flow rules are both associative (e.g. Callisto & Calabresi, 1998) and non-associative (e.g. Kirkgard & Lade, 1993; and Callisto & Rampello, 2002).

Table 6.8 Failure criteria (after Potts & Zdravkovic, 1999)

| Failure criteria   | Parameters   |
|--|--|
| <u>Mohr-Coulomb model</u><br>Failure criterion: $f = \sqrt{3J_2} - M(\theta)(p'+c'\cot\phi') = 0$<br>where $M(\theta) = \frac{3\sin\phi'}{\sqrt{3}\cos\theta + \sin\theta\sin\phi'}$                     | $c' = 0$<br>$\phi' = 32^\circ$ (for $\alpha=0^\circ&90^\circ$ )<br>$= 27^\circ$ (for $\alpha=45^\circ$ )                             |
| <u>Extended Tresca model</u><br>Failure criterion: $f = \sqrt{J_2} \cos\theta - k = 0$<br>where $M(\theta) = \frac{\sqrt{3}k}{p'\cos\theta}$   | $k = 65$ kPa (for $\alpha=0^\circ&90^\circ$ )<br>$= 54$ kPa (for $\alpha=45^\circ$ )   |
| <u>Drucker-Prager model</u><br>Failure criterion: $f = \sqrt{3J_2} - M(\phi')(p'+c'\cot\phi') = 0$<br>where $M(\phi') = \frac{6\sin\phi'}{3 - \sin\phi'}$  | $c' = 0$<br>$\phi' = 32^\circ$ (for $\alpha=0^\circ&90^\circ$ )<br>$= 27^\circ$ (for $\alpha=45^\circ$ )                             |
| <u>Lade-Duncan model</u><br>Failure criterion: $f = \sqrt{3J_2} - M(\theta)(p'+c'\cot\phi') = 0$<br>where $M(\theta)$ are roots of:<br>$2M(\theta)^3 \sin 3\theta + 9M(\theta)^2 - 10.67 = 0$            | $c' = 0$<br>$\phi' = 32^\circ$ (for $\alpha=0^\circ&90^\circ$ )<br>$= 27^\circ$ (for $\alpha=45^\circ$ )<br>$\eta = 27.40, m = 0.40$ |
| <u>Matsuoka-Nakai model</u><br>Failure criterion: $f = \sqrt{3J_2} - M(\theta)(p'+c'\cot\phi') = 0$<br>where $M(\theta)$ are roots of:<br>$24.25M(\theta)^3 \sin 3\theta + 82.11M(\theta)^2 - 84.32 = 0$ | $c' = 0$<br>$\phi' = 32^\circ$ (for $\alpha=0^\circ&90^\circ$ )<br>$= 27^\circ$ (for $\alpha=45^\circ$ )                             |

Note:  $\theta$  = Lode angle

$$\phi' = \sin^{-1} \left[ \frac{3M}{6\sqrt{1-b+b^2} - (2b-1)M} \right]$$



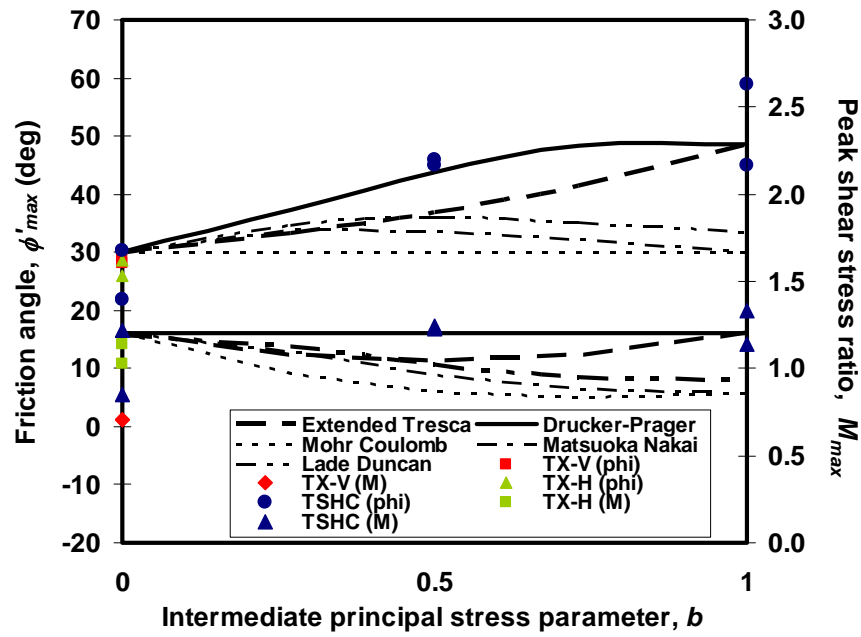
Table 6.9 Summarized  $\phi'_{max}$  and  $M_{max}$  in failure surface

| Test No. | $\alpha$<br>(°) | $b$ | $\phi'_{max}$<br>(°) | $M_{max}$ | Extended Tresca      |           | Drucker Prager       |           |
|----------|-----------------|-----|----------------------|-----------|----------------------|-----------|----------------------|-----------|
|          |                 |     |                      |           | $\phi'_{max}$<br>(°) | $M_{max}$ | $\phi'_{max}$<br>(°) | $M_{max}$ |
| A00B00   | 0               | 0   | 30.4                 | 1.22      | 32.3                 | 1.3       | 32.3                 | 1.30      |
| A00B05   | 0               | 0.5 | 45                   | 1.22      | 40.55                | 1.13      | 48.64                | 1.30      |
| A00B10   | 0               | 1   | 59                   | 1.33      | 56.08                | 1.3       | 56.08                | 1.30      |
| A45B00   | 45              | 0   | 27.3                 | 1.10      | 26.54                | 1.05      | 26.54                | 1.05      |
| A45B05   | 45              | 0.5 | 40.2                 | 1.11      | 31.70                | 0.91      | 37.32                | 1.05      |
| A45B10   | 45              | 1   | 34.6                 | 1.00      | 39.52                | 1.05      | 39.52                | 1.05      |
| A90B00   | 90              | 0   | 21.8                 | 0.85      | 28.85                | 1.15      | 28.85                | 1.15      |
| A90B05   | 90              | 0.5 | 45.9                 | 1.24      | 35.57                | 1.04      | 41.60                | 1.15      |
| A90B10   | 90              | 1   | 45                   | 1.15      | 45.34                | 1.15      | 45.34                | 1.15      |

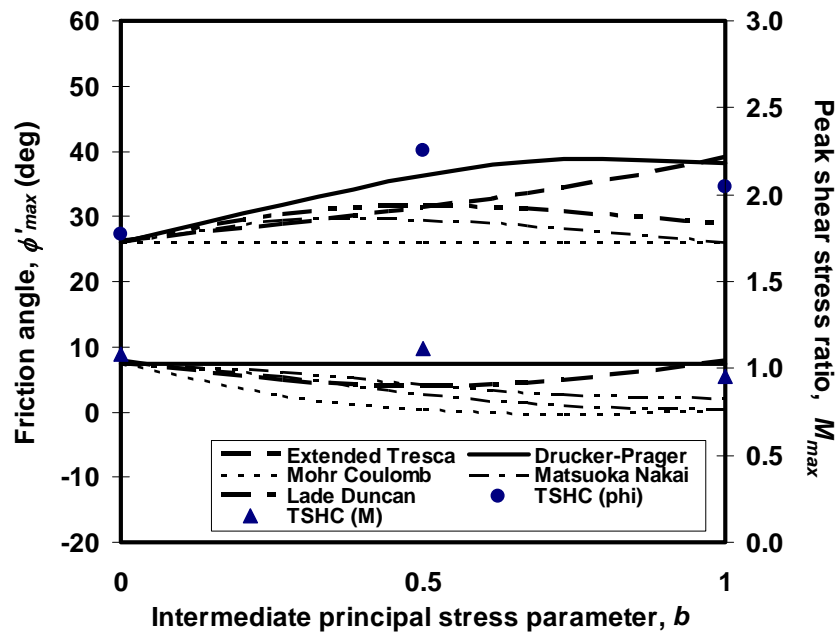
Table 6.10 Lode angles of stress and strain increment

| Test No. | $\theta_{\sigma}$<br>(°) | $\theta_{\epsilon}^*$<br>(°) | $\theta_{\perp}(\text{extended Tresca})$<br>(°) | $\theta_{\perp}(\text{Drucker Prager})$<br>(°) |
|----------|--------------------------|------------------------------|---|--|
| A00B00   | -30                      | -31.90                       | -30   | -  |
| A00B05   | 0                        | 0                            | 0   | 0  |
| A00B10   | +30                      | +30.96                       | +30   | -  |
| A45B00   | -30                      | -30.67                       | -30   | -  |
| A45B05   | 0                        | +0.17                        | 0   | 0  |
| A45B10   | +30                      | +30.19                       | +30   | -  |
| A90B00   | -30                      | -29.48                       | -30   | -  |
| A90B05   | 0                        | +0.05                        | 0   | 0  |
| A90B10   | +30                      | +30.90                       | +30   | -  |

Remark; \* at  $\epsilon_q=5\%$

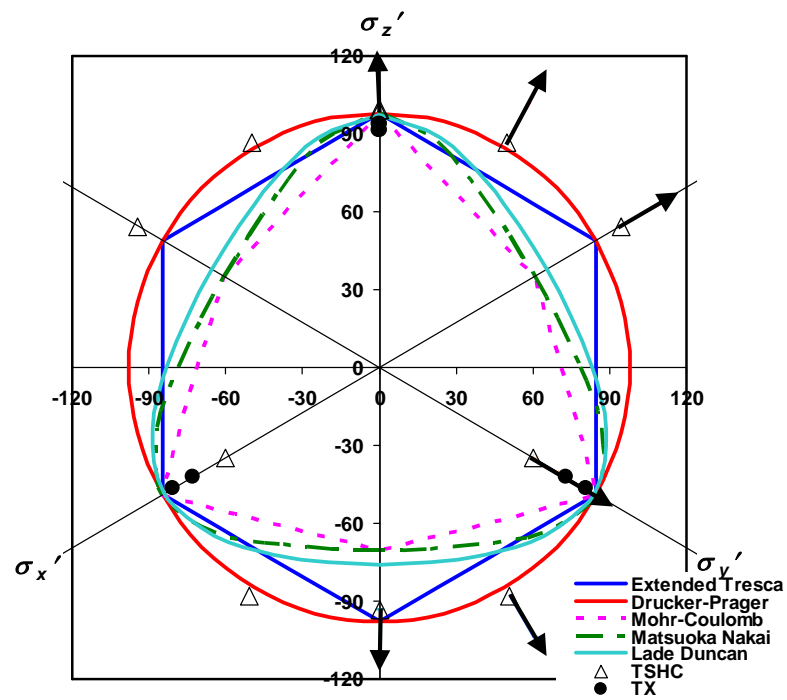


(a)

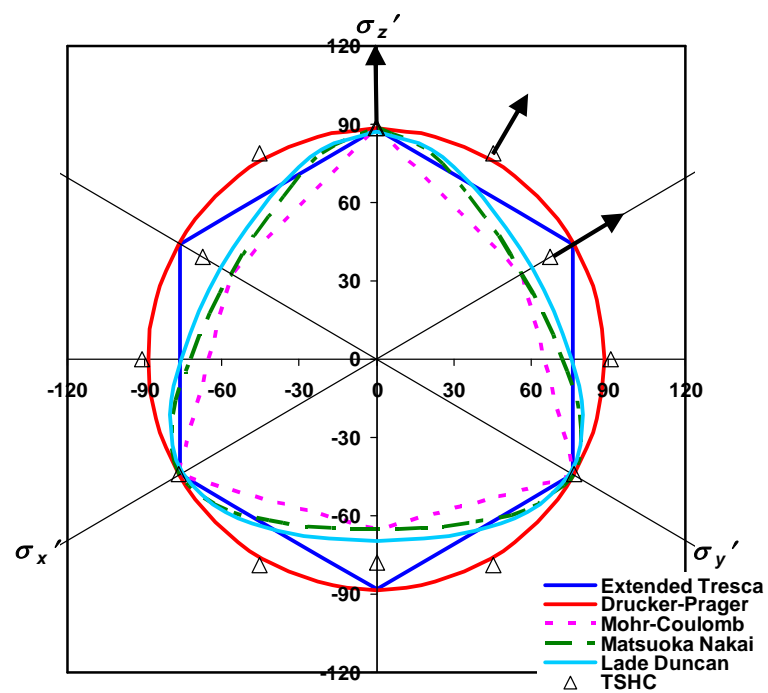


(b)

Figure 6.27 Variation of  $\phi'_{max}$  and  $M_{max}$  at failure versus  $b$  parameter for (a)  $\alpha=0^\circ$  &  $90^\circ$  and (b)  $\alpha=45^\circ$



(a)



(b)

Figure 6.28 Three-dimensional failure surface for Bangkok Clay in an octahedral plane ( $p \approx 100$  kPa) (a)  $\alpha = 0^\circ$  &  $90^\circ$  and (b)  $\alpha = 45^\circ$

## CHAPTER VII

### Conclusions

The research finding can be separated into two parts followed in the laboratory testing i.e. Triaxial test and Torsional shear hollow cylinder test.

#### 7.1 Deformation under isotropic consolidation

Multiple recompression lines obtained from undisturbed Bangkok Clay samples were nearly parallel throughout the consolidation path. The recompression curves were non-linear with the average Cam-Clay swelling parameter,  $\kappa=0.093$  calculated from the relationship of  $\kappa=\Delta e/\Delta \ln p'$ . This value corresponded to the average recompression ratio  $RR=2.7\%$  derived from  $C_r=\Delta \varepsilon_{vol}/\Delta \log p'$ . This result is close to the typical value of  $RR$  of 2.77 from the oedometer test reported by Shibuya and Tamrakar (1999).

#### 7.2 Cross-Anisotropic elastic parameter of Bangkok Clay

Most natural soils are deposited through a process of sedimentation which is followed by one-dimensional consolidation under accumulative overburden pressure for a long period of time. In this condition, the depositions of natural soil would be horizontally layered in either microscopic scale or macroscopic scale or both. This can be suggested that natural soils should have a form of anisotropy, called cross-anisotropic, in which the vertical axis (normal to the bedding plane) at any points is an axis of radial symmetry. The investigation of the complete set of cross-anisotropic elastic parameters of Bangkok Clay was presented in this study.

$$G_{vh}=1700F(e)p^{0.4} \quad (7.1)$$

$$G_{hh}=1450F(e)p^{0.4}$$

$$E_v=2850F(e)p^{0.4}$$

$$E_h=2250F(e)p^{0.4}$$

$$\nu_{vh} = 0.088$$

$$\nu_{hv} = 0.070$$

$$\nu_{hh} = 0.15$$

### 7.3 Anisotropy of Bangkok Clay

The deformation under isotropic consolidation is anisotropic. The specimens are stiffer in the horizontal direction. From torsional shear hollow cylinder test result, the average ratio is around 2.34. This result agrees with the result of anisotropic deformation characteristic of Bangkok Clay observed by triaxial test as reported in chapter 4. The average ratio is around 2.14. The average ratio of anisotropic deformation in torsional shear hollow cylinder test shows slightly higher than those obtained from triaxial test. The different might be caused by the capability of external and local measurement systems in the torsional shear hollow cylinder and triaxial results, respectively.

The ratios of  $G_{hv}/G_{vh}$  and  $E_h/E_v$  observed from triaxial test are 0.85 and 0.80, respectively. The anisotropy of undrained Young's modulus ( $E_{u,90}/E_{u,0}$ ) observed from torsional shear hollow cylinder is found to be approximately 0.66. An inconsistency is found with the data of San Francisco Bay Mud, which is also of similar stress history to Bangkok Clay. Therefore, the effects of stress history on undrained stiffness anisotropy should require further investigation.

### 7.4 Effects of $\alpha$ and $b$ on Bangkok Clay characteristic

Several behaviors are investigated and discussed including: (i) stress-strain and pore pressure behaviors, (ii) stiffness characteristics, and (iii) strength characteristics. The study shows evident influences of direction of  $\alpha$  and magnitude of  $b$  on the observed behaviors which can be summarized in Table 7.1. Most of the obtained experimental results from Bangkok Clay are more or less similar to previous findings reported for undisturbed and reconstituted clays. However, the result of stiffness of

Bangkok Clay is quite unique from other studies where it is found that  $b$  has small effects on shear stiffness. This characteristic may require further investigation.

**Table 7.1** Summary of effects of  $\alpha$  and  $b$

| Parameters            | Effects as $\alpha$ increases  | Effects as $b$ increases                               |
|-----------------------|--|--|
| $s_u/p_o'$            | Decreases, especially when $\alpha$ increases from $0^\circ$ to $45^\circ$ | Somewhat decreases or constant                         |
| $\Delta u_f/p_o'$     | Increases, especially when $\alpha$ increases from $0^\circ$ to $45^\circ$ | Increases, except when $\alpha = 45^\circ$             |
| $\phi_f'$             | Minimum at $\alpha = 45^\circ$   | Increases, especially when $b$ increases from 0 to 0.5 |
| $M_f$                 | Minimum at $\alpha = 45^\circ$   | Constant   |
| $G_{oct,0.01\%}/p_o'$ | Decreases  | Small effects  |

### 7.5 Failure surface and plastic potential

Both failure surface and plastic potential in deviatoric plane of Bangkok Clay are found to be isotropic and of circular shape (Drucker-Prager) which also implies associated flow rule. These results of Bangkok Clay are quite unique when compared with those of other clays. Most of other undisturbed clays are represented to have their failure envelopes similar to Lade-Duncan type with anisotropic characteristic. Moreover, the plastic flow rule in deviatoric plane of other clays is mostly non-associative. As a result, if Bangkok Clay is modeled by fitting non-circular failure surface in deviatoric plane (e.g. Mohr-Coulomb) to triaxial compression data, as always done in normal finite element work, the strength analysis results of plane-strain condition should be underestimated (Grammatikopoulou et al., 2007).

Moreover, the failure surface shrinks as  $\alpha$  increases from  $0^\circ$  to  $45^\circ$ , when it reaches its minimum, and expands as  $\alpha$  further increases from  $45^\circ$  to  $90^\circ$ . As a result, if Bangkok Clay is modeled by fitting constant-size circular failure surface in deviatoric plane (e.g. Drucker-Prager) to triaxial compression data, as commonly assumed in any analysis, the strength analysis results should be overestimated.

It is note that the failure surface obtained in this study is considered at the maximum stress which corresponded to large-strain level. Therefore if the result is

considered in smaller range of the strain, the failure surface might not present isotropic behavior and circular shape. More observation may require further investigation.

## REFERENCES

- Afifi, S. S. and Richart, F. E. Jr. 1973. Stress-history effects on shear modulus of soils. Soils and Foundations 13, 1: 77-95.
- Atkinson, J. H. 2000. Non-linear soil stiffness in routine design. Géotechnique 50, 5: 487-508.
- Atkinson, J. H., Richardson, D. and Stallebarass S. E. 1990. Effect of recent stress history on the stiffness of overconsolidated soil. Géotechnique 40, 4: 531-540.
- Bishop, A. W. 1966. The strength of soils as engineering materials. 6<sup>th</sup> Rankine Lecture. Géotechnique 16, 2: 91-128.
- Black, D. K. and Lee, K. L. 1972. Saturating laboratory samples by back pressure. Journal of the Soil Mechanics and Foundations Division, ASCE 99, SM1: 75-93.
- Brignoli, E. G. M., Gotti, M. and Stokoe, K. H., II. 1996. Measurement of shear waves in laboratory specimens by means of piezoelectric transducers. Geotechnical Testing Journal, ASTM 19, 4: 384-397.
- Burland, J. B. 1989. Small is beautiful - the stiffness of soils at small strains. Canadian Geotechnical Journal 26: 499-516.
- Callisto, L. and Calabresi, G. 1998. Mechanical behaviour of a natural soft clay. Géotechnique 48, 4: 495-513.
- Callisto, L. and Rampello S. 2002. Shear strength and small-strain stiffness of a natural clay under general stress conditions. Geotechnique 52, 8: 547-560.
- Coop, M. R. and Jovicic, V. 1999. The influence of state on the very small strain stiffness of sands. Proc. 2nd Intl. Sym. on pre-failure deformation characteristics of geomaterials, (IS Torino '99) Balkema, Rotterdam: 175-181.



- Cuccovillo, T. and Coop, M. P. 1997. The measurement of local axial strains in triaxial test using LVDTs. Géotechnique 47, 1: 167-171.
- Daramola, O. 1980. Effect of consolidation age on stiffness of sand. Géotechnique 30, 2: 213-216.
- Dyvik, R. and Madshus, C. 1985. Laboratory Measurements of  $G_{\max}$  Using Bender Elements. Proc. of the ASCE Annual Convention: Advances in the art of testing soils under cyclic condition, Detroit, ASCE: 185-196.
- Georgiannou, V. N., Rampello, F. and Silvestri. 1991. Static and dynamic measurement of undrained stiffness on natural OC clay. Proc. of the European conference on soil mechanics, Florence 1: 91-96.
- Graham, J. and Houlsby, G. T. 1983. Anisotropic elasticity of a natural clay. Géotechnique 33, 2: 165-180.
- Grammatikopoulou, A. Zdravkovic, L., and Potts, D. M. 2007. The effect of the yield and plastic potential deviatoric surfaces on the failure height of an embankment. Geotechnique 57, 10: 795-806.
- Hardin, B. O. 1978. The natural of stress-strain behaviour for soils. Earthquake Engineering and Soil Dynamics, Proc. of the ASCE Geotechnical Engineering Division Specialty Conference 1: 3-90.
- Hardin, B. O. and Black W. L. 1968. Vibration modulus of normally consolidated clay. Journal of the Soil Mechanics and Foundations Division, ASCE 94, SM2: 353-369.
- Hardin, B. O. and Blandford, G. E. 1989. Elasticity of particulate materials. Journal of Geotechnical Engineering, ASCE 115, 6.
- Hardin, B. O. and Ritchart, F. E., Jr. 1963. Elastic wave velocities in granular soils. Journal of the Soil Mechanics and Foundations Division, ASCE 89, SM1: 33-65.

- Hight, D. W., Bennel, J. D, Chana, B., Davis, P. D, Jardine, R. J and Porovic, E. 1997. Wave velocity and stiffness measurements of the Crag and Lower London Tertiaries at Sizewell. Géotechnique 47, 3: 451-474.
- Hight, D. W., Gens, A. and Symes, M. J. 1983. The development of a new hollow cylinder apparatus for investigating the effects of principal stress rotation in soils. Géotechnique 33, 4: 355-383.
- Hight, D. W. and Higgins, K. G. 1994. An approach to the prediction of ground movements in engineering practice: Background and applications. Pre-failure deformation of geomaterials, Balkema, Rotterdam 2: 909-945.
- Houlsby, G. T. and Wroth, C. P. 1991. The variation of shear modulus of a clay with pressure and overconsolidation ratio. Soils and Foundation 31, 3: 138-143.
- Ishihara, K. 1996. Soil Behaviour in Earthquake. Géotechnique Clarendon Press, Oxford.
- Ismail, M. A. and Rammah, K. I, 2005. Shear-plate transducers as a possible alternative to bender elements for measuring  $G_{max}$ . Géotechnique 55, 5: 403-407.
- Iwasaki, T., Tatsuoka, F. and Takagi, Y. 1978. Shear moduli of sands under cyclic torsional shear loading. Soils and Foundations 18, 1: 39-56.
- Jamiolkowski, M., Lancellotta, R., and Lo Presti, D. C. F. 1994. Remarks on the stiffness at small strains of six Italian clays. Proc. of the 1<sup>st</sup> International Symposium on Pre-failure Deformation Characteristics of Geomaterials, IS-Hokkaido-94 (eds. Shibuya et al., Balkema, Rotterdam) 2: 817-836.
- Jamiolkowski, M., Lo Presti, D. C. F. and Pallara, O. 1995. Role of In-Situ Testing in Geotechnical Earthquake Engineering. Proc. of the 3<sup>rd</sup> International Conference of Recent Advances in Geotechnical Earthquake Engineering and Soil Dynamics, St. Louis, Missouri 3: 1523-1546.

- Jardine, R. T. 1994. One perspective of the pre-failure deformation characteristic of some geomaterials. Proc. of the 1<sup>st</sup> International Symposium on Pre-failure Deformation Characteristic of some Geomaterials, IS-hokkaido-94, (eds. Shibuya et al., Balkema, Rotterdam) 2: 855-885.
- Jardine, R. J., Potts, D. M., Fourie, A. B., and Burland, J. B. 1986. Studies of the influence of non-linear stress-strain characteristics in soil-structure interaction. Géotechnique 36, 3: 377-396.
- Jardine, R. T., Potts, D. M., St. John, H. D. and Hight, D. W. 1991. Some applications of a non-linear ground model. Proc. 10<sup>th</sup> Eur. Conf. Soil Mech. and Foundn Engrg, Florencel: 223-228.
- Jardine, R. J., Zdravkovic, L., Porovic, E., 1997. Anisotropic consolidation including principal stress rotation: experiments, results and practical applications. In Proc. of the 14th International Conference on Soil Mechanics and Foundation Engineering 4. A. A. Balkema, Hamburg, Germany: 2165–2168.
- Jovicic, V., and Coop, M. R. 1997. Stiffness of coarse-grained soils at small strains. Géotechnique 47, 3: 545-561.
- Jovicic, V. and Coop, M. R. 1998. The Measurement of Stiffness Anisotropy in Clays with Bender Element Tests in the Triaxial Apparatus. Geotechnical Testing Journal, ASTM 21, 1: 3-10.
- Kim, T. C. and Novak, M. 1974. Dynamic properties of some cohesive soils of Ontario. Canadian Geotechnical Journal 18: 371-389.
- Kirkgard M. M. and Lade P. V. 1993. Anisotropic three-dimensional behavior of a normally consolidated clay. Canadian Geotechnical Journal 30: 848-858.
- Kokusho, T. 1980. Cyclic triaxial test of dynamic soil properties for wide strain range. Soils and Foundations 20, 2: 45-60.
- Kokusho, T., Yoshioka, Y. and Esashi, Y. 1982. Dynamic properties of soft clay for wide strain range. Soils and Foundation 22, 4: 1-18.

- Kumruzzaman, Md. and Yin J. H. 2010. Influence of principal stress direction and intermediate principal stress on the stress-strain-strength behaviour of completely decomposed granite. Canadian Geotechnical Journal 47: 164-179.
- Kuwano, R. 1999. The stiffness and yielding anisotropy of sand. PhD. Thesis, Imperial College of Science, Technology and Medicine, University of London.
- Kuwano, J. and Bhattarai, B. N. 1989. Deformation characteristics of Bangkok Clay under three dimensional stress conditions. Geotechnical Engineering, SEAGS 20, 2: 111-137.
- La Rochelle P., Track B., Tavenas F. and Roy M. 1974. Failure of test embankments on sensitive Champlain clay deposits. Canadian Geotechnical Journal 11: 142-164.
- Lam, W. K. and Tatsuoka, F. 1988a. Effects of initial anisotropic fabric and  $\sigma_2$  on strength and deformation characteristics of sand. Soils and Foundations 28, 1: 89-106.
- Lam, W. K. and Tatsuoka, F. 1988b. Triaxial compression and extension strength of sand affected by strength anisotropy and sample slenderness. Advanced triaxial testing of soil and rock. ASTM STP 977, Ed. Donaghe R. T., Chaney R. C. and Silver M. L: 655-666.
- Lo Presti, D. C. F. 1994. General report: Measurement of shear deformation of geomaterials in the laboratory. Proc. of the 1<sup>st</sup> International Symposium on Pre-failure Deformation Characteristics of Geomaterials, IS-Hokkaido-94 (Eds. Shibuya et al., Balkema, Rotterdam) 2: 1067-1088.
- Lo Presti, D. C. F., Pallara, O., Lancellotta, R., Armandi, M. and Maniscalco, R. 1993. Monotonic and cyclic loading behavior of two sands at small strains. Geotechnical Testing Journal, ASTM 18, 1: 15-31.

- Mair, R. J. 1993. Developments in geotechnical engineering research: application to tunnels and deep excavations. Civil Engineering, Proc. of the Institute of Civil Engineers, UK 93 (Feb): 27-41.
- Marcuson, W. F., III and Wahls, H. E. 1972. Time Effects on Dynamic Shear modulus of Clays. Journal of the Soil mechanics and Foundation Division, ASCE 98, SM12: 1359-1373.
- Menkiti, C. O. 1995. Behaviour of clay and clayey-sand with particular reference to principal stress rotation. Msc. Dissertation, Imperial College of Science, Technology and Medicine, University of London.
- Menzies, B. K. 1988. A computer controlled hydraulic triaxial testing system. Advanced Triaxial Testing of Soil and Rock, ASTM STP 977 (Eds. Donaghe et al., American Society for Testing Materials): 82-94.
- Miura, K., Miura, S. and Toki, S. 1986. Deformation behaviour of anisotropic dense sand under principal stress axis rotation. Soils and Foundations 26, 1: 36-52.
- Nakata, Y., Hyodo, M., Murata, H. and Yasufuku, N. 1998. Flow deformation of sands subjected to principal stress rotation. Soils and Foundations 38, 2: 115-128.
- Nguyen, A. M. 2006. An investigation of the anisotropic stress-strain-strength characteristics of an Eocene clay. PhD. Thesis, Imperial College of Science, Technology and Medicine, University of London.
- Nishimura, S., Minh, N. A., and Jardine, R. J. 2007. Shear strength anisotropy of natural London Clay. Geotechnique 57, 1: 49-62.
- Oda, M., Koishikawa, I. and Higuichi, T. 1978. Experimental Study of Anisotropic Shear Strength of Sand by Plane Strain Test. Soils and Foundations 18, 1: 35-38.

- Porovic, E. 1995. Investigations of soil behaviour using a resonant column torsional shear hollow cylinder apparatus. PhD. Thesis, Imperial College of Science, Technology and Medicine, University of London.
- Prashant, A. and Penumadu, S. 2004. Effect of intermediate principal stress on overconsolidated kaolin clay. Journal of Geotechnical and Geoenvironmental Engineering, ASCE 130, 3: 284-292.
- Prashant, A. and Penumadu, D. 2005. A laboratory study of normally consolidated kaolin clay. Canadian Geotechnical Journal 42: 27-37.
- Prashant, A. and Penumadu, S. 2007. Effect of microfabric on mechanical behavior of kaolin clay using cubical true triaxial testing. Journal of Geotechnical and Geoenvironmental Engineering, ASCE 133, 4: 433-444.
- Rampello, S., Silvestri, F. and Viggiani, G. 1994. The dependence of small strain stiffness on stress on stress state and history for fine grained soils: the example of Vallericca clay. Proc. of the 1<sup>st</sup> International Symposium on Pre-failure Deformation Characteristics of Geomaterials, Sapporo 1: 273-278.
- Rampello, S., Viggiani, G. and Amorosi, A. 1997. Small strain stiffness of reconsolidated clay compressed along constant triaxial effective stress ratio paths. Géotechnique 47, 3: 475-489.
- Reinaldo, R. 2003. The anisotropic stress-strain-strength behaviour of brittle sediments. PhD. Thesis, Imperial College of Science, Technology and Medicine, University of London.
- Roesler, S. K. 1979. Anisotropy Shear Modulus due to Stress Anisotropy. Journal of the Geotechnical Engineering Division, ASCE 105, GT7: 871-880.
- Saada, A. S. and Townsend, F. C. 1981. State of the art: Laboratory strength testing of soils. Laboratory shear strength of soil, ASTM STP 740: 7-77.
- Sayão, A. and Vaid, Y. 1991. A critical assessment of stress non-uniformities in hollow cylinder test specimens. Soils and Foundations 31, 4: 349-362.

- Sayão, A and Vaid, Y. 1996. Effect of intermediate principal stress on the deformation response of sand. Canadian Geotechnical Journal 33: 822-828.
- Seah, T. H. and Lai, K. C. 2003. Strength and Deformation Behavior of Soft Bangkok Clay. Geotechnical Testing Journal, ASTM 26, 4: 421-431.
- Seed, H. B. 1979. Considerations in the earthquake-resistant design of earth and rockfill dams. Géotechnique 29, 3: 215-263.
- Shibuya, S. 1985. Undrained behaviour of granular materials under principal stress rotation. PhD. Thesis, Imperial College of Science, Technology and Medicine, University of London.
- Shibuya, S., Hight, D. W. 1987. On the stress path in simple shear. Geotechnique 37, 4: 511-515.
- Shibuya, S. and Hight, D. W. 1996. Anisotropy of  $K_0$ -consolidated sand. IC internal report.
- Shibuya, S., Hight, D. W. and Jardine, R. J. 2002a. Establishing the local boundary surface of a loose sand: Hollow cylinder tests on isotropically consolidated samples. Soils and Foundations.
- Shibuya, S., Hight, D. W. and Jardine, R. J. 2002b. Local boundary surfaces of a loose sand dependent on consolidation path. Soils and Foundations.
- Shibuya, S., Hwang, S. C. and Mitachi, T. 1997. Elastic shear modulus of soft clays from shear wave velocity measurement. Géotechnique 47, 3: 593-601.
- Shibuya, S. and Tamrakar, S. B. 1999. In-situ and laboratory investigations into engineering properties of Bangkok clay. Characterization of Soft Marine Clays, Tsuchoda & Nakase (eds): 107-132.
- Shibuya, S., Tamrakar, S. B., and Theramast, N. 2001. Geotechnical site characterization on engineering properties of Bangkok Clay. Geotechnical Engineering, SEAGS 32, 3: 139-151.

- Shibuya, S. and Tanaka, H. 1996. Estimate of elastic shear modulus in Holocene soil deposits. Soils and Foundations 36, 4: 45-55.
- Shirley D. J. and Hampton L. D. 1978. Shear-wave measurements in laboratory sediments. Journal of Acoustical Society of America 63,2: 607-613.
- Simpson, B., O'Riordan, N. J. and Croft, D. D. 1979. A computer model for the analysis of ground movements in London Clay. Géotechnique 29: 149-175.
- Skempton, A. M. 1954. The pore pressure coefficient A and B. Géotechnique 4: 143-147.
- Stallebarass S. E. and Taylor R. N. 1997. The development and evaluation of a constitutive model for the prediction of ground movements in overconsolidated clay. Géotechnique 47, 2: 235-253.
- Stokoe, K. H., Hwang, S. K., Lee, J. N.-K. and Andrus, R. D. 1995. Effect of various parameters on the stiffness and damping of soils at small to medium strains. Pre-failure deformation of geomaterials, Balkema, Rotterdam 2: 785-816.
- Stokoe, K. H., II, Lee, S. H.-H., and Knox, D. P. 1985. Shear moduli measurements under true triaxial stresses. Advances in the Art of Testing Soil Under Cyclic Condition, ASCE, New York: 363-376.
- Stokoe, K. H., II, Lee, J. N.-K., and Lee, S. H.-H. 1991. Characterization of soil in calibration chambers with seismic waves calibration. Chamber Testing, Ed. A.-B. Huang, Elsevier Science Publishing: 363-376.
- Symes, M. J. 1983. Rotation of principal stresses in sand. PhD. Thesis, Imperial College of Science, Technology and Medicine, University of London.
- Symes, M. J., Gens, A. and Hight, D. W. 1984. Undrained Anisotropy and Principal Stress Rotation in Saturated Sand. Géotechnique 34, 1: 11-27.



- Tatsuoka, F. and Shibuya, S. 1991. Deformation Characteristics of Soils and Rocks from Field and Laboratory Tests. Proc. of the 9<sup>th</sup> ARCSMFE, Bangkok 1: 101-170.
- Tatsuoka, F., Sakamoto, M., Kawamura, T and Fukushima, S. 1986. Strength and deformation characteristics of sand in plane strain compression at extremely low pressures. Soils and foundations 26, 1: 65-84.
- Tavenas F, Mieussens C. and Bourges F. 1979. Lateral displacements in clay foundations under embankments. Canadian Geotechnical Journal 16: 535-550.
- Vaid, Y. P., Sivathayalan, S., Uthayakumar, M. and Eliadorani, A. 1995. Liquefaction potential of reconstituted Syncrude sand. 48th Canadian Geotechnical Conference 1: 319-328.
- Viggiani, G. and Atkinson, J. H. 1995. Stiffness of fine-grained soil at very small strains. Géotechnique 45, 2: 249-265.
- Weiler, W. A. 1988. Small strain shear modulus of clay. Proc. of a special conference on earthquake engineering and soil dynamics, Pack city: American Society of CIVIL engineers: 331-345.
- Wijewickreme, D. and Vaid, Y. 1991. Stress nonuniformities in hollow cylinder torsional experiments. Geotechnical testing journal 14, 4: 349-362.
- Wong, R. K. S, and Arthur, J. F. R. 1985. Induced and inherent anisotropy in sand. Géotechnique 35, 4: 471-481.
- Yeats, J. A. 1983. The stability of single and multistage embankments on soft clay. MSc. Dissertation, Imperial College of Science, Technology and Medicine, University of London.
- Yimsiri S. and Soga K. 2002. A review of local strain measurement systems for triaxial testing of soil. Journal of The Southeast Asian Geotechnical Society: 41-52.

- Yoshimine, M. and Ishihara, K. 1998. Flow potential of sands during liquefaction. Soils and Foundations 38, 3: 189-198.
- Yu, P. and Richart, F. E., Jr. 1984. Stress ratio effects on shear modulus of dry soils. Journal of Geotechnical Engineering, ASCE 110, 3: 331-345.
- Zdravkovic, L. 1996. The stress-strain-strength anisotropy of a granular medium under general stress conditions. PhD. Thesis, Imperial College of Science, Technology and Medicine, University of London.
- Zdravkovic, L. and Jardine, R. J. 2000. Undrained anisotropy of  $K_o$ -consolidated silt. Canadian Geotechnical Journal 37: 178-200.
- Zdravkovic, L. and Jardine, R. J. 2001. The effect on anisotropy of rotating the principal stress axes during consolidation. Geotechnique 51, 1: 69-83.
- Zdravkovic, L, Potts, D. M. and Hight, D. W. 2001. The effect of strength anisotropy on the behaviour of embankments on soft ground. Géotechnique.

## BIOGRAPHY

**Name:** Wanwarang Ratananikom  
**Date of Birth:** April 30, 1983  
**Telephone:** Mobile (+668)-1544-3350  
**E-mail:** khakhanang\_r@hotmail.com

|                   |                    |                         |                            |
|-------------------|--------------------|-------------------------|----------------------------|
| <b>Education:</b> | <b><u>YEAR</u></b> | <b><u>INSTITUTE</u></b> | <b><u>DEGREE</u></b>       |
|                   | 2005               | Burapha University      | B.Eng. Hons I (Civil Eng.) |

### **Award and Scholarship**

1<sup>st</sup> Class Honor Bachelor's degree in Civil Engineering from Burapha University  
 Award for a good performance during B.Eng from Engineering Institute of Thailand  
 Siemens Innovative Spirit of Youth Scholarship  
 AUN/SEED-Net Doctoral Degree Program Scholarship

### **Publications (International Conference Papers)**

Ratananikom, W., Yimsiri, S. and Likitlersuang, S. 2007. Development of Triaxial System for Soil Testing at Wide Strain Range: Preliminary Results. Proc. of International Symposium on Engineering, Ground Improvement and Geosynthetics for Human Security and Environmental Preservation, Bangkok, Thailand: 395-407.

Ratananikom, W. and Fukuda F. 2008. Effect of Intermediate Principal Stress on Bangkok Clay Behavior under Quasi Simple Shear Condition. The 1st Thailand-Japan International Academic Conference (TJIA 2008), Japan: 149-150.

Yimsiri S., Ratananikom W. and Likitlersuang S. 2009. Investigation of some anisotropic characteristics of Bangkok Clay. 17th ICSMGE, Egypt Vol. 1: 1068-1071.

Ratananikom, W., Yimsiri, S., Fukuda F. and Likitlersuang, S. 2010. Effects of Major Principal Stress Direction and Intermediate Principal Stress on Undrained Shear Strength of Bangkok Clay. The 17<sup>th</sup> Southeast Asian Geotechnical Conference, Geo-engineering for Natural Hazard Mitigation and Sustainable Development, Taipei, Taiwan: pp. 25-28.